(Bio)functionalization of Annealed Nanostructures for Diagnostic Applications

Lan Zhou

Thèse
de doctorat
de l'UTT

Lan ZHOU

(Bio)functionalization of Annealed Nanostructures for Diagnostic Applications

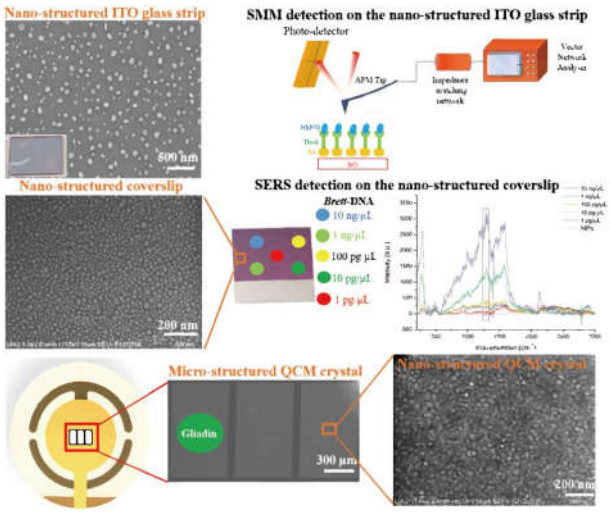

Champ disciplinaire :
Sciences pour l'Ingénieur

2021TROY0004

Année 2021

utt
UNIVERSITÉ DE TECHNOLOGIE
TROYES

THESE

pour l'obtention du grade de

DOCTEUR
de l'UNIVERSITE DE TECHNOLOGIE DE TROYES

en SCIENCES POUR L'INGENIEUR

Spécialité : MATERIAUX, MECANIQUE, OPTIQUE, NANOTECHNOLOGIE

présentée et soutenue par

Lan ZHOU

le 21 janvier 2021

(Bio)functionalization of Annealed Nanostructures for Diagnostic Applications

JURY

M. Pierre-Michel ADAM	PROFESSEUR DES UNIVERSITES	Président
Mme Monika FLEISCHER	PROFESSOR DOKTOR	Rapporteure
Mme Jasmina VIDIC	INGENIEURE DE RECHERCHE INRAE - HDR	Rapporteure
M. Jean-Louis BIJEON	PROFESSEUR UTT - HDR	Examinateur
M. Éric LESNIEWSKA	PROFESSEUR DES UNIVERSITES	Examinateur
Mme Elena Rodica IONESCU	PROFESSEURE ASSOCIEE UTT - HDR	Directrice de thèse

Acknowledgement

This thesis would not have been possible without the patient instruction, insightful criticism and expert guidance that I received from my talented supervisor, Professor Elena Rodica Ionescu, who lead me to develop genuine biosensors based on annealed gold nanoparticles. Her guidance and advice will not only help me in all the time of research and writing of the thesis, but also inspire my entire research career. Sincerely hope to be able to collaborate with Prof. Ionescu in the near future.

Apart from my great supervisor, I would also like to thank Professor Eric Lesniewska and Professor Eric Bourillot from the Department of Nanoscinces (University of Bourgogne Franche-Comte), for their great help on the analysis of the microvave spectroscopic measurements. Thanks also Professor Pierre-Michel Adam from L2n (University of Technology of Troyes) and Professor Marisa Manzano from the Department of Agriculture Food Environmental and Animal Sciences (University of Udine), for their valuable guidance in the either discussing the optical LSPR and SERS spectra and for providing the DNA strains for the optical and acoustic geno-biosensing, respectively.

Utmost gratitude and heartfelt appreciation for all the members in comité de suivi individuel (CIS), Professor Jérôme Plain, Professor Christophe Couteau and Professor Olivier Bergossi, who help to smooth my research, give me some kind suggestions and encourage me a lot.

I will not forget to express the gratitude to rest members in laboratory of Light, Nanomaterials and Nanotechnologies (L2n) at University of Technology of Troyes

(UTT), for their help in the experiments and discussion. Especially I am grateful for the talented teachers and engineers like Jeremie Beal, Régis Déturche, Seigei Koscheev, Rumyantseva Anna, Safi Jradi, Komla Nomenyo and etc, for their constantly and timely training and techonomic support of various instruments and experimental set-up, and thank giving me valuable advice and skills.

I would like to express my deepest gratitude to the members of my jury: Prof. Pierre-Michel Adam, Prof. Jean-Louis Bijeon, Prof. Monika Fleischer, Prof. Elena Rodica Ionescu, Prof. Eric Lesniewska and Ing. Jasmina Vidic.

My sincere thanks are for my special friends Simone Poggesi and Casari Bariani Giuliocesare from Department of Agriculture Food Environmental and Animal Sciences in University of Udine, and Rakesh Mittapalli from L2n at UTT, for providing a kind and pleasant working atmosphere during Sept.-Dec. 2018.

Thanks to the happy and wonderful times spent with my friends, Xiaolun, Yizhuo, Shijie, Qingmeng, Borui, Hao, Yanli, Pengcheng, Tingting and others. Specially, thanks to Binbin, Yi, Fang, Feifei, Shijian and Junze, they already got the PhD degree at UTT and they gave me a lot of appreciate suggestions in the life and science research in France.

Thanks to the financial support from China Scholarship Council (CSC) in the frame of CSC-UT/INSA, which provide me an excellent opportunity to study in France.

Finally, my special thanks would go to my beloved family and boyfriend Ao Li, who give me consistent support and encouragement during this challenging period.

Table of contents

Lists of figures

Abbreviations list

SERS	Surface enhanced raman spectroscopy
LSPR	Localized surface plasmonic resonance
QCM	Quartz crystal microbalance
SMM	Scanning microwave microscopy
AFM	Atomic force microscopy
ITO	Indium-tin oxide
Au	Gold
NPs	Nanoparticles
hHsp70	Human heat shock proteins 70kDa
BPE	1,2-bis-(4-pyridyl)-ethene
CS_2	Carbon disulfide
Cl	Chlorine
$HAuCl_4$	Chloroauric acid
AuNCs	Gold nanocages
EBL	Electron beam lithography
SPR	Surface plasmon resonance
AuNRs	Gold nanorods
NMR	Nuclear magnetic resonance
FRET	Fluorescence resonance energy transfer
BL	Biochemical luminescence
TCL	Thermo chemical luminescence
ECL	Electrochemiluminescence
GOx	Glucose oxidase
EM	Electromagnetic
SPP	Surface plasmon polariton
MNPs	Metallic nanoparticles
HIV	Human immunodeficiency virus
VNA	Vector network analyzer

HS-AFM	High-speed atomic force microscopy
MUA	11-Mercaptoundecanoic acid
NHS	N-Hydroxysuccinimide
Tris- HCl	Tris (hydroxymethyl)
ddH_2O	Deionized water
Pt-Ir	Platinum-Iridium
SiO_2	Silicon dioxide
RH	Relative humidity
NaCl	Sodium chloride
NaH_2PO_4	sodium phosphate monobasic
Na_2HPO_4	sodium phosphate dibasic
EDTA	ethylenediaminetetraacetic acid
PEG	Polyethylene glycol
PBS	Phosphate buffer saline
OD	Optical density
EC	European Union Regulation
Q-PCR	Quantitative real-time polymerase chain reaction
AuNIs	Gold nano-islands
EDC	1-ethyl-3-[3-dimethylaminopropyl]-carbodiimide hydrochloride
RELS	Resonance elastic light scattering
hcys	Homocysteine
GHS	Glutathione

Abstract in English

Highly sensitive biosensors derived from nanotechnology have found applications in various fields in recent years, thanks to the direct, real-time and label-free detection of many biological and chemical substances. In the framework of this thesis, three biodetection platforms were developed on glass substrates. Specifically, glass slide coated with thin layers of indium tin oxide (ITO), glass coverslip and quartz crystal microbalance (QCM) were nanostructured. With the first platform, biomolecules were detected by using scanning microwave microscopy (SMM) while the second platform made it possible the fabrication of optical genosensors based on either enhanced surface Raman spectroscopy (SERS) or localized surface plasmon resonance spectroscopy (LSPR). Finally, the third platform implemented the acoustic detection of biomolecules on commercial quartz crystal modified with nanostructures in a controlled manner.

Key words

- Biosensors
- Microwave spectroscopy
- Surface plasmon resonance
- Microbalances
- Nanostructures

Résumé en Français

Les biocapteurs hautement sensibles issus de la nanotechnologie ont trouvé des applications dans divers domaines ces dernières années, grâce à la détection directe, en temps réel et sans marquage de nombreuses substances biologiques et chimiques. Dans le cadre de cette thèse, trois plates-formes de biodétection ont été développées en synthétisant des nanostructures d'or sur trois différents substrats, respectivement une lame de verre recouverte d'oxyde d'indium-étain (ITO), des lamelles de verre et un quartz utilisé dans les microbalances à quartz (QCM). Avec la première plateforme, des biomolécules ont été détectées de façon spécifique en utilisant une analyse spectroscopique dans le domaine des micro-ondes (SMM). La seconde a permis de réaliser un génocapteur utilisant comme méthode de détection optique soit la spectroscopie Raman exaltée de surface (SERS), soit la résonance plasmonique de surface (LSPR). La troisième a mis en œuvre la détection acoustique de l'interaction entre une biomolécule et des nanoparticules biofonctionnalisées et réparties de façon contrôlée sur la surface.

Mots Clés

- Biocapteurs
- Spectroscopie de microondes
- Résonance plasmonique de surface
- Microbalances
- Nanostructures

General introduction

The optical biosensors are used in diverse fields including clinical diagnosis, biomolecular engineering, drug design, environmental control or food industry[1]. They provide quantitative analysis and show extraordinary potential for rapid multiplexing and miniaturization thanks to various nano-structuration that make possible rapid recognition and targeting events of specific chemical and biological molecules[2]. Considering the potential prospects and research interests in the biosensor field, the PhD thesis focuses on the fabrication of stable annealed nanostructures and their used in the construction of sensitive and selective optical biosensors based on scanning microwave spectroscopy (SMM), surface enhanced Raman spectroscopy (SERS), localized surface plasmonic resonance (LSPR)), and quartz crystal microbalance (QCM), respectively. In addition, two surface characterization techniques namely scanning electric microscopy (SEM) and atomic force microscopy (AFM) where employed for above detection techniques.

There is drawback to use thick microscopic glass slides for deposition of thin metallic films due to the instability of noble metal films on bare glass substrates after exposure to aqueous solutions, solvents and buffers used in biosensor applications. The instability of gold film deposited on glass substrate has been confirmed [3–5]. However, to overcome this drawback the previous work has developed a protocol to stabilize the binding of the thin gold film on the surface of glass substrates, which includes deposing thin gold film on the glass and embedding the gold nanoparticles in glass substrates by high temperature annealing[6]. In this thesis, an improved protocal is proposed for high

temperature annealing gold nanoparticles on the glass coverslips instead of the regular glass substrates as has been reported by the same group in 2013[6]. Therefore, on the basis of the annlead thin gold films on ultrafine glasses, **three major scientific issues** addressed in this PhD thesis. The scientific issues solve in four chapters:

i). Can annealed nanostructured supports be considered a universal platform for highly sensitive and reproducible biosensors with different detection transducer types? (issue addressed in chapter 2, 3, 4)

ii). Are ultrafine coverslips suitable for high temperature annealing process for metallic nanostructuration? (issue addressed in chapter 3)

iii). Are annealed nanostructured surface stable to biological buffers used in the construction of biosensors? (issue addressed in chapter 5)

In Chapter 1, the noble metal nanomaterials, the assemble and fabrication methods of the gold nanostructures and the various properties of the noble metal NPs have been introduced and summarized. On the basis of the optical properties of the noble metal NPs, the fundamental of optical biosensor have been explained. Furthermore, the classification of label-based and label-free detection based on the optical biosensor have been introduced. The principles and applications of four analyte detection techniques namely scanning microwave spectroscopy (SMM), localized surface plasmonic resonance (LSPR)), surface enhanced Raman spectroscopy (SERS) and quartz crystal microbalance (QCM), have been also summarized.

In Chapter 2, as a label-free microscopy detection technique, scanning microwave microscopy (SMM) combines the principles of atomic force microscopy (AFM) with

microwave frequency measurements to obtain a characterization of materials, thereby achieving detection of samples properties. In this work, microwave microscopic detection of human Heat Shock Proteins 70kDa (Hsp70) Protein has been reported. The conductive indium-tin oxide (ITO) and non-conductive glass substrates were modified with gold nanoparticles (AuNPs) formed by controlled thermal annealing at high temperature of 550 °C for 8 h in oven. And the Hsp70 protein was chosen as a model biomarker of body stress disorders for microwave spectroscopic investigations based on the modified substrates with AuNPs. Finally, microwave screening at the frequency of 4.33 GHz, a lower limit concentration of Hsp70 protein was detected at 12 ng / μL / cm^2, and the SMM technique has evidenced its capacity and sensitivity to follow each step of the (bio)functionalization of the biochip (SiO_2 / AuNP, SiO_2 / AuNP / Thiols, and SiO_2 /AuNP / Thiols / Hsp70) and statistically confirmed the uniformity of the SMM responses.

In Chapter 3, robust SERS platforms based on annealed gold nanostructures formed on ultrafine glass substrates, then a novel genosensors (*Brett DNA*) have been developed. In this work, the first part, the protocol of preparation of gold nanostructures on the coverslips was optimized, which using gold thin layers (2 nm, 4 nm, 6 nm, and 8 nm) at 25 ˚C for evaporation on the coverslips substrates and annealed at high temperatures (350 ˚C, 450 ˚C, and 550 ˚C) on a hot plate for different periods of time to ensure the optimization protocol. The second part, SERS was used to identify the spectral performances of gold nanostructures on the coverslips in the presence of different concentrations of a model molecule, namely 1,2-bis-(4-pyridyl)-ethene (BPE).

Therefore, we have developed a protocol which is 4 nm gold-coated coverslip heated at 550 ˚C on a hot plate for 3 h, and after SERS measurements, the results demonstrated the gold-coated coverslips had the greater sensitivity of the SERS spectrum to different BPE concentrations. In particularly, it was possible to detect a lower BPE concentration of 10^{-12} M. The third part, on the basis of these results, making use of LSPR and SERS for the detection of *Brettanomyces bruxellensis* yeast in the wine. SERS technique made possible the detection of Brett-DNA at 0.1 ng / μL (57.2 nM), while LSPR revealed detection of a real DNA extracted from *Brettanomyces bruxellensis* DKA in the laboratory (0.5 ng/μL).

In Chapter 4, at the first, two kinds of the controlled AuNIs on the QCM crystal were prepared for the acoustic sensitive biosensing platform. One is prepared with gold film (30 nm and 50 nm) deposition through a TEM grid with 3 slots on the crystal gold electrode (named Q-TEM grid). Another is prepared with annealed gold nanoparticles (thickness of the evaporated gold 0 nm, 2 nm, 4 nm and 6 nm) on quartz glass and gold electrode (named QCM-color crystal). Subsequently, five different concentrations of gliadin have been detected by acoustic measurements on the basis of these two nanostructured substrates. Thus, the acoustic detection using home-prepared nano-patterned QCM crystal (Q-TEM grid (30 nm Au) and QCM-color) has proved to be efficient immuno-detection platforms for instance of gliadin.

In chapter 5, as chapter 3 has been reported, the high temperature annealed AuNPs on the coverslips showed a sensitive and specific biosensing detection based on the plasmonic properties and considering the biological buffer plays an important role in

the aliquots and (bio) functionalization preparation steps, in this work, the SSPE and PBS buffer have been investigated in the influence on the stability of the annealed gold nanostructured coverslips by using the characterization of SEM, AFM and LSPR measurements. Meanwhile, under the 4 ℃ wet media, the LSPR sensing of Raman model molecule- BPE on the annealed AuNPs on the coverslips was possible to over two weeks.

Chapter 1 Optical biosensors

A biosensor is a device that uses specific biochemical reactions mediated by isolated enzymes, immune-system, tissues, organelles, or whole cells to detect chemical compounds, usually by electrical, thermal or optical signals[7]. It includes a biometric layer designed to bind specific substances and a physical transducer that converts the biochemical interactions into quantifiable signals[1].

Biosensors can be divided into the following categories according to the classification[8,9]: i) It can be classified into different groups depending on the transducers: optical (surface plasmonic resonance (LSPR), refractometric fluorimetric, interferometric), electrochemical (amperometric, potentiometric, conductometric, capacitive), and physical (calorimetric, electronic, piezoelectric, magnetic); ii) On the basis of the different bioactive materials in biosensors, it can be divided into: gene-biosensors, immunosensors, enzyme sensors, microbial sensors, tissue sensors, and cell sensors, etc; iii) According to the different interaction methods between the identification element and the analyte in the biosensor, it can be mainly divided into: catalytic biosensor and affinity biosensor.

The definition and principle of biosensor shown in **Figure 1.1**.

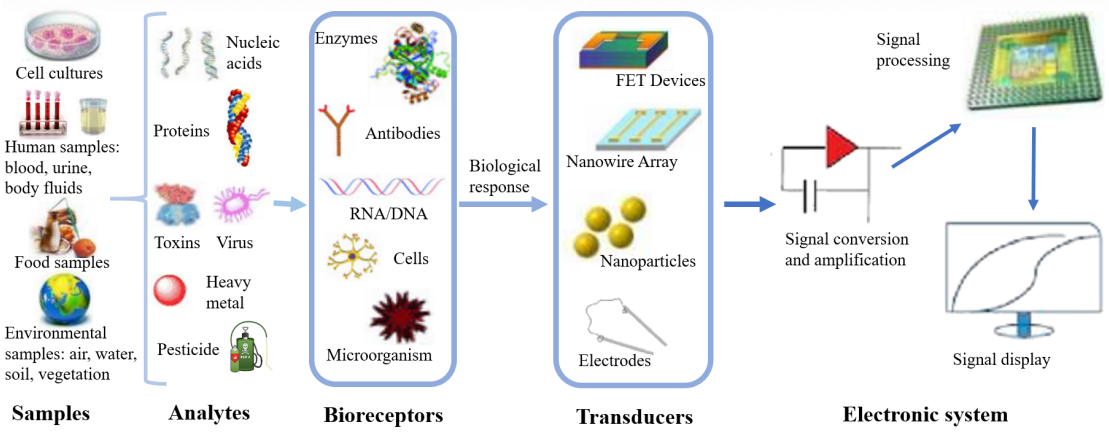

Figure 1. 1 The working principle of biosensors.

Nowadays, the technological progress experienced in the field of nanotechnology has significantly promoted the expansion of the biosensor market and there is a great interest in the development of sensitive and selective biosensors, new research in the field of biosensor plays an important role in daily life. A variety of high-sensitivity biosensors based on nanotechnology have been reported in recent years[10]. In addition, biosensors have been progressively applied to continuous monitoring of biological and synthetic processes in industrial and clinical chemistry[11]. Biosensors are becoming more and more popular in the field of food analysis[12], environmental control[13], bioterrorism[14], and human health diagnostics[15]. Among the detection methods of biosensors, highly-sensitivity optical transducers combined with the exquisite specificity, affinity and versatility of biomolecular interactions have driven the development of a wide variety of optical biosensors[16]. While the optical detection is commonly used in noble metal sensors. Compared with conventional analytical techniques, high-sensitivity optical biosensors offer great advantages, they can detect a variety of biological and chemical substances directly, in real-time and

without labels. Furthermore, optical detection can achieve the advantages include high specificity, sensitivity, small size and cost-effectiveness[17], and it is widely used in the detection of noble metal biosensors.

Owing to the nanoparticles which have the characteristics of small volume and large specific surface area, the functionalized biosensors generally have the property of a large specific surface area of materials, so that they can be used as carriers for biomolecules, to enhance the immobilization ability of biological cells and receptors[18]. In addition, they have good catalytic reaction and electron transfer capabilities, as well as good biocompatibility and stability thereby they can be well used for the research of biomolecules and biological processes. Many research results show that biosensors based on noble metal can significantly amplify the output signal, making it more sensitive, and greatly improving the detection and quantification capabilities of biomolecules and different bio-ions[19–22]. Although the methods and detection techniques of noble metal biosensors still have certain limitations and cannot be used as routine detection methods and tools in clinical experiments and homes, they are expected to become more powerful diagnostic and therapeutic tools and have broader practical application prospects.

Among the noble metal, gold nanoparticles (AuNPs) are currently widely used in various biomedical fields due to their size-dependent chemical, electronic and optical properties. The related physical properties include a high surface-to-volume ratio, biocompatibility, besides, the size of the metal NPs is comparable to those of biomolecules such as proteins (enzymes, antibodies) or DNA, and the dimension of

these biomolecules is in the range of 2-20 nm, giving the structural compatibility of these two classes of material[23]. In addition, predictability, reproducibility, stability, biocompatibility, biodegradability and easy modification are the most important advantages of its nanostructure[24]. Moreover, the multiple available shapes of AuNPs allow simple surface functionalization with probes and other compounds of interest, thereby adapting them to a variety of detection modalities and technologies in the field of optical biosensors. In particular, the plasmonic biosensing resonance can be modulated with Au NPs through different shape, size, and surface coupling [25].

Therefore, considering the controlling morphology and optical properties of Au NPs, while the development of biosensors based on plasmonic has been reported. The biomolecules detection based on the AuNPs with optical spectra measurements were developed in this study.

1.1 Noble metal nanomaterials

1.1.1 Development of noble metal nanomaterials

Nanoparticles synthesized with rare metals are called noble metal nanoparticles, and these particles have an order of magnitude less than 100 nm in at least one dimension[26]. Among noble metal nanoparticles, especially gold and silver nanoparticles, show strong scattering and absorption in the visible light wave region[27]. It can be added to the production process of the glass and vases and becoming the beautiful color source of stained glass. In the 4th and 5th centuries of Egypt and China, gold nanoparticles were the first nanoparticles used for treatment and decoration[28]. The most famous example is the Lycurgus cup made by the Romans in the fourth century. It will appear

red under the transmission light (when the light source is irradiated inside the cup), and it will be green under the reflected light (when the light source is irradiated outside the cup), as shown in **Figure 1.2**, Modern chemical analysis shows that this glass is not much different from the glass used today. However, it contains very small amounts of gold (about 40 ppm) and silver (about 300 ppm), which are in the form of Au-Ag particles with a diameter of about 70 nm[29].

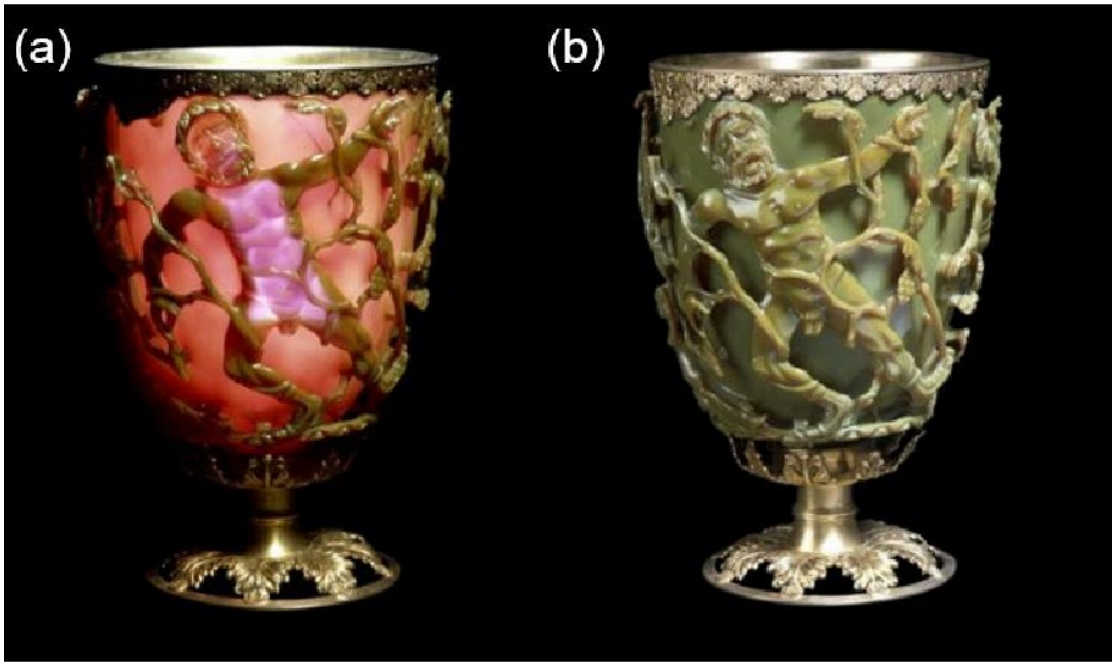

Figure 1. 2 a) Lycurgus cup appear red under the transmission light, b) green under the reflected light[29].

In 1857, Michael Faraday reported the first scientific paper on the chemical synthesis of gold nanoparticles. In carbon disulfide (CS_2), chlorine (Cl) was used to reduce the aqueous solution of chloroaurate. He was the first to disperse gold nanoparticles into a uniform deep red solution[30], this is considered to be an important step in the development of nanotechnology. In 1861, Graham coined the word "colloid" in the French word "colle"[28]. In 1889, Frens, Overbeek and Lea achieved an important

milestone in the field of chemistry, they reduced silver nitrate by using ferrous sulfate, which was then protected with citric acid ions to prepare silver colloids for the first time. In the 20th century, a large number of experimental methods reported on gold nanoparticles successfully synthesized[31,32]. In 1908, Gustav Mie used the Maxwell equation to explain the scattering and absorption spectra of spherical particles of any size[33]. In 1952, Pines and Bohm proposed "plasmon"[34], because in the presence of light, the resonance oscillation of free electrons excited on the surface of the particle is surface plasmon resonance, also known as local surface plasmon resonance (LSPR), in 1957, Ritchie first named "surface plasmon"[35].

This phenomenon shows that the noble metal nanoparticles have unique optical properties, and since then has opened a wave of research on the optical and photothermal properties of the noble metal nanoparticles. Plasma resonance can not only radiate light (Mie scattering), but also gradually applicated in the field of optics and imaging, opening up a variety of application prospects for noble metal nanoparticles in new fields.

In recent years, with the development of nanotechnology, the shape of noble metal nanoparticles has gradually evolved from the original spherical nanoparticles to form various shapes such as nano-cubes[36], triangles[37], rods[38], sheets[39], disks[40], etc., from simple 0D structures gradually developed into 3D and composite nanostructures. Due to the size, shape, and composition are important factors, affecting the physical and chemical properties of nanoparticles element, so different configurations and types of nanoparticles show different characteristics and advantages in light, heating and

electricity[41]. Specially, the gold nanoparticles exhibit excellent optical properties, catalytic properties, high conductivity and reflectivity, dielectric properties, and biocompatibility[42].

1.1.2 Fabrication of gold nanoparticles

The surface and core properties of AuNPs can be manipulated for specific applications such as molecular recognition, chemical sensing, and imaging[43]. However, there are challenges that require overcoming to improving the control over their size and shape through the synthesis techniques of gold nanoparticles. Including the reproducibility, reliability, scalability of biosensing detection methods based on AuNPs and long-term stability. The development of synthesis methods has also reached a higher level by systematically studying the special properties of nanostructures in terms of the quality, quantity and yield etc. Until now, various approaches of synthesizing AuNPs have been developed[44–52]. Researchers have made considerable efforts to develop new synthetic methods (as shown in **Figure 1.3**).

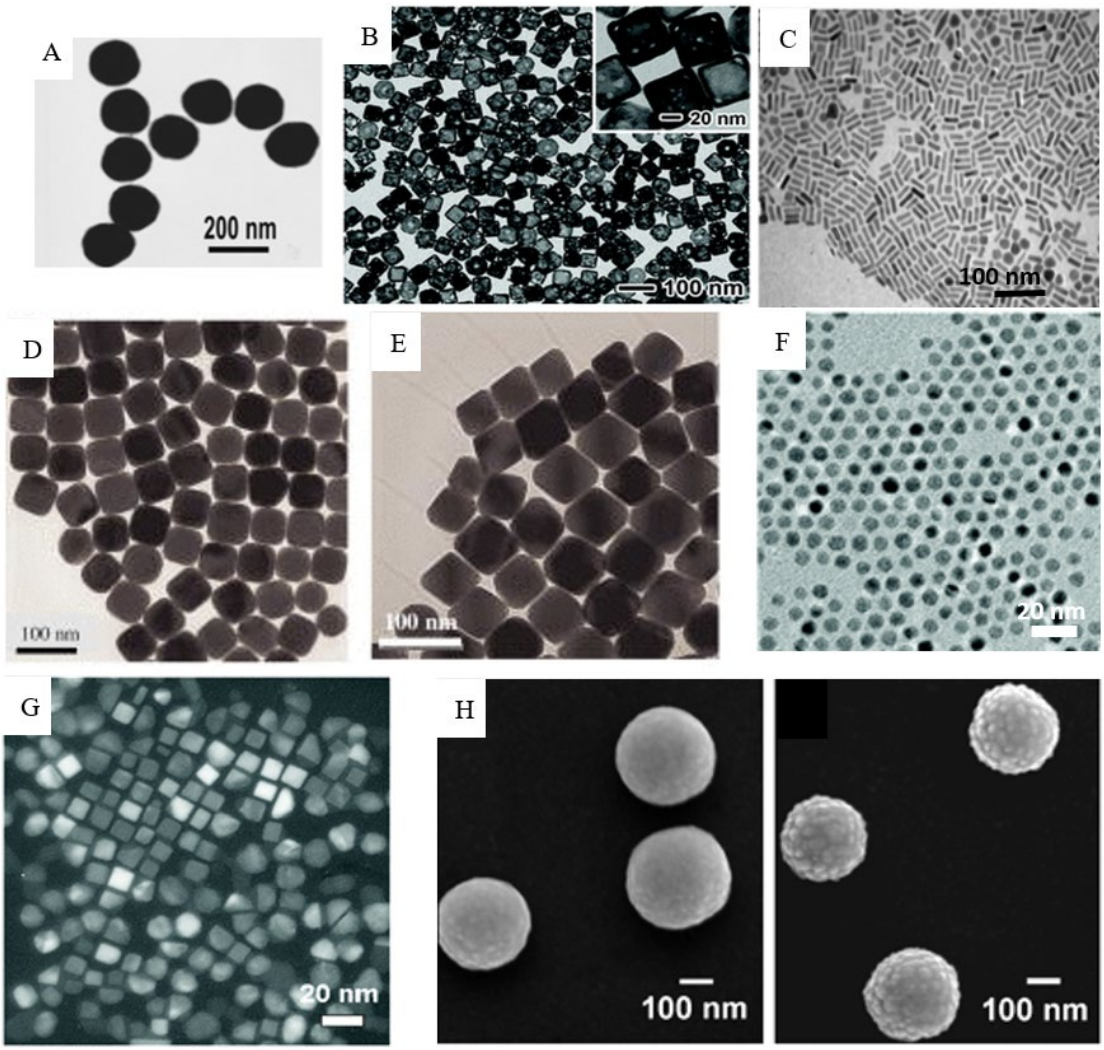

Figure 1. 3 Different synthesizing Au nanostructures. (A) Silica-coated Au spheres (core diameter = 162 ± 10 nm) with increasing silica shell thickness (8nm)[53], (B) Au nanocages (AuNCs) (edge length ≈ 50 nm)[54]. (C) Dense ensembles of Au nanorods synthesized with a reaction conditions (Au seed concentration was 2.5×10^{-7} M)[55]. (D) Au nanocubes (the nanocubes have an average edge length of 65±5 nm)[56]. (E) Au nano-octahedra which have an average edge length of 49±4 nm[56]. (F) AuNPs with a diameter of 6.0 ± 0.5 nm[57]. (G) Au nanocubes converted from Au clusters (average lateral dimension ~10 nm)[57]. (H) Au nanoshells before etching and after immersed in 50 mM cysteamine for 1 h[58].

Generally speaking, the synthesis of nanoparticles can be divided into "top-down" and "bottom-up" methods[59]. The top-down approach is to synthesize nano-sized particles by destroying the entire material, shaping or cutting. However, in the bottom-up approach, atoms or molecules are gradually assembled into nanoparticles. The main advantage of the top-down method is the large-scale synthesis of the desired nanomaterials in a short period of time. On the other hand, the main advantage of the bottom-up approach is that it allows the synthesis of homogenous nanostructures that can perfectly exhibit crystal and surface structure[60]. The synthetic methods can also be classified into chemical, physical, and biological methods.

The most common method to produce colloidal stable AuNPs is using solution phase synthesis, for example, the method first invented by Turkevich et al. in 1951[61] to synthesize AuNPs by reducing chloroauric acid ($HAuCl_4$) in aqueous phase. On the basis of the method invented by Turkevich et al., Frens et al.[62,63] improved the synthesis scheme in which sodium citrate was used as the reducing agent and the blocking agent during the reaction between hot chlorauric acid solution and sodium citrate solution. And the AuNPs with a diameter of 10-20 nm could be produced. Until now, the solution-phase synthesis method is still used to prepare colloidal AuNPs, which were synthesized by reacting $HAuCl_4$ with a sodium citrate solution as a reducing agent and stabilizer in the AuNPs fabrication field[64–66].

On the other hand, AuNPs can also be assembled into complex nanostructures through template molecules. In particular, DNA has emerged as a promising biomaterial for the assembly of various nanostructures based on their programmable base pairings.

Other interesting properties include stability, remarkable biocompatibility, and the ability to be easily modified by functional groups for further applications. As a widely used biomaterial, DNA is used to fabricate pre-designed nanostructures and nanodevices that are structurally programmable, spatially addressable, dynamically dynamic, and biocompatible[67]. In 1996, Mirkin et al.[68] and Alivisatos et al.[69] initiated the DNA (no complementary/ complementary DNA oligonucleotides) assembled gold nanostructures. Since then, a variety of assembled DNA-AuNPs were developed. For instance, Bidault et al.[70] developed the facile synthesis of AuNPs on a well-defined DNA template by hybridizing monoconjugated gold-DNA building blocks, Mastroianni et al.[71] created discrete pyramids of DNA with gold nanocrystals, Lo et al.[72] demonstrated a DNA-templated approach to construct nanotubes for encapsulation of 20 nm gold nanoparticles within these DNA nanotubes, Storhoff et al.[73] reported that DNA-linked gold nanoparticle aggregates containing oligonucleotide linkers of varying length, and other synthesized DNA-AuNPs have been reported[74–77]. In recent years, in addition to DNA, several other classes of biological molecules have been successfully used for biological templates in the preparation and application of biosensors. Such as peptides, proteins, virus and bacteria[78–81].

However, even though various AuNPs have been prepared by using a chemical bottom-up approach and displaying homogenous nanostructures, challenges remain to obtain the well-patterned NPs with uniform shape and size for biosensing applications based on plasmonic properties. Amomg the physical top-down methods, there is a typical method called electron beam lithography (EBL)[82–84], which produces extremely

controlled patterned gold nanostructures by rasterizing them onto a thin polymer coating (resist) using a high energy focused electron beam, followed by metal evaporation and photoresist sripping[85]. There is an example of controlled patterned gold nanostructures obtained by EBL showed in **Figure 1.4**. EBL readily allows the precision control of the size and interspacing of the gold nanopillars, ideal for the spectral tuning of plasmon resonant gold nanoarrays and study of their electromagnetic interactions[86].

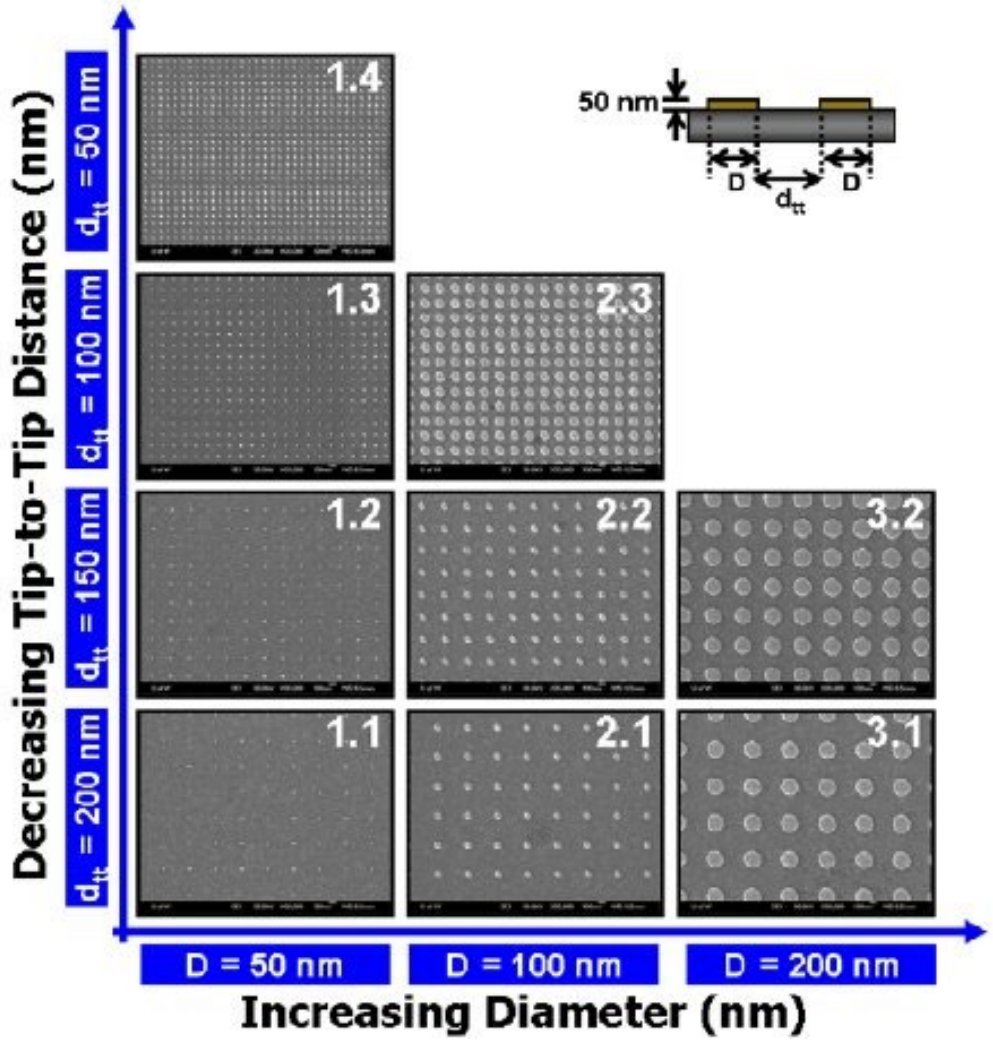

Figure 1. 4 SEM images of gold nanoarrays by EBL[86].

In summary, the greater versatility and ease of preparation of AuNPs is one of the

advantages of that have been widely studied and used in large quantities. Electron beam evaporation of a thin film on glass substrates and subsequent thermal annealing in oven or on a hot plate, were chosen for this thesis, due to their relatively low cost, ease of manufacture and potential for large scale fabrication[6].

1.1.3 Properties of noble metal nanoparticles

Noble metal nanoparticles are widely used in materials science, biology, imaging, catalysis and medical treatment because of their special physical, chemical, radiative and non-radiative properties[87].

Physical properties: The surface plasmon resonance (SPR) effect, in the main publication written by Mie in 1908, the property of SPR was theorized. According to Mie theory, the total cross section composed of SPR absorption and scattering is the sum of all electromagnetic oscillations, solving the Maxwell equations with appropriate boundary conditions quantitatively describes the phenomenon of surface plasmon resonance. Mie theory attributed the plasmon resonance of spherical particles to the dipole oscillations of free electrons in the conduction band occupying energy states above the Fermi level[88]. Different sizes, shapes and types of noble metal nanoparticles have different absorption characteristics, thereby they will show different colors. As shown in **Figure 1.5**[89], it is a schematic diagram of LSPR after spherical nanoparticles are excited. Correspondingly, it has only one absorption spectrum peak. However, for the absorption spectrum of gold nanorods (AuNRs), there are two obvious absorption peaks. Due to the length and short-axis electronic oscillation of gold nanorods, there will be longitudinal and transverse plasma bands (see **Figure 1.6**)[89]. More and more

reports link the spectral characteristics of gold particles with Mie theory. Therefore, SPR provides a lot of information for the development of metal nanostructures, and has been a hot spot for extensive research on the optical spectral properties of noble metal nanoparticles[90].

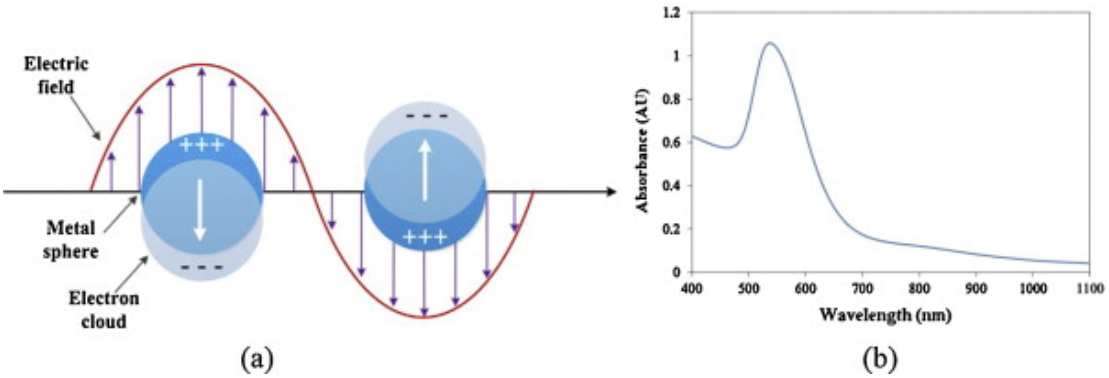

Figure 1. 5 (a) Schematic illustration of LSPR excitation for AuNPs. (b) A typical LSPR absorption band of AuNPs.

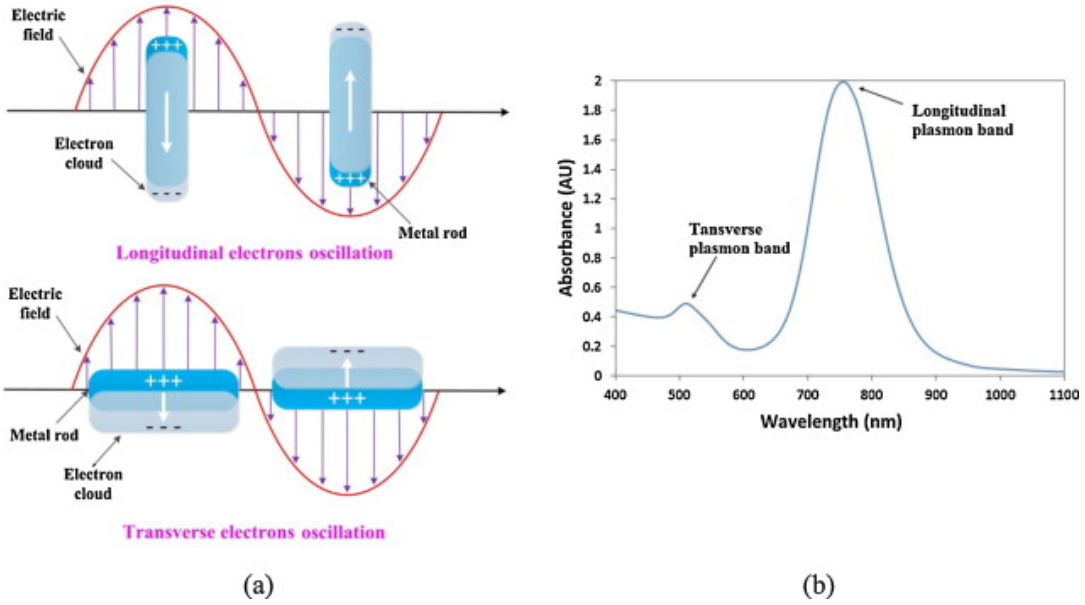

Figure 1. 6 (a) Schematic illustration of LSPR excitation for AuNRs and (b) LSPR absorption bands of AuNRs: longitudinal and transverse plasmon bands corresponding to the electron oscillation along the long axis (Fig. 1.6(a) top) and the short axis (Fig. 1.6(a) below) of AuNRs respectively.

Chemical properties: The noble metal nanoparticles stably present in the ligand can react with some thiol ligands to form covalent bonds, and thus have a substitution reaction with the ligands on the particle surface. The rate of the reaction depends on the chain length of the thiol molecule, the steric hindrance and the charge carried, and the charge carried by the noble metal nanoparticles[91]. Acid-base chemistry has been involved in molecular recognition applications and has been studied using various technologies. For example, for amino-functional AuNPs, IR and ^{1}H Nuclear Magnetic Resonance (NMR) studies have shown that the strength of the H bond in the molecule depends on the distance between the amide and the material[92]. Therefore, noble metal nanoparticles modified with different acid-base groups also have supramolecular properties[28].

Radiative properties: Noble metal nanoparticles have very strong scattered light near the SPR frequency, so optical imaging and labeling applications in biological systems are very promising[93,94]. There is a competing relationship between scattering and absorption, scattering increases rapidly as the volume of nanostructures increases. For example, when the scattering of smaller AuNPs (10 nm) is negligible, the scattering from larger nanoparticles (80 nm) is 5 magnitudes greater than the typical dye emission value[95]. The highly enhanced cross-section of nanoparticles provides sensitive and highly contrasted imaging technology. Individual nanoparticles can also be imaged, so they can be identified using a simpler but powerful dark field microscope. At the frequency of SPR of nanoparticles, the AuNPs in the microscope are seen as bright, colored spots[96] as shown in **Figure 1.7**. By combining AuNPs with specific target

molecules, dark field microscopy can be effectively used to specifically image biomolecules[94].

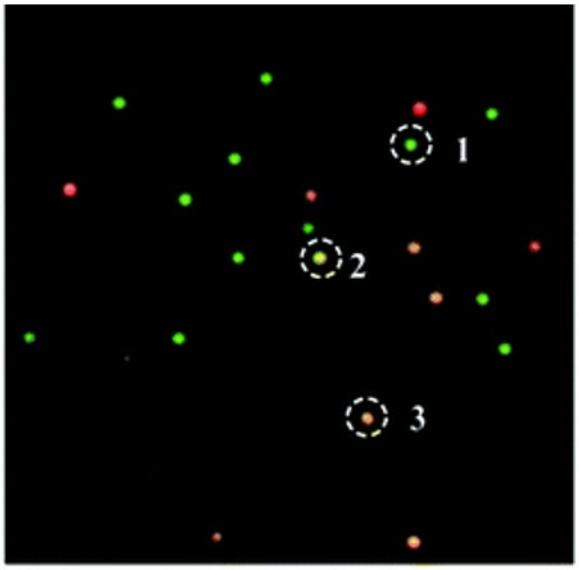

Figure 1. 7 Dark-field images of three AuNPs (1-3) with different diameters.

Non-radiative properties: In order to generate light scattering, the plasma non-radiative relaxation throughs electron-electron (internal-or inter-band excited state), electron lattice and electron surface collision, resulting in nanoparticles to absorb photons[97]. Spectroscopic studies of low laser energy in ultrafast lasers have shown that after the free electrons of metal nanoparticles are excited by light, they are cooled back to equilibrium through energy exchange with lattice photons, and the nanoparticles will be heated at a rate of 1 ps. When excited at a faster deposition rate than the lattice cooling energy, photothermal heating can lead to nanoparticle ablation or surface desorption, and it may even melt or reshape the nanoparticles (30 ps). Under a slower rate of excitation, the lattice is cooled by quantum-quantum (100 ps), which can heat the surrounding medium of the nanoparticles, thereby it can be used for photothermal treatment of cancer[98,99].

1.2 Optical biosensors

1.2.1 Classification of optical biosensors

Optical biosensors are the most commonly reported category of biosensors. Optical detection is performed using the interaction of a light field with a biometric element. The basic goal of an optical biosensor is to generate a signal proportional to the concentration of the analyte. As **Figure 1.1** shows, the optical biosensor can use various biological materials, including enzymes, antibodies, antigens, receptors, nucleic acids, whole cells and tissues as biorecognition elements. Generally, optical biosensing can be mainly divided into two general modes: label-free and label-based. Briefly, label-based sensing involves the use of markers, and then generates an optical signal by colorimetric, fluorescent, or luminescent methods[17]. In contrast, in the label-free mode, the detected signal is directly caused by the interaction between the material being analyzed and the transducer. These two modes would be described in this section.

1.2.2 Label-based detection

In label-based detection, on the basis of the optical signal, it mainly can be divided into three methods shown below:

In Colorimetric detection, much progress has been made in understanding the interactions between various substrates and AuNPs, and how to exploit these interactions as colorimetric reporters in biosensors[23]. Monodisperse spherical AuNPs have a red wine color. This color comes from light absorbed by AuNPs in the green-blue range (~ 450 nm) and reflected in the red wavelengths (~ 700 nm). As the AuNPs vary in size, shape, inter-particle distance, and dielectric environment, the boarding

surface plasma absorption changes local SPR frequency by shifting from visible to invisible (near infrared) wavelengths. This color shift is the key phenomenon that makes it promising for the development of colorimetric visual biosensors.

In fluorescent detection, chromophore-functionalized AuNPs based on the fluorescence resonance energy transfer (FRET) between fluorescent dyes and AuNPs have been used in fluorescence "turn-on" sensing systems to detect a variety of analytes[100]. For instance, an AuNP sensor based on fluorescence modulation between the chromophores and AuNPs has been developed to detect chromophore modifications of thiols in aqueous solutions.

In luminescent detection, chemical luminescence-based biosensors can be used to measure or image light produced by biochemical luminescence (BL, CL), thermo chemical luminescence (TCL), or electrochemiluminescence (ECL) reactions[101]. They are based on light absorption or photoluminescence, and different transduction principles and offer an interesting and powerful alternative or complementary method relative to other optical biosensors.

1.2.3 Label-free detection

The label-free analysis technology eliminates the need for complex labels, thus enabling rapid detection; it does not require the introduction of second-stage analysis probes (e.g., secondary antibodies), thereby greatly expanding the number and types of targets to be analyzed. Since the preparation and manipulation of label-free analytical methods are greatly simplified, they have the advantages of simplicity, speed, and low cost, and are suitable for the rapid, sensitive, and low-cost development of diagnostic

technology[102]. Therefore, this is a great promising development for diagnostic applications.

In label-free detection of optical biosensors, the biosensors can be mainly divided into enzyme sensors, cells sensors, immunosensors and genosensors based on the sensitive substances on biomolecule recognition elements and the specific biomolecules interaction.

Among them, enzyme-based biosensor is the earliest a commercial biosensor to use enzymes as biometric recognition elements[103]. It has the advantages of high sensitivity, specificity, low detection limit, good selectivity, simple operation, portability, and continuous outdoor online monitoring. Simple molecules such as glucose can be detected by enzymatic oxidation. The glucose analysis of blood is by far the most commercially successful application of biosensors, namely handheld glucose meters used by diabetics. The basic principle of the glucose biosensor is based on oxygen molecules and is used as an electron receptor. The amount of hydrogen peroxide produced by the reduction or glucose oxidase (GOx) oxidation of glucose is measured directly or indirectly by a sensor that detects the substrate content[104], their reaction sequences can be described by the following reactions: (1) and (2).

$$\text{Enzyme layer: } GOx_{(ox)} + \text{glucose} \longrightarrow \text{gluconolactone} + GOx_{(red)} \quad (1)$$

$$GOx_{(ox)} + O_2 \longrightarrow GOx_{(ox)} + H_2O_2$$

$$\text{Electrode: } H_2O_2 \longrightarrow O_2 + 2H^+ + 2e^- \quad (2)$$

At present, enzyme-based biosensors are widely used in environmental monitoring, food safety inspection, biomedical inspection, and other fields.

On the other hand, based on the interaction of specific biomolecules, cell-based sensors use physiological responses of whole living cells as sensing component, such as oxygen consumption, surface chemistry or electrical potential, mobility or genetic activity[105]. Thus, whole cells provide multipurpose catalysts, especially where multiple enzymatic processes need to be sequentially engaged.

Besides, the immunosensor is developed by exploiting the recognition of antibodies (antigens) against antigens (antibodies)[106]. For instance, an ultra-highly sensitive immunosensor was developed to detect carcinoembryonic antigen based on the gold and silver bio/nano-hybrids by Nakhjavani al.[107]. Currently, the label-free immunosensing on the basis of QCM is more and more popular in the research of the immunosensors fields[108–112], the QCM biosensing will introduced in further part.

Genosensors or gene-based biosensors/DNA biosensors typically use a immobilized DNA probe as an identification element and measure specific binding processes, such as the formation of DNA-DNA and DNA-RNA hybrids, and the interactions between protein or ligand molecules and DNA on the sensor surface[113].

Among these biosensors, with the rapid advances in the fields of molecular biology and genetic engineering, research on the application of genosensors in genetic diagnosis, environmental monitoring, and drug research has received widespread attention. Generally, studies of genobiosensors can be divided into three categories: electrochemical genobiosensor, mass genobiosensor (using a quartz crystal oscillator (QCM) as a transducer) and surface plasmon resonance (SPR) genobiosensor. In particular, SPR genobiosensor are widely used for detection due to the advantages of

non-destructive and high sensitivity of optical methods.

In the thesis, to realize the label free detection, four approaches were choosed for the diagnostic applications. The biosensing detection based on these four techniques will be introduced next.

1.3 Scanning microwave spectroscopy (SMM) technique

1.3.1 Principle of SMM technology

SMM as an electrical characterization technique combines the nanoscale spatial resolution of atomic force microscopy (AFM) with vector network analyzer (VNA) which covers a broad microwave frequency range of 1–20 GHz to realize the extraction of various materials properties such as conductivity and dielectric constant[114]. The schematics and construction of SMM is shown in **Figure 1.8**. The well-known measurement tool AFM is used for material characterization, allows for nanometre lateral resolution imaging, and VNA is used for high frequency signal measurement, provides high precision impedance and admittance measurements at broadband frequencies from MHZ to GHZ[115]. Under the reflection mode of SMM, the VNA detects the properties of the sample under test through probing the scattering reflection parameter, which represents the ratio of the reflected and an incident microwave signal sent by the VNA through a conductive tip/ sample contact point. Determined on the impedance of the tip and sample interface, part of the microwave signal is reflected and measured by the VNA as scattering S_{11} reflection signal. Together with the reflection signal coming from the tip/sample interface, reflections are also generated from RF cables and connectors. These add up to the measured S_{11} signal and a de-embedding

step is necessary in order to obtain from the measured S_{11} calibrated values of relevant physical quantities such as complex impedance, capacitance, and resistance.

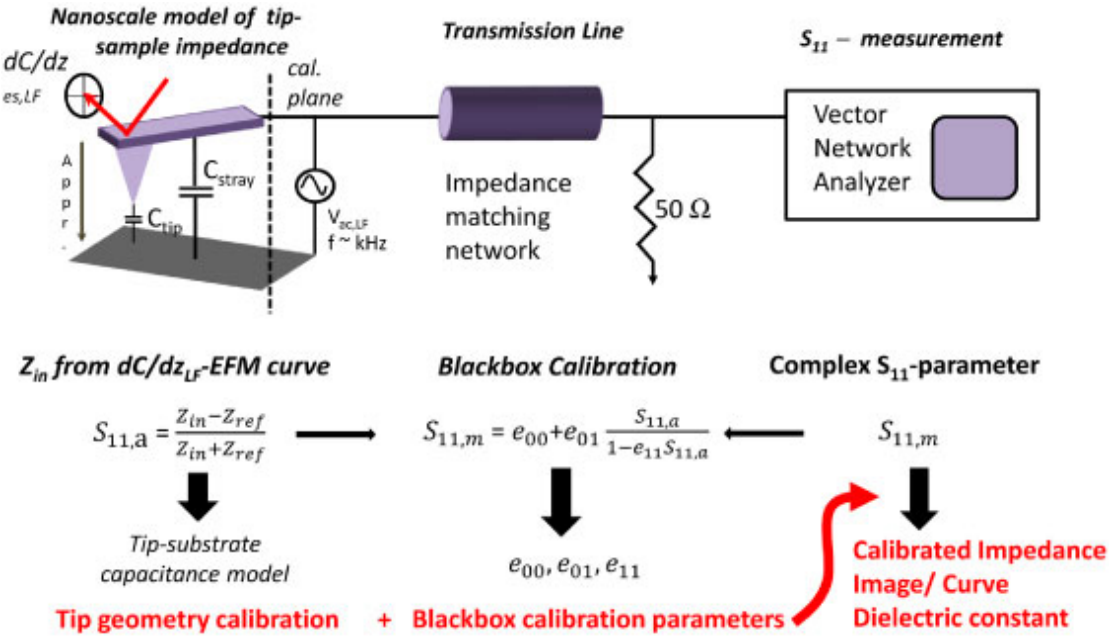

Figure 1. 8 Schematics of SMM, the calibration plane, and the calibration procedure. The conductive AFM-tip is connected to a vector network analyzer by a transmission line and impedance matching network (50 Ω shunt). The black box calibration procedure compares measured S_{11} values with capacitance values measured at low frequencies by electrostatic force microscopy (EFM) during an approach curve in order to define the calibration parameters e_{00}, e_{01}, e_{11}. From the approach curve also the tip geometry is extracted for the dielectric constant evaluation[116]. Where $Z_{ref} = 50\ \Omega$ is the characteristic impedance of the VNA. The three complex parameters e_{00}, e_{01}, and e_{11} have to be determined with the measurement of three reference samples of known impedance.

1.3.2 Application of SMM technology

In recent years, the scanning microwave microscopy appeared as a potential technique to obtain the electromagnetic properties of samples with high spatial resolution[117], SMM measurements can be also related to the electrical impendence of the samples and further to their local complex permittivity[118,119]. As the combination of the high resolution and broad microwave frequency range, the SMM represents a unique technology to capture high spatial resolution images of the surface and internal electromagnetic properties of materials[120,121]. SMM has been applied to analyze the local doping of semiconductors[122]. For instance, Buchter et al. presented a scanning microwave microscopy (SMM) with a calibration algorithm based on one-port vector network analyzer (VNA) calibration and used to extract quantitative carrier densities from a semiconducting n-doped GaAs multilayer sample[123]. The applications of related research also involve other related complex systems, for example, Tai et al. studied the extreme and local electrodynamic properties of Niobium (Nb), and using the microwave microscopic measurements which operated in the superconducting state (superconductor)[124] to aquire the response of Nb to RF magnetic fields up to the critical field (Hc) at microwave frequencies (few GHz), and at temperatures down to 4.2 K, Xu et al. measured the transport properties of single-walled carbon nanotubes[125] (SWCNT) films in the microwave frequency range from 10MHz to 30GHz by using the Corbino reflection technique from temperatures of 20–400K, Kalugin et al. used near-field scanning microwave microscopy for quantitative imaging at 4 GHz of the local impedance for monolayer and few-layer graphene[126], ect.

Besides its widely applying in inorganic samples, nowadays, SMM also has

becoming applied in biological systems[127–130], but a few examples of applications of SMM to biology are found in the literature. For example, Biagi et al. quantified the electric permittivity of single bacterial cell at microwave frequencies and nanoscale spatial resolution by means of near-field SMM[117]. In fact, compared with the inorganic samples of solid substrates, there are a number of difficulties for the SMM measurements of biological samples, such as the soft nature, the necessary of the special working conditions and their non-planar and irregular shapes. However, with the development of the AFM-based SMM systems, combined indirect contact topographic imaging and microwave imaging[128,129,131], obtaining the images in liquid medium are becoming possible[132,133], it solved some of these difficulties for the SMM measurements of biological samples. The examples of SMM measurements of biological samples were showed in **Table 1.1**.

Table 1.1 SMM measurements for biological samples

Target	Substrates	Resonant frequency	Force constant	References
capillary vessels in pig's osseous tissue	$LaAlO_3$ and $SrTiO_3$	1.5 GHz	10 μN/m	Park J. et al.[131]
C2C12 muscle cells	bundles of multi-walled carbon nanotubes	5.36 GHz	0.15 N/m	Farina M. et al.[127]
THP1 cells (Cells were maintained between 2×10^5 and 9×10^5 cells ml^{-1})	Glass	2.356 GHz, 4.437 GHz, 6.846 GHz (Figure 1.9_I part)	0.3 N/m	Oh Y. J. et al.[128]
THP1 cells (Cells were maintained between 2×10^5 and 9×10^5 cells ml^{-1})	Gold	2.136 GHz, 2.213 GHz, 2.304 GHz, 2.385 GHz (Figure 1.9_II part)	0.3 N/m	Oh Y. J. et al.[128]
oligonucleotide DNA film	Silicon	4.5 GHz	8.7 kN/m	Kim S. H. et al.[134]
Jurkat human lymphocyte cells	polyethylene-terephthalate slide coated with ITO	1.8 GHz, 3.6 GHz, 5.4 GHz, 7.2 GHz, 9.0 GHz	0.2 N/m	Jin X. et al.[130]

MCF-7 breast cancer Cells	ITO-coated glass Slide	20.21 GHz	2.8 N/m	Farina M. et al.[135]
Jurkat cells	Sapphire	4 GHz	-	Fabi G. et al.[136]

Note:

MCF-7: Michigan Cancer Foundation-7 breast cancer cells

From these a few study of the SMM application, the results indicated variations in the dielectric properties of biological cells at different resonant frequencies[128] by studying on the SMM measurements of biological cells THP1 cell on the solid substrates (gold substrate and glass coverslips), see **Figure 1.9**.

I part: glass substrate

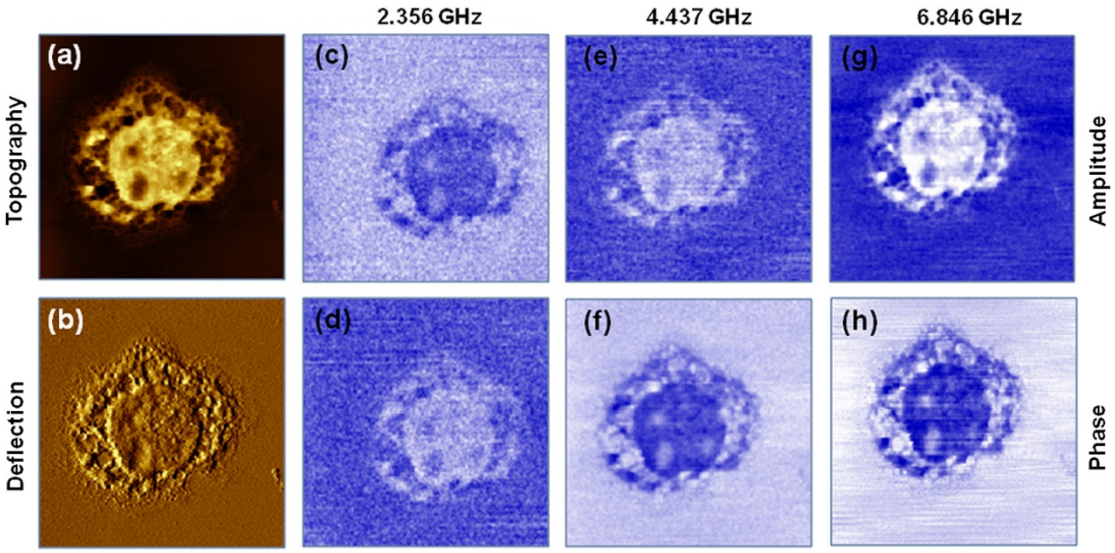

II part: gold substrate

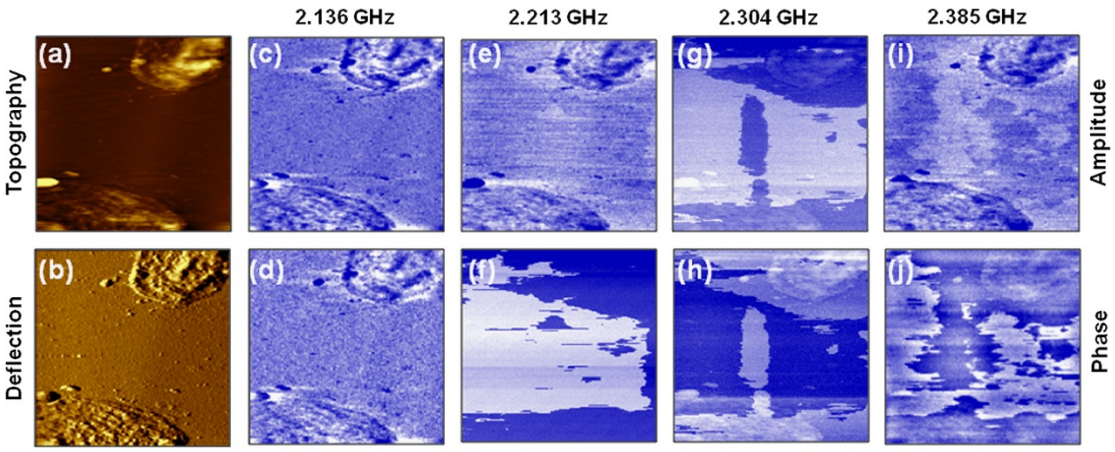

Figure 1. 9 SMM measurements of THP1 cell at different frequencies on glass substrate

(*I part*) and gold substrate (*II part*). *I part*: (a) Topography. (b) Deflection image. (c, e, g) PNA amplitude images. (d, f, h) PNA phase images using different resonance frequencies. Images are 42×42 μm^2 in area. *II part*: (a) Topography. (b) Deflection image. (c, e, g, i) PNA amplitude images in the upper panel and (d, f, h, j) PNA phase images in lower panel, acquired at different resonance frequencies. Images are 60×60 μm^2 in area[128].

Furthermore, it was found that the difference in the dielectric constant between the cell wall and the cytoplasm in the plant epidermal cell at 1.5 GHz, due to the differing amounts of water in the cell wall and in the cytoplasm produce the drastic differences in the SMM signals, and the body fluid in the blood vessels produces higher values of the dielectric constant than the bone matrix by SMM measurements[131]. By modifying both the hardware and software of a narrowband commercial SMM, a broadband scanning microwave microscope was developed and the broadband SMM can enable microwave spectroscopy (quantify the SMM data) and 3D tomography of intracellular structures in a live cell was confirmed[130]. Additionally, microwave imaging and local complex admittance mapping of a single dried Jurkat cell were extracted and the dielectric constant of Jurkat cells around 2.6 ± 0.3 was obtained by using SMM[136]. Different dielectric constant obtained with different layer or different multi-layer measured by SMM at different frequency. However, among these studies of the applications of biological samples, there is hardly any investigation of the different concentrations of the biological samples on the solid substrates.

Therefore, in our study, we studied the SMM measurements of the different

concentrations of human Hot shock proteins 70 on the annealed gold covered ITO glass substrates, and investigated the effects of the surface propeties on the basis of the interaction between the biological samples and inorganic substartes to obtain the relationship between the aplitude and the detected layer.

1.4 Optical biosensors based on plasmonic for LSPR and SERS detection

1.4.1 Plasmonics

Plasmon is defined as the collective excitation for quantiative oscillations of electrons in a metal. Surface plasmon are then the collective oscillation of electrons on a metal surface under the influence of an external electromagnetic (EM) field. Surface plasmons can be divided into two types: surface plasmon polariton (SPP) and localized surface plasmonic resonances (LSPR). The difference between propagating and localized surface plasmons shown in **Figure 1.10**.

In the case of surface plasmon polaritons, plasmons propagate in the x- and y-directions along the metal-dielectric interface. The interaction between the metal surface-confined EM wave and the surface layer of molecular of interest results in a shift in the plasmon resonance condition, which can be observed in three modes: a) angular resolution, b) wavelength shift, and c) imaging. In the first two modes, one measures the reflectance of light from the metal surface based on either the angle of incidence (at constant wavelength) or wavelength (at constant angle of incidence). The third method uses light of constant wavelength and angle of incidence to interrogate the

two-dimensional region of the sample, mapping the reflectance of the surface as a function of position.

1.4.2 Localized surface plasmonic resonances (LSPR)

For localized surface plasmons, the interaction of light with particles (a radius R) is much smaller than the incident wavelength ($2\pi R << \lambda$) (**Figure 1.10 b**), LSPR is a non-transitive surface plasmon resonance that is caused by excitation on the surface of nanostructured metals. The LSPR extinction spectral band is influenced by various parameters, including metal dielectric function, the particle shape, size and size distribution, interparticle distance and local refractive index near the nanoparticles surface [105]. Typical materials for plasmonic applications are noble metals, especially silver or gold. Although silver shows sharper and stronger LSPR spectral bands than gold, the higher chemical stability of gold nanostructures makes it preferable for biosensing application[138] as previously introduced. Since LSPR is very susceptible to changes in refractive index in the local dielectric medium, changes in peak wavelengths or absorption peaks in the absorption spectrum of metal nanoparticles (MNPs) in the sensor system will be used as a measure of LSPR sensor feedback[139]. The light absorption of gold nanospheres affected by LSPR can be defined by using the Mie solution to Maxwell's equations[140]. On the basis of the Mie theory, the extinction cross-section, C_{ext} for separated spherical nanoparticles with a radius R (that is smaller than the wavelength of light λ ($R/\lambda < 0.1$)), can be indicated as:

$$C_{ext} = \frac{24\pi^2 R^3 N \varepsilon_m^{\frac{2}{3}}}{\lambda} \frac{\varepsilon_i}{(\varepsilon_r + 2\varepsilon_m)^2 + \varepsilon_i^2} \qquad (1)$$

where ε_m is the dielectric constant of the surrounding medium, ε_r is the real part of the

dielectric function of metallic nanoparticles, ε_i is the imaginary part of the dielectric function of the MNPs and N is the number of spheres per unit volume. From this relationship, it can be seen that C_{ext} has a maximum value when the denominator is minimum. According to equation, the physical parameter that ultimately defines the LSPR peak is the dielectric constant $\varepsilon(\omega)$ of the particle, given by the following equation:

$$\varepsilon(\omega)=\varepsilon_r(\omega)+i\varepsilon_i(\omega) \qquad (2)$$

where $\varepsilon_r(\omega)$ and $\varepsilon_i(\omega)$ are the real and imaginary parts, respectively. The dielectric constant of bulk materials is generally considered to be constant with respect to its size and shape. Except for nanocrystals with extremely small feature sizes, the dielectric constant of ordinary nanocrystals is known[141]. Hence, the plasmon absorption band appears when $\varepsilon_r = -2\varepsilon_m$[142].

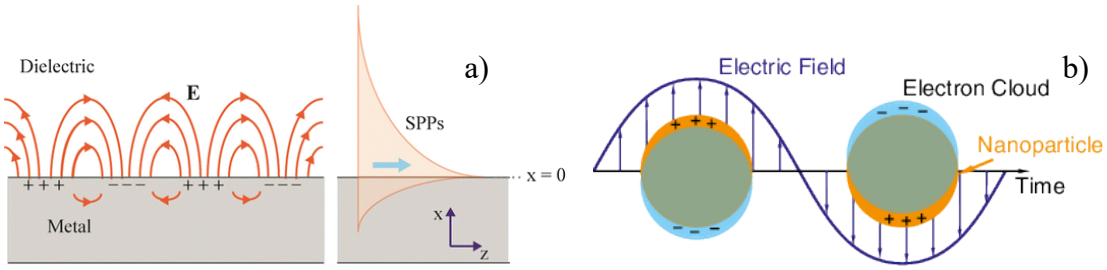

Figure 1. 10 a) Geometry of surface plasmon polaritons propagation at metal-air interface[143]; b) Schematic of localized surface plasmon resonance[144].

The so-called *localized surface plasmon resonance spectrum* can be said to be an effective platform for detecting changes in the refractive index of molecular close to the surface of noble metal nanoparticles. The LSPR phenomenon occurs because the incident wavelength of light resonates with the electrons in the metal particles, which

in turn causes the collective oscillation of the conduction band electrons of the metal nanoparticles, it can lead to two important results: (1) The wavelength of the collective oscillatory light wave can be selectively absorbed by the nanoparticles, so it can be monitored by ultraviolet-visible spectroscopy to achieve the purpose of detection; (2) The enhancement of the electromagnetic field extending from the surface of the nanoparticles can be formed, which an effect should be related to the huge enhancement observed in the SERS surface enhancement spectrum. The combination of metallic micro-nano structures used to generate the LSPR field and the Raman spectroscopy technology can form the SERS effect, which can increase the Raman scattering signal of molecules adsorbed on the substrate and improve the recognition of target molecules.

1.4.3 Surface enhanced Raman spectroscopy (SERS)

With the discovery of surface enhanced Raman spectroscopy by Martin Fleischmann in 1973[145], the interest of the research in Raman spectroscopy as an analytical method has been revived. This part aims at summarized the phenomenon of Raman scattering and SERS.

Collisions of light with molecules can be divided into two categories, i.e. elastic and inelastic collisions. The scattering of light can be seen as a change in the direction of movement of photons after collision with molecules. If an elastic collision occurs, i.e., the photon only changes its direction of movement and there is no energy exchange during the collision, this scattering is Rayleigh scattering; if an inelastic collision occurs, i.e., the photon not only changes its direction of movement, but also has energy exchange during the collision, this scatterinsg is Raman scattering (Raman

scattering)[146]. Combined with **Figure 1.11**, it's more clearly to understand the scattering process of light.

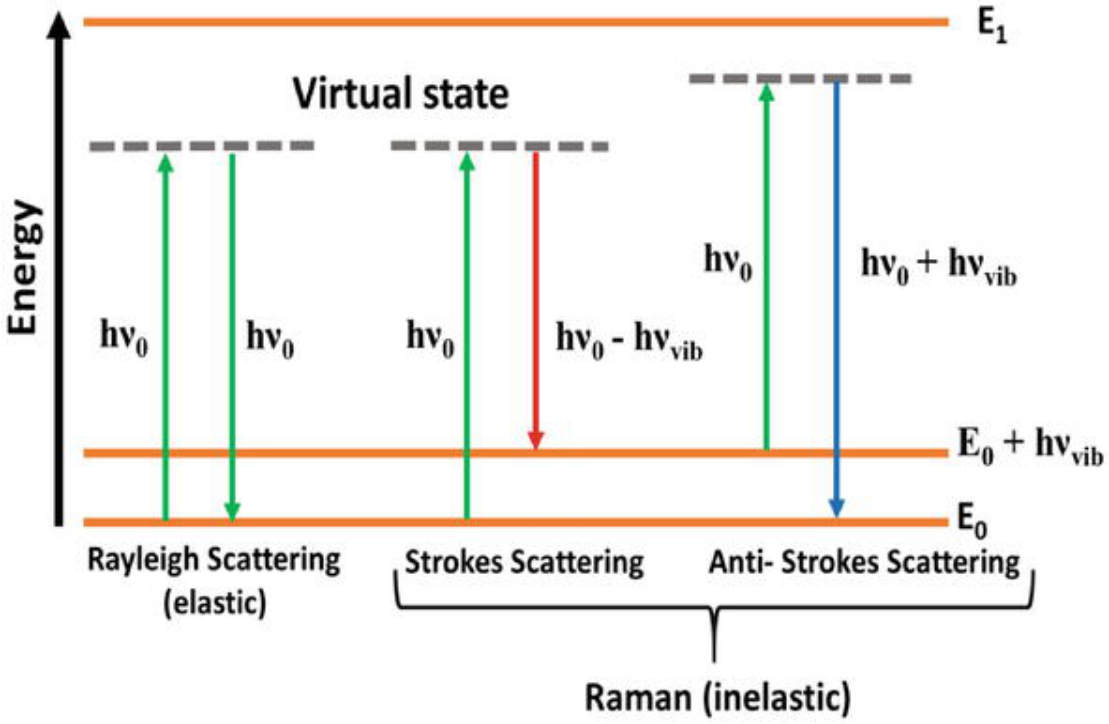

Figure 1. 11 Energy level diagram for Rayleigh and Raman scattering, where $\Delta E = h\nu_{vib}$ represents the difference in vibration energy levels[146]. Stokes process: An incident photon $h\nu_0$ excites a molecular vibration $h\nu_{vib}$ and is thus scattered with the corresponding difference in energy $h(\nu_0 - \nu_{vib})$ (red shift). Anti-Stokes process: The photon acquires vibrational energy and is scattered with a higher energy $h(\nu_0 + \nu_{vib})$ (blue shift).

Under the excitation of excitation light, the molecule leaps from one of its vibrational states (ground or excited) to an excited imaginary state, leaping back to the ground state in picosecond time scales, accompanied by the release of photons. At this point, most of the photons released during the leap back to the ground state have the same wavelength as the excited light, which is the Rayleigh scattering line. There are a

few photons with wavelengths different from the excited light, i.e. Raman scattering lines, which can be divided into two categories (**Figure 1.11**): Stokes scattering and anti-Stokes scattering. Since the number of molecules in the vibrational ground state at room temperature is much greater than the number of molecules in the vibrational excited state, the Stokes lines are much stronger than the inverse Stokes lines. The Raman spectrum is concerned with the difference between the frequency of the Raman scattered light and the incident light, i.e., the Raman shift. Different excitation light produces different frequencies of Raman scattered light, but the Raman frequency shift is the same. The Raman shift characterizes the vibrational-rotational energy level of a compound, and in this respect the Raman spectrum is very similar to the infrared spectrum.

Surface Enhanced Raman Scattering (SERS) was first introduced in 1974[145]. It was found that a significant enhancement in the Raman spectra of pyridine molecules adsorbed on silver electrodes in electrochemical cells, which they explained as an increase in the surface area of the electrode due to the roughness of the electrode surface. However, it was soon found that the enhancement of the Raman signal could reach 10^6-10^{11} orders of magnitude. This value is much larger than the increase in surface area. This phenomenon was then named as surface-enhanced Raman scattering.

However, SERS does not occur on any surface and can only be effectively produced on a limited number of metal surfaces. While Ag and Au are commonly used, SERS has now been found to occur on Pt, Cu, Al and alkali metal surfaces. However, it is not always possible to generate SERS with the suitable metal; SERS occurs only

on roughened metal surfaces, and SERS is not observed on smooth metal surfaces. Moreover, there are many differences between SERS and normal Raman scattering. For example, the relative shapes and intensities of the bands in SERS are different from those of ordinary Raman, and many vibrational bands that are not present in ordinary Raman spectra can be observed in SERS.

1.4.4 Applications of plasmonic based optical biosensors

As the unique optical properties of the noble metal NPs introduced previously, metal nanostructures have been developed rapidly in recent year, especially in the applications of plasmonic based on optical biosensor. SPR biosensors were first most widely used in immunoassays to analyze samples of proteins, nucleic acids, sugars, viruses, bacteria, drugs, and toxins[147], and **Figure 1.12** shows a schematic representation of some typical SPR immunosensor formats. In fact, SPR technology was first applied to biological systems to characterize the resistance to interactions between bodies and antigens. In 1983, Liedberg et al[148] immobilized an antibody to IgG on the surface of an SPR sensor gold film and detected the specific binding of this antibody. Thus, demonstrating the potential of SPR technology for biosensing applications.

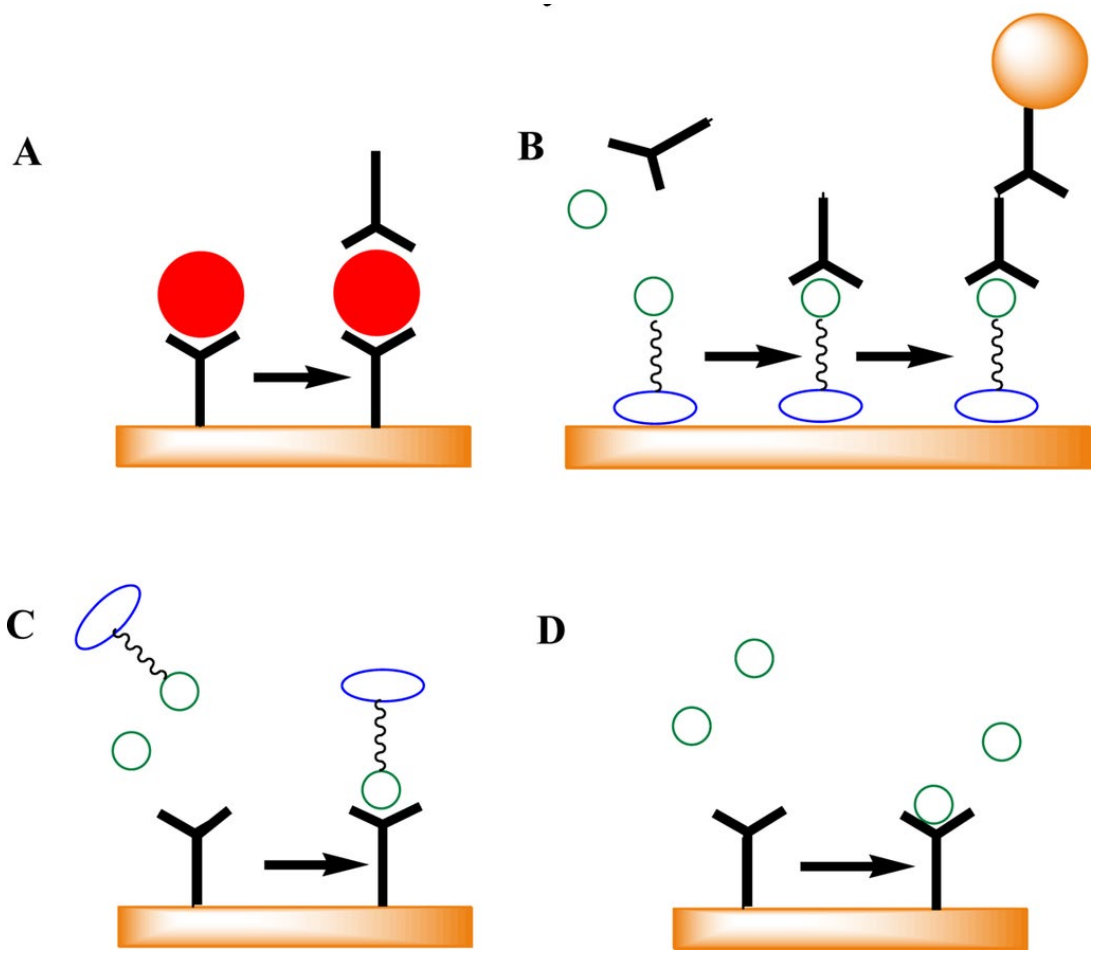

Figure 1. 12 A schematic of some typical SPR immunosensor formats. (A) Sandwich immunoassay for large molecules. (B) Protein conjugate immobilized indirect inhibition immunoassay (can also link via self-assembled monolayers (SAMs) or carboxymethyl dextran polymers) with optional secondary antibody-gold nanoparticle labeling in a second step. (C) Protein-labeled inhibition immunoassay. (D) Direct small molecule immunoassay[147].

Although the SPR biosensors have proven to remain an important commercial tool in the field of optical biosensors, the local surface plasmon resonance (LSPR) detection of metal nanoparticles or nanoparticle arrays can effectively improve the sensitivity, selectivity, spatial resolution, and integrability of SPR sensors, and it has become an

important direction of research and application in the field of detection and sensing. Due to the good spectral tunability of LSPR and the controlled plasmonic nanoparticles, there have been many studies of LSPR biosensors for the detection of many different kinds of biomolecules[149–154]. For instance, immune-LSPR biosensors based on antibody-antigen interactions are essential, mainly due to the strong and highly specific binding capacity of antibodies. Typically, the capture antibody is immobilized on a thiolated plasmonic surface and then the non-specific binding site is passivated to probe specific recognition of the target analyte (antigen) in a dose-dependent resonance wavelength shift. Lee et al.[155] proposed an LSPR-based mechanism for the detection of human immunodeficiency virus (HIV). The binding of biological molecules on the surface of AuNPs is quantified by changes in absorbance, due to specific binding resulting from immune response in the absence of any marker substance, resulting in changes in refractive index of the AuNPs on the transparent indium tin oxide (ITO) substrate, **Figure 1.13**.

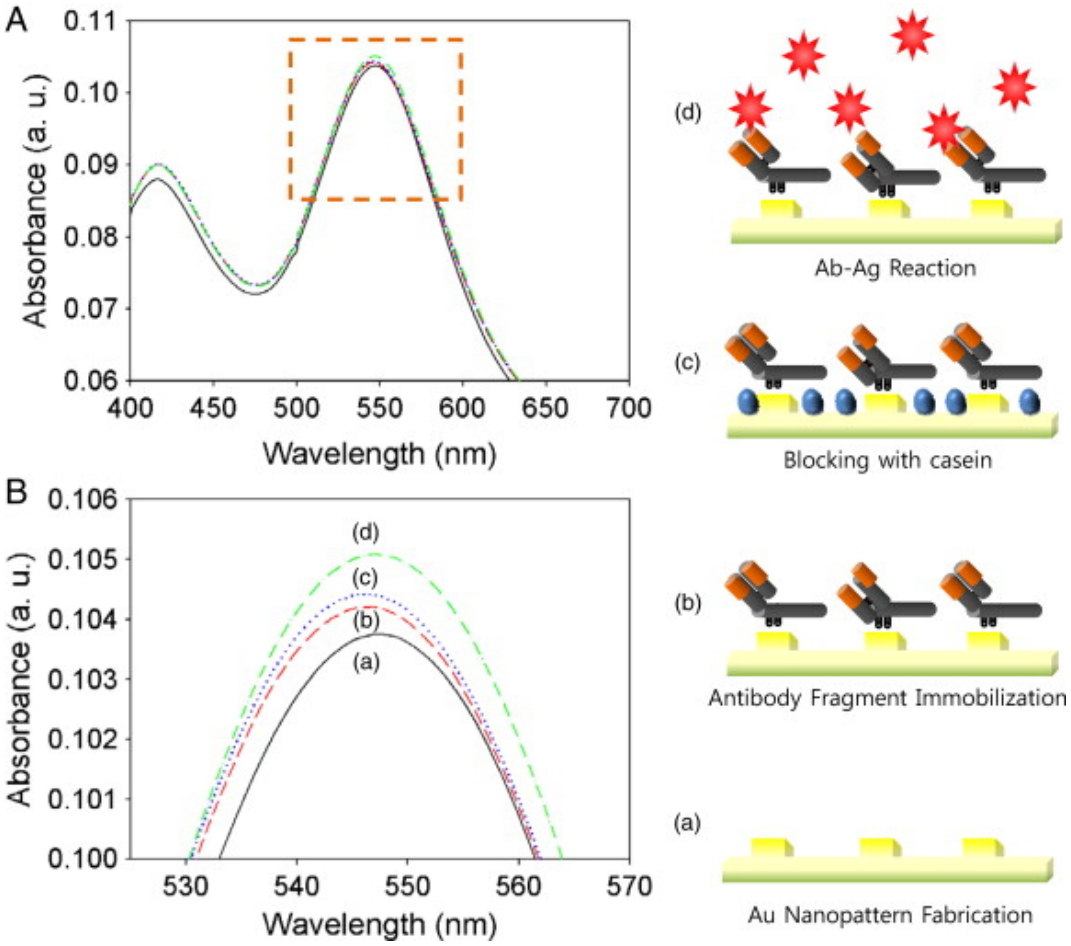

Figure 1. 13 LSPR detection based on gold nanoparticle array platform. (A) Optical characteristics of the (a) bare Au nanopattern on ITO substrate, (b) fragmented antibody immobilized layer, (c) blocking with casein, (d) HIV-1 VLPs immuno reacted layer, respectively. (B) LSPR spectra of zoomed part.[155]

Comparably, Hall at al.[156] developed a method to amplify the wavelength shift which observed from LSPR bioassays using gold nanoparticle-labeled antibodies by taking advantage of electrostatic and covalent interactions between the antibody side chains and nanoparticle surfaces, this amplification strategy improved the sensitivity of plasmon-based bioassays, see **Figure 1.14**.

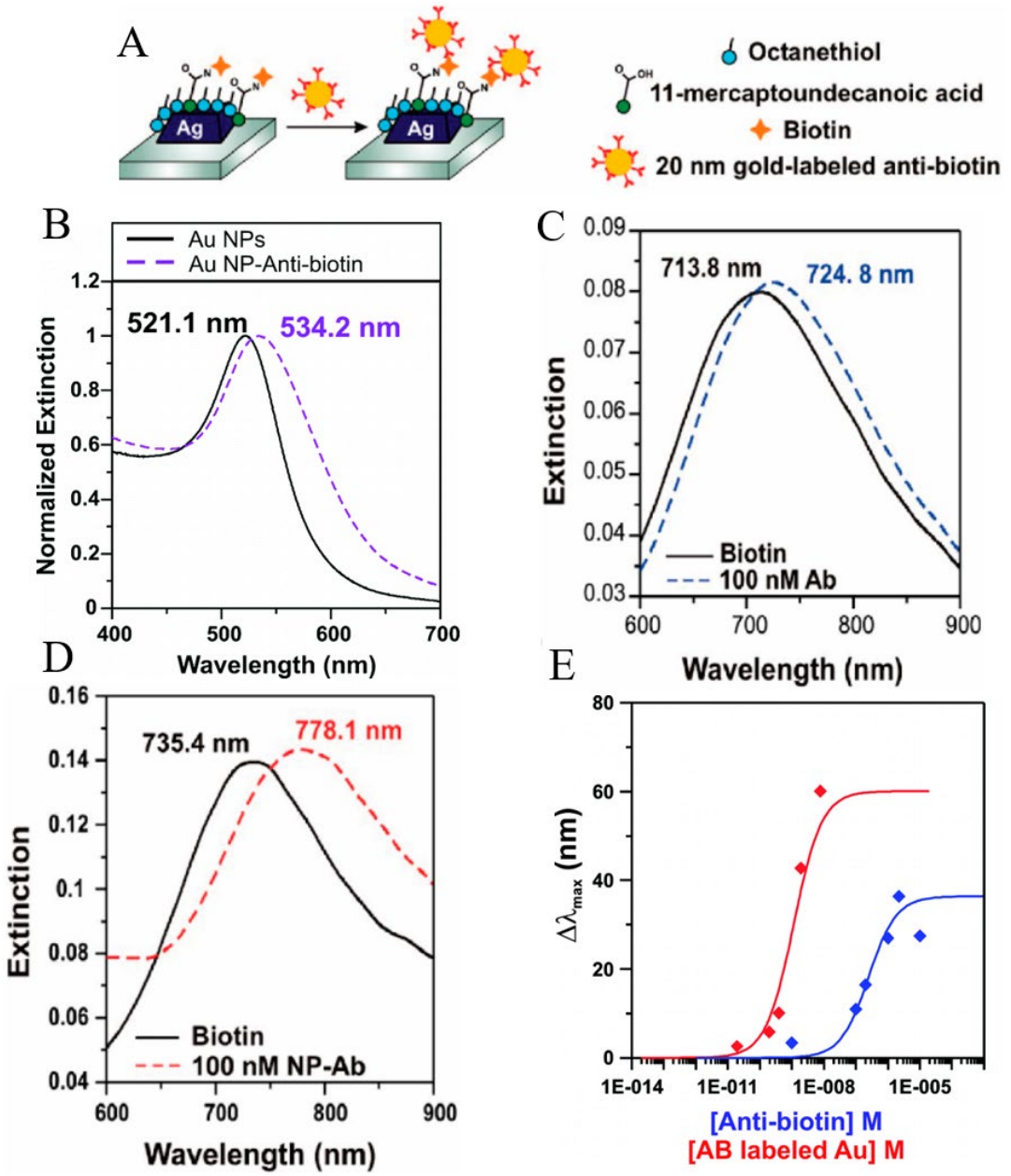

Figure 1. 14 LSPR sensor based on gold nanoparticle (A) Experiment schematic, biotin is covalently linked to the nanoparticle surface using EDC coupling agent, and antibiotin labeled gold nanoparticles are subsequently exposed to the surface. LSPR spectra are collected before and after each step. (B) LSPR spectra of bare AuNPs (shows a λ_{max} of 521.1 nm) and AuNPs after incubation with antibiotin (λ_{max} shifts 13.1 nm). (C) LSPR spectra before and after binding of native antibiotin, showing a $\Delta\lambda_{max}$ of 11 nm. (D) LSPR spectra before and after binding of antibiotin labeled nanoparticles,

showing a $\Delta\lambda_{max}$ of 42.7 nm. (E) Quantitative LSPR response curves for native antibiotin and antibiotin labeled Au[156].

Despite the LSPR allows qualitative and quantitative detection of plasmonic resonance peaks by detecting (bio)molecules of the target species, there are still challenges in using LSPR detection to obtain detailed chemical structures of analyte (bio)molecules. Therefore, another plasmonic technique based on optical biosensing, SERS, can take advantage of the large surface electromagnetic field enhancement effect of nanostructures to directly measure surface molecules and can determine the structure and orientation of the molecules. Thus, it can act as a "direct biosensors" by detecting specific signals from target biomolecules[157–159]. With the development of the SERS biosensor, the SERS measurements on the substrate choices, nanostructures fabrication protocols, biofunctionalization process, etc., have been increasingly studied[160–164]. Depending on the development of SERS biosensors, more and more molecules were used for the biofunctionalization to realize the biosensing detection with SERS measurements nowadays, as shown in **Table 1.2.**

Table 1.2 SERS detection of biomolecules.

Target	Metal NPs	Detection method and detection limit	Optical Response	Reference
S. aureus bacteria	Colloidal AgNPs	3 µL dropped on a fluted glass slide, 1.5 cfu/mL	735 cm^{-1}	Gao W.C. et al.[165]
PCB-77	AgNRs arrays on AAO templates	immersed 3.3×10^{-8} M	656 cm^{-1}, 733 cm^{-1}	Sun K.X. et al.[166]
M13mp18 virus strand - DNA	Au/Ag NPs on SiO_2	0.4µL drop 0.4 nM	1652 cm^{-1}, 1470 cm^{-1}, 1588 cm^{-1}	Prinz J. et al.[167]
C reactive protein	Ag/Au NPs on PCBs	immersed 478 fg/mL	595 cm^{-1}	Liu B. et al.[168]
WNV -DNA	colloidal AuNPs	immersed on glass slide 10 pM	1330 cm^{-1}	Zhang H. et al.[169]
Fructose	Au Q3D-PNAs	immersed 0.018 mM	1079 cm^{-1}, 1585 cm^{-1}	Sun F. et al.[170]
λ-DNA	Au nanoplates films on ITO glass	immersed 10^{-6} mg/mL	1005 cm^{-1}, 126cm^{-1}, 1445 cm^{-1}	Bi L.Y. et al.[171]
Melamine	Au nanorods on Silicon	5µL drop 10^{-12} M	1051 cm^{-1}	Sivashanmugan K.D. et al.[172]
PAH	AuNPs on silicon	1.2×10^{-8} M	1375 cm^{-1}, 1418 cm^{-1}, 1390 cm^{-1}, 591 cm^{-1}	Gu H.X. et al.[173]
R6G	AuNPs on Si nanowires	immersed 10^{-6} M	1360 cm^{-1}	Li Y. et al.[174]

Note:

PCB-77: 3,3′,4,4′-tetrachlorobiphenyl

AAO templates: Conical Pore Anodic Aluminum Oxide Templates

PCBs: Photonic crystal beads

WNV: West Nile virus

Au Q3D-PNAs: Gold quasi-three-dimensional plasmonic nanostructure arrays

PAH: Polycyclic aromatic hydrocarbons

R6G: Rhodamine 6G

Interestingly, a popular plasmonic biosensing technique combines LSPR and SERS to detect target molecules, characterize them by LSPR technique and then identify them with the second technique SERS on quantitative and qualitative binding information. For example, Potara et al.[175] reported a dual functionality of plasmonic platform which evaluated through the combined LSPR-SERS detection of significant biological molecules, adenine (**Figure 1.15**).

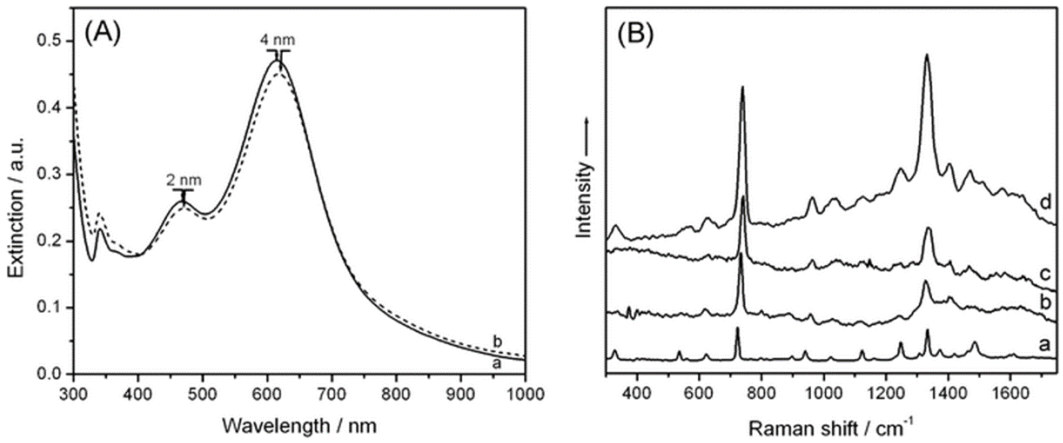

Figure 1. 15 (A) UV-VIS-NIR extinction spectra of silver colloid (a) before adding adenine and (b) after adding adenine. (B) The normal Raman spectrum of solid adenine (a) and SERS spectra of adenine recorded by laser excitation wavelengths 785 nm (b), 633 nm (c), and 532 nm (d). The final concentration of adenine molecules in the sample solution is 12×10^{-6} M[175].

1.5 Quartz Crystal Microbalance (QCM) biosensing

1.5.1 Principle of QCM technology

Quartz crystal microbalance (QCM) is an acoustic sensing system used in chemistry, physics, and biology to study the viscoelasticity of substances, the adsorption of molecules, or the motion of living cells, etc. The QCM is a thickness shear type (TSM) acoustic resonator in which an AT-cut (from a high-purity quartz crystal cut at 35°15′ to the main optical axis of the quartz crystal) thin quartz disk is sandwiched between two metal electrodes, usually made of gold (**Figure 1.16**). Due to the piezoelectric property of the quartz material, the alternating electric field produces a shear deformation with the 2 surfaces parallel but moving in opposite directions, resulting in a moving wave propagating through the crystal material in a direction perpendicular to the surface of the electric field[176].

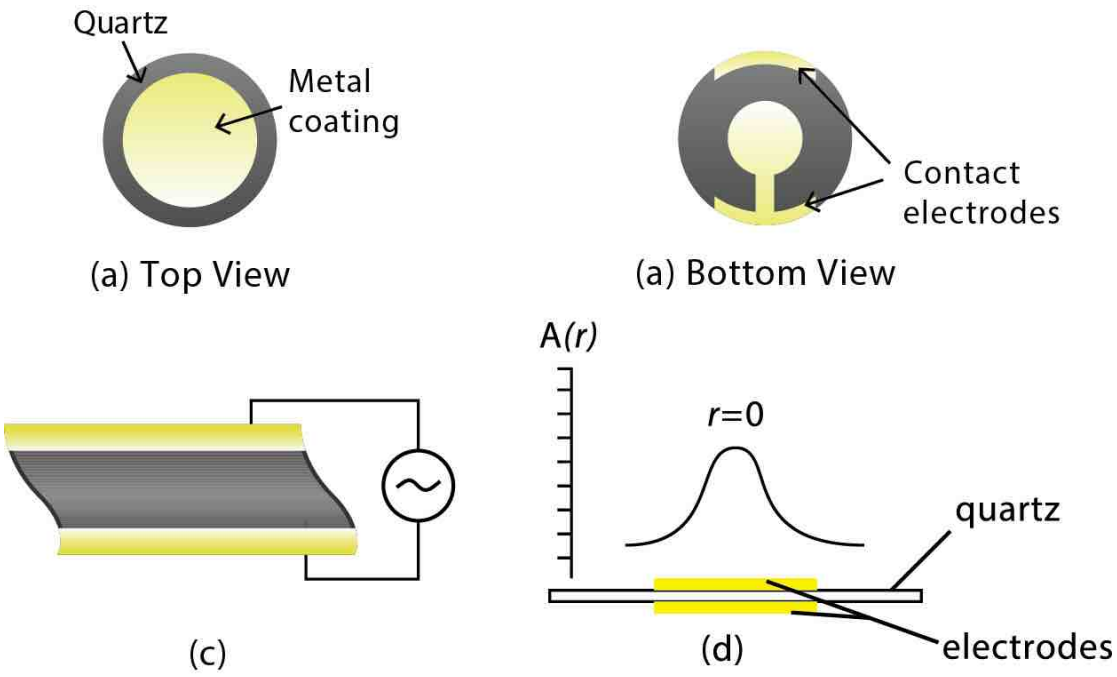

Figure 1. 16 Design of quartz crystal (grey) with electrodes (yellow); (a) top view (b) bottom view. (c) A schematic illustration of the strain induced in an AT cut crystal on application of AC voltage. (d) A schematic illustration of how amplitude of vibration (A(r)) varies with the distance (r) from the center of the sensor. The area of vibration is called the active surface area and is sensitive to mass changes[177].

By relating the mass of the crystal material to the density, it is possible to predict the resonant frequency change associated with the small mass increase (Δm) at the sensor surface, as shown by the equation:

$$\Delta f_m = [-2nf_0^2/(\rho_q\mu_q)^{1/2}] \times [\Delta m/A] \qquad (3)$$

where Δf_m is the frequency change due to mass loading, f_0 is the resonant frequency of the fundamental mode, n is the harmonic or overtone number, ρ_q and μ_q are, the density and the shear mode of the crystal, respectively, A is surface area of the material, Δm is the mass change occurring at the surface of the sensors. This is the Sauerbrey equation[178], which establishes a linear relationship between the resonant frequency and

the small mass increment. In general, the Sauerbrey equation estimates the total mass of the adsorbate based on the total frequency change obtained, or establishes a direct relationship between the frequency change (signal) and the mass[179]. The frequency decreases when the substance is adsorbed on the crystal surface. This model assumes that no energy dissipation occurs and that the deposition of mass on the crystal surface and the formation of thin films follow the vibration of the crystal, and this equation applies to thin, rigid and homogeneous films with similar acoustic properties.

However, when the resonator is immersed in a liquid as required for biosensing applications, or when the added viscoelastic probe layer has significantly different acoustic properties than the crystal sensor layer, energy is lost to the liquid through the so-called viscous coupling. Based on this, assuming that no slip occurs at the solid-liquid interface, the viscous coupling effect was modeled[180], i.e., the liquid near the crystal surface moves at the same velocity as the surface, and that the resonant frequency of the sensor will decrease because the liquid damping is proportional to the liquid viscosity and density. So, the QCM will respond to mass deposition and liquid loading. In addition, the QCM will also respond to differences in buffer and injected sample viscosities as well as temperature-induced viscosity changes, since frequency changes are strongly influenced by liquid density and viscosity. A model for the total frequency change was derived, and that accounts for the simultaneous effects of mass and liquid loading on the sensor signal[181]. Although the QCM as a sensor mainly utilizes the direct relationship between mass and frequency, i.e., the Sauerbrey equation, it does not take into account the viscoelastic effect of the adsorbed layer. Therefore, this

measurement method is usually biased. The dissipative quartz crystal microbalance (QCM-D) adds a dissipation factor D to the QCM, which represents the viscoelasticity of the adsorbed film layer on the sensor surface. The larger the D, the softer the film on the crystal and the more viscoelastic the adsorbed layer[182]. Dissipation is defined as the inverse of the crystal's quality factor, Q, as expressed by

$$D = 1/Q = E_{dissipation} / (2\pi * E_{stored}), \quad (4)$$

where $E_{dissipation}$ is the energy dissipated in one cycle and E_{stored} is the energy stored in the oscillating system. When the piezoelectric quartz crystal resonates, the electrical current and mass oscillate simultaneously. In QCM-D method, the quartz crystal is excited to its resonant frequency by applying a driving voltage for a short period of time. The driving voltage is then turned off and the voltage decay on the crystal is recorded against time[183].

Despite its shortcomings, the QCM technique can still successfully use standard oscillator techniques and frequency counting to continuously monitoring of the resonant frequency of the sensor. Following the applications of sampling, the variation of the resonant frequency can be further obtained by comparison with a reference value, which in turn allows for applicated studies on viscoelasticity of substances, adsorption of molecules, dynamic monitoring, etc[176]. The application of OCM technique will be introduced below.

1.5.2 Applications of QCM technology

QCM, as a label-free acoustic sensing technology, allows real-time monitoring of cell adhesion interactions with the surface of sensing elements. Over the past 20 ans,

this unique capability of QCM has made it particularly attractive in the field of cell biology[184]. Applications of QCM in the field of cell biology are focused on interactions such as adhesion and morphological changes on the cell surface[185]. As a piezoelectric sensor, QCM is a fast and convenient tool for studying eukaryotic cells, providing real-time information on processes such as cell adhesion, morphological changes, and apoptosis, and can be used to detect the physiological effects, toxicity, and biocompatibility of new drugs[186]. A novel method was introduced for monitoring the deformability of red blood cells (RBCs) by combining a quartz crystal microbalance and a mathematical model[187]. It is able to accurately distinguish between normal erythrocytes and artificially sclerotic erythrocytes consistent with the disease state, and to infer qualitative and quantitative information related to changes of cell elasticity.

QCM is also a popular immunosensing technology (**Table 1.3**), which is important for the study of biomolecules due to its simplicity, convenience, low cost, and fast real-time response. Using QCMs as immunosensors, highly sensitive sensor systems can be established for the detection of tiny amounts of environmental pollutants or disease markers. For example, a QCM-based immunotransmitter was developed by immobilizing targeted antibodies on the gold surface of a quartz crystal microbalance by a photonic immobilization technique. The detection limits of QCM for parathion and patulin were reduced to 50 and 140 nM, respectively[188]. A label-free gliadin immunosensor was developed on QCM crystal modified with colloidal 25 nm AuNPs with a detection limit of 8 ppb gliadin in 60% ethanol[189].

Besides the use of colloidal AuNPs, another approach to fabricate nanostructures

directly on the gold electrode of QCM crystal. To do this, the evaporation and annealing processes were included in the chapter 4.

Table 1.3 QCM technique for immunosensing.

Target	Diameter of gold electrode	Modification of the gold electrode with colloidal AuNPs/ evaporated Au layer	Detection limit	Reference
L. monocytogenes	-	S-QCM	1×10^7 cells/mL	Vaughan R.D. et al.[190]
Salmonella Typhimurium	5.5 mm	S-QCM	10^2 cells/mL	Su X. L. et Li Y.B.[191]
OTA mycotoxin	-	S-QCM	17.2 ng/mL	Pirincci S.S. et al.[192]
Salmonella Typhimurium	0.68 cm	S-QCM	10° CFU/mL	Fulgione A. et al.[193]
HAS	0.68 cm	S-QCM	10 U/L	Ventura B.D. et al.[194]
Parathion peticicide	0.68 cm	Colloidal AuNPs with a diameter of 10 nm	0.8 µg/L	Ventura B.D. et al.[195]
DPSCs	4.5 mm	S-QCM	0.5 ng	Maglio O. et al.[196]
BAECs	2 mm	chrome (Cr) layer with 20 nm thickness and 200 nm of Au layer (evaporation)	1.5×10^4 cells/cm^2	Liu F. et al.[197]
Gliadin in food samples	-	Colloidal AuNPs	1 ppm	Chu P.T. et al.[189]
Gliadin	-	Colloidal AuNPs (25 nm)	8 ppb	Chu P.T. et al.[189]
Gliadin in food samples	-	Au thickness of 2 nm, 4nm and 6nm (evaporation and annealing)	0.0001 ppm	Giuliocesare C.B. et al.[198]
Giadin	-	Au 30nm thickness (evaporation)	0.0001 ppm	Giuliocesare C.B.et al.[198]

Notes:

S-QCM: Standard QCM crystal

L. monocytogenes: Listeria monocytogenes cells

AI H5N1 virus: pathogenic avian influenza (AI) H5N1 virus

OTA: Ochratoxin A mycotoxin

HAS: Human Salivary α-Amylase

DPSCs: dental pulp stem cells

BAECs: Bovine aortic endothelial live cells

1.6 Summary

Based on the above research, many technologies have been or are being developed and used for chemical and bioanalytical applications of sensors. Among them, with the

rapid development of detection technologies and nanomaterials science, a broader platform is provided for the preparation and research of noble metal nanostructures on the basis of biosensors. In particularly, the optical biosensors have attracted great attention and interests in the field of research, especially the label free optical biosensing. In this study, the scanning microwave microscopy was developed to detect biomolecules besides obtained the electrical properties. Due to the unique optical properties of the AuNPs, and the combination of plasmonic technique with LSPR and SERS, a number of ultrafine platforms have been prepared based on the plasmonic biosensing to improve the stability, repeatability and sensitivity of biosensors. In addition, for the immunosensor, the detection of gliadin molecules based on modification of QCM was studied.

Chapter 2 Microwave Spectroscopic Detection of Human Hsp70 Protein

As introduced in the previous chapter, AuNPs were used for SMM biological applications. However, there are no studies concerning the real time analysis of the bio-functionalization of solid metallic active supports with SMM technique. Therefore, in this chapter, the potential using of the microwave spectroscopy technique is to characterize the modification of annealed gold- (ITO) glass substrates with (bio)molecules for the detection of human 70 kDa heat-shock proteins (Hsp70), and to better understand the (bio)functionalization of the AuNPs on the glass substrates.

Heat shock proteins [199] are an important part of the cellular machinery responsible for protein folding and protecting the cell from stress. In particular, the Hsp70 protein is either overexpressed on the surface of cancer cells or in peripheral blood (such as diabetic patients), and constitutes the core component of the cellular molecular chaperone[200,201] network, and plays a role in many biological events, including protein folding and assembly, post-translational modification, transportation, secretion, inflammation[202], and degradation.

For this study, I was mainly involved in preparation of AuNPs on the conductive (ITO) and non-conductive glass substrates with different thickness of the evaporated Au film at the high temperature, and performed the morphological characterization and NPs size distribution analysis of the AuNPs. The analysis of these results were published in Biosensors[203] on 2018.

In this study, a quantitative non-destructive nanoscale surface investigation based

on high-speed atomic force microscopy (HS-AFM) coupled with surface enhanced Raman spectroscopy (SERS), allow high speed imaging of molecular chaperones such as Hsp Lo18 or hHsp70 and their chemical recognizing useful for biosensor development. High-speed atomic force microscopy (HS-AFM) instrument can perform imaging at a speed of 5-20 frames/s (fps) without interfering with the functions of fragile proteins and delicate protein-protein and DNA-protein interactions. The application of this prototype high-speed AFM (HS-AFM) in the field of biology is almost limitless because the additional dimensions of the time evolution of biological processes are evaluated (structural and functional dynamics). Therefore, research on membrane-related processes (important in signal transmission, transportation, and energy production), research of protein-DNA complexes[204], (important in genetic and transcriptional regulation), as well as the studies of the effects of surface properties and confinement on selectivity, reactivity and biological activity of proteins[205] (interactions between proteins and inorganic materials) are important for the development of biosensors. In addition to imaging of supramolecular assemblies, nanotechnology is used to understand the ion selectivity, activity, chemical reactivity and conformational changes of biomolecules in vitro under the influence of the geometric shape of the restrictive support and its physic-chemical properties, to obtain the effect of the surface on the thermodynamic properties of biomolecules. Different planar and charged surfaces have been selected, and these surfaces have the potential to bind to proteins. The interactions between the protein and the substrate could be adjusted by changing the type and concentration of ions in solution, by changing the temperature and

chemically modifying the surface. Planar and nanostructured surfaces (with and without proteins) could be characterized by HS-AFM in solution[206]. From image information, we could obtain geometric information (**Figure 2.1**): transitions, local changes, connections, topology, morphology, the existence of known shape models, statistics and frequency characterization. In this study, three different concentrations modification of ITO biochip characterized designed to detect tumoral biomarkers.

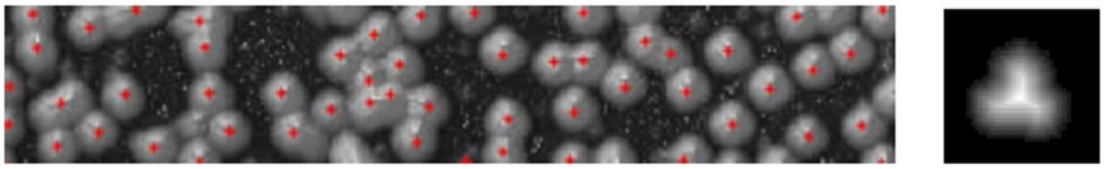

Figure 2. 1 HS-AFM image of heat shock proteins hHsp70 deposited on ITO substrate (size 250 nm). The HS-AFM image information was extracted automatically from the center for density calculations.

2.1 Experimental materials and methods

2.1.1 Materials

The materials used in this chapter are shown in **Table 2.1**. All the chemicals were of analytical grade and used as received without further treatment unless specially mentioned.

Table 2.1 The compounds and materials used in different steps of SMM detection experiment.

Materials	Abbreviation	Company, city, country	Function
Heat Shock Proteins 70kDa	Hsp70	Prospec, Rehovot, Israel	analyte for detection
11-Mercaptoundecanoic acid	MUA	Sigma-Aldrich, St. Louis, MO, USA	Au biomodification
N-Hydroxysuccinimide	NHS	Sigma-Aldrich, St. Louis, MO,	Au biomodification

		USA	
Tris (hydroxymethyl) aminomethane hydrochloride	Tris-HCl	Sigma-Aldrich, St. Louis, MO, USA	buffer preparation
deionized water	ddH_2O	Millipore, Molsheim, France	sample washing
detergent	Decon90	Fisher Scientific, Göteborg, Sweden	sample washing
Ethanol	-	Sigma-Aldrich, St. Louis, MO, USA	sample washing
glass slide	-	Carl Roth, Karlsruhe, Germany	glass substrate

2.1.2 Instrumentations

Instruments of AuNPs preparation: In the fabrication of the gold nanostructured glass substrates, the ultrasonic water bath Elmasonic S30H (Elma Schmidbauer GmbH, Singen, Germany) and the hotplate (Thermo Fisher Scientific, Waltham, MA, USA) were used for sample cleaning and sample drying, respectively. The vacuum evaporator (Playssys, MEB 400, Marolles-en-Hurepoix, France) and the high temperature oven (Model N.60/65A; No. 171,693; T_{max} = 650 ˚C, Nabertherm, Germany) were used for metal evaporation and subsequent sample annealing, respectively.

Instrument of AuNPs morphological characterization: The morphology of gold films deposited on non-conductive and ITO-conductive substrates, and after thermal annealing were systematically analyzed through the scanning electron microscopy (SEM) (FEG-SU8030, Hitachi, Tokyo, Japan).

Scanning microwave microscope measurement: The analyses of the samples were carried out by Scanning Microwave Microscope (AFM 5600 LS) from Agilent Technology. The working frequency of SMM is usually at microwave frequencies from 1 MHz to 18 GHz. The SMM set-up is shown in **Figure 2.2A**.

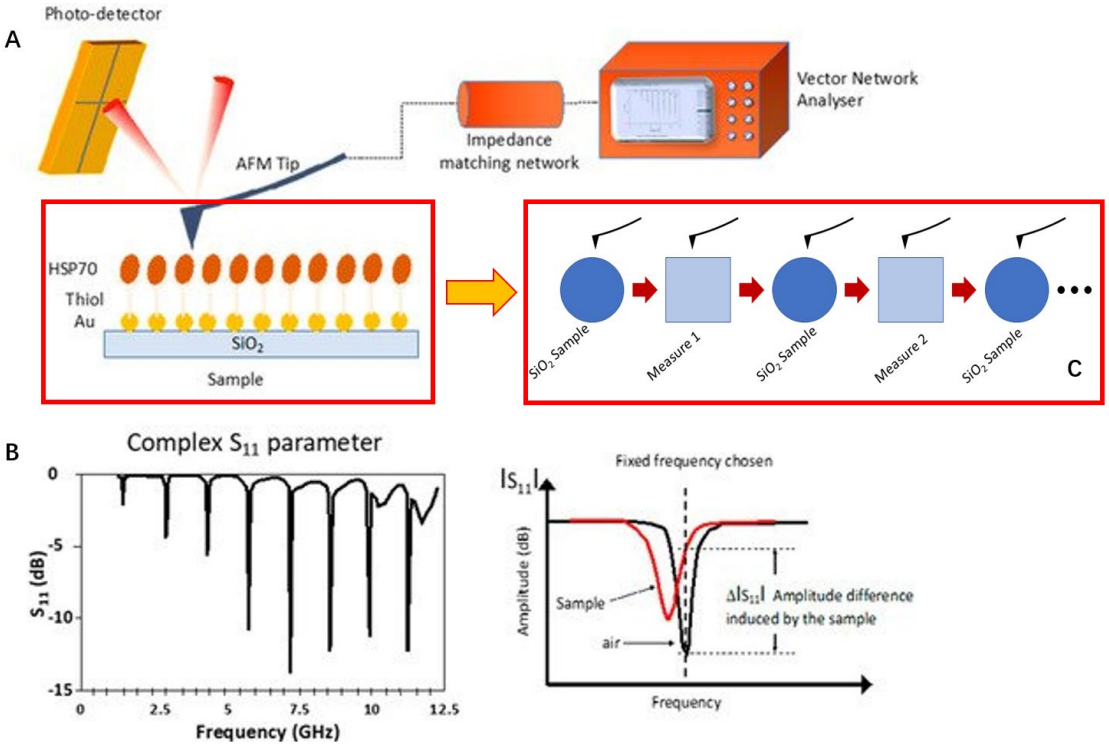

Figure 2. 2 Experimental set-up for microwave spectroscopy experiments. AFM tip-to-sample distance control and measured amplitude signal (A). S_{11} -the complex reflection coefficient (B). Step-by-step protocol for microwave AFM measurements (C).

Bruker's SCM-PIT probe is based on the AFM FESP high-performance probe, with a nominal spring constant of 1 N/m, and a conductive platinum-iridium-coated tip (Pt-Ir), which is ideal for electrical characterization applications. The Pt-Ir coating on the front end of the cantilever provides a metal electrical path from the cantilever die to the tip. The cantilever and the probe act as a local radiating antenna for transmitting and receiving microwave signal.

The microwave spectroscopy includes measuring the amplitude of the microwave signal reflection of each frequency in the spectrum, so that the physical characteristics of the test sample can be detected. The 1-port Vector Network Analyser 1 MHz–18 GHz (Copper Mountain Technologies R180) associated with a specific impedance matching

resonator circuit can measure the ratio of the incident signal to the reflected signal at the tip, the so-called scattering S_{11} parameter (**Figure 2.2B**).

Using a microwave microscope for measurement can detect local changes in various material properties, such as electrical conductivity or chemical composition. In the present case, elements with different chemical compositions are tested by changing their concentration. These different chemical compositions will cause a change in the dielectric constant, which will be quantified with the response in the air. This distinction will be achieved by selecting the signal in the air as a fixed reference frequency, and the signal in the air will be compared with the signal in the presence of the sample in contact with the tip. The amplitude change of this difference ΔS_{11} will give the influence of the sample on the microwave signal (**Figure 2.2B**). In order to increase space detection compatibility with nano-sized objects, the device uses a near-field technology due to the close sample of the AFM tip. The S_{11} parameter depends on the dielectric constant value of the medium, in the interaction with the microwave. Therefore, all modifications, such as bio-functionalization, molecular absorption, molecular grafting, DNA hybridization and immune response, affecting the dielectric constant of the medium will be easily detected. The detection principle is based on the comparison between the S_{11} value in air and the S_{11} value in presence of the tested sample at a given frequency.

2.1.3 Preparation of gold nanostructures on glass substrates

In the preparation of AuNPs process, the silicon dioxide (SiO_2) lime non-conductive and ITO conductive substrates were used for gold film deposition[6], annealed

AuNPs were fabricated on glass in three steps: cleaning, gold evaporation, and oven annealing at 550 °C. At the beginning, all glass substrates were cleaned with a mixed solution of detergent (Decon90) and deionized water (ddH_2O) in an ultrasonic water bath at 50 °C for 15 min. Further, the glass samples were thoroughly rinsed with ddH_2O, dried under N_2 steam, sonicated three times in deionized water at 50 °C for 5 minutes, and then rinsed with fresh deionized water. Finally, dry again under a N_2 steam, transfer the substrate on a hotplate, and dry it completely at 100 °C for 10 min. In the gold evaporation step, the cleaned ITO glass strips were placed on a support-plate inside the metal evaporation chamber in a vacuum evaporator under a lower pressure of 1×10^{-6} Torr at 25 ℃. By changing the value of the working current during the rotation of the support with the glass samples, the metal deposition rate was maintained at 0.01 nm/s to obtain a uniform deposition of gold films on the non-conductive and conductive substrates. In order to investigate the influence of three gold thicknesses on functionalization and SMM detection of Hsp70 protein, the three thickness of evaporated gold film was set in 2 nm, 4 nm, and 8 nm, respectively. After gold evaporation, the Au-modified glasses were transferred to a high-temperature oven and annealed at a high temperature of 550 ℃ for 8 h.

2.1.4 Biofunctionalization of gold nanostructures on glass and ITO substrate

The annealed gold nanostructures on glass substrates were exposed to 150 µL MUA-thiol (8 mM) dissolved in ethanol in a petri dish used as a humid chamber at 4 ˚C for 1 h. After 1 h, the samples were rinsed with ethanol, dried, and incubated with 100 µL NHS-solution (4.5 mg/mL) for 20 min, then rinsed with the Tris-buffer. In

addition, five activated AuNPs substrates were biofunctionalized with 2 μL of human heat-shock proteins (hHsp70) solutions of a given concentration at room temperature for each protein concentration over 30 min, followed by rinsing with Tris-buffer and dd H_2O. At room temperature (23.5 °C) with a relative humidity (RH) of 32%, microwave spectroscopy was used to detect five concentrations of human heat-shock proteins (50, 40, 25, 20 and 12 ng/ μL/cm^2, respectively).

2.1.5 Microwave AFM measurements

The established microwave measurement protocol to monitor the influence of each element developed by the nanochip is illustrated in **Figure 2.2C**. Microwave spectrum acquisition is obtained by point-to-point recording of data from each region of interest. Each sample analysis is preceded and followed by an analysis of the SiO_2 reference substrate. Having a homogeneous structure in thickness and component allows us to check that no drift appeared in the measurement phase of the samples, or take it into account if necessary. Therefore, in order to ensure the reproducibility of the measurements, as shown in **Figure 2.2C**, there are nine measuring points on each specific area. Perform twenty-resonance frequency spectra to determine which one will get the best sensitivity and stability.

2.2 Results and Discussion

2.2.1 SEM characterization and size distribution of AuNPs on different substrates

The morphology images of the evaporated and annealed specific gold layers (4 nm) on different substrates (glass and ITO substrates, respectively) were shown in

Figure 2.3 (A-D). The SEM images of annealed AuNPs on non-conductive and conductive substrates are shown in **Figure 2.3C, D** which were corresponding to the size distribution, respectively. The results are described in **Figure 2.3E, F**. The size distribution was analyzed using the Public Domain ImageJ software developed by the National Institutes of Health.

It should be noted that on the glass substrate, the AuNPs in the range of 5-30nm have been observed to have a wide size distribution, of which NPs in the range of 10nm-30nm account for the majority (**Figure 2.3E**), while the AuNPs deposited on the ITO substrate have a size distribution, it is narrower in the range of 30-40nm (**Figure 2.3F**). It indicates that size distribution (23.4%) of 10 nm AuNPs on glass substrate is greater than the size distribution (3.2%) of the AuNPs on ITO substrate. In addition, the percentage of size distribution on glass substrate is 23.4% (10 nm) > 21.8% (20 nm) > 18.4% (30 nm) > 11.5% (5 nm). However, compared with other size distributions, the 40 nm AuNPs on ITO glass has the highest size distribution (26.2%), followed by 30 nm size distribution (24.3%).

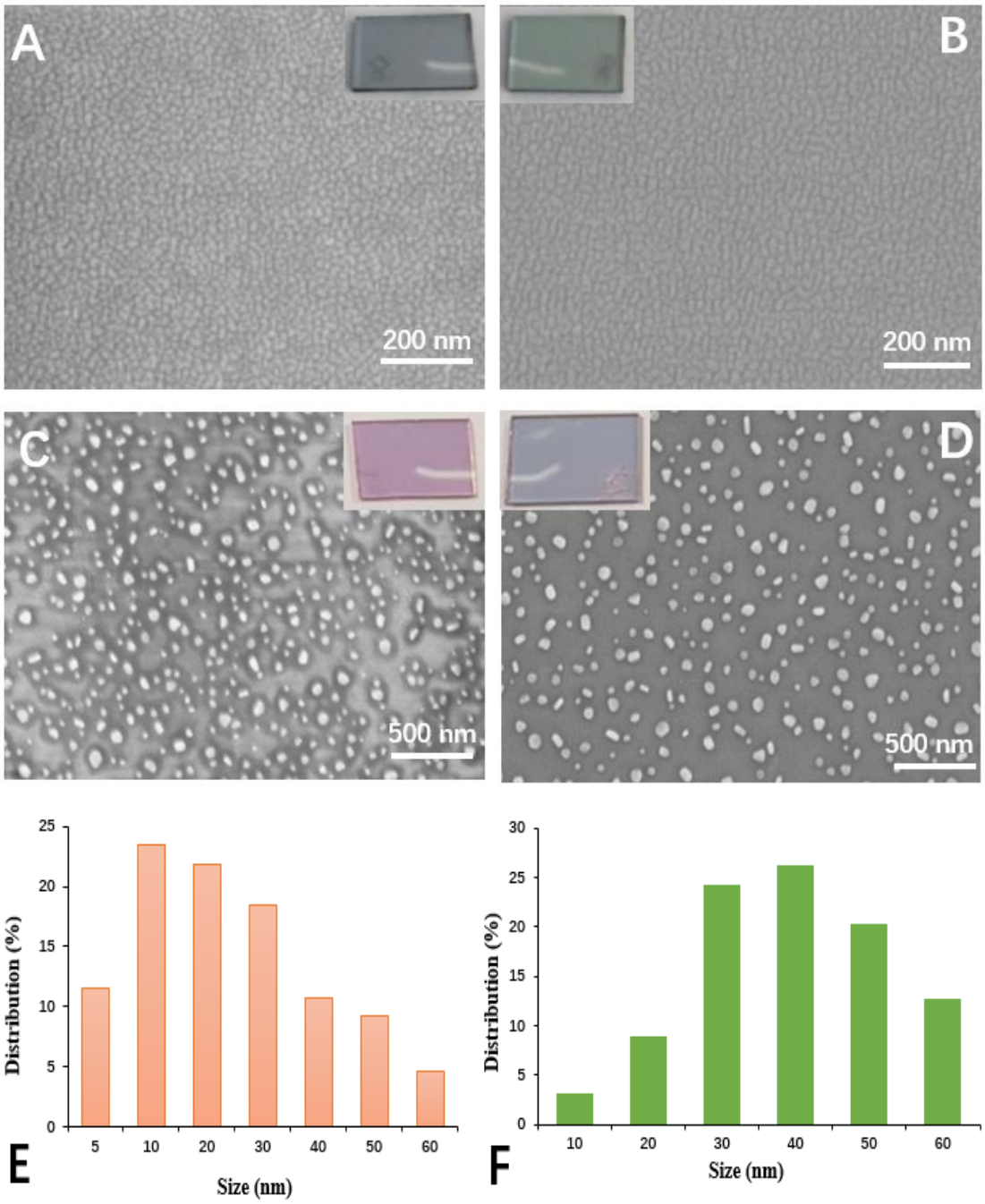

Figure 2. 3 SEM images of gold films (4 nm) as evaporated (A) on glass substrate; (B) on ITO substrate; and after annealing at 550 °C for 8 h (C) on glass substrate and (D) on ITO substrate. The size distribution result of annealed AuNPs (4 nm) (E) on glass substrate and (F) on ITO substrate. Insert-photo is real glass sample.

2.2.2 Microwave spectroscopy measurements for 2 nm, 4 nm, and 8 nm Au–glass

samples

On the basis of the investigation of the morphological images and the size distribution on the glass and ITO substrates, the Microwave spectroscopy measurements on the gold coated glass sample with the thickness of 2 nm, 4 nm and 8 nm were studied. As previously introduced in the microwave measurement protocol, nine spectrum acquisitions are performed on each component, in this work, SMM is performed on four kinds of surface of substrates: 1) SiO_2 alone; 2) SiO_2 plus AuNPs; 3) SiO_2 plus AuNPs plus thiol; 4) SiO_2 plus AuNPs plus thiol and five Hsp70 protein concentrations (12, 20, 25, 40 and 50 ng/μL/cm^2).

In order to select the frequency suitable for the SMM measurements, a frequency sweep was performed in the range of 1 GHz to 10 GHz, with 64,001 acquisition points. The quantity to be evaluated, amplitude (dB), is the value ΔS_{11} plotted as a function of the frequency. All microwave measurements are performed in a controlled atmosphere (22 °C, 35% RH). The amplitude signal as a function of the frequency for every modification step of the surface with three different gold film thickness (2 nm, 4nm and 8 nm, respectively) for different concentration of Hsp70 proteins were compared, three concentrations 12, 25 and 50 ng/ μL/ cm^2 were selected to make the graphs for the relationships between amplitude and Hsp 70 protein concentrations (**Figure 2.4 (A-C)**).

The **Figure 2.4A** shows the variation of amplitude versus frequency for 2 nm gold thickness biochip functionalized with three Hsp 70 concentrations (12, 25, and 50 ng/ μL/cm^2). Starting from the SiO_2 signal, it can be observed that in the large number of resonances visible in the graph, the addition of each chemical entity changes the

microwave signal. Indeed, each building modifies the equivalent impedance of the sample so the dielectric constant of the material is studied at the frequencies used. However, for each frequency, depending on the different molecules added, the sensing response does not necessarily have a linear consistency. Only a frequency of 4.33 GHz seems to provide a "linear" response for this research system based on different elements.

Interestingly, in the spectral characterization with gold film thickness of 4 nm (**Figure 2.4B**), it's also found that only the frequency of 4.33 GHz seems to give a "linear" response for this studied system based on the different elements. Furthermore, SMM measurements with a gold film thickness of 8 nm were also performed (**Figure 2.4C**). The conclusion is the same as the previous two cases, but with a slightly difference that we will discuss.

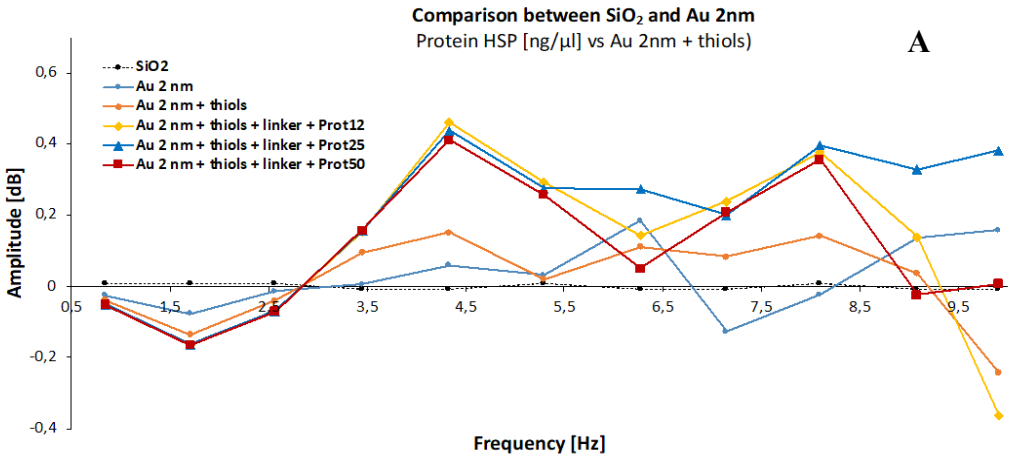

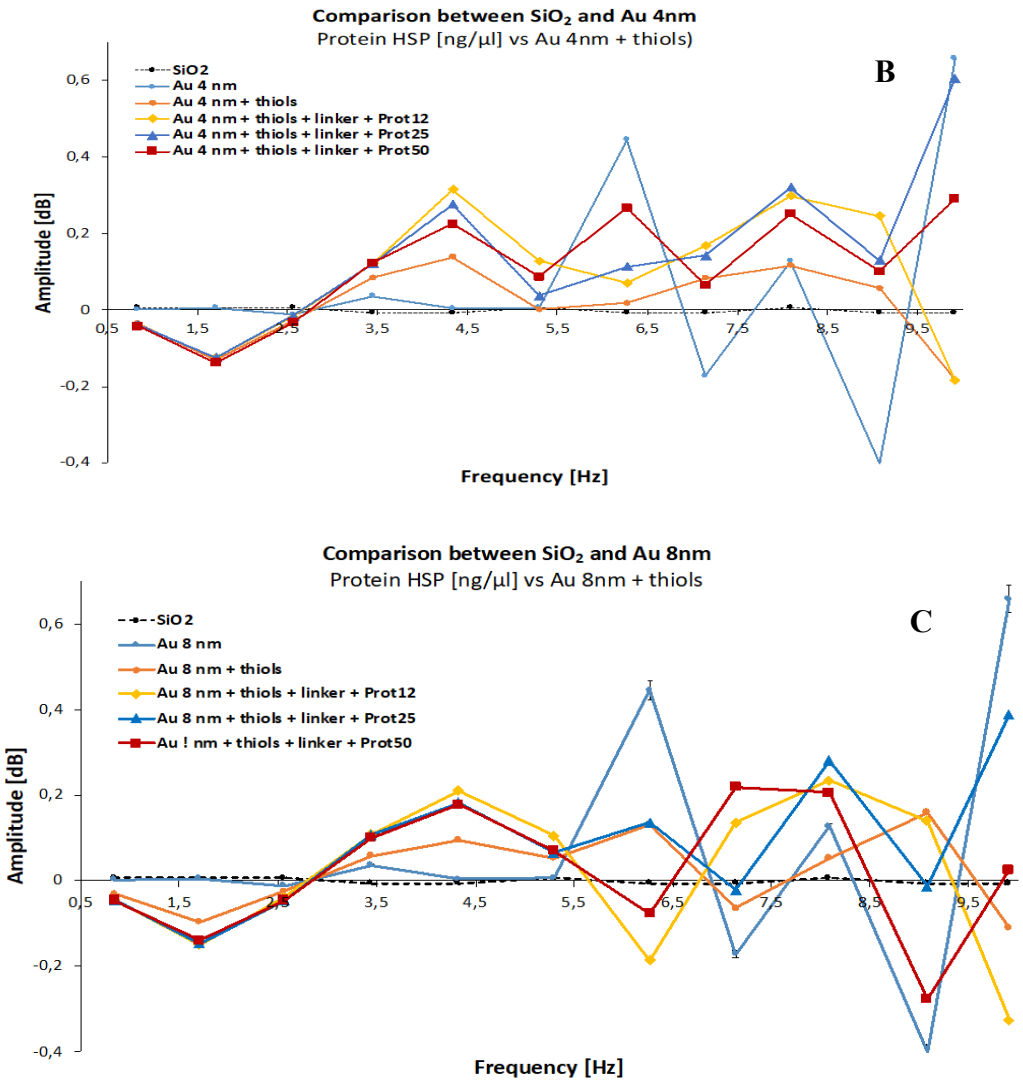

Figure 2. 4 Spectral characterization of materials with gold film thickness of A) 2 nm, B) 4 nm and C) 8 nm for different Hsp70 protein concentrations (12, 25 and 50 ng/µL/cm^2).

In conclusion, for each Au thickness (2nm, 4nm, 8nm) at 4.33 GHz, it observed that with the substance added (Au/Au+thiol/Au+thiol+Hsp70), the amplitude increased. However, for adding Hsp70, with the concentrations increasing, the amplitude decreasing. The reason is in this frequency 4.33GHz, the dielectric constant of each concentration of Hsp70 protein is changed.

2.2.3 Optimization of microwave measurements using three independent gold

thicknesses on glass samples

For the purpose of optimization of microwave measurements, five different concentrations of Hsp70 proteins were tested on the three different thickness (2 nm, 4 nm and 8nm) of evaporated gold film on the glasses, respectively, with the different tested frequencies (range from 1 to 10 GHz), the optimal microwave (bio)sensing results were obtained at 4.33 GHz (**Figure 2.5**). For a given concentration, except the highest one (50 ng/µL for Au 4 nm and Au 8nm), as the NPs size increases, the amplitude of the signal decreases. Moreover, for crucial point, it is noticed that the 2nm and 4nm Au –substrates present a linear evolution of amplitude (dB) (R^2=0.97 for Au 2nm and 0.99 for Au 4nm) for the three tested concentrations of protein hHsp70 (ng/µL/cm^2) with the value of slope equal to -13.10^{-4} and to -23.10^{-4} dB/(ng/µL) respectively for Au 2nm and Au 4nm. It is worthwhile to notice that the slope of the curve is higher for 4nm gold-glasses, which indicates that the sensibility is better for this particle size. In the case of 8nm Au-samples, a saturation amplitude signal was obtained for concentrations of proteins higher than 25ng/µL/cm^2. It was also found that the amplitude measurements have a linear evolution for a lower concentration of proteins in the range of 50ng/µL/cm^2.

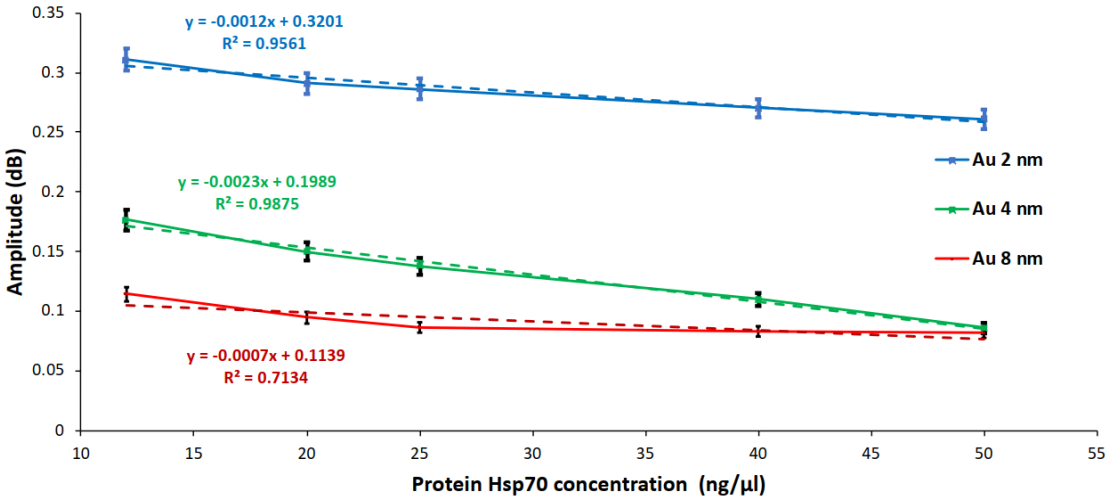

Figure 2. 5 Microwave calibration curves for three protein Hsp70 concentrations using 2nm, 4nm an 8 nm, respectively Au coated glasses at 4.33 GHZ.

2.3 Conclusion and Perspectives

In this work, instead of the commercial test and in-house Sandwich-ELISA (Enzyme-Linked Immunosorbent Assay) detection of Hsp70 protein[207], the microwave spectroscopy detection has been performed for different Hsp70 protein concentrations. The high temperature annealed gold nanoparticles on ITO glass strips were prepared with different evaporated Au thicknesses and the resulted AuNPs size distribution were analyzed based on the SEM characterization. Followed by the SMM technique has been clearly shown its capacity and sensitivity to follow each step of the (bio)functionalization of the biochip (SiO_2 / AuNPs, SiO_2 / AuNPs / Thiols and SiO_2 / AuNPs / Thiols / Hsp70) and statistically confirmed the uniformity of the SMM responses. Especially, for a frequency of 4.33 GHz, it has been found that in addition to this capacity, the technique makes it possible to follow in a linear the evolution of the variation of protein concentration with a sensitivity of 12 ng/ µL/ cm^2. In conclusion,

based on these results, the SMM technique is full of expect developing to use based on other substrates with different metal nanostructures and can be used to sensitively and specifically detect biomolecules targets in the biosensing detection field.

Although SMM has many characterization applications in the nanotechnology, and preliminary effect of the SMM detection of biomolecules obtained in this work, in the biosensing detection field, there still are challenges for their real application. For example, to improve the sensitively and stability of detection platform, the optimization of the fabrication of the noble metal nanostructures on the different substrates should be provided and proved. The solid substrate (ITO glass strip) with modification of high temperature annealed AuNPs is already proven to be an economical and sensitive platform for the biosensing detection. Thus, studies on the optimized fabrication parameters of the annealed AuNPs on the solid substrates (glass coverslips) and their use for genosensing is reported in the next chapter.

Chapter 3 SERS detection of Brettanomyces bruxellensis yeast on nanostructured ultrafine glass supports

As the chapter 1 introduced and the chapter 2 shown, gold nanoparticles (AuNPs) in the field of light-matter interactions and the biosensing detection have shown increasing interest in recent decades. Because of their excellent chemical stability, they play an important role in the biomedical, agriculture, environmental and forensic sciences. Furthermore, the unique physical and chemical properties induce these nanotechnologies to be perfect platforms for the development of high detection devices and ultrasensitive assays[208,209].

In the past few years, various SERS-based sensing platforms have been developed, with high sensitivity detection levels for the detection of analytes[210]. Furthermore, SERS has received wide applications, the mostly applicated in the identification of unknown substances in the traits of analytical chemistry[211], electrochemistry[212], physical chemistry[213], solid state physics, biochemistry and biophysics and even medicine[214–216]. SERS as an ultrasensitive fingerprint method for microorganisms[217,218] and different tapes of chemicals, is widely used for specific detection of (bio)molecules: DNA or RNA[163,219–223], whether in its native form or after interacting with additional molecules in the buffer solution. According to Campion and Kambhampati 1998[164], a rough surface requires a light source with a wavelength that resonates with the electronic absorption band to the excite surface plasmons, when the intensity of the Raman line is mainly determined by the properties of the excited electronic state. Thus, SERS technology is suitable for multi-channel detection and is recommended for

(bio)sensing with lower detection limit[224].

On the other hand, *Brettanomyces bruxellensis* is an important spoilage yeast that causes the so-called "*Brett off-flavor*" in wine. The *Brettanomyces* yeast is one of the most complicated and controversial problems encountered in the process of red wine making. Although production of some red wines has some complex taste flavor, such as plastic or smoky or exotic aromas, it is usually not expected to be responsible for the long-lasting aromas[225–227]. Some compounds present in grape juice and/or wine, such as p-coumaric acid and ferulic acid, are converted into 4-ethylphenol and 4-ethylguaiacol, these volatile phenols are responsible for the devaluation of wine[227–231]. *B. bruxellensis* also produces volatile fatty acids such as acetic acid and isovaleric acid, which help produce negative aromas[232]. So, in order to avoid the spread of *Brettanomyces* in wineries, rapid, specific and sensitive detection methods must be developed.

Currently, wineries around the world have adopted different methods to identify the presence of *Brett* yeast. The diagnostic method is based on classic microbiological plate method, molecular method and on the metabolite analysis[233], they present drawbacks, such as long incubation periods, required specialized staff, and the obtainment of results in the presence of interfering molecules or a minimum of Brett cells as 10 CFU/mL[234]. However, several detection methods such as fluorescence[235,236], chemiluminescence[237], electrochemistry[238,239], surface-enhanced Raman spectroscopy (SERS) on either aggregated silver or gold nanoparticles modified with whole-cells of different yeast species[240,241] and localized surface plasmon resonance (LSPR)[242], have

been used to sensitively detection of *Brett* from different sources to replace traditional methods. Among them, the SERS and LSPR technologies are potentially effictive tools for biosensing because of their advantages: simple operation, non-destructive detection, rapid diagnostics[15,243,244], multiplexing and miniaturization capabilities[224,245]. For example, robust DNA-LSPR biosensors on annealed gold nanostructures on thick glass was developed to detect 10 ng/μL DNA - *Brettanomyces bruxellensis* in an aqueous SSPE buffer solution[242].

Therefore, in this chapter, by using SERS and LSPR to develop a simple, rapid and sensitive genosensor for *Brettanomyces bruxellensis* DNA detection on the annealed gold modified coverslip glass substrates.

In this study, I was mainly involved in the optimization of the manufacture protocol of stable gold nanoparticles on glass coverslips. Thus, glasses were coated with gold thin layers (2 nm, 4 nm, 6 nm and 8 nm) at 25 °C and annealled at high temperatures (350 °C, 450 °C and 550 °C) on a hot-plate for different periods of time (1 h, 3 h, 6 h and 9 h), confirmed by SEM morphological characterization. Specifically, a model molecule BPE with different concentrations, were used for the modification on gold nanostructured (AuNPs) coverslips.

In this study, on the basis of the optimization of fabrication of ultrafine SERS platform (coverslip coated with 4 nm Au annealed at 550 °C for 3 h on a hotplate), a novel genosensor (*Brett DNA*) has been developed. In this section, the ultrafine SERS platform was produced for the Brett DNA detection and analyzed the morphological characterization of each (bio)functionalization step (data not shown). The obtained

results were described in two publications, Biosensors[246] and Optik[247] on 2019, respectively.

3.1 Experimental materials and methods

3.1.1 Materials

The materials used in this chapter are shown in **Table 3.1**. All the chemicals were of analytical grade and used as received without further treatment unless specially mentioned.

Table 3.1 The compounds and materials were used in different steps of the SERS detections.

Materials	Abbreviation	Company, city, country	Function
Brettanomyces bruxellensis Thiol-probe	Brett-Thiolprobe	Eurofins Genomic, Tubingen, Germany	thiolation
Brettanomyces bruxellensis spoilage yeast	-		analyte for SERS detection
trans 1, 2-bis-(4-pyridyl)-ethene	BPE	Sigma-Aldrich, Schnelldorf, Germany	SERS detection for the SERS platform confirmation
11-Mercaptoundecanoic acid	MUA	Sigma-Aldrich, St. Louis, MO, USA	Au biomodification
N-Hydroxysuccinimide	NHS	Sigma-Aldrich, St. Louis, MO, USA	Au biomodification
Tris (hydroxymethyl) aminomethane hydrochloride	Tris-HCl	Sigma-Aldrich, St. Louis, MO, USA	buffer preparation
sodium chloride	NaCl	Sigma-Aldrich, St. Louis, MO, USA	buffer preparation
sodium phosphate monobasic	NaH_2PO_4	Sigma-Aldrich, St. Louis, MO, USA	buffer preparation
sodium phosphate dibasic	Na_2HPO_4	Sigma-Aldrich, St. Louis, MO, USA	buffer preparation
ethylenediaminetetraacetic acid	EDTA	Sigma-Aldrich, St. Louis, MO, USA	buffer preparation

polyethylene glycol	PEG	Sigma-Aldrich, St. Louis, MO, USA	buffer preparation
sodium dodecyl sulfate	-	Sigma-Aldrich, St. Louis, MO, USA	buffer preparation
TCEP	-	Sigma-Aldrich, St. Louis, MO, USA	deprotection of thiol group
sodium acetate	-	Sigma-Aldrich, St. Louis, MO, USA	deprotection of thiol group
deionized water	ddH_2O	Millipore, Molsheim, France	sample washing
detergent	Decon90	Fisher Scientific, Göteborg, Sweden	sample washing
ethanol	-	Sigma-Aldrich, St. Louis, MO, USA	sample washing
coverslips glass	-	Carl Roth, Karlsruhe, Germany	glass substrate

3.1.2 Instrumentations

The metal evaporation was performed with Plassys MEB 400 (Plassys, Bestek, France), while a hot plate (Thermo Fisher Scientific, USA) was used for annealing under clean room conditions. The ultrasonic bath provided by Elmasonic S30H (Elma Schmidbauer GmbH, Singen, Germany) is systematically used to clean coverslips before biofunctionalization, the coverslips samples are dried in an oven provided by VWR company (DRY-Line drying oven DL 53), the biofunctionalization of glass (**Figure 1**) was made under a bio-hood provided by Thermo-Scientific MSC 1.2 ADV (Illkirch Cedex, France). All reagents were sterilized in a Tuttnauer Autoclave Steam Sterilizer 2540 ML (Tuttnauer, Villenoy, France).

A Scanning Electron Microscope (SEM) (FEG-SU8030, Japan) was used to characterize the morphology of AuNPs on the nanostructured coverslips. A UV–vis spectrophotometer (Carry 300 Agilent) was used to characterize the absorbance (Abs) of gold modified glass substrate before and after annealing at 500 °C. Before the

measurements, the baseline has been measured without any sample between the source and the detector.

SERS spectrum recording and backscattering geometry uses a modified Jobin-Yvon LabRAM (Horiba scientific, Longjumeau, France) with an excitation wavelength of 632.8 nm (11 mW) from the He-Ne laser source and all the spectrum recordings with a 10x objective Olympus MPlanFl. The acquisition time ranges from 10 to 120 sec and all the spectra are recorded 3 times with a D filter range from 0 to 0.3.

3.1.3 Gold nanostructured substrate preparation and the protocol optimization

Glass coverslips (Carl Roth GmbH +Co.KG, Germany) with Millipore distilled water and detergent solution (Decon 90) (ratio 2:8, v/v) in an ultrasonic distilled water bath (Elmasonic S30H) at 50 °C degreasing for 15 min, according to Jia et al.[6]. In addition, using only distilled water in an ultrasonic bath at 50 °C for 5 min. The next step is to carefully rinse each coverslip with distilled water, dry it under a stream of nitrogen, and deposit it on a hot plate at 100 °C for 10 min. Further, the coverslips were labelled on the outside with a scotch band for the proper handling, fixed on a circular evaporation plate (200 mm diameter), and finally exposed to gold vapors in the evaporator. Gold of different thicknesses (2 nm, 4 nm, 6 nm, and 8 nm, respectively) were evaporated on squared glass coverslips at a pressure of $1x10^{-5}$ Torr at 25 °C and an evaporation rate of 0.03 nm/s. The obtained gold-coated glasses (4 groups of 12 coverslips/group) are systematically heated for different time periods (1, 3, 6, and 9 h, respectively) on a preheating hot plate at three different temperatures (350 °C, 450 °C and 550 °C).

3.1.4 Biofunctionalization

Thiol-DNA modification: Annealed coverslips were soaked in 70% ethanol ultrasonic bath at 30 °C for 20 minutes, and then rinsed with sterilized water (autoclave sterilization at 121 °C (1.5 bar) for 15 min). A further washing with sterile water in an ultrasonic bath for 10 min at 30°C, then the coverslips were dried in oven at 50 °C for 20 min. Next, the annealed glass coverslips were modified by adding 10 µl of 10 ng/µL Thiol-DNA in 1xSSPE, overnight at 4 °C. They were subsequently washed with 1.5 mL of sterile water and dried in the bio-hood. In order to release thiol-DNA, thiol-DNA was treated with a solution of 10mM TCEP and 3M sodium acetate in advance.

Hybridization tests: Thiol-functionalized coverslips with Brett DNA complementary sequence (for specific experiments) and non-complementary sequence (for control experiments) at different concentrations of 100 ng/µL, 10 ng/µL, 1 ng/µL, 100 pg/µL, 10 pg/µL and 1 pg/µL were suspended in 1x SSPE buffer for hybridization experiments. The hybridization was performed overnight at 4 °C, then washed with sterile water and drying at RT. The SERS test using genomic DNA extracted from Dekkera bruxellensis DKA was also performed, using the optimized conditions for the complementary and non- complementary sequences **(Figure 3.1)**.

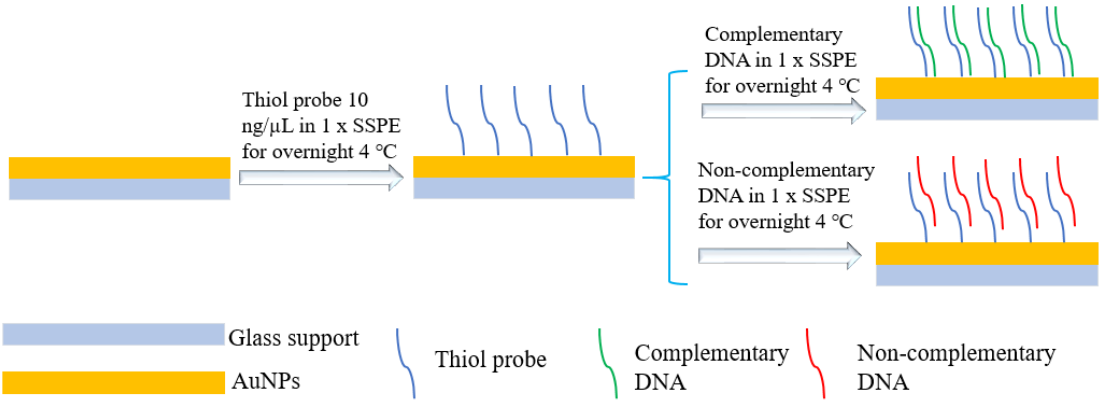

Figure 3. 1 Biofunctionalization of AuNPs on coverslips with biomolecules and after incubation with complementary/non-complementray DNA sequences.

SERS phylogenetic tree: DNA extracted from 16 yeast strains (**Table 2**) was analyzed by DNA drop procedure (2 μL of 100 ng/μL) onto AuNPs coated coverslips for SERS analysis, the collection time was 10 sec for 3 times, and the filter was fixed at 0.

Table 2. List of yeast strains tested in SERS to prove the specificity of Brett-DNA sequence in the presence of Thiol-probe.

Saccharomyces paradoxus DI4A 11[c]	Saccharomyces uvarum UCD 169[b]
Saccharomyces ellipsoideus DI4A 1[c]	Candida ethanolica UCD 37[b]
Saccharomyces pastorianus DSMZ 6581[a]	Torulaspora delbrueckii DSMZ 70607[a]
Saccharomyces bayanus DSMZ 70412[a]	Millerozyma farinosa UCD 6017[b]
Saccharomyces cerevisiae var carlbergensis DSMZ 70424[a]	Zygosaccharomyces bailii UCD 915[b]
Saccharomyces cerevisiae Montrachet UCD 522[b]	Hansenula uvarum UCD 6717[b]
Saccharomyces ellipsoideus CRO 2[e]	Dekkera bruxellensis DSMZ 70726[a]
Saccharomyces bayanus Superlievito DC[d]	Dekkera bruxellensis DKA[e]

Note:

[a] Deutsche Sammlung von Mikroorganismen und Zellkulturen GmbM, Braunschweig, Germany.

[b] University of Davis, CA, USA.

[c] University of Udine, UD, Italy.

[d] Commercial yeast for wine.

[e] University of Udine, UD, Italy

3.2 Results and discussion

3.2.1 Optimization of the preparation protocol of gold nanostructured coverslips

It is well known that the SERS performance of gold nanostructures is greatly

affected by the size, distribution and spacing between particles[248]. The preparation process of the AuNPs, includ cleaning, evaporation and annealing protocols. Several fabrication parameters were optimized: the ratio of Millipore and decon90 distilled water, gold film thickness, evaporation pressure, evaporation rate, annealing time and annealing temperature.

Therefore, four different gold film thicknesses (2 nm, 4 nm, 6 nm and 8 nm, respectively), three different annealing temperatures (350 ℃, 450 ℃ and 550 ℃) and four different annealing times (1, 3, 6 and 9 hrs) (**Figure 3.2**) are SEM investigated. SEM studies, and analyzed the proportion of background and size distribution are based on the SEM images using the public domain software Image J developed by National Institutes of Health.

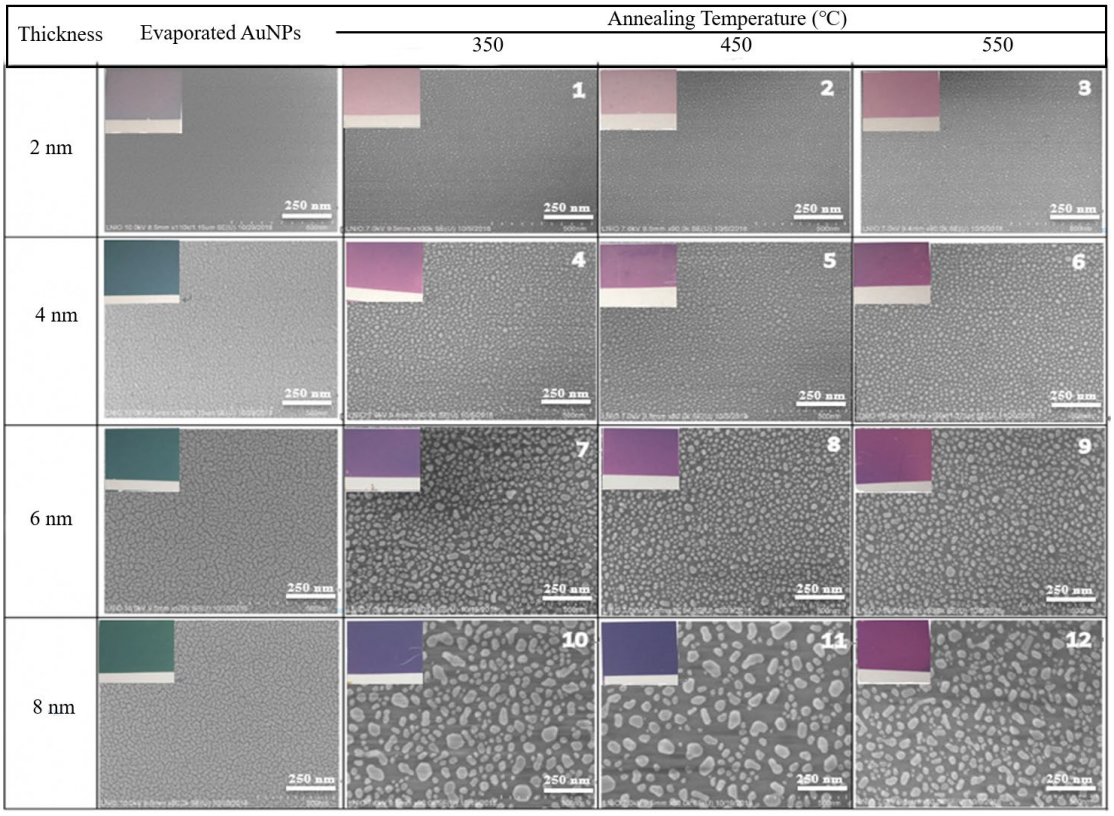

Figure 3. 2 SEM images of square glass coverslips gold coated (2 nm, 4 nm, 6 nm, and

8 nm) after 3 hours at different temperatures (350 °C, 450 °C and 550 °C).

3.2.1.1 Influence of the annealing temperature on the formation of AuNPs

As mentioned in the previous experimental part, four different thicknesses (2 nm, 4 nm, 6 nm and 8 nm, respectively) of gold films were evaporated. The prepared evaporated gold films have different colors, from light blue (2 nm Au) to blue (4 nm Au) to light green (6 nm Au) and to dark green (8 nm Au). After the gold films of various thicknesses are annealed at different temperature for 3 hours, these colors change significantly. In the experiment, the high annealing temperature makes the thinnest gold film (2 nm) appear purple, while for the deposition thicknesses (4 nm, 6 nm) and the thickest gold film (8 nm), the colors appear from light violet to dark purple, respectively (**Figure 3.2**). In this case, the SEM images of the evaporated samples and the annealed samples are also shown in **Figure 3.2**. It can be seen that when the annealing temperature is greater than 550 ℃, the AuNPs obtained will become more uniform than the samples with a lower annealing temperature. Furthermore, as the initial thickness of the film (2 nm, 4 nm, 6 nm and 8 nm) increases, the size of the gold nanoparticles also increases. And this corresponds to the color change at different temperature before annealing and after annealing, so the higher annealing temperature used, the darker colors were observed.

In addition, the proportion of the background increasing when the annealing temperature increased from 350 ℃ to 450 ℃, and stabilized from 450 ℃ to 550 ℃ as shown in **Figure 3.3** (with the exception of the gold film thickness of 2 nm). The proportion of background of the annealed samples at 550 ℃ was displayed lower than

that of the annealed samples at 450 ℃, with thicknesses of 6 nm (550 ℃ to 60.94 %, 450 ℃ to 61.39 %) and 8 nm (550 ℃ to 63.63 %, 450 ℃ to 65.53 %). The higher the background ratio, the lower the surface coverage of AuNPs. Interestingly, the proportion of background for the sample with 4nm Au showed an insignificant tendency ranging from 350 ℃ to 60.29 %, from 450 ℃ to 60.07 % and from 550 ℃ to 60.41 %.

In conclusion, the annealing temperature strongly influences on the background ratio and the surface coverage of gold nanoparticles, thus affecting the sizes/shapes of the gold nanoparticles and the interparticle distances with respect to the gold thickness evaporated on coverslips.

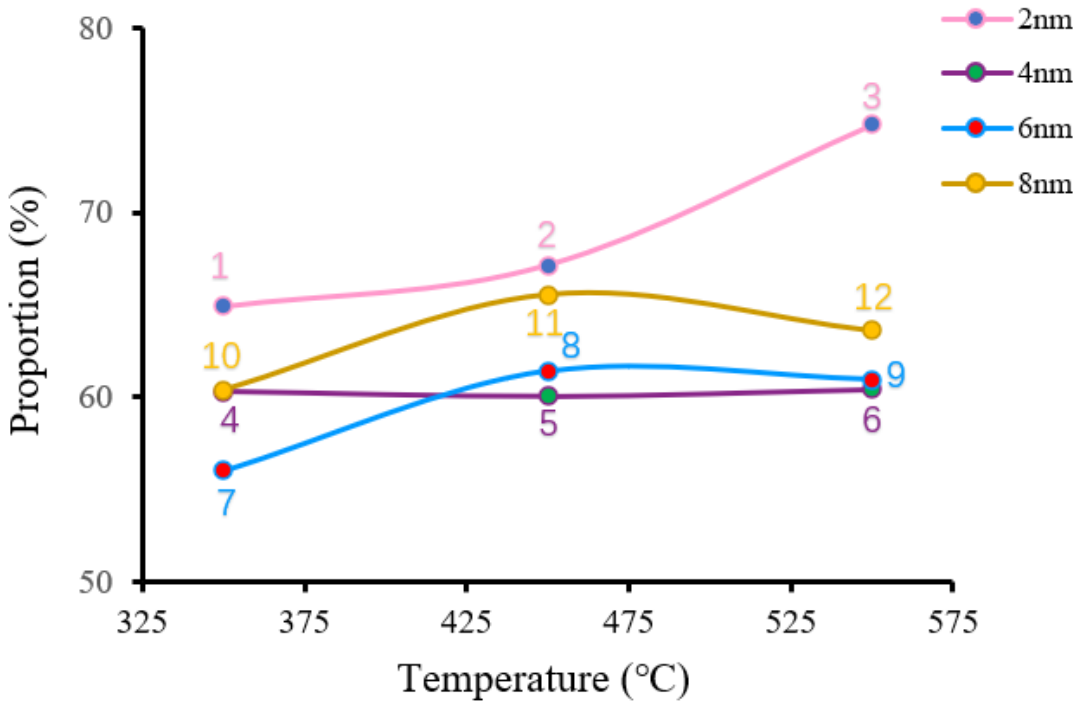

Figure 3. 3 The proportion of background for annealed square glass coverslips gold coated (2 nm, 4 nm, 6 nm, 8 nm, respectively) after exposure at three different temperatures (350 °C, 450 ℃ and 550 °C).

3.2.1.2 Influence of evaporated gold thickness on nanoparticle formation

In addition to the known parameters that strongly influence the SERS spectra, such as the annealing temperature, the size and shape of the nanoparticles are also found in the thickness of the gold film by evaporation in the present work. Thus, systematic SERS studies using multiple thicknesses of gold film by evaporation (2 nm, 4 nm, 6 nm, 8 nm) were annealed at 550 ℃ for 3 hours using a size distribution analysis of the proportion of background based on SEM images (**Figure 3.2**). The results of the particle size distribution and the proportion of the background are illustrated in **Figure 3.4**.

A

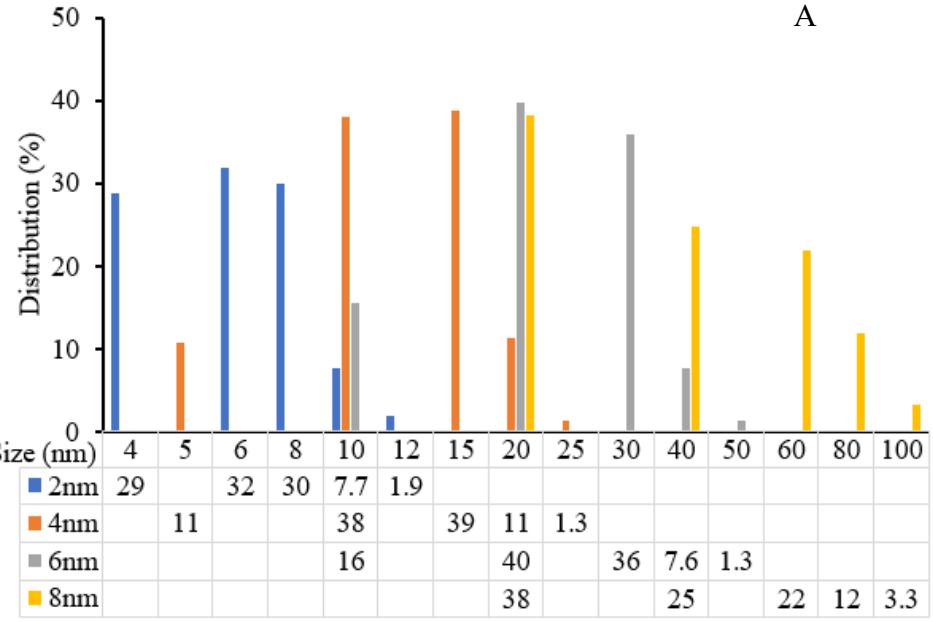

Size (nm)	4	5	6	8	10	12	15	20	25	30	40	50	60	80	100
2nm	29		32	30	7.7	1.9									
4nm		11			38		39	11	1.3						
6nm					16			40		36	7.6	1.3			
8nm								38			25		22	12	3.3

B

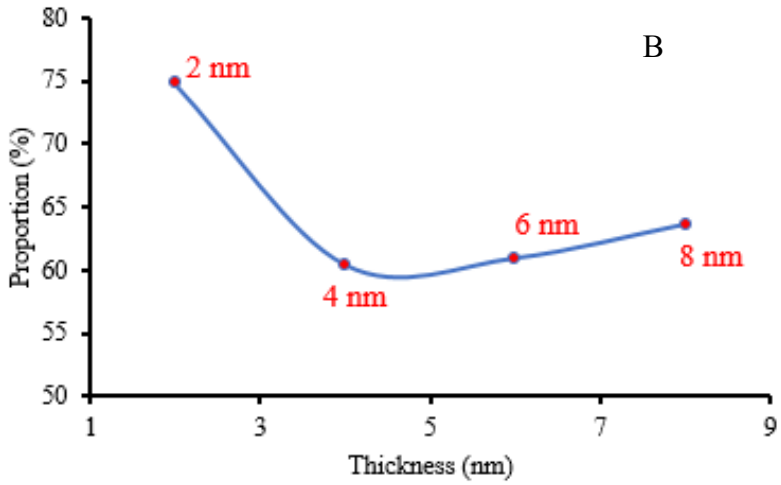

Figure 3. 4 Analysis of AuNPs SEM images (A) the Gold nanoparticles size distribution on cover slips substrates and (B) the proportion of background with four different thicknesses (2 nm, 4 nm, 6 nm, 8 nm) annealed at high temperature 550 ℃ for the same annealing time 3 hours.

Obviously, from the size distribution (**Figure 3.4A**), it is shown that as the thickness of the evaporated gold film increases, the size of the gold nanoparticles and the size distribution range become larger. It is well known that the size of the nanoparticles will affect the available inter-distance between particles. In this case, at a thickness of 2 nm, the size range of AuNPs is mainly from 6 nm (size distribution 31.8 %) to 8 nm (29.9 %), at 4 nm thickness, the range is from 10 nm (37.9 %) to 15 nm (38.8 %), at 6 nm thickness, the range is largely from 20 nm (39.7 %) to 30 nm (35.9 %), at 8 nm thickness, the range is between 20 nm (38.1 %) to 40 nm (24.8 %).

Furthermore, the proportion of background with four thicknesses (2 nm, 4 nm, 6 nm, 8 nm) annealed at 550 ℃ for 3 hours is shown in **Figure 3.4B**, the proportion of background with a thickness of 4 nm is the smallest (60.41 %) compared with three other thicknesses (2 nm, 6 nm, 8 nm), the proportion of background with a thickness of 2 nm is the largest (74.77 %), while a thickness of 6 nm to 60.94 % and a thickness of 8 nm to 63.63 % were obtained.

The larger the background ratio, the smaller the surface coverage of the nanoparticles. On the contrary, the lower the proportion of background, the greater the surface coverage of the nanoparticles. In our experiment, 4 nm thickness shows a greater surface coverage than the other thicknesses. Finally, a denser surface coverage

may correspond to a lower interparticle distance.

3.2.1.3 Influence of annealing time on the formation of gold nanoparticles

In order to prepare well-defined AuNPs with stable optical characteristics, with the exception of the annealing temperature and the thickness of the evaporated gold film which have been studied previously, the effect of the annealing time on the formation of particles is studied in the present work. As shown in the **Figure 3.5** and **Figure 3.6**, the SEM images of the AuNPs with a 4 nm evaporated gold film were annealed at 550 ℃ after different annealing time (1, 3, 6, 9 h), the AuNPs size distribution and the proportion of background were summarized.

Experimentally, the coverslip was heated at 550 °C for 1h and the range of nanoparticles formed was 15 nm (36.8 %) to 20 nm (23 %). After heating at the same temperature for 6h, similar sample evolution is obtained when NPs range from 10 nm (23.6 %) to 15 nm (38.8 %), while the AuNPs size after 3 h showed a range from 10 nm (37.9 %) to 15 nm (38.8 %) of uniform distribution, compared with others and corresponds to the SEM image (**Figure 3.5**).

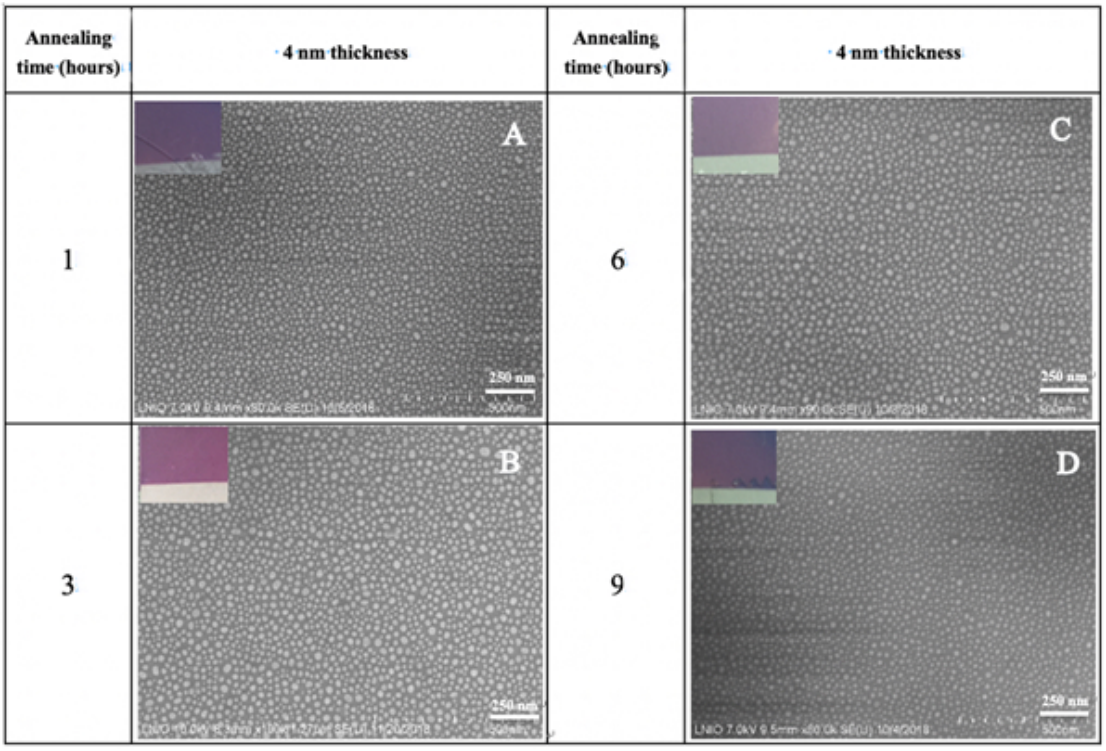

Figure 3. 5 SEM images of gold NPs on square glass coverslips coated with 4 nm and annealed for different time periods (A) 1 h, (B) 3 h, (C) 6 h and (D) 9 h at 550 °C.

In contrast, the glass annealed after 9 h has a higher distribution at 5 nm (45.8 %) to 10 nm (19.0 %) (see in **Figure 3.6A**). However, as shown in **Figure 3.6B**, the proportion of background increases with the annealing time increase, 9 h (70.72 %) > 6 h (64.87 %) > 3 h (61.19 %) > 1 h (56.51 %). In detail, even if the 9 h sample has a very high size distribution of 45.8 % at 5 nm, the maximum proportion of the sample background is 70.72 %, which is corresponds to the minimum area coverage of the 9 h sample. On the other hand, the proportion of 1 h and 3 h samples are lower than that of 6 h and 9 h samples. Taking into account the uniform distribution of nanoparticles and better surface coverage, we used the samples annealed at 550 °C for 3 h, and got a lower proportion of background with larger surface coverage.

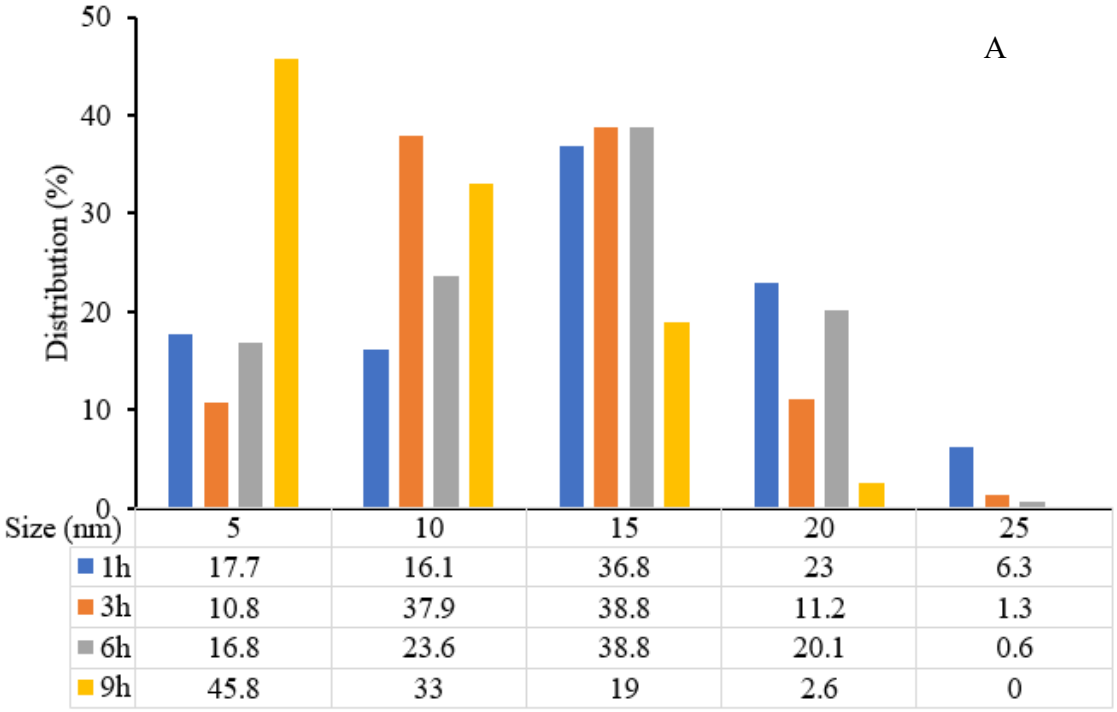

Size (nm)	5	10	15	20	25
1h	17.7	16.1	36.8	23	6.3
3h	10.8	37.9	38.8	11.2	1.3
6h	16.8	23.6	38.8	20.1	0.6
9h	45.8	33	19	2.6	0

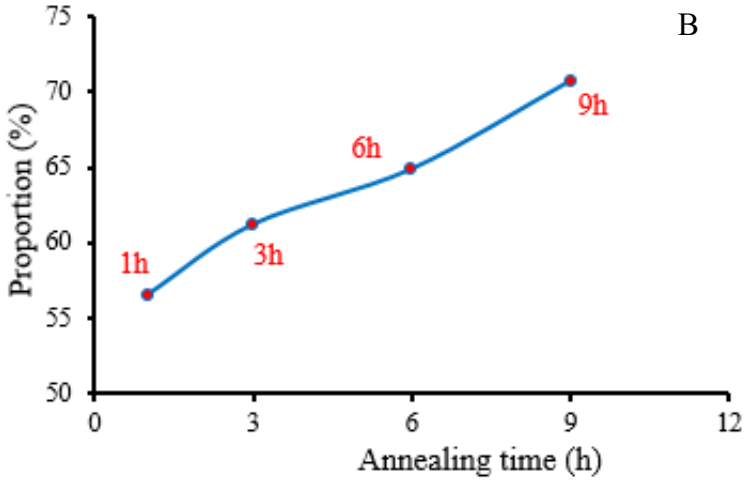

Figure 3. 6 SEM Analysis of AuNPs. A) gold nanoparticles size distribution on annealed coverslips and B) the proportion of *"no particles"* background after annealing at 550°C the gold coated (4 nm) coverslips for different time periods (1, 3, 6 and 9 hrs).

3.2.2 SERS evaluation of different substrates

The SERS tests performed on classical microscope glass slide supports modified with 4 nm gold film and annealed at 550°C in the oven for 8 h according to Jia et al.[6]

are inappropriate, because the glass slide produced strong fluorescence interferences that abnormally altered the SERS signals. Thus, several SERS tests using plastic petri dish, glass coverslip, plastic pipette, Eppendorf tube, plastic cuvette and quartz crystal microbalance (QCM) as solid supports were recorded and analyzed (**Figure 3.7**). Such tests conclude that the best robust SERS supports are the ultrafine glass coverslips for gold nanostructure. In addition, the SEM topography of modified coverslips confirmed the evolution of SERS signals for different gold thicknesses annealed at 350°C, 450°C and 550°C for 3 h (**Figure 3.8**)

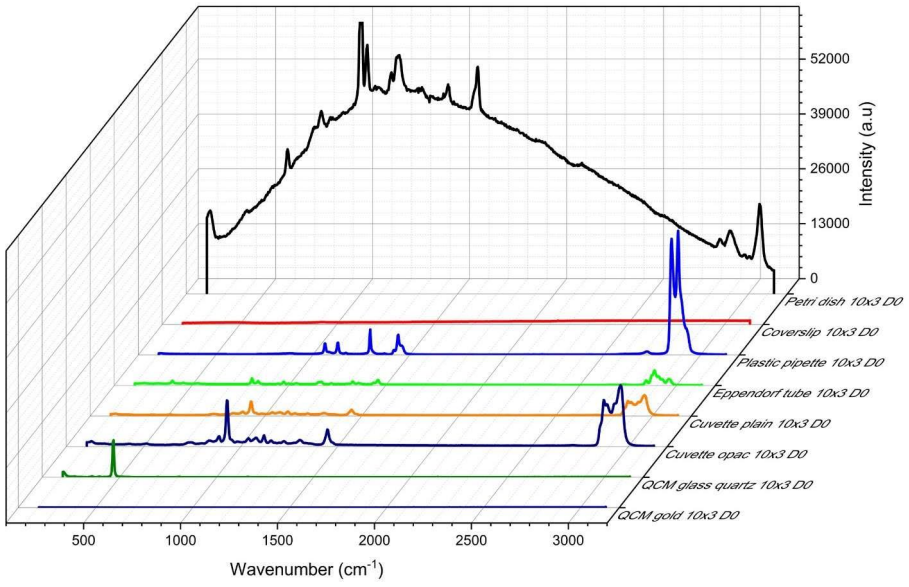

Figure 3. 7 SERS spectra of various naked solid supports: plastic petri dish, glass coverslip, plastic pipette, Eppendorf tube, plastic cuvette and quartz QCM crystal.

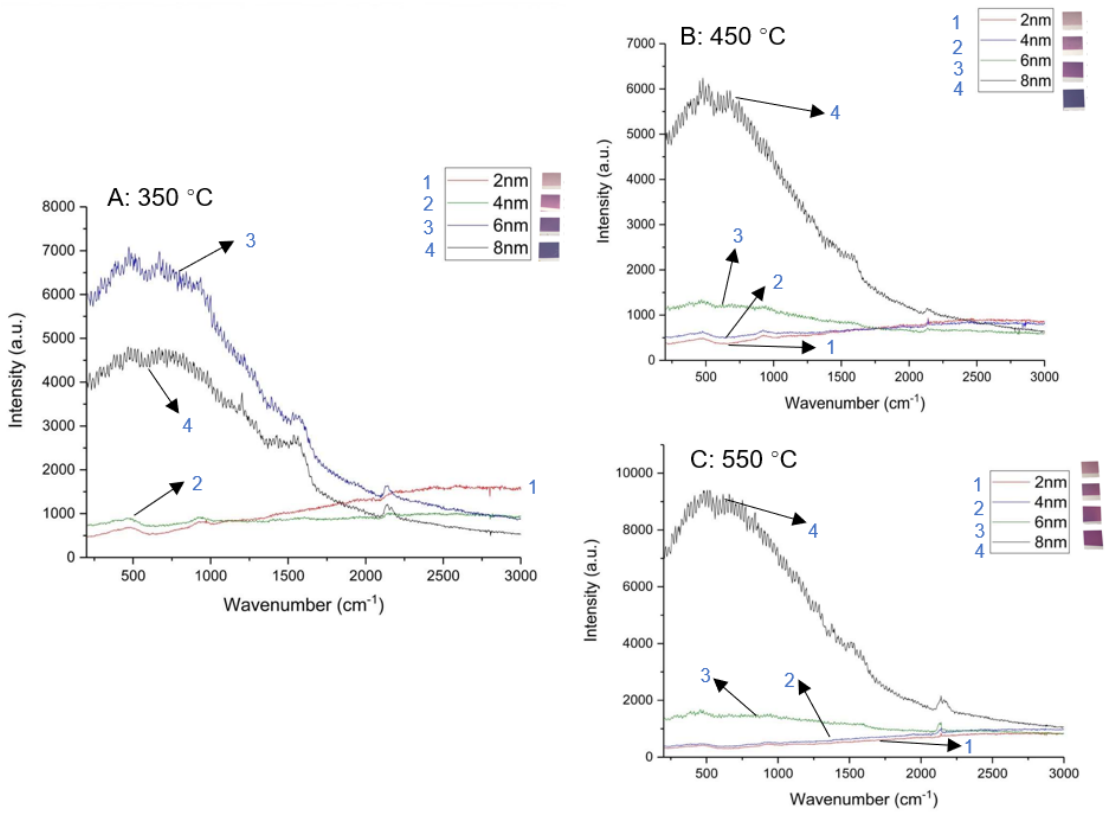

Figure 3. 8 SERS signals of naked annealed gold films (2, 4, 6 and 8 nm) on coverslips after 3h for 350 °C (A), 450 °C (B) and 550 °C (C).

Among different spectroscopic investigations (**Figure 3.9**), it is also confirmed that the best SERS substrate is the ultrafine square glass coverslips coated with 4 nm Au (**Figure 3.9B**) annealed at 550°C for 3 h (**Figure 3.8C**) because its fluorescence is very weak and produces no SERS peaks, once it's immobilized on nanoparticles, it could be masked by the SERS peaks produced by (bio)molecules.

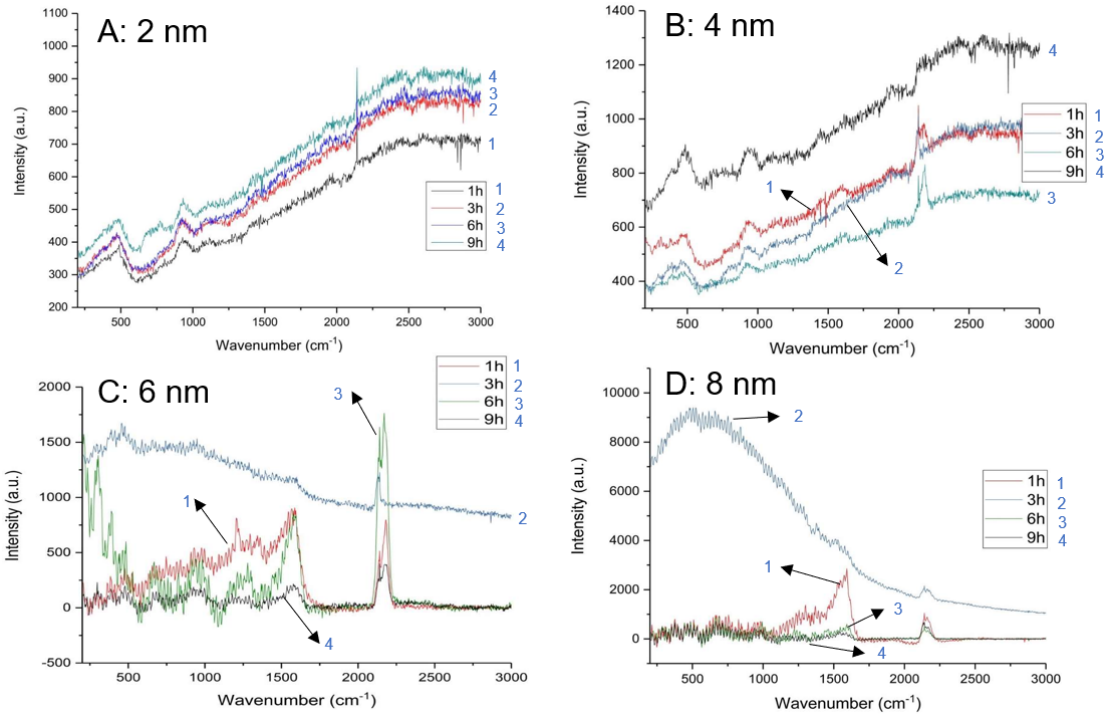

Figure 3. 9 SERS signals of naked annealed gold films on coverslips at 550 °C for different periods with different thickness of evaporated gold film, 2nm (A), 4 nm (B), 6 nm (C) and 8 nm (D), respectively.

3.2.3 SERS spectrum verification on 4nm gold annealed coverslip

3.2.3.1 SERS spectrum of BPE model molecule

As shown in **Figure 3.10**, the SERS tests were performed in the presence of a model molecule, 1,2-bis-(4-pyridyl)-ethene (BPE), the molecule has interesting bonds and atoms, when used with homemade annealed gold coated coverslips, good SERS spectrums can be obtained, As has been reported, the main peaks at 1601 and 1630 cm^{-1} correspond to the C-N stretching mode in pyridyl ring and the vibration of BPE vinyl group respectively[249], while peaks at 1193 and 1235 cm^{-1} refer to the pyridine's ring breathing mode and the vibrational movement of nitrogen atom in pyridyl. Therefore, in this work, the peak at 1012 cm^{-1} can be attributed to the chemical absorption on

AuNPs by BPE.

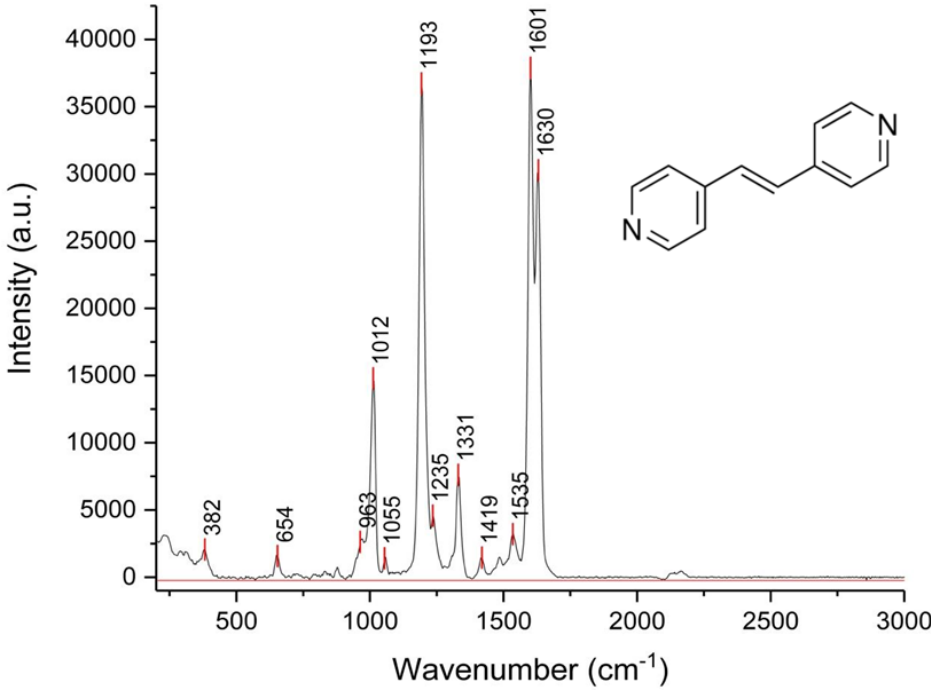

Figure 3. 10 SERS spectrum of BPE molecule (1 mM) on gold nanostructured coverslip (4 nm Au, 550 °C for 3 h on a hotplate) after 3 times of acquisition 10 sec spectra and using an D0 filter.

3.2.3.2 SERS spectra of different BPE concentrations

Several BPE solutions were prepared from 97% concentrated stock solution, to form six concentrations that were subsequently tested in ultrapure water: 10^{-3} ,10^{-5} ,10^{-7} ,10^{-9}, 10^{-12} and 10^{-15} M, respectively. The SERS signals of different BPE concentrations deposited on gold annealed coverslips were recorded and compared. These SERS measurements results confirmed that 4 nm Au on glass heated at 550 °C for 3 h is the best conditions for detecting extremely low concentrations of BPE. As shown in **Figure 3.11**, gold nanostructured coverslips reduce the optical density (OD) of BPE molecule to 10^{-12} M. The fabricated platform in this study for the SERS

detection of BPE molecules shows more sensitivity compared with the SERS detection of BPE molecules which could be reached to 10^{-9} M on the gold nanoparticles (diameter of 60 nm) sliding on recyclable nanohoodoos (GNRH) reported by Wu K.Y[250].

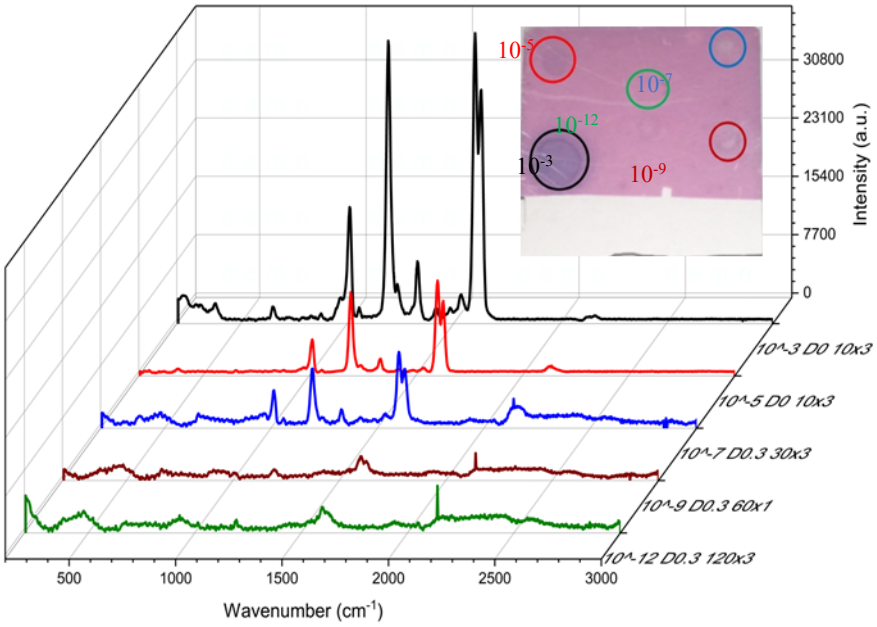

Figure 3. 11 SERS spectra of BPE molecules of different concentrations (10^{-3}, 10^{-5}, 10^{-7}, 10^{-9} and 10^{-12} M) using 4 nm gold coated coverslips annealed at 550 °C for 3 h on a hotplate. Inset-photo of coverslip after the deposition of five different BPE concentrations.

3.2.4 SERS phylogenetic tree for geno-sensing of *Breettanomyces bruxellensis*

As the results are shown above, several parameters in the protocol of gold nanostructured coverslips have been optimized, it was found that a 4 nm gold-coated coverslip annealed at 550 °C on a hot plate for 3 hrs shows the greatest stability of SERS spectra of different BPE concentrations, and a lower limit of detection 10^{-12} M BPE was obtained. On the basis of the optimization results, 4 nm gold annealed (annealed at 550 °C for 3 hrs) coverslips can be considered as ideal substrates in the

construction of SERS nano-biosensor in the next step.

3.2.4.1 SERS spectra of different buffers

In order to create a friendly environment to the attachment of the probe to nanoparticles and the subsequent attachment of the complementary Brett-DNA sample, for Brett-Thiol probe biofunctionalization of AuNPs coverslips, various types of buffers were tested, such as phosphate buffer saline (PBS) (sodium chloride 1.5 M, sodium phosphate dibasic 81 mM, sodium phosphate monobasic 19 mM, pH 7.4), SSPE buffer (sodium chloride 3 M, sodium phosphate dibasic 0.23 M, ethylenediaminetetraacetic acid 25 mM, pH 7.4), TE buffer (Tris(hydroxymethyl) aminomethane hydro-chloride 0.5 M, ethylenediaminetetraacetic acid 0.1 mM, sodium chloride 1 M, pH 8.0), and polyethylene glycol buffer (PEG buffer) (PEG 6000 12.5 mM, sodium chloride 0.5 M, sodium phosphate dibasic 0.2 M, ethylenediaminetetraacetic acid 5 mM, sodium dodecyl sulfate (0.5 % (w/v)). The protocol includes deposition of tiny drop (2 μL buffer) on a gold nanostructured coverslip initially coated with 4 nm Au and annealed on a hotplate at 550 °C for 3 h. The SERS spectrum for each buffer was recorded from three drop zones; (1) the outside, (2) the outer area near the middle crystal formation as a result of water evaporation, and (3) the inside. The SERS test time of four buffers is 10 s x 3 times and the filter D 0.3 is used (**Figure 3.12**).

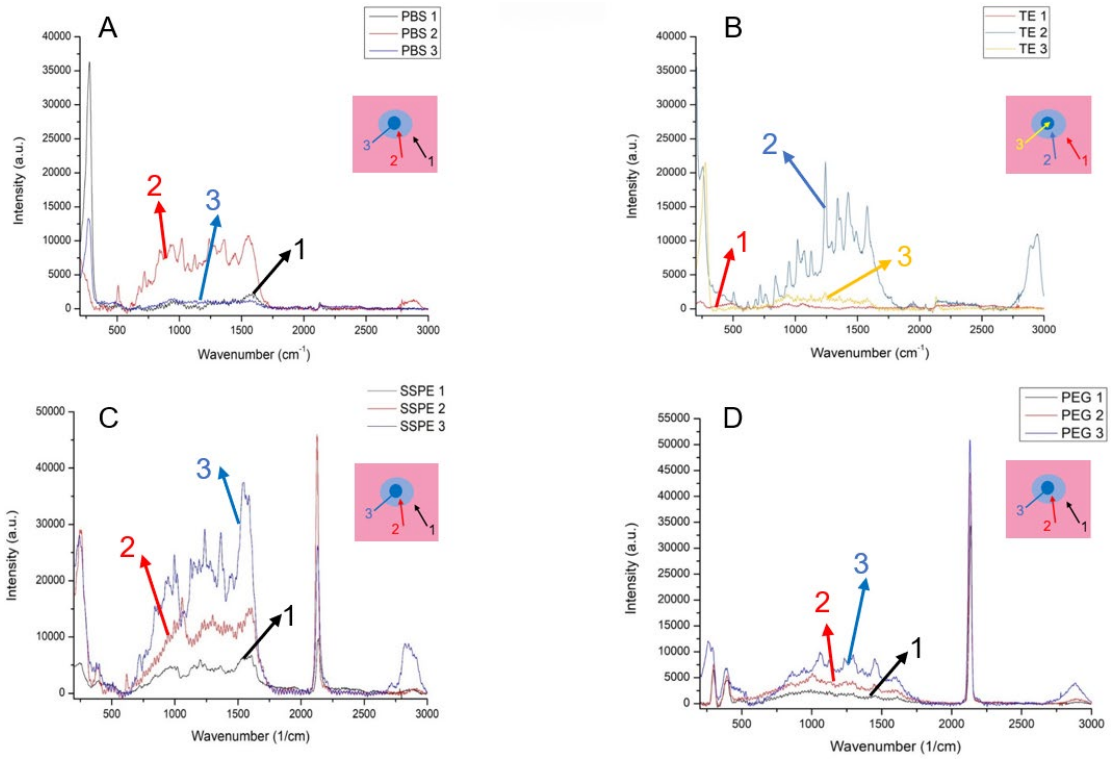

Figure 3. 12 SERS spectra of 2 µL tiny drop of PBS buffer (A), TE buffer (B), 1 x SSPE (C), PEG buffer (D) on AuNPs coverslip, respectively. The acquisition time was 10 sec x 3 times with filter D0.3.

After analysis, the SSPE was selected for the biofunctionalization steps. Other buffers (PBS, TE and PEG) induced visible modifications of gold nanoparticles, despite their low SERS spectrum intensity (**Figure 3.13A**, influence of PBS). For example, **Figure 3.13B** shows the SERS graph of the DNA thiol probe deposited overnight at 4 °C, and the effect of TE buffer biofunctionalization with DNA-probe on the nanoparticles and washing with water. The PEG buffer was problematic because it creates a hydrophilic environment, so it is impossible for DNA micro-spotting on supports.

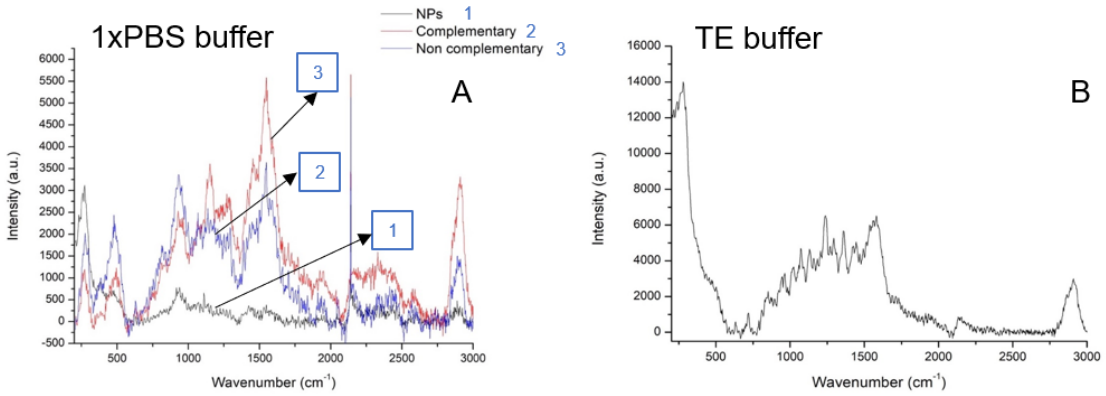

Figure 3. 13 SERS spectra of annealed AuNPs on the coverslips glass (A) after biofunctionalization with DNA-probe and complementary in 1xPBS buffer, 60 sec x 3 times filter D0.3 and (B) DNA-thiol probe in TE buffer after incubation with 10 µL overnight 4 °C, 10 sec x 3 times, filter D0. The in-set picture is the sample after biofunctionalization with Thiol-Probe in 1 x PBS buffer (a) and in TE buffer (b) on AuNPs.

SERS spectra of Brett-Thiol probe (100 pmol/µL) in water and 1xSSPE aqueous buffer were compared. It was found that in the case of water, at 1604,87 cm^{-1} (**Figure 3.14A**), the most significant increase of SERS intensity (6500 a.u.) was obtained, while for SSPE, at almost the same wavenumber (1600.07 cm^{-1}) (**Figure 3.14B**), a very intense peak (25000 a.u.) was obtained.

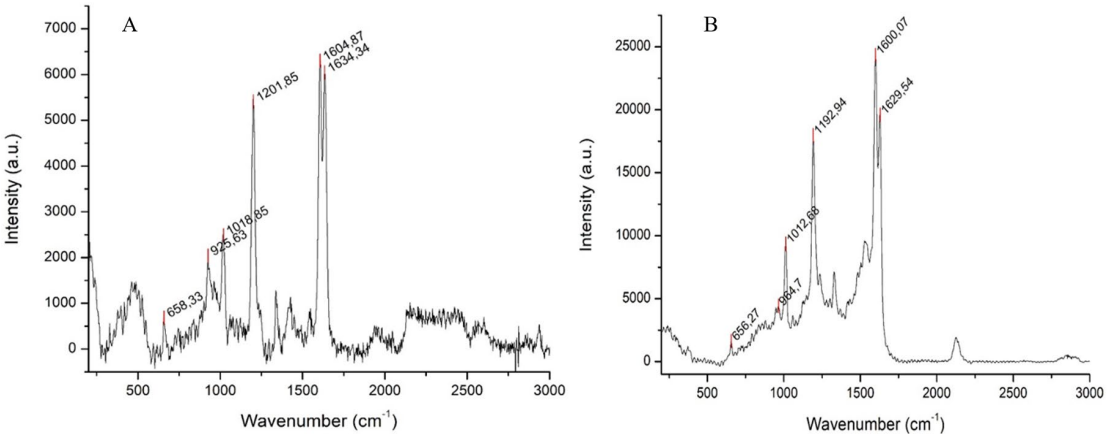

Figure 3. 14 SERS spectra of thiol-DNA probe (100 pmol /µL) suspended in water (A) and 1xSSPE (B) after an overnight at 4 °C and were collected from tiny drops (2 µL) deposited on AuNPs coverslips. The acquisition time was 10 sec x 3 times with a D 0 filter. The red bars indicate the maximum intensity of SERS signal.

In this case, the evolution of other SERS peak characteristics of Brett-Thiol probe is shown in **Table 3**. For the purpose of the evaluation the signal stability and the robustness of the biofunctionalization protocol, three SERS sensing configurations were prepared, which are obtained after mixing in Eppendorf tubes. The SERS spectrum of each configuration was obtained from a 2 µL drop on gold nanostructured coverslips and repeated for three consecutive days. The results showed that, compared with the other two configurations (aqueous solution of Brett-Thiol probe (10 ng/µL) and genomic DNA of Brettanomyces bruxellensis DKA (100 ng/µL), the configuration (aqueous solution of Brett-Thiol probe (10 ng/µL) and genomic DNA of Brettanomyces bruxellensis DKA (100 ng/µL)) has the strongest SERS spectra modifications; the Thiol-probe (10 ng/µL) aqueous solution and the complementary sequence (100 ng/µL) suspended in PEG buffer).

Table 3. Position of SERS peaks of Brett-Thiol probe suspended either in water or 1xSSPE on gold nanostructured coverslips after an overnight incubation at 4 °C (**Figure 3.12C**).

Thiol-probe in water Wavenumber (cm^{-1})	Thiol-probe in 1xSSPE Wavenumber (cm^{-1})
658	656
925	964
1018	1012
1201	1192
1604	1600
1634	1629

3.2.4.2 SERS spectra of different species of Saccharomyces genus

To evaluate the specificity of the Brett-Thiol-probe, different yeast strains that can be found in winery or vineyard environments were tested. The DNA extracted from 16 yeast strains was analyzed by SERS, DNA drpping procedure (2 µL of 100 ng/µL) was used to drop onto AuNPs coated coverslips, using a collection time of 10 s for 3 times, and the filter was fixed as 0. The selected yeasts belong to the yeast class and Saccharomycetales order that include 4 genus (*Pichiaceae, Debaryomycetaceae, Saccharomycodaceae* and *Saccharomycetaceae*). Each genus contains specific microorganisms that have been partially or totally studied using the SERS technology. The recorded spectra were shown in **Table 4**.

Table 4. SERS spectra of microorganism from Saccharomycetes class.

Genus	Species	SERS peaks					
		350-550 cm^{-1} (blue)	**600-1000 cm^{-1} (green)**	**1250-1450 cm^{-1} (navy)**	**1600-1800 cm^{-1} (orange)**	**1850-2000 cm^{-1} (brown)**	**2700-2900 cm^{-1} (navy)**
Saccharomycetaceae	All listed in **Table 2**	450-550	850-1000	Different shapes of peaks for each type of yeast (few differences but recognizable)	One peak in 1600	Some differences	Some differences and different shape of peaks
Pichiaceae	***Dekkera Bruxellensis* DKA**	417, 485	698	Some differences	1644, 1688, 1757	X	x
	Dekkera Bruxellensis DSMZ 70726	Some differences	Some differences	**Strong differences**	Some differences	X	x
Debaryomycetaceae	*Millerozyma farinose*	Min: 300	850-1050	Max 1500	1500-1750	Max 2050	Max 2850
Saccharomycodaceae	*Hansenula uvarum*	Min: 300	X	Different shapes of peaks	x	X	x

In the case of *Brettanomyces bruxellensis* (*Pichiaceae genus*), spectroscopy investigation was performed on 3 species: *Candida ethanolica, Dekkera bruxelensis DKA* and *Dekkera bruxelensis DSMZ*. Experimentally, it shows that the SERS spectra of *Brettanomyces bruxellensis DKA* and *Brettanomyces bruxellensis DSMZ* 70726 are strongly modified at 1250 and 1450 cm^{-1}(**Table 3**). Furthermore, the SERS spectra of *Saccharomycodaceae genus* and *Debaryomycetaceae* (*Millerozyma farinosa*) and *Saccharomycodaceae* (*Hansenula uvarum*) were also recorded, and the most relevant peaks at 1250-1500 cm^{-1} were highlighted see **Figure 3.15**. Therefore, the SERS spectra of the yeasts of *Saccharomycetes* class at 1205-1500 cm^{-1} or/ and 1550-1800 cm^{-1} showed major modifications.

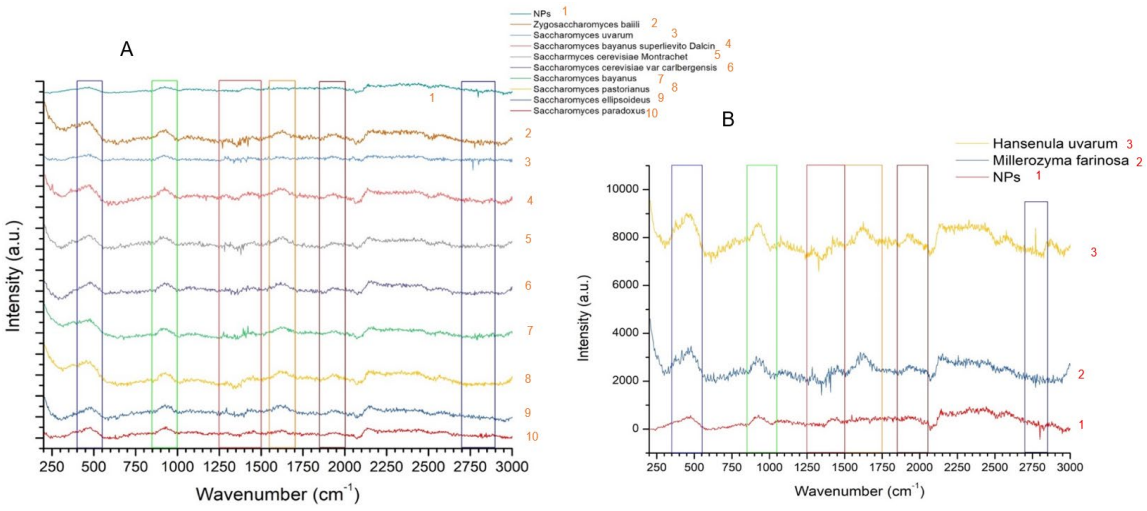

Figure 3. 15 SERS spectra of different microorganisms of *Saccharomycetales* (A), and *Debaryomycetaceae* (*Millerozyma farinosa*) and *Saccharomycodaceae* (*Hansenula uvarum*) (B), using an acquisition time 10 sec x 3 times with D0 filter and a drop (2 µL) was deposited on round AuNPs coverslip NPs, respectively.

3.2.4.3 SERS spectra of specific and non-specific Brett-DNA genosensors

In the Figure 3.16, it shown Brett-DNA (specific tests) and DNA strains from fourteen interfering yeasts in wine (non-specific tests). For SERS experiments, five concentrations of complementary Brett-DNA and of non-complementary sequence were prepared: 1 pg/µL, 10 pg/µL, 100 pg/µL, 1 ng/µL and 10 ng/µL.

It should be noted that all SERS spectra were recorded 3 times over 30s on the same area. From the resulted SERS spectra, the intensity values of more representative peaks at 1294 cm^{-1} in the case of specific tests was obtained, and it is found that the detection limit is consequently estimated to be 0.1 ng/µL, and the dynamic range of the genosensor extends from the detection limit to the highest concentration (10 ng/µL) tested in this experiment. Since the concentrations was lower than 0.1 ng/µL, a slight

increase of the SERS intensity was observed, and there was no significant difference in spectra between the non-specific and the specific DNA-targets. In the case of the specific experiments repeated several times, it was observed the SERS spectra increase up to 1000 a.u. starting from 1 ng/µL Brett-DNA, while for the non-specific experiments, the SERS spectra intensity is about 400 a.u.

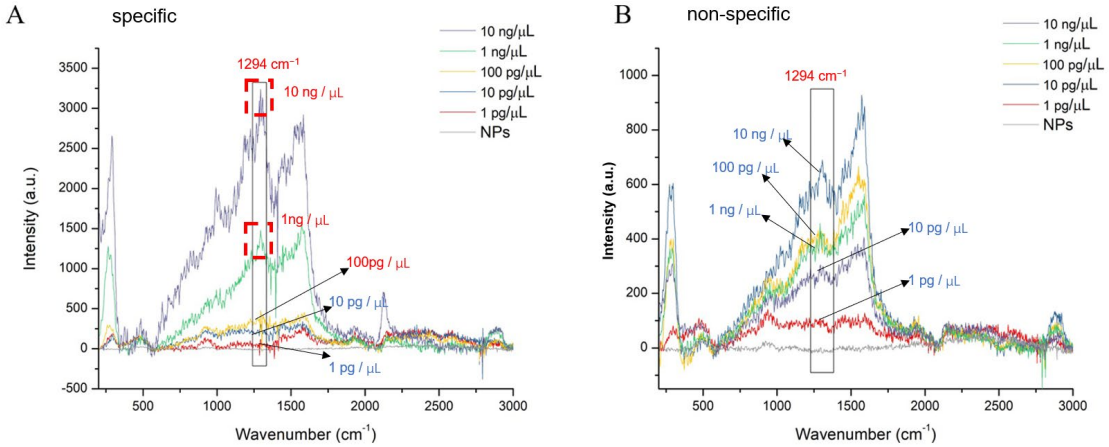

Figure 3. 16 SERS spectra of (A) specific and (B) non-specific Brett-genosensors. The acquisition time was set at 10 s x 3 times using a D 0.3 filter.

3.2.4.4 LSPR spectra of specific and non-specific Brett-DNA genosensors

In addition to the SERS spectrum of Brett-DNA genosensor, the complementarity investigation of proposed yeast selective biosensor wasalso detected by localized surface plasmonic resonance (LSPR), see **Figure 3.17**. The spectroscopic data were collected to evaluate the specific and non-specific Brett-DNA (bio)functionalization of gold nanostructured coverslips. It was found that in the case of specific Brett-DNA (**Figure 3.17A**) and real-DNA from Brettanomyces bruxellensis DKA biosensors (**Figure 3.17C**), as the target-DNA concentration increase, the LSPR evolution is logical, whereas for non-specific (control) DNA-yeasts biosensors, the random LSPR

peak increases are recorded (**Figure 3.17B**).

In the future non-specific experiments, attention need to be paied to reduce the non-specific absorbtion on nanoparticles, therefore, the LSPR signal also decrease as expected.

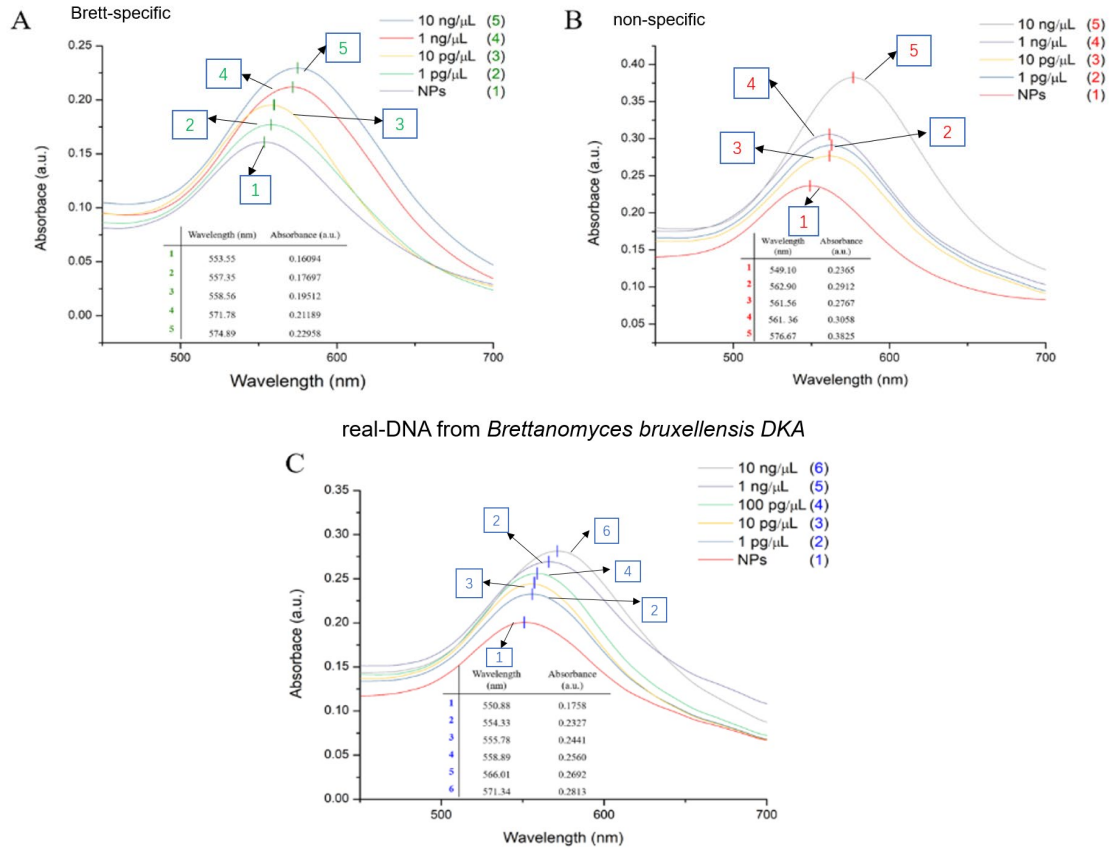

Figure 3. 17 LSPR spectra of genosensors based *Brett*-specific (A), non-specific (B) and real-DNA from *Brettanomyces bruxellensis DKA* (C). The insets show the values of the maximum absorbance and its wavelength peak position of naked and modified gold nanoparticles with different DNA concentrations on coverslips.

3.3 Conclusion and Perspectives

In recent years, the biosensing technology and its applications based on SERS spectroscopy have been rapidly developed. In this work, a rapid and simple SERS

genosensing method is developed based on the specific recognition of biological molecules *Brett-DNA* as sensing elements and their ability to transform interaction information into easily detectable SERS signals. And a preliminary exploration of the detection and diagnosis of biological molecules and organic small molecules with high selectivity and sensitivity is achieved by means of surface plasmonic technology based on the large-scale annealed gold nanostructures fabricated on ultrafine glass coverslips.

In the first step, three fabrication parameters were optimized and it was found that a 4 nm gold-coated coverslip heated at 550 °C on a hot plate for 3 hrs shows the greatest sensitivity of SERS spectra over time to the five different concentrations of BPE molecules. Meanwhile, the lower limit of detection for 10^{-12} M BPE was obtained by using the novel SERS annealed coverslips platforms. On the basis of such results, annealed gold coverslips were considered as the ideal substrates for the construction of ultrasensitive SERS nanobiosensors.

In the second step, as the specific and fast identification of DNA sequences is essential in various fields: medicine, environment, food and beverage industry. And the SERS genosensors have a promising future thanks to their simplicity and accessibility, the biofunctionalization protocol easily transferable to the food industry for rapid identification of pathogenic microorganisms. In this study, The *Brett-DNA* biosensors have been successfully developed on gold nanostructured coverslips and showed excellent specificity and selectivity based on SERS and LSPR detections of *Brettanomyces bruxellensis yeas*t in wine. Specifically, SERS technique made possible the detection of Brett-DNA in pM range, while LSPR revealed detection of a real DNA

extracted in the laboratory (10 pg/μL). Thus, SERS genosensors could be easily replacing/complementing the classical microbiology, ELISA techniques or the need of detection of the 4-ethylphenol yeast-product. And in future, it's necessary to create a specific DNA-SERS database for monitoring the presence of different categories of pathogens and their interfering products.

At present, the combination of new spectrally enhanced materials constructed by nanotechnology and molecular biology technology is driving the rapid development of SERS biosensors. At the same time, the application of SERS biosensors also faces greater challenges in practical applications such as analytical science, environmental monitoring and consumer markets. In addition, the detection of complex living systems is one of the most important applications of biosensors, not only for the direct detection of important biological molecules, but also for the real-time detection of important weak interactions in living systems (e.g., protein-to-protein, specific recognition of cancer cells and drug-cancer cell interactions). Therefore, the development of portable, fast, inexpensive, accurate and sensitive SERS biosensors and their application systems has good prospects for development.

In order to meet the needs of biosensing trace, fast, in-situ detection, efficient, sensitive, miniature, intelligent, applicable SERS biosensors and others biosensing techniques will become the main target of research and development direction, and multi-functional biosensors are also an important direction of development. The SERS biosensing has been certificated a fast and sensitively biosensor on the basis

of Brett-DNA detection on the ultrafine platform (glass coverslips) with annealed AuNPs in this chapter, the one of another quickly biosensing technique (acoustic detection) on the QCM quartz crystal with Au nano-islands and modified with biomolecules will be studied in the next chapter.

Chapter 4 Acoustic detection of gliadin biomolecules on the controlled micropatterned QCM crystal

This chapter reports on the fabrication of multi-patterned QCM crystal with TEM-grids after additional evaporation of thin gold layers, for acoustic sequencial detection of different concentrations of a model food biomolecule such as gliadin.

Gliadin is a class of proteins found in grains, such as wheat, rye, barley, oats, etc. It is a component of gluten, and gliadin plays a key role in determining the unique baking qualities of wheat. However, for some people it is also an allergen. There are three different gluten-related pathologies: gluten allergy, celiac disease, and gluten sensitivity[251]. Gliadin have been extensively studied for the related autoimmune disease with virous manifestations [252]. Therefore, it's important to develop highly sensitive and efficient methods for detection of gliadin in the food industry.

The scientific community is currently focused on finding a quick and inexpensive way to detect gluten in food stuffs. The European Union Regulation (EC) No. 41/2009 stipulates that a gluten limit of < 20mg/kg (20 ppm) for all foodstuffs with a "*gluten free*" label, and approximately 20-100 mg/kg (100 ppm) for the "*very low gluten*"[253]. Over the past few decades, a number of methods have been developed to detect gluten: immunological techniques[254,255]; mass spectrometric and chromatographic techniques[256]; western blotting and proteomic techniques[257,258]; quantitative real-time polymerase chain reaction (Q-PCR)[259]; aptamers against gliadin, as an alternative to antibodies[260]. According to Pei-Tzu Chu *et al.*[189], the use of AuNPs to label quartz crystals for acoustic balance detection should be associated with an increase in the

number of antibodies absorbed on the surface of crystal. As a result, an increase in the number of binding sites against the targeted antigen (gliadin) should allow for higher sensitivity of the system[261]. Specially, more and more gliadin detection by QCM-based immunosensor shows excellent sensitivity, for instance, a resulting immunosensor has a limit of gliadin detection of about 4 ppm by using QCM on the gold substrates[262], and another QCM-based immunosensor was modified by colloidal 25 nm AuNPs with a detection limit of 8 ppb gliadin[189]. Therefore, it's creative to develop a higher sensitivity immunosensor by improved QCM crystal with gold modification.

Therefore, in the present work, simple and reproducible protocols are proposed to perform commercial QCM quartz crystals with robust gold-structures using TEM-grids patterning home-evaporated gold thin films to form gold nano-islands (AuNIs). To assess the role of gold nanoparticles in modulating acoustic sensitivity, different gold thicknesses were tested; after labeling the nanostructured crystals with anti-gliadin antibodies, they were used for acoustic biosensing of different concentrations of gliadin.

The aim of this work was to evaluate the sensing performances in real-time and to compare the frequency variation (ΔF) of QCM crystals modified with TEM-grids/gold film to compared to non-structured quartz crystals.

In this study, I was mainly involved the performation of different modification of commercial QCM quartz crystal (evaporated Au with TEM grid) and described the analysis of the AuNPs size distribution based on the SEM characterization. The results presented here are published in Nanomaterials[198] on 2020.

4.1 Experimental materials and methods

4.1.1 Materials and instruments

The materials used in this chapter are shown in **Table 4.1**. All the chemicals were of analytical grade and used as received without further treatment unless specially mentioned.

Table 4.1 The compounds and materials were used in different steps of the acoustic detections.

Materials	Abbreviation	Company, city, country	Function
gliadin	-	Sigma-Aldrich, Schnelldorf, Germany	analyte for biosensor
anti-gliadin antibody	-	Sigma-Aldrich, Schnelldorf, Germany	antibody for biosensor
anti-BSA antibody	-	Sigma-Aldrich, Schnelldorf, Germany	control antibody for biosensor
11-Mercaptoundecanoic acid	MUA	Sigma-Aldrich, St. Louis, MO, USA	Au biomodification
1-ethyl-3-[3-dimethylaminopropyl] carbodiimide hydrochloride	EDC	Sigma-Aldrich, St. Louis, MO, USA	Au biomodification
N-Hydroxysuccinimide	NHS	Sigma-Aldrich, St. Louis, MO, USA	Au biomodification
deionized water	ddH_2O	Millipore, Molsheim, France	sample washing
detergent	Decon90	Fisher Scientific, Göteborg, Sweden	sample washing
ethanol	-	Sigma-Aldrich, St. Louis, MO, USA	sample washing
transmission electron microscope sample grid	TEM grid	TED Pella	gold evaporation mask
scotch tape	scotch	Elami	gold evaporation mask
glass square coverslips	-	Carl Roth, Karlsruhe, Germany	gold evaporation mask

For the instruments, in order to sterilize ddwater, a Tuttnauer Autoclave Steam Sterilizer 2540ML (Tuttnauer, France) has been used. In the drying processes, a VWR DRY-Line dry DL 53 oven was used while the biofunctionalization steps were made under a biological hood MSC 1,2 ADV (Thermo-scientific, USA). QCM crystals were cleaned using an ultrasonic bath (Elmasonic S30H). For the fabrication of the nanostructured QCM quartz crystal, a gold evaporation step was performed with the evaporator Plassys MEB 400 (Plassys, Bestek, France). And all acoustic measurements were performed with the QCM200 quartz crystal microbalance (Stanford Research System), including a crystal oscillator QCM25 and a crystal holder that can accommodated 5 MHz (2.54 cm) AT-cut quartz crystal with gold electrodes on both sides (Cr/Au) (SRS California, USA).

To morphologically characterize the surface of nanostructured QCM crystal surface, a scanning electron microscope (SEM) (FEG-SU8030, Japan) was used.

4.1.2 Preparation of different gliadin concentrations

Five gliadin concentrations were freshly prepared for each set of QCM sensing experiments: 1 mg/L (1 ppm), 10^{-1} mg/L (0.1 ppm), 10^{-2} mg/L (0.01 ppm), 10^{-3} mg/L (0.001 ppm) and 10^{-4} mg/L (0.0001 ppm). Firstly, a stock solution of 80 g/L of gliadin in ethanol/water solution (6:4 v/v ratio) was made by weighing 0.08 g ± 0.001 g of gliadin (commercially available poder) and mixing it with 0.6 mL of ethanol and 0.4 mL of ultra-pure sterilized water. From the stock solution, all gliadin concentrations have been prepared by diluting with ultra-pure sterilized water.

4.1.3 Preparation of S-QCM crystals modified with TEM-grid/ gold film

Two kinds of modification of S-QCM were prepared: Standard quartz crystals were modified with either 30 nm or 50 nm gold and evaporated through a TEM-grid mask (Q-TEM) (**Figure 4.1**). The details protocol of preparation was shown below.

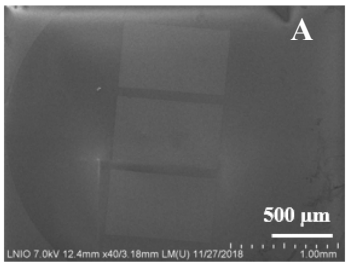

Figure 4. 1 No annealed Q-TEM grid crystal with gold electrode modified with 30 nm Au evaporated through a TEM-grid with 3 slots.

Cleaning of standard quartz crystals: Standard quartz crystals were washed in an ultrasonic bath with ultrapure water and detergent (Decon 90) solution (2:8, v/v ratio), at 50 °C for 15 min. Then they were rinsed and washed again in an ultrasonic bath with ultra-pure water at 50°C for 5 min. Afterwards, the crystals were rinsed with plenty of ultra-pure water, dried under nitrogen stream and deposited on a hot plate at 100°C for 10 min to completely dry the surface.

Fabrication of patterned QCM-TEM grid crystal: One cleaned crystal was labelled with a 3 slots TEM-grid before evaporation, and all the rest of the surface was covered with scotch. The evaporation was performed at 1 x 10^{-5} Torr pressure and 25 °C. An evaporation rate of 0.2 nm/s has been set and a thickness of 30 nm and 50 nm of gold have been deposited without any annealing, see **Figure 4.1 A**.

4.1.4 Biofunctionalization of S-QCM and Q-TEM grid quartz crystals

Cleaning and thiol-functionalization of S-QCM and Q-TEM grid quartz crystals

The S-QCM and Q-TEM grid quartz crystals were first cleaned in an ultrasonic bath at 40 °C for 20 min with ethanol solution (70 %). And then washed in an ultrasonic bath at 40 °C for 10 min with only ultrapure water to avoid the traces of ethanol on the crystal surface. Soon, the washed crystals were dried at 50 °C for 20 min. Subsequently,

the crystals were thiolate by dipping in 5 mL of 11-MUA (10^{-3} M) in ethanol solution (70 %) at room temperature overnight. The day after, the crystals were thoroughly rinsed with ethanol and ultra-pure sterilized water, and dried under a biological hood.

Biofunctionalization of S-QCM and Q-TEM grid quartz crystals with specific or non-specific antibodies

The thiolated QCM crystals were activated in 5 mL of EDC/NHS 0.4/0.1 mM solution for 30 min at room temperature, followed by washing with ultra-pure sterile water and drying under the biological hood. Finally, the crystals were bio-functionalized with anti-gliadin antibodies (**Figure 4.2**) by suspending 40 µL of antibodies at a concentration of 100 µg/mL in dd water and left at 4 °C overnight.

In order to verify the specific detection of different gliadin concentrations, control experiments were performed on S-QCM and Q-TEM grid (30 nm) crystals biofunctionalized with anti-BSA antibody. The two QCM crystals were washed twice with sterile ddwater and incubated with anti-BSA antibody (40 µL, 125 µg/mL in ddH_2O) at 4 °C overnight. The day after, the two QCM crystals were abundantly rinsed with ddwater, dried and ready for acoustic detection of different gliadin concentrations.

For S-QCM crystals, two sets of the biofunctionalization procedures were carried out, one crystal was labeled with specific antibodies (anti-gliadin antibodies) and the other crystal was labeled with non-specific antibodies (anti-BSA antibodies) to make the modifications.

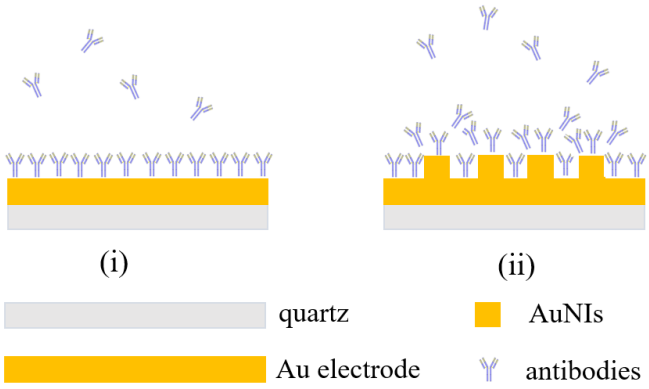

Figure 4. 2 A simple representation of the (bio)functionalization of Au electrode of quartz crystal (thiolated before) with antibodies when using: (i) S-QCM crystal; (ii) Q-TEM grid crystals (AuNIs: gold nano-islands)

4.1.5 Acoustic Measurements

During the experiment, the antibody biofunctionalized QCM crystal was fixed on the crystal holder of the acoustic balance, and stabilized the absolute frequency baseline of the crystal in the air. After stabilization, 10 µL S-ddwater was deposed as a reference signal. After 20 min the S-ddwater was collected, and the crystal left dry to stabilize the absolute frequency for 15 min. Two kinds of experiments were performed with S-QCM and Q-TEM grid crystals: the first was labeled with specific anti-gliadin antibody, and the second labeled with non-specific BSA antibody. The standard gliadin solutions were tested starting from the lowest analyte concentration (10^{-4} mg/L) to the highest 1 mg/L). Each drop of 10 µL gliadin solution was deposited on the crystal for 40 min, and then collected, and the crystal rinsed twice with S-ddwater before 10 µL of a different gliadin concentration (10^{-3} mg/L) deposited on the QCM crystal for 40 min. Each concentration was collected after 40 min sedimentation, and the crystal rinsed twice, before any new sedimentation with 10 µL S-ddwater. 20 min were necessary to stabilize of the absolute

frequency before analysis.

4.2 Results and Discussion

4.2.1 SEM characterization of nanostructured QCM crystals

The SEM characterization of S-QCM and Q-TEM, crystals is shown in **Figure 4.3** for the gold electrode and outside the electrode which is the transparent part of crystals. Around the gold electrodes for S-QCM and Q-TEM crystals, a uniform structure without particles was observed, corresponding to the expected structure of bare quartz glass crystals observed by Niu et al.[263]. The gold electrode of the S-QCM quartz is composed of regular 50 nm sized grains, which are well connected and without porosity. However, deposing 30 nm Au to obtain Q-TEM crystal induced a regular height modification of a visible the gold electrode structure with the previous layer.

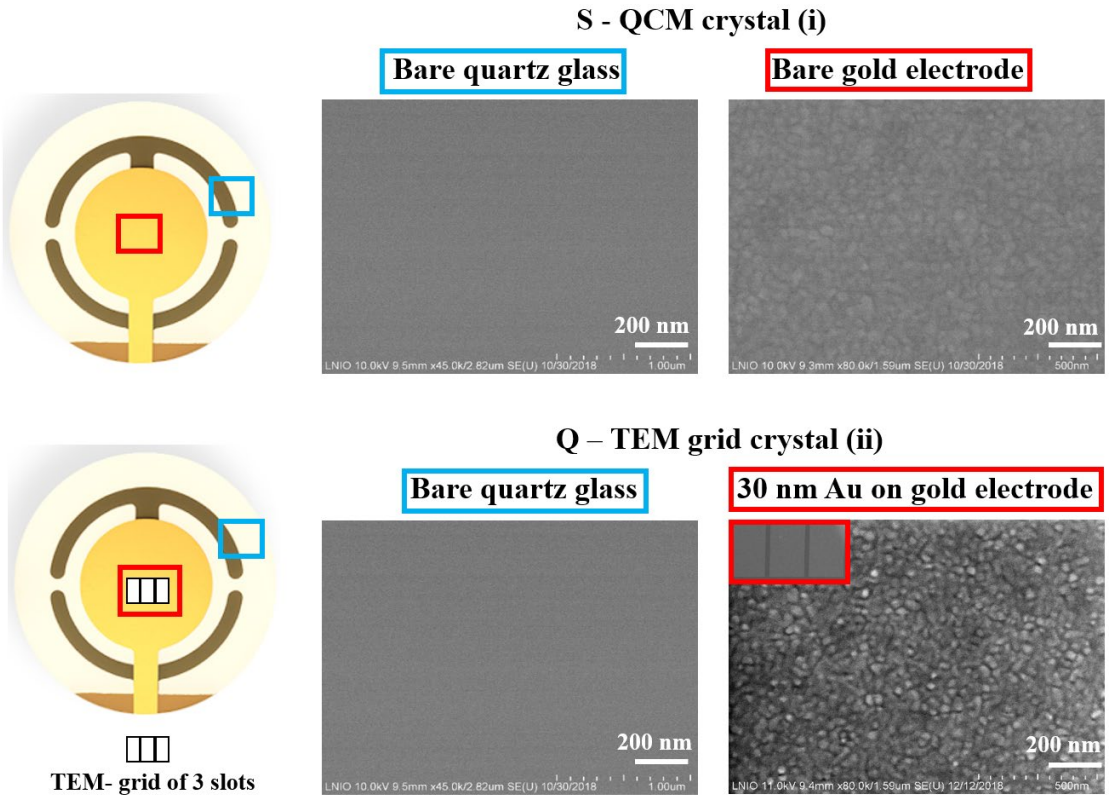

Figure 4. 3 SEM images of three types of QCM crystals used for (bio)functionalization and detection of gliadin (i) bare S-QCM crystal, S-standard; (ii) no annealed Q-TEM grid crystal with gold electrode modified with 30 nm Au evaporated through a TEM-grid.

4.2.2 Acoustic gliadin detection using S-QCM and Q-TEM grid crystals

Figures 4.4-4.6 show the sensograms obtained by S-QCM, Q-TEM grid (30 nm Au) and Q-TEM grid (50 nm Au) crystals respectively, when making of the deposition of the concentrations ranging from 10^{-4} mg/L (0.0001 ppm) to 1 mg/L (1 ppm) of gliadin (10 µL).

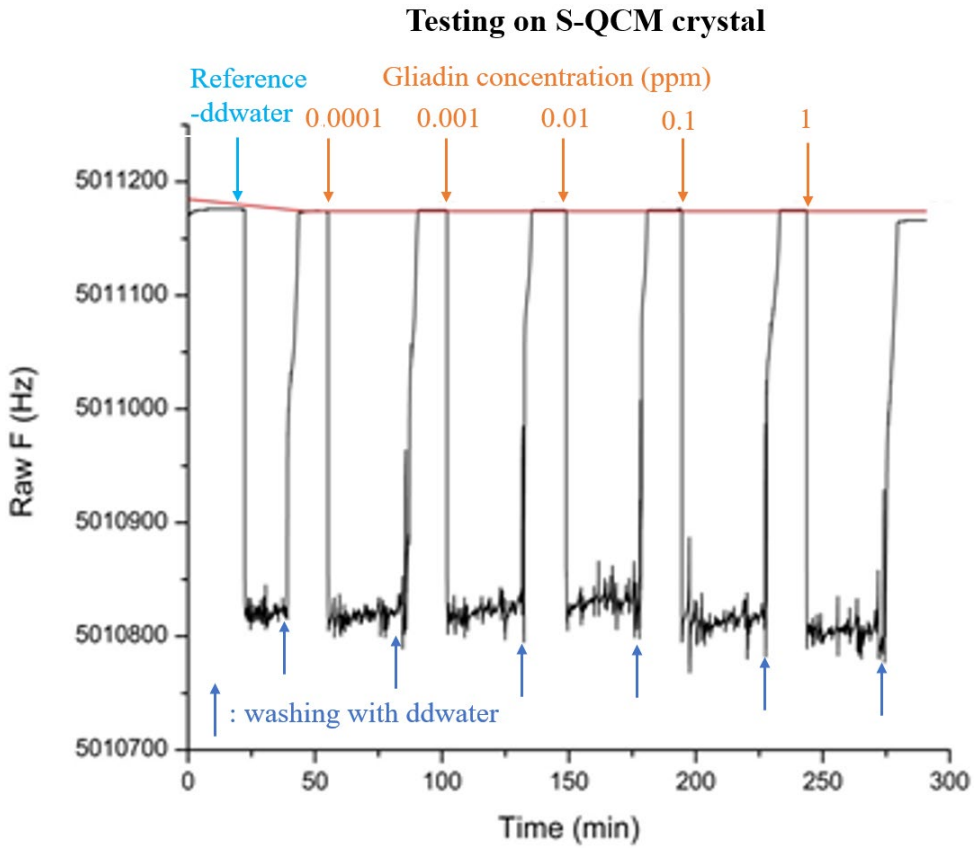

Figure 4. 4 Sensogram of S-QCM crystal biofunctionalized with an anti-gliadin antibody and exposed to different concentrations of gliadin.

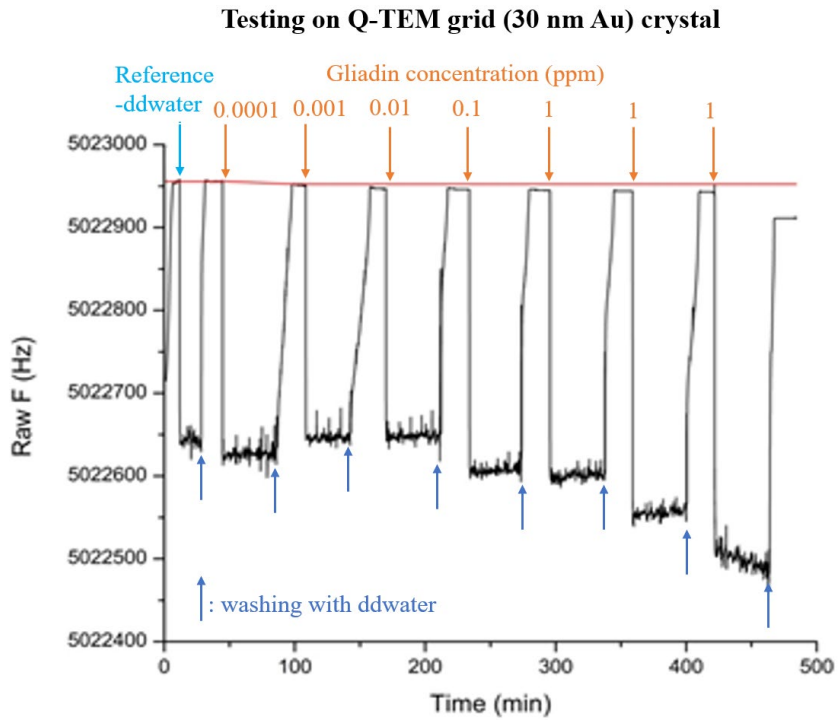

Figure 4. 5 Sensorgram of Q-TEM grid (30 nm Au) crystal biofunctionalized with an anti-gliadin antibody and exposed to different concentrations of gliadin.

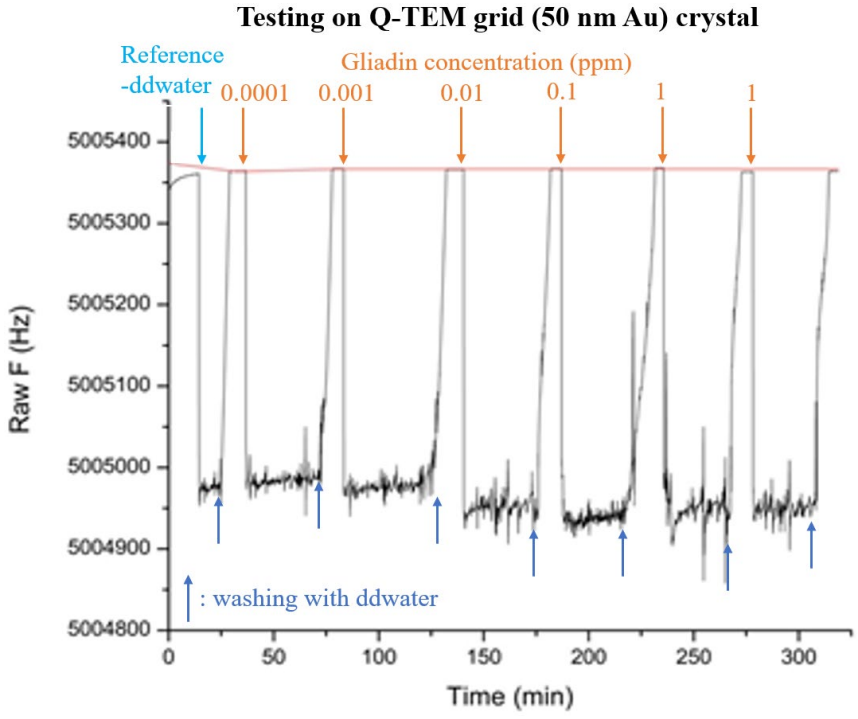

Figure 4. 6 Sensorgram of Q-TEM grid (50 nm Au) crystal biofunctionalized with an anti-gliadin antibody and exposed to different concentrations of gliadin.

From these figures, the frequencies are extracted when the signal is stabilized after collecting the drops and plotted as a function of the concentration of gliadin (**Figure 4.7**), contributing to the construction of dose/response curves.

S-QCM crystal

Gliadin (ppm)	Frequency (Hz)
0.0001	5011176.42
0.001	5011176.42
0.01	5011176.42
0.1	5011176.42
1	5011167.34

Q-TEM grid (30 nm) crystal

Gliadin (ppm)	Frequency (Hz)
0.0001	5022950.79
0.001	5022947.59
0.01	5022946.59
0.1	5022945.24
1	5022942.39

Q-TEM grid (50 nm) crystal

Gliadin (ppm)	Frequency (Hz)
0.0001	5005367.16
0.001	5005365.89
0.01	5005365.89
0.1	5005363.04
1	5005363.04

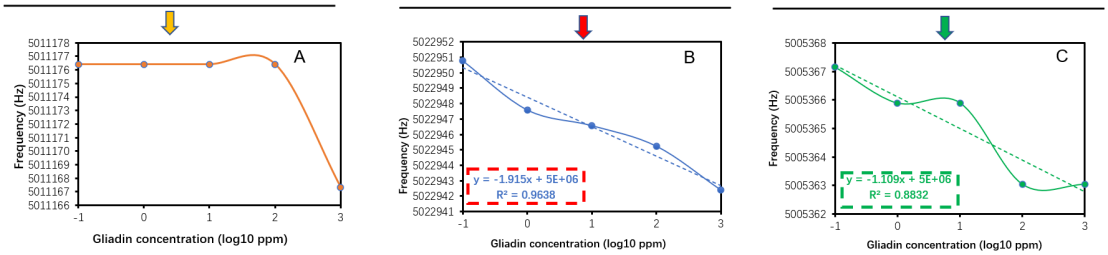

Figure 4. 7 Curves dose/response of the immune-acoustic gliadin detection on: (A) S-QCM crystal; (B) Q-TEM grid (30 nm) crystal; (C) Q-TEM grid (50 nm) crystal. In the table are reported the frequency values.

For S-QCM (**Figure 4.7A**), the frequency remains constant from 0.0001 ppm to 0.1 ppm, and begins to decrease by 1ppm. This indicates that the detection limit is above 0.1 ppm. In the case of the two Q-TEM grid crystals (**Figure 4.7 B,C**), a decrease in frequency from 0.0001 ppm to 1 ppm is observed, indicating that the detection limit is equal to or less than 0.0001 ppm. In addition, the response of Q-TEM grid crystal with 30 nm Au (R^2=0.9636) is more linear than the Q-TEM grid crystal with 50 nm Au (0.8834). Moreover, the Q-TEM grid crystal 30 nm seem to be more sensitive for the detection of gliadin traces. These results demonstrate the beneficial effects of the deposed gold layer through the TEM grid, by improving the detection limit and the dependance of the response on the gold thickness.

4.2.3 Control experiments – non-specific antibody for gliadin

Two kinds of quartz crystals: S-QCM crystal (**Figure 4.8A**) and Q-TEM grid (30 nm Au) crystal (**Figure 4.8B**) were bio-functionalized with non-specific anti-gliadin antibody namely anti-BSA antibody. As expected, for both crystals no shift of resonant frequency was recorded in the presence of different gliadin concentrations.

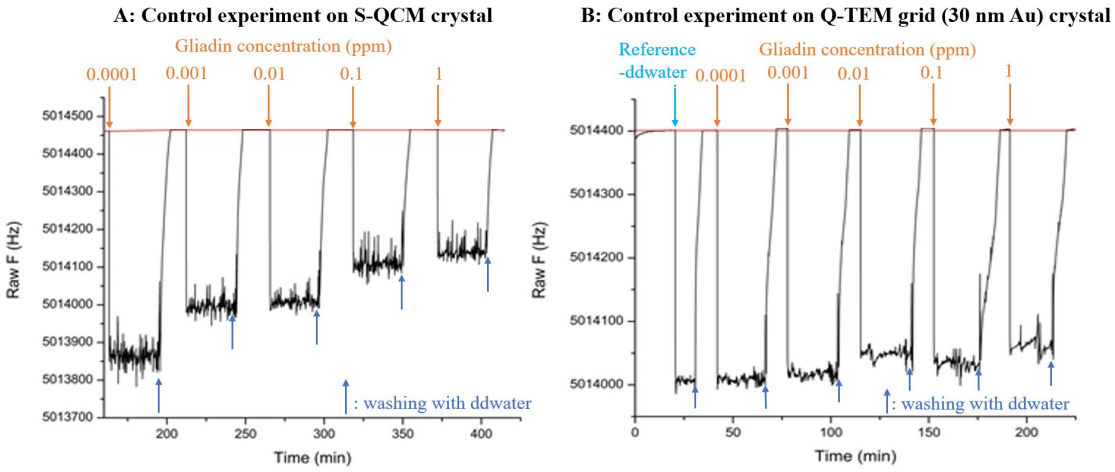

Figure 4. 8 Control experiments - Acoustic detection of gliadin in the presence of anti-BSA antibodies using a drop-deposition procedure upon the deposition of different concentrations of gliadin on either a S-QCM crystal (A) or on a Q-TEM grid (30 nm) crystal (B).

4.3 Conclusions and Perspectives

In this work, platforms based on QCM quartz crystal fabrication protocols are reported. It has shown a simple and inexpensive method to fabricate the Au nanostructures, which is as effective as the other synthesis methods. The purpose of this study is to investigate the performance of anti-gliadin antibody labeled gold nanostructured QCM crystal for gliadin immunodetection in standard solutions with

acoustic measurements. It is found that the homemade Q-TEM grid (30 nm Au) could be an efficient platform for acoustic detection of gliadin. Compared the commercial standard QCM crystal, the detection limit of the Q-TEM grid crystal has been greatly improved, at least in a ratio of 1000. In this case, the linearity of the sensor response was obtained relies on the gold thickness deposed on the TEM grid.

As the importance of biosensing relies on the highly sensitivity and specificity that allows detection of analytes in a very low limit. Therefore, further improve the nanostructures on the commercial standard QCM crystal is potential direction, and to detect analytes in complex samples.

Chapter 5 Influence of saline buffers over the stability of annealed gold nanoparticles formed on coverslips

As introduced in the chapter 1, metallic nanoparticles are attractive active supports for various optical (bio)sensing applications[264–266]. Especailly the AuNPs are responsible for improved sensitivity and stability of optical sensing properties[267–269] and imaging[270]. AuNPs represent an excellent nanoplatform in the development of various configurations of sensing chemicals and biomolecules including viruses[271]. The shape, size and inter-distance of the biosensing Au nanostructures have effect on the sensitively, stability, repeatability of biosensors. Several research groups had been investigated on the effect of Au nanostructures. The aggregation of colloidal AuNPs has been used and observed for colorimetric[272], electrochemical[273] and atomic force microscopy[274] investigations. In such applications, the choice of buffer composition is critical to the analytical performances of the sensing scheme. For example, saline buffers SSPE and PBS were widely used in the dissolution, dilution or long-term storage of biomolecules in biosensor fields[242,275,276]. In other cases, the buffers were mainly used to study the effect of the electrocatalytic performance of the modified electrode of the electrochemical biosensors[277–280].

In the chapter 2, 3 and 4, different biosensing detection platforms were developed based on the Au nanostructures on the solid substrates (ITO glass strips, glass coverslips and QCM quartz crystal). In each (bio)functionalization process, different saline buffers were used for the biomolecules storage or substrates washing. However, the influence of saline buffers on the stability of nanoparticles sizes and dispersion on solid supports

has not yet been studied.

In this chapter, considered effect of buffers on the AuNPs on glass substrates, the glass coverslip was chosen as the support for the annealed AuNPs. The SSPE and PBS buffers were chosen to investigate the influence on the stability of high temperature annealed 4 nm gold film coated ultrafine glass coverslips, using an optimized AuNPs synthesis scheme in the chapter 3. And considering the low detection limit (10^{-12} M) of BPE molecules was obtained by SERS spectra on the anneald 4 nm gold film glass coverslips in chapter 3, five concentrations (10^{-3}, 10^{-5}, 10^{-7}, 10^{-9} and 10^{-11} M) of BPE molecules in this study were used for investigation on the stability of AuNPs by LSPR detection. The AuNPs modified with different solutions under the working conditions of dry and wet media. LSPR is used for sensing diagnostics through monitoring the changes in the AuNPs size, shape, composition, inter-particle distance, the dielectric constant (refractive index) of the surrounding medium[281] and the linear and/or non-linear optical properties of AuNPs[282]. Substrate surface characterizations such as SEM and AFM in the presence of selected buffers were recoreded and discussed. The results were published in Bioengineering[283] on 2020.

5.1 Experimental materials and methods

5.1.1 Chemicals

The materials used in this chapter are shown in **Table 5.1**. All the chemicals were of analytical grade and used as received without further treatment unless specially mentioned.

Table 5.1 The compounds and materials were used in different steps of the stability study.

Materials	Abbreviation	Company, city, country	Function
sodium chloride	NaCl	Sigma-Aldrich, St. Louis, MO, USA	buffer preparation
sodium phosphate monobasic	NaH_2PO_4	Sigma-Aldrich, St. Louis, MO, USA	buffer preparation
sodium phosphate dibasic	Na_2HPO_4	Sigma-Aldrich, St. Louis, MO, USA	buffer preparation
ethylenediaminetetraacetic acid	EDTA	Sigma-Aldrich, St. Louis, MO, USA	buffer preparation
trans 1, 2-bis-(4-pyridyl)-ethene	BPE	Sigma-Aldrich, Schnelldorf, Germany	LSPR detection
deionized water	ddH_2O	Millipore, Molsheim, France	sample washing
detergent	Decon90	Fisher Scientific, Göteborg, Sweden	sample washing
squared glass coverslips	-	Carl Roth, Karlsruhe, Germany	glass substrate

5.1.2 Instruments

Metal evaporation was performed with Plassys MEB 400 (Bestek, France), and a hot plate (Thermo Fisher Scientific, Waltham, MA, USA) was used for shortly drying and thermal annealing of gold films under the clean room conditions.

The nanostructured coverslips were characterized by scanning electron microscope (SEM) (FEG-SU8030, Tokyo, Japan) and atomic force microscope (AFM) (Bruker ICON, Billerica, MA, USA). The cantilever of AFM ScanAsyst-Air is in silicon nitride and the height of the tip is 2.5 - 8.0 mm. The spring constant of 0.4 N/m and the back reflective aluminium coating in the standard ScanAsyst-Air mode were used to characterize the morphology of AuNPs. The AFM PeakForce-mode is used for topographical characterization of annealed coverslips.

In the morphological characterization analysis, the nanoparticles size distribution analyzed using the Public Domain ImageJ software developed by the National Institutes of Health based on the SEM images. Collected AFM images (1 μm x 1 μm) were analysed using Gwyddion software that adjusts the colour scale according to the maximum and minimum height per line scan. This causes regions onto nanostructured glass coverslips to appear darker (i.e. lower) between nanoparticles. In addition, two parameters (R_a and R_{rms}) were used to estimate the surface roughness of annealed coverslips, whether exposed naked AuNPs in air or after exposure to water or aqueous buffers (SSPE and PBS). R_a is defined as the average roughness (in μm), which describes the height characteristics of the overall profile, (less sensitive to large structures and valleys), while R_{rms} is the root mean square between the average height deviation of the annealed surface and the average line/surface in the evaluation length/area. These parameters account for the roughness of coverslips after different buffer treatments, and calculate the distance between nanoparticles and valleys. The larger distance corresponds to the rougher surface.

The measurement of LSPR is using a Ø = 50 μm of the thin fibre QP50-2-UV-BX (Ocean Optics, EW Duiven, Netherlands) optical spectrophotometer Maya 2000 Pro and white light source (DH-2000-BAC, Ocean Optics, EW Duiven, Netherlands) performed between 200 nm and 1100 nm, all spectra were recorded with a 10× objective. The schematic experimental set-up of LSPR detection in our study shown below **Figure 5.1**:

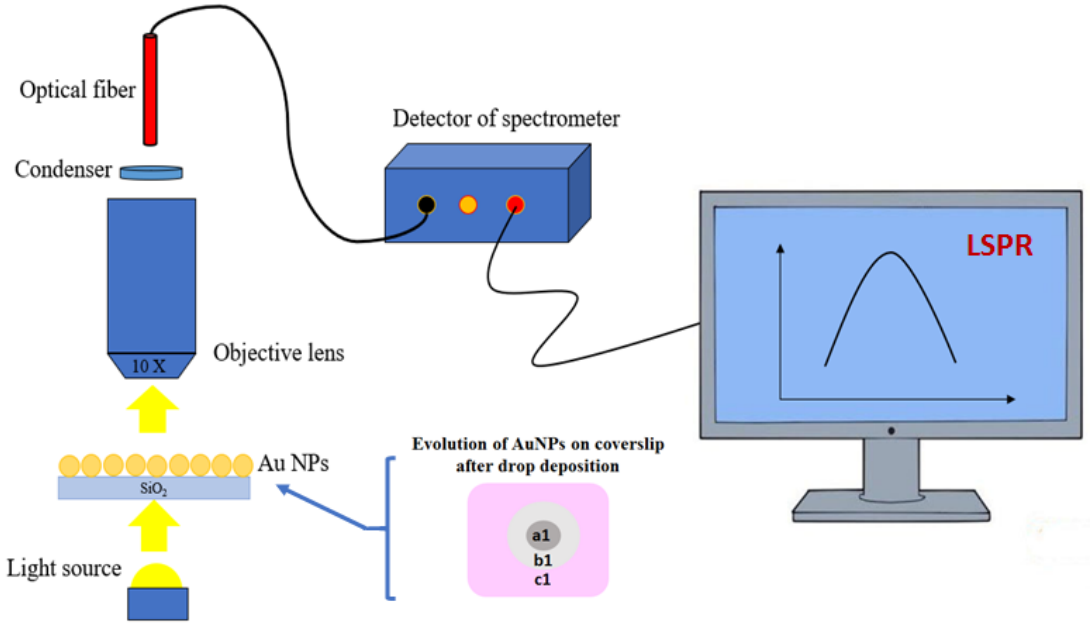

Figure 5. 1 The experimental set-up for LSPR investigations of annealed AuNPs on coverslips exposed to drops of aqueous and saline-buffers. Once the different drops of buffers were collected from the coverslips, three areas were observed and named **a1** (under the drop), **b1** (in the vicinity of the drop), **c1** (far from the drop).

5.1.3 Preparation of saline buffers

In order to investigate the stability of the nanoparticles with biological solutions, a stock 20 x SSPE buffer contains 3 M sodium chloride, 0.23 M sodium phosphate dibasic and 25 mM ethylenediaminetetraacetic acid dissolved in dd-water, pH 7.4. For all experiments, 1 x SSPE buffer was freshly prepared. The PBS buffer solution contains 1.5 M sodium chloride, 81 mM sodium phosphate dibasic and 19 mM sodium phosphate monobasic dissolved in dd-water, pH 7.4. Using dd-water as diluting solvent, a 97 % concentrated BPE stock solution was used to prepare five concentrations of BPE solutions (10^{-3}, 10^{-5}, 10^{-7}, 10^{-9} and 10^{-11} M).

5.1.4 Preparation of annealed gold nanostructures on coverslips

At the first step, the squared glass coverslips were degreased with an aqueous solution of Decon90 detergent (2:8 v/v, dd-water: detergent), in an ultrasonic distilled water bath (Elmasonic S30H) at 50°C for 15 min. In addition, ultrasonicated in dd-water bath for 5 min at 50 °C with three times. Further, each coverslip was extensively rinsed with dd-water, dried under a nitrogen stream, placed on a hot plate at 100 °C for 10 min. Nest step, the cleaned substrates were fixed on a circular evaporation plate, subsequently, scotch-labelled at the bottom and used for coating with gold thin (4 nm) films in an evaporator (Plassys MEB 400) using a high purity 99.99% gold source (Neyco, Vanves, France) under $1x10^{-6}$ Torr pressure at 25 °C with an evaporation rate of 0.01 nm/s. Finally, the 4 nm gold coated coverslips were thermally annealed on a hot plate at 550 °C for 3 hr.

5.1.5 Influence of buffers over the stability of annealed AuNPs on thin glasses

In the study of the stability of the nanoparticles on the coverslips, 1x SSPE buffer, and PBS buffer were prepared for the modification on the annealed gold on the glass coverslips. For the purpose of better understanding, the effect of buffer solutions on the Au NPs, two methods were used to the effects of the drops of water (2 µL), 1 x SSPE (2 and 5 µL) and PBS (5 µL) buffers on annealed gold nanostructures on coverslips, the two methods have a common step, that's overnight at 4 °C, in the presence of (i) humid chamber petri dish - called *wet media* or (ii) no petri dish -called *dry media* (**Figure 5.2).** After, different concentrations of BPE (5 µL) were prepared for the modification on the annealed gold on coverslips under the *wet media* overnight at 4 °C.

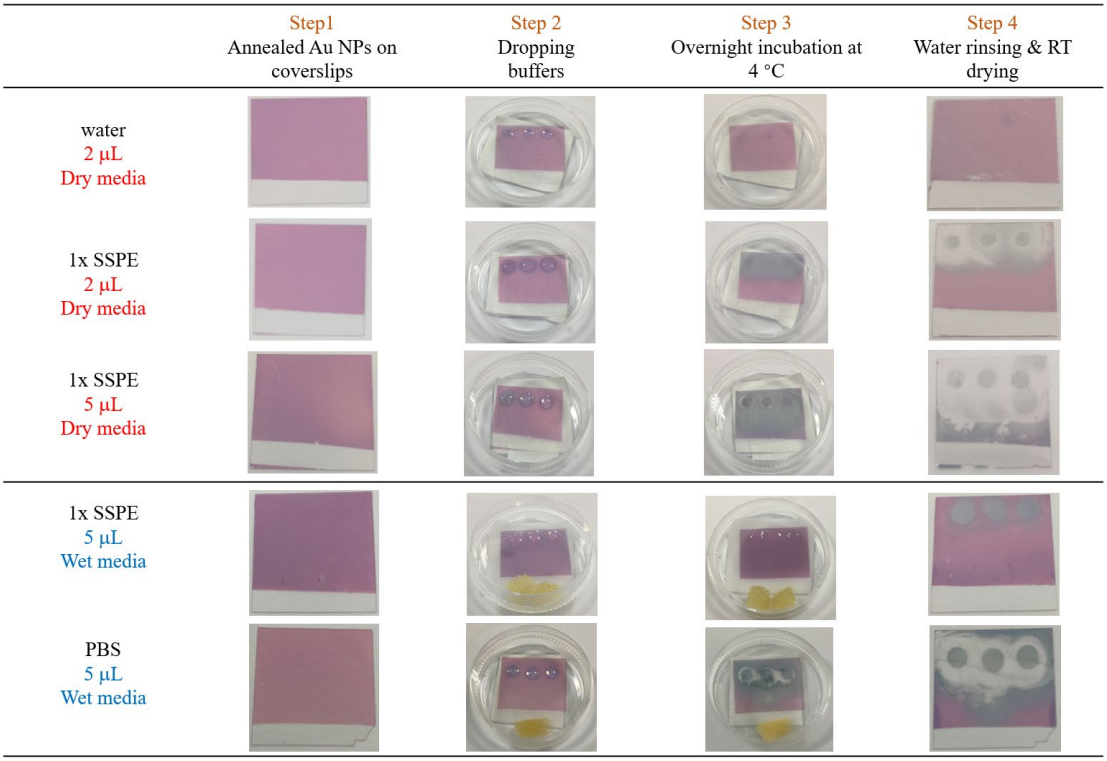

Figure 5. 2 The protocol and photos of modification of annealed gold nanoparticles with different buffer solutions.

5.2 Results and Discussions

5.2.1 Characterization of annealed gold coated coverslips – bare AuNPs

The prepared annealed gold nanoparticles on the coverslips were investigated by AFM measurement, SEM measurement and optical spectrometer LSPR. In the **Figure 5.3**, it displays a detail investigation sequence of the experimentally prepared nanoparticles.

It should be noted that the SEM and AFM images depict a uniform distribution of spherical nanoparticles, which is confirmed by the size distribution mainly in the narrow range of 4 nm - 16 nm, where most AuNPs (82 %) exhibit 8-10 nm in diameter. AFM images and recorded LSPR spectra also confirmed the uniformity

of AuNPs, from the line profile analysis with roughness values 1.410 nm R_a and 1.785 nm R_{rms} based on the AFM characterization and the overlap of five LSPR spectra collected from five different areas of the annealed coverslip with the maximum plasmonic resonance at 542 nm on the basis of spectra investigation of AuNPs.

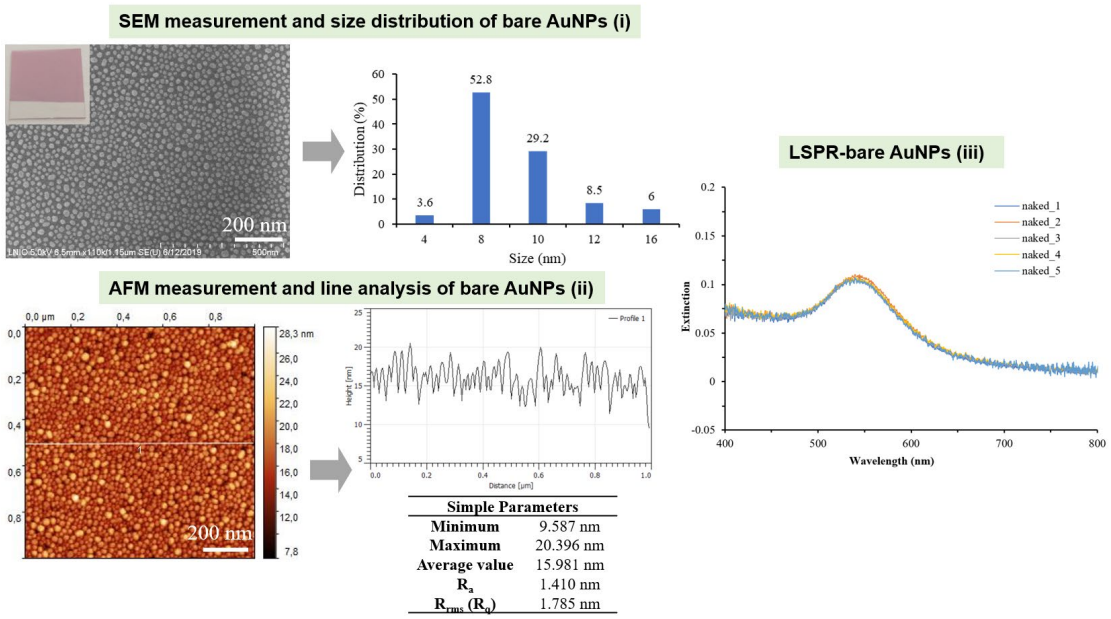

Figure 5. 3 SEM (i), AFM (ii) and LSPR (iii) characterizations of annealed gold nanostructured (AuNPs) coverslips. The size distribution of AuNPs (based on SEM image) and line profile analysis (based on AFM images) were also presented in the middle panel. The SEM, AFM and LSPR measurements were performed in the cleanroom with the temperature 21 °C.

5.2.2 Influence of water and saline buffers over the stability of annealed Au NPs on coverslips

5.2.2.1 Study of water solvent

SEM imaging characterization with the corresponding size distribution, AFM

characterization with the height profile analysis and the LSPR collecting spectra of the nanostructured coverslips modified by dd-water drop (2 µL) for overnight at 4 °C were illustrated in **Figure 5.4**. More specifically, there are three areas on the coverslip were characterized: a1-just below the drop, b1- near the drop, c1- far away from the drop.

Interestingly, from SEM imaging (**Figure 5.4, i**), very similar morphologies of nanoparticles whatever the tested position are observed. Therefore, the nanoparticles are spherical and homogeneously distributed. This was confirmed by the size distribution analysis of AuNPs, and no significant difference was observed in the size distribution of AuNPs. The diameter of the nanoparticles is mostly 8-10 nm, and the size distribution is the highest at 8 nm (a1-59.3 %, b1-52.2 %, c1-53.2 %) and the distribution is quite narrow. According to the SEM images and the size distribution, the deposition of water drop has no significant effect on the geometry of nanoparticles and does not affect their stability on the coverslip substrate.

In addition, these observations are also confirmed by the AFM imaging (**Figure 5.4, ii)**, roughness values of the three selected areas are very similar, R_a (nm) (a1- 2.01; b1 - 2.2.06; c1 - 2.05) and R_{ms} (nm) (a1- 2.53; b1 - 2.57; c1 - 2.55). Followed by the LSPR spectra measurements of the three parts, the spectra are shown in **Figure 5.4, iii**, it's observed that the a1, b1 and c1 areas have a similar plasmonic peak evolution λ_{max} at 559.78 nm, and the maximum OD (Optical Density) values of a1 is 0.183, b1 is 0.182 and c1 is 0.179.

SEM-Water on annealed AuNPs coverslip (i)

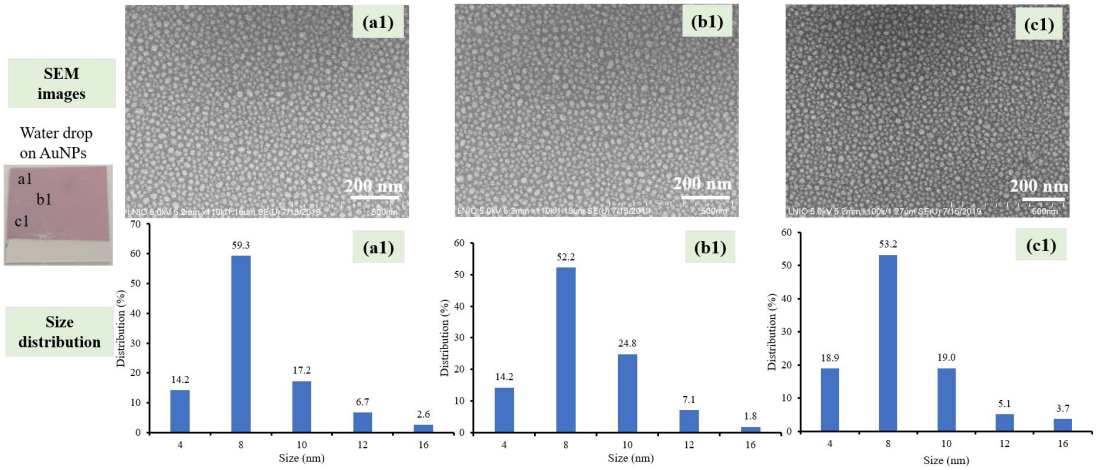

AFM – water on annealed AuNPs coverslip (ii)

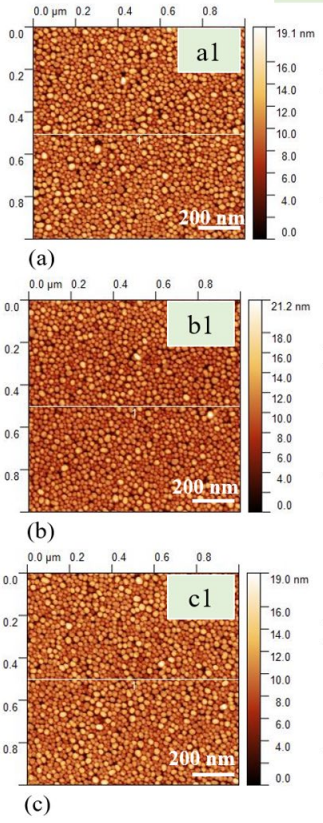

a1

Simple Parameters	
Minimum	2.35 nm
Maximum	16.28 nm
Average value	9.15 nm
R_a	2.01 nm
R_{rms} (R_q)	2.53 nm

b1

Simple Parameters	
Minimum	0.71 nm
Maximum	12.91 nm
Average value	8.19 nm
R_a	2.06 nm
R_{rms} (R_q)	2.57 nm

c1

Simple Parameters	
Minimum	0.95 nm
Maximum	12.68 nm
Average value	8.43 nm
R_a	2.05 nm
R_{rms} (R_q)	2.55 nm

Line analysis

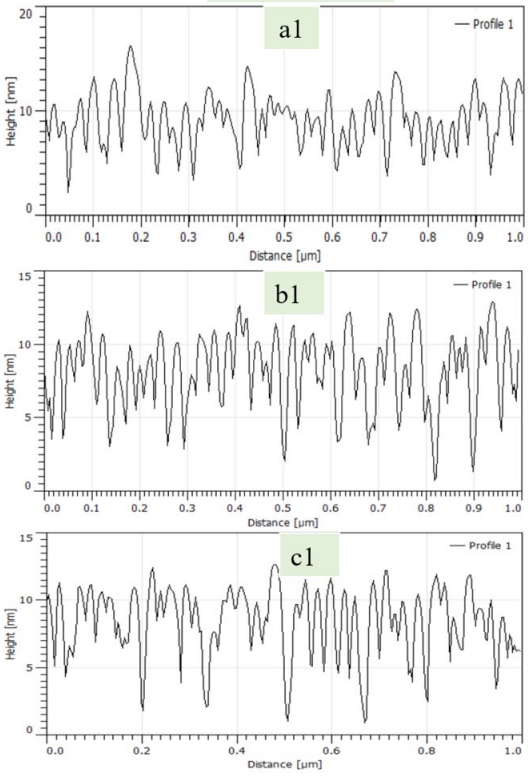

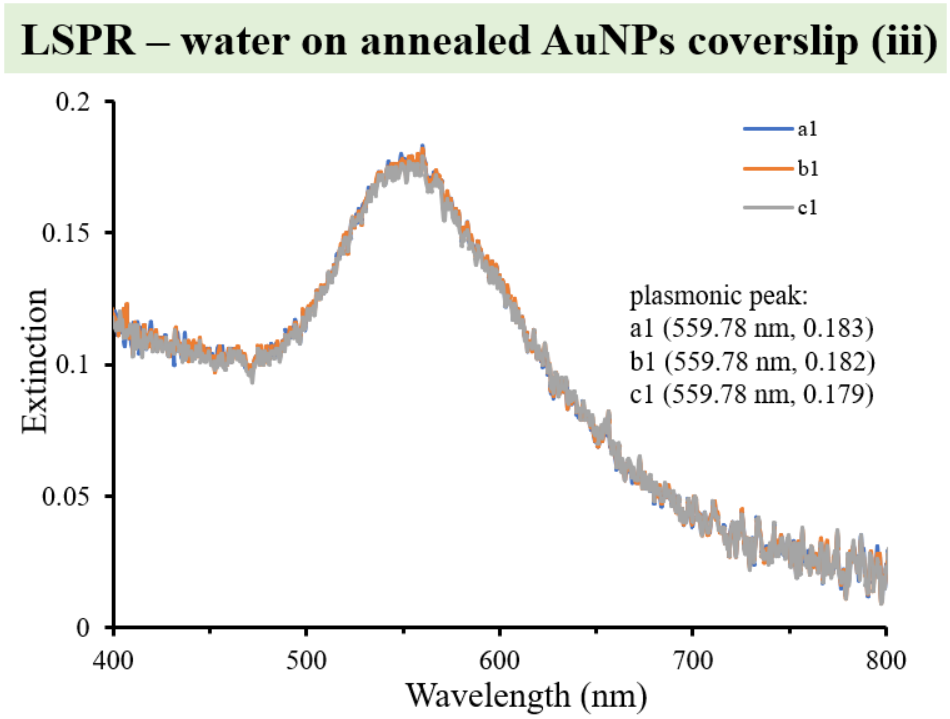

Figure 5. 4 Morphological characterization and plasmonic of Au NPs modified by water. SEM (i), AFM (ii) and LSPR (iii) characterizations of annealed gold nanostructured (AuNPs) coverslips exposed to water drops, air dried and with three investigated areas: a1 (under the drop), b1 (in the vicinity of the drop), c1 (far from the drop). The size distribution of AuNPs (based on SEM image) and line profile analysis (based on AFM images) were acquired for a1, b1 and c1. The pH of water was 7.0. The SEM, AFM and LSPR measurements were performed in the cleanroom with the temperature 21 °C.

5.2.2.2 Study of SSPE buffer

As shown in the SEM images of **Figure 5.5**, the morphological characterization of SSPE modified gold nanoparticles were measured. The SEM image in a1 area shows that worm-like aggregates of nearly ten AuNPs are formed

when dropped 1 x SSPE buffer under dry media (2 and 5 µL), while smaller aggregates are formed under wet media (5 µL), and the AuNPs after modified under dry media (2 and 5 µL) are shown more space between AuNPs clusters than AuNPs under wet media (5 µL).

Besides, the SEM image of the b1 area shows that the morphology under dry media is similar to the morphology under the wet media in the a1 area. Under dry condition, AuNPs are almost absent on the substrate for the highest buffer concentration. Under wet condition, the appearance of the AuNPs is very similar to the annealed AuNPs observed in **Figure 5.3**. In particular, the SEM image (**Figure 5.5, i)** in the c1 area shows a similar morphology (uniformly dispersed shape) for 1 x SSPE buffer under dry media (A) and for the wet media (C), compared with the annealed AuNPs in **Figure 5.3**. For the 5 µL buffer under dry media (B), the image of the c1 area evidences some aggregation.

To conclude, under the modification of the dropping of 1 x SSPE buffer, clearly affect the morphology and the stability of annealed AuNPs on coverslips, especially under dry media and strongly in the presence of 5 µL buffer under dry condition.

Therefore, due to the analysis of the above results, and the related AFM characterization is also analyzed. As can be seen from **Figure 5.5 ii**, the line profile analysis based on AFM images were acquired for a1, b1 and c1 areas. It is noted that the surface morphology of the Au NPs in a1 area from AFM images of the sample which was modified under dry media (2 µL and 5 µL) and wet media (5 µL) is

corresponding to the SEM characterization in **Figure 5.5, i**. Moreover, in the b1 area, the changes of the R_{rms} values of drying media (2µL -4.977 nm) were similar with the wet media (5 µL -3.852 nm), and there is no further change in the c1 area, but it has a great influence on a1 area for both media. Furthermore, the smallest R_{rms} value was obtained for the 5 µL 1 x SSPE in wet condition in a1 area - 4.395 nm. And the highest R_{rms} value of 2 µL 1 x SSPE in dry condition in a1 area - 7.638 nm is observed probably due to faster evaporation of the drop.

As shown in **Figure 5.5, iii**, the LSPR spectra of the three types of samples with different modification conditions were captured. In each condition, the three drops were performed and the LSPR spectra also detected in each drop, the LSPR spectra results of the other two modification drops are not shown.

As expected, under the dry (2 µL and 5 µL) and wet media (5 µL), the similar LSPR resonant spectra with a maximum of extinction versus wavelength were obtained for the naked AuNPs in the c1 area. For the b1 area in dry media, the LSPR measurement results shown no plasmonic resonant spectra contrary to a well-defined spectrum for sample under wet media. However, for a1 area of all tested samples, no LSPR peak was possible. Especially, the spectra were obtained in each area (a1, b1 and c1) and the intensity comparison of plasmon resonance peaks is c1>b1>a1, for the sample modified overnight at 4 °C in the wet condition with 5 µL per drop, and these results also apply to the other two modification drops. When compared the LSPR spectra of the a1 area modified by SSPE drop in wet condition to SERS spectra of SSPE drop area in chapter 3 (Figure 3.12C number 3), it was found a

strong displayment of AuNPs from the coverslips surface in the presence of SSPE buffer overnight in wet condition, this is because the protocol of modification in these two chapters was different, after modification by SSPE overnight in the wet condition, the SSPE drop was rinsed with water in this chapter.

In conclusion, the Au NPs clusters and aggregation of the Au NPs were displayed after the Au NPs modified by 1x SSPE, and the decreased LSPR spectra were obtained in wet modification condition compared the no modified Au NPs. While the Au NPs after modified under the wet condition shows good stability whatever from the morphologic characterization and the LSPR measurements compared with the protocol in the dry condition. Therefore, the protocol of annealed AuNPs modified overnight at 4 °C in the wet condition show good particle stability on coverslip and it was used for PBS buffer study.

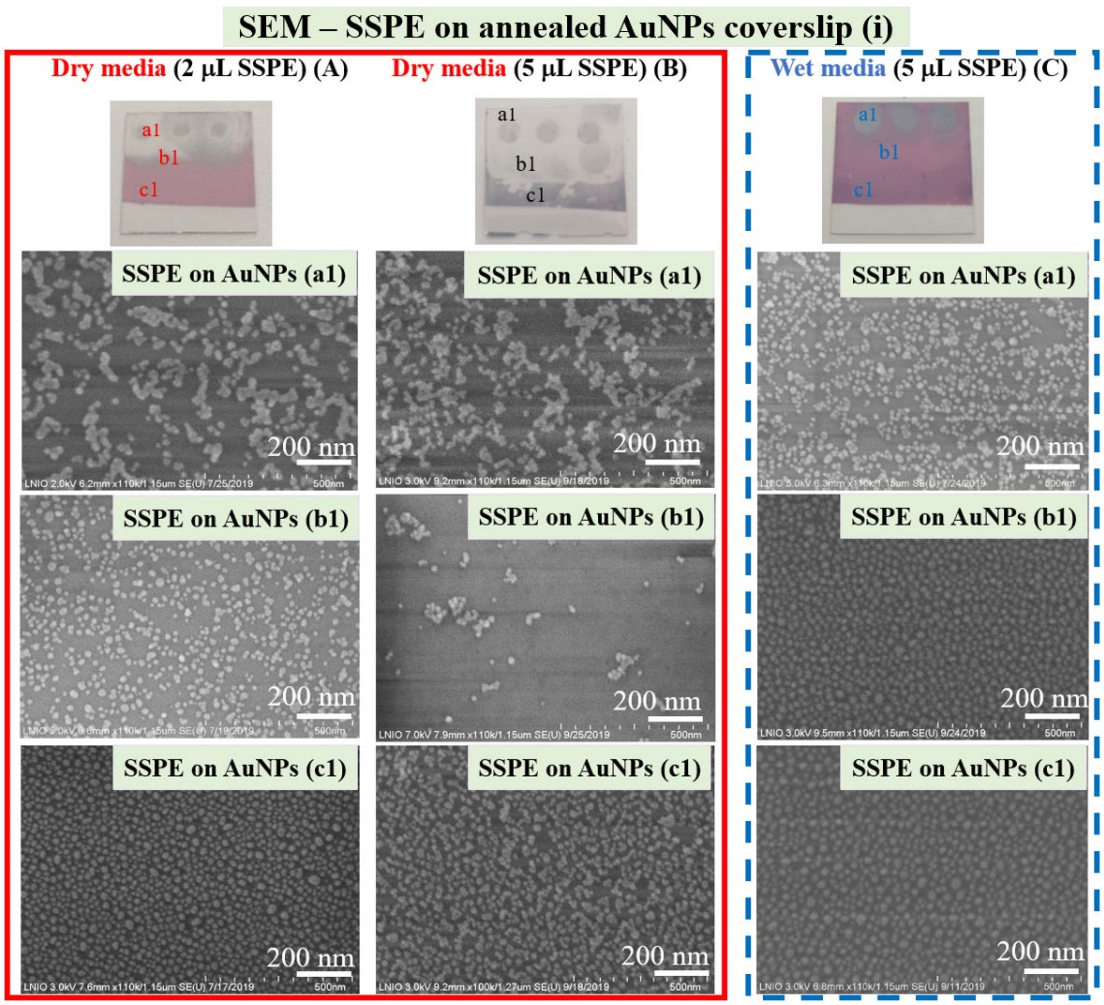
SEM – SSPE on annealed AuNPs coverslip (i)
Dry media (2 µL SSPE) (A)
Dry media (5 µL SSPE) (B)
Wet media (5 µL SSPE) (C)
a1
b1
c1
SSPE on AuNPs (a1)
SSPE on AuNPs (b1)
SSPE on AuNPs (c1)
200 nm

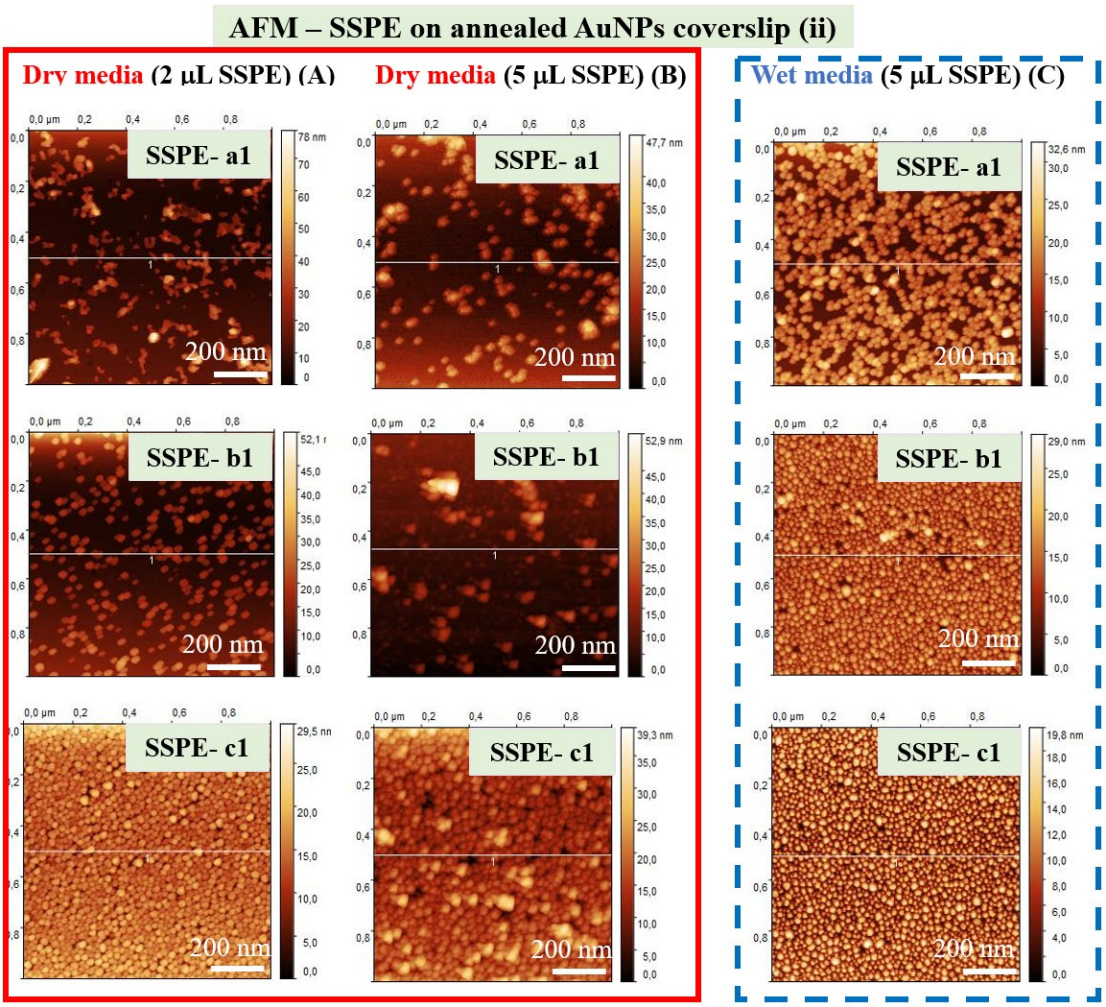

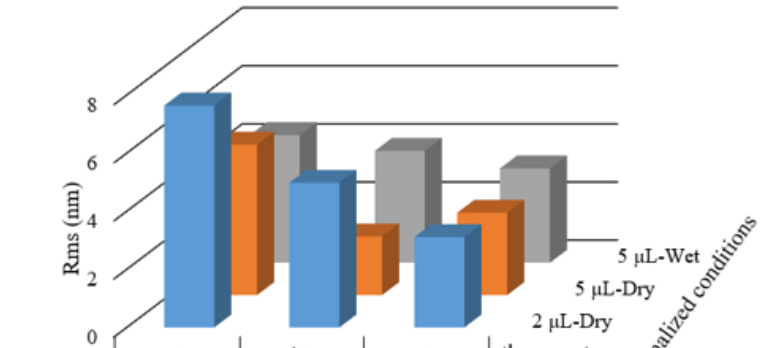

	a1	b1	c1
2 µL-Dry	7.638	4.977	3.110
5 µL-Dry	5.176	2.017	2.832
5 µL-Wet	4.395	3.852	3.246

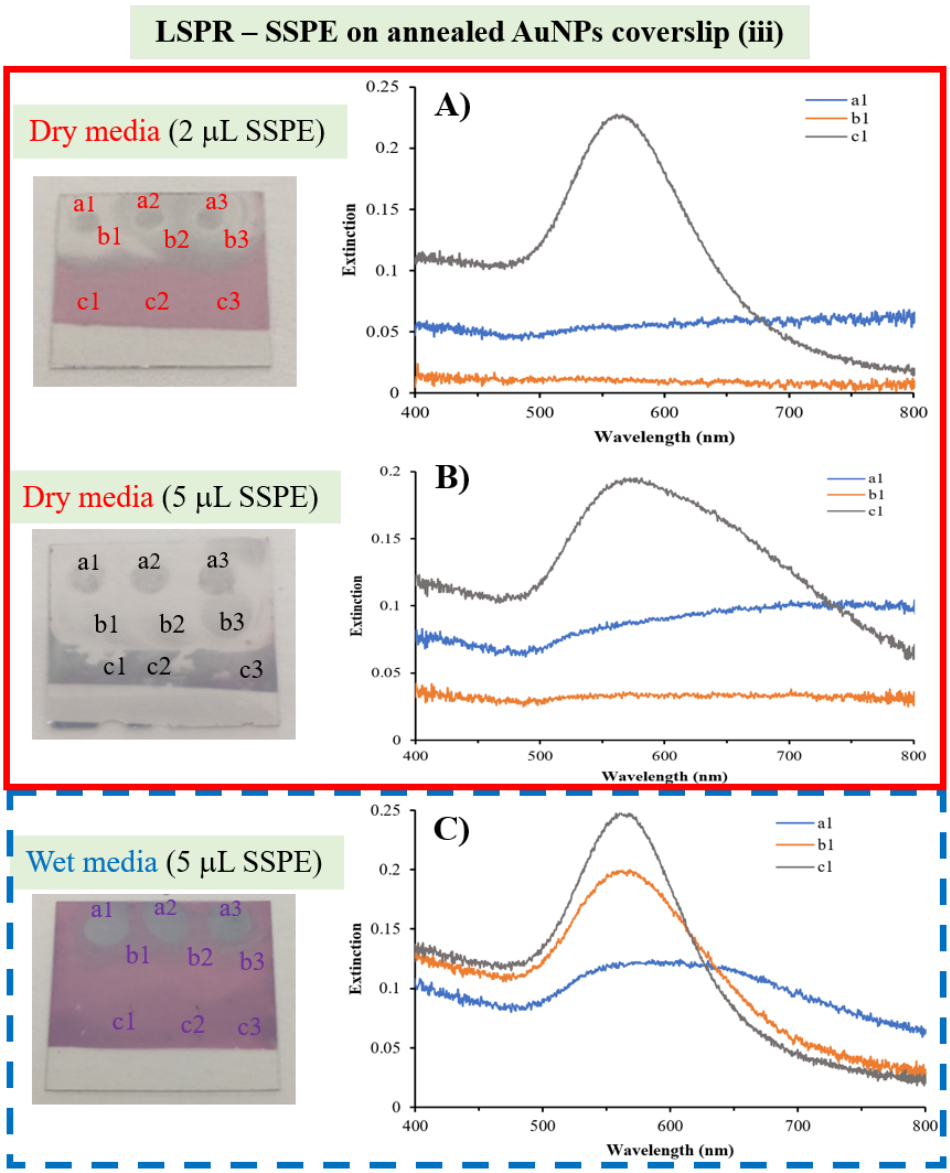

Figure 5. 5 SEM (i), AFM (ii) and LSPR (iii) characterizations of annealed gold nanostructured (Au NPs) coverslips exposed to three drops of SSPE per coverslip with three areas investigated for each deposited/removed drop (a1, under the drop, b1, in the vicinity of the drop, and c1, far from the drop). Two approaches were tested (A) 2 µL SSPE drop and (B) 5 µL SSPE drop on coverslip for an overnight at 4 °C under dry media; (C) 5 µL SSPE drop on coverslip for an overnight at 4 °C under wet media (1× SSPE buffer, pH = 7.4). The SEM, AFM and LSPR measurements were performed under cleanroom conditions at 21 °C.

5.2.2.3 Study of PBS Buffer

In order to investigate more about the stability of the annealed gold nanoparticles in the presence of biological buffer, the Au NPs modified by PBS buffer with 5 μL per drop and overnight at 4 °C in a wet condition was also detected.

As can be seen from **Figure 5.6, i**, the aggregated gold particles were acquired after modifying by PBS buffer for a1 area and the nanoparticles were connected in a chain. This is a similar behavior close to those images obtained in the presence of SSPE buffer (5 μL- dry media). The homogeneous morphology of annealed Au NPs was present in SEM image of c1 area. Specially, in the b1 area, the several sporadic Au NPs were observed, it indicates the strong effect of the PBS buffer over the annealed AuNPs. These observations are also confirmed by AFM imaging (**Figure 5.6, ii**), the a1 area was shown the same Au NPs aggregates, and for the b1 part, the corresponding line profile analysis with R_{rms} roughness values of 6.33 for a1, 1.94 for b1 and 2.91 nm for c1.

Furthermore, the LSPR spectra were collected from annealed AuNPs after the deposition of three PBS drops with three tested areas (a1, b1 and c1) per drop. The obvious resonant peak was found in the LSPR measurements with c1 area, for a1 area and b1 area shown no resonant peaks in the visible light area, see **Figure 5.6, iii**. The same phenomenon was also found in the LSPR detections of the other two modified drops and each area. The experimental drop showed grey colour and no resonant peaks, it could be caused by the aggregated Au NPs after modifying by PBS buffer.

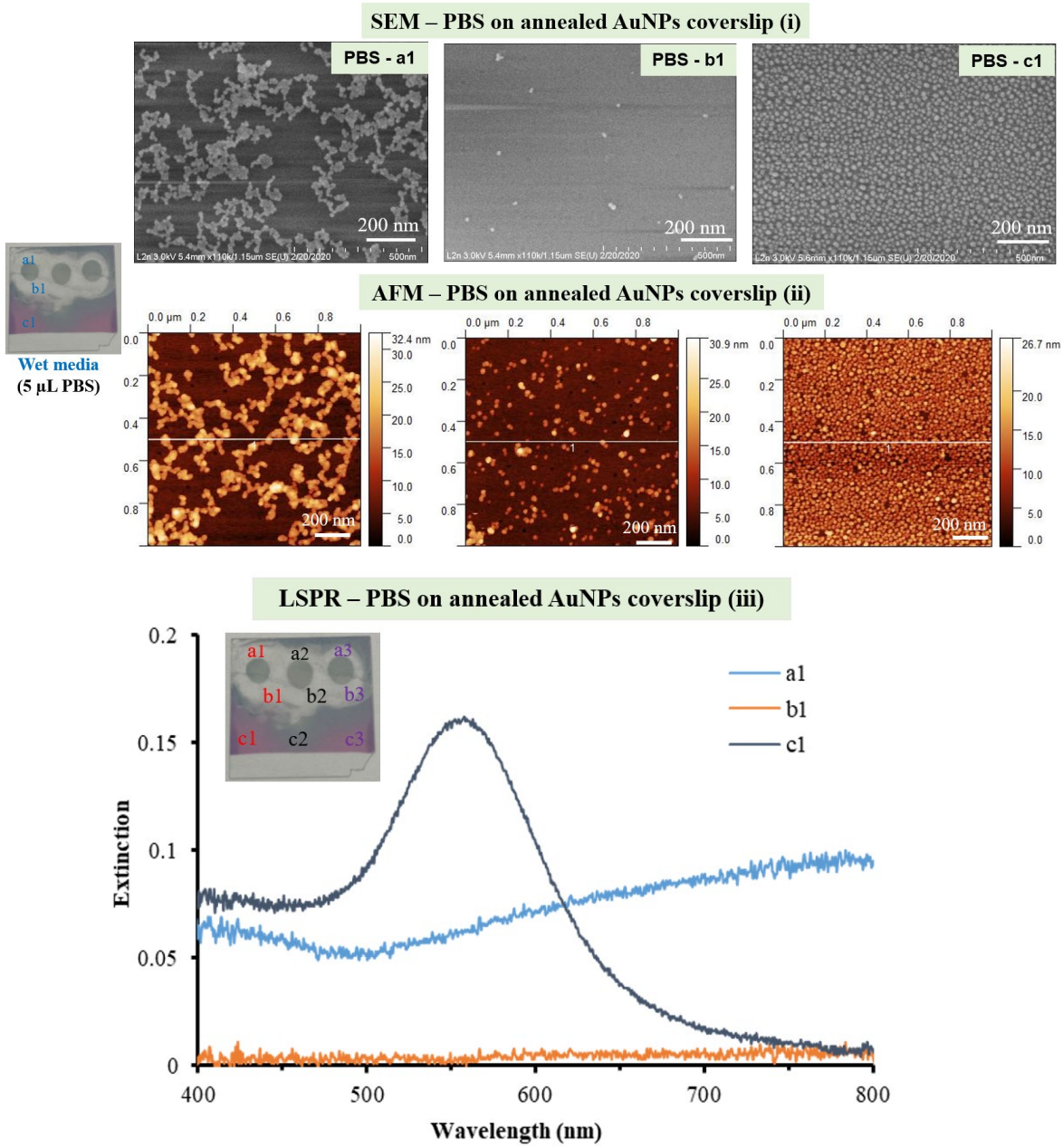

Figure 5. 6 SEM (**i**), AFM (**ii**) and LSPR (**iii**) characterizations of annealed gold nanostructured (Au NPs) coverslips exposed to three drops of PBS (5 µL) per coverslip under wet media with three areas investigated for each deposited/removed drop: a1, under the drop, b1, in the vicinity of the drop, and c1, far from the drop (10 × PBS buffer, pH = 7.4). The SEM, AFM and LSPR measurements were performed under cleanroom conditions at 21 °C.

5.2.2.4 Sensing of Chemical BPE Molecules in Aqueous Solution with SEM, AFM and LSPR Characterization

Based on the previous investigation of stability of annealed AuNPs by using different buffers and water to modifying the AuNPs, the functionalization of AuNPs in the presence of model BPE molecules in aqueous solution was also studied.

As is evident from the SEM images in **Figure 5.7**, most of the Au NPs are spherical in shape and the size distribution of the five modified samples are almost consistent. It is observed that the size distribution of five different concentration of BPE molecules modified samples were mainly distributed in a narrow scale from 4 nm to 16 nm. Especially, the size of nanoparticles distributed in 8 nm of five different concentrations is the highest, 10^{-3} M (30.3%), 10^{-5} M (49.8%), 10^{-7} M (48.3%), 10^{-9} M (50.6%) and 10^{-11} M (46.6%). Furthermore, the size distribution in 8 nm of the naked sample is also the highest at 52.8 %. The order of the distribution in other sizes of AuNPs is 10 nm > 12 nm > 16 nm for the AuNPs modified by BPE concentrations. The size distribution stays similar with no modified AuNPs, 10 nm (29.2 %) >12 nm (8.5 %) > 16 nm (6.0 %).

Basing on the results observed, compared size distribution, it seems no significant differences were found between the naked sample and samples modified by chemical functionalization of different concentration of BPE molecules, and the aggregated Au NPs were also not obtained compared with samples modified by SSPE and PBS. However, from the SEM images, as the concentration increased, the presence of gaps between the nanoparticles obtained, see the red marker (also other no marker part) inside the SEM images in **Figure 5.7**.

In addition, the AFM examination of BPE modified Au NPs was detected, see **Figure 5.8**. The AFM images confirm the homogeneous surface morphology of AuNPs on the coverslips shown with SEM images. Moreover, the R_{rms} of the modified samples changes in a pretty limited range from 3.5 nm to 4.5 nm but higher than the naked AuNPs (R_{rms} = 2.55), more space between nanoparticles was also found as the BPE concentration decreased from AFM images, see the blue marker (also other no marker part) inside the AFM images in **Figure 5.8**.

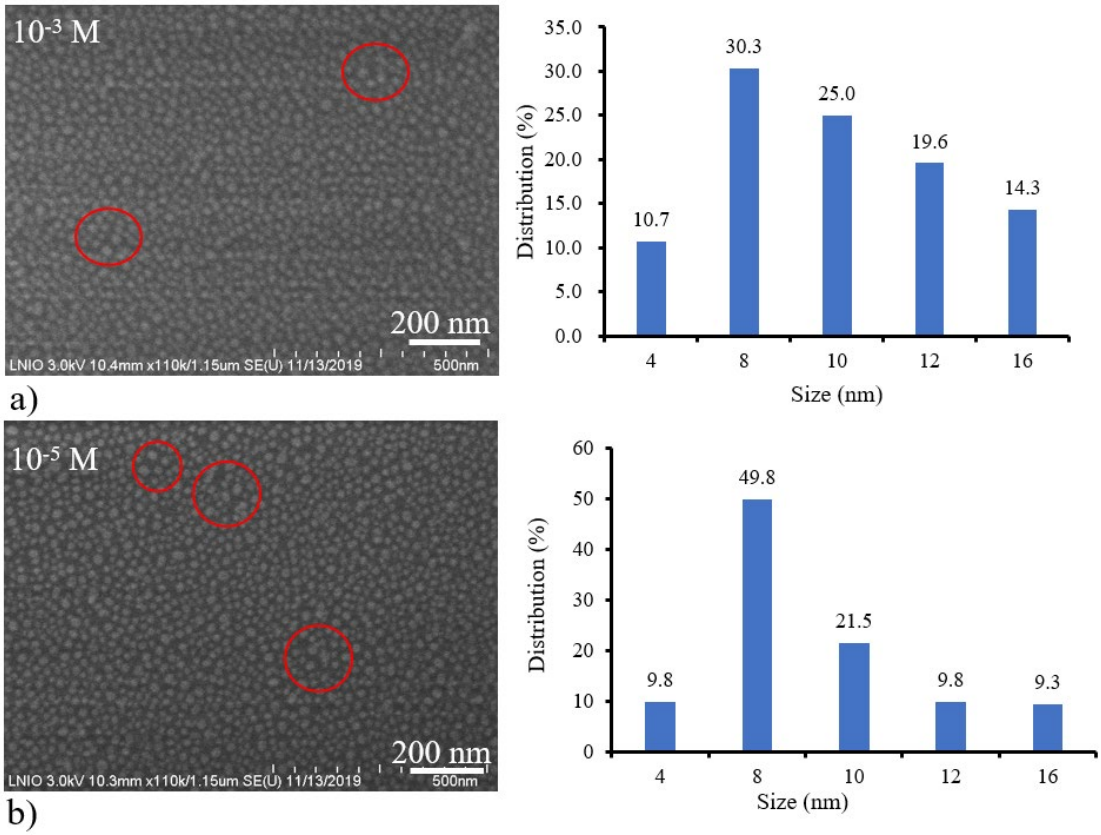

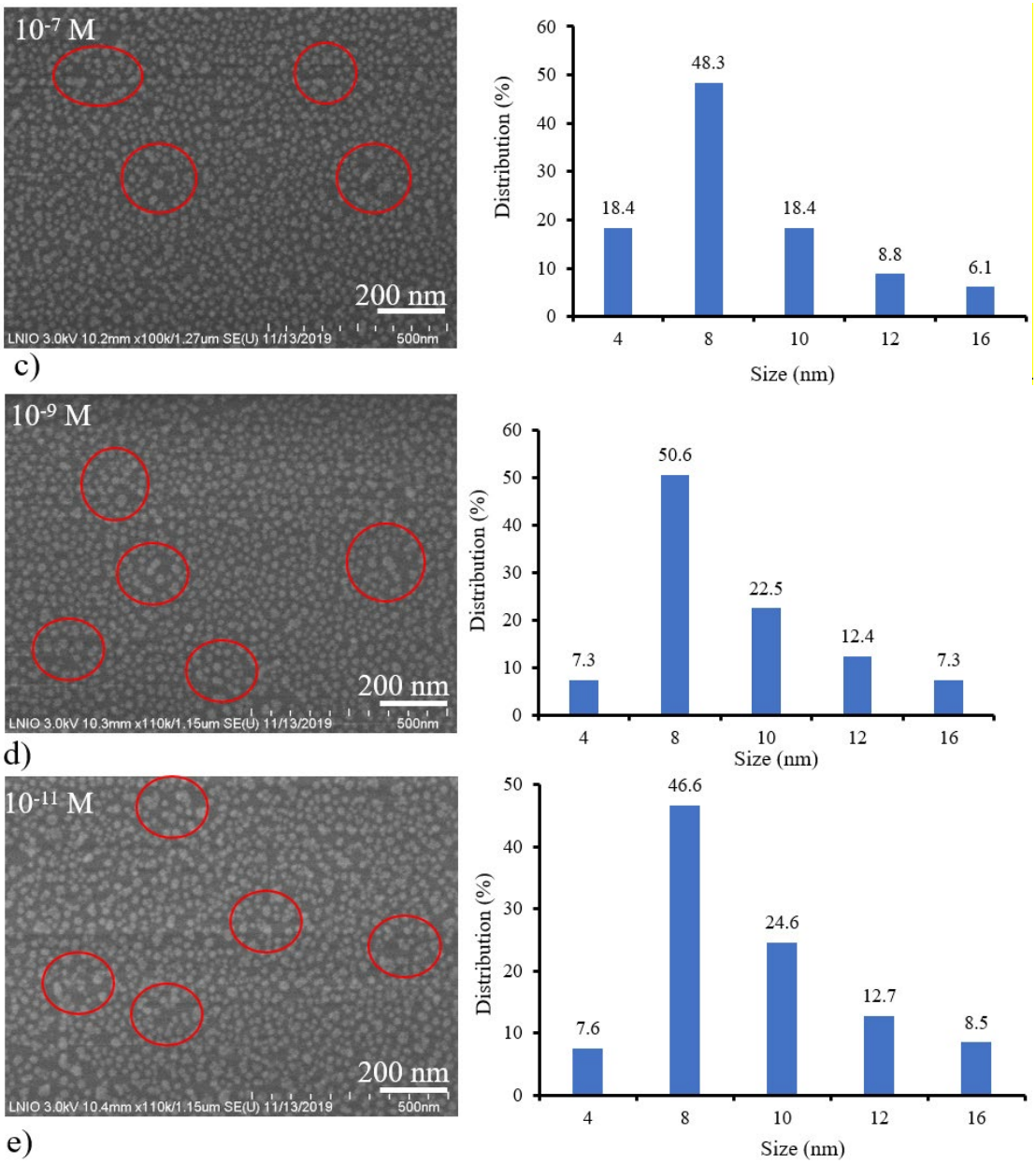

Figure 5. 7 SEM images and the size distributions of annealed gold nanoparticles modified by BPE molecules with 5 different concentrations, respectively. a) 10^{-3} M BPE; b) 10^{-5} M BPE; c) 10^{-7} M BPE; d) 10^{-9} M BPE; e) 10^{-11} M BPE. The SEM measurements were performed under cleanroom conditions at 21 °C.

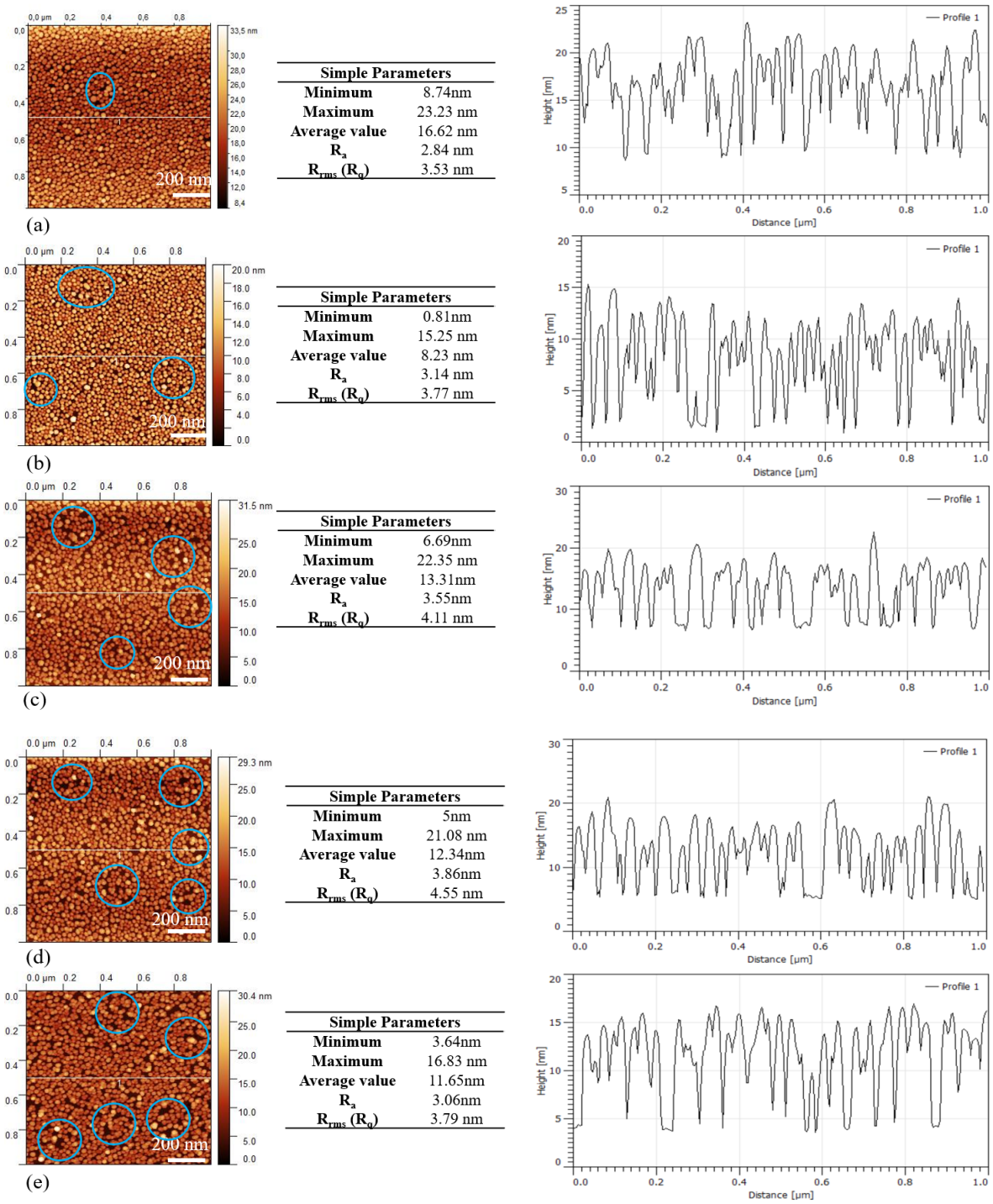

Figure 5. 8 AFM images of annealed AuNPs modified by different concentrations of BPE model molecules, cross-section analysis was based on the profile line analysis. (**a**) 10^{-3} M BPE; (**b**) 10^{-5} M BPE; (**c**) 10^{-7} M BPE; (**d**) 10^{-9} M BPE; (**e**) 10^{-11} M BPE. The AFM measurements were performed under cleanroom conditions at 21 °C.

This morphological characterization results indicate that in the presence of BPE molecules, the size and shape of annealed Au NPs had no further changes but the space between Au NPs changed. It also led to the influence on the Au NPs modified by BPE on LSPR spectra (with the concentration increased the maximum value of the optical density decreased).

Following the research of LSPR spectra of Raman model molecule BPE on the nanostructure, variation of the maximum resonant wavelength length and the maximum OD as a function of the different period of time for different concentrations of BPE buffer modification on the gold nanoparticles surface are reported in **Table 2.** Additionally, very reproducible LSPR spectra were recorded in a relatively large test area (about 1 cm^2).

Table 2. Evolution of LSPR spectra of AuNPs functionalized with different BPE concentrations over five weeks. The LSPR measurements were performed under cleanroom conditions at 21 °C.

[BPE]		Fresh Functionalization	After One Week	After Two Weeks	After Three Weeks	After Four Weeks	After Five Weeks
10^{-3} M	λ_{max} (nm)	548.210	549.904	550.792	553.910	552.660	552.660
	OD_{max}	0.13240	0.16940	0.18220	0.17680	0.16668	0.16760
10^{-5} M	λ_{max} (nm)	548.566	549.814	550.260	553.110	552.660	552.660
	OD_{max}	0.12480	0.16760	0.18100	0.17440	0.17420	0.17540
10^{-7} M	λ_{max} (nm)	550.706	549.636	548.566	553.110	559.780	552.660
	OD_{max}	0.12300	0.14680	0.15720	0.14320	0.13960	0.14600
10^{-9} M	λ_{max} (nm)	551.864	551.062	550.440	553.288	559.780	559.780
	OD_{max}	0.10820	0.13380	0.14560	0.12980	0.14600	0.14680
10^{-11} M	λ_{max} (nm)	551.864	539.290	542.412	548.654	559.870	552.660
	OD_{max}	0.10740	0.13020	0.14540	0.13940	0.12640	0.13140

In terms of the lower limit of detection, 10^{-11} M of BPE is detectable using AuNPs on coverslips. Moreover, the OD_{max} values increased for the AuNPs modified by five BPE concentrations with the time passed until the second week (**Figure 5.9**). After two weeks, the value of OD_{max} was shown decreased trends for each concentration modification but were still higher than those obtained in the day of functionalization (named Fresh). Besides, it can be found that from the preparation day to the third week, the λ_{max} value of the annealed AuNPs modified by modified increased as expected from the concentration of 10^{-11} to 10^{-3} M. After the third and fourth week, the plasmonic properties is strongly degraded.

Considering the λ_{max} value, it should be noted that with the concentration increased, the λ_{max} value decreased (the defference is within 3 nm), the reason is that the plasmon resonance peak were obtained by averaged value, each concentration modified drop was detected 5 times by LSPR, and in the whole surface of AuNPs on the coverslips, it couldn't be verified the same shape and same size, therefore, it leads to the λ_{max} value shown negligible differences.

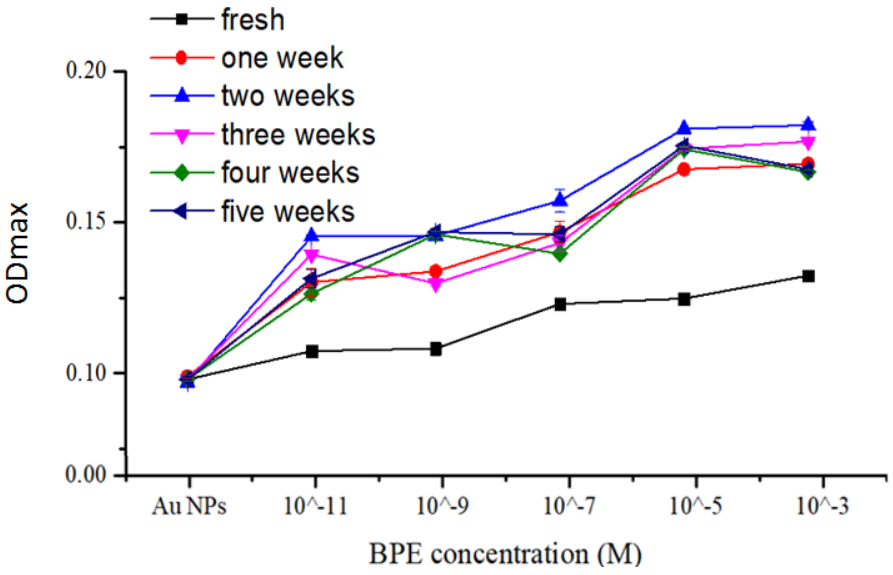

Figure 5. 9 Evolution of maximum optical density (OD_{max}) of annealed AuNPs functionalized with five BPE concentrations over five weeks (fresh-the day of functionalization). The coverslip was evaporated with 4 nm Au and annealed at 550 °C for 3 h.

To conclude, under the LSPR measurements for five weeks, by comparing the two plasmonic parameters (λ_{max}, OD_{max}) of BPE modified annealed AuNPs, it is recommended to conduct a two-weeks LSPR investigation on the stability of BPE functionalized AuNPs on coverslips.

5.4 Conclusions and Perspectives

In this work, a well-fined annealed Au NPs has been successfully prepared on the coverslips, the homogenous gold nanoparticles with a wider plasmonic peak were obtained. As the biological buffers (for instance SSPE and PBS) play an important role in the (bio) functionalization preparation process. SEM/AFM/LSPR studies of AuNPs stability with respect to the functionalization with these biological buffers SSPE and PBS on annealed AuNPs surface are reported. The effect of dd-water and BPE aqueous solutions for sensing on an annealed AuNPs surface is also investigated. There is no effect in the presence of dd-water, and the AuNPs are less affected by saline SSPE and PBS buffers under wet media at 4 °C. By using Raman model molecules BPE, the proposed ultrafine annealed gold nanoparticles exhibited good reproducibility, acceptable stability and low detection limit of 10^{-11} M, furthermore, the stability of LSPR plasmonic resonant peaks of BPE molecules over two weeks was also observed.

Therefore, this study has potential application in biosensor markets to investigate the stability of gold nanoparticles, to develop a rapid and sensitive biosensor.

Conclusion

Over the past decade, many sensing technologies have been developed and a significant number of them are at or very close to commercialization. To enable the detection of different target molecules in biological systems, many cross-cutting techniques are now being applied to the design of metal nanosensors that allow surface chemical modification, bio-functionalization, and modulation of optical properties of metal nanoparticles. With the continuous development of modern science and technology, research on biological and chemical sensing and analysis is very fruitful. These new techniques have not only greatly increased the sensitivity and limits of detection, but have also led to new analytical capabilities that allow scientists to discover molecular information related to diseases or other biological processes. All these results clearly demonstrate and justify the importance of biological nanosensing in modern science and the advancement of knowledge. Therefore, combined the developed metal nanosensors and sensing technologies, this thesis aimed at developing nano-biosensors using annealed nanostructured conductive and non-conductive substrates, to investigate the analytical performances of optical biosensors for diagnostic applications.

At the beginning, the noble metal nanomaterials have been introduced to explain the nanotechnology development of nanostructures, even the assemble and fabrication methods of the gold nanostructures have been introduced and the various properties of the noble metal NPs have been summarized. Afterwards, on the basis of the optical properties of the noble metal NPs, the fundamental of optical biosensor have been

explained, thereby the classification of label-based and label-free detection based on the optical biosensor. Subsequently, the applications of the optical biosensors based on the SMM, LSPR, SERS and QCM have been summarized.

Then, the biosensing detection of the microwave spectroscopy based on the modified AuNPs has been presented in the chapter 2. In this section, the experimental operation on the preparation of the high temperature annealed AuNPs with different thickness of evaporated Au film on the conductive (ITO) and non-conductive (glass) substrates have been conducted. To understanding the process of the SMM technique, the different concentrations of Hsp70 protein biomolecules were used for the biofunctionalized on the AuNPs, then the SMM measurements on the modified solid substrates have been performed step by step. The SMM is proved to be an efficiency and sensitively biosensing detection technique combined the annealed AuNPs.

Next, a *Brett-DNA* genosensor has been developed through LSPR and SERS measurements on the annealed AuNPs modified coverslips. In the chater 3, for the purpose on the developing a more sensitively and stability biosensing platform with AuNPs on the solid substrates, the fabrication protocol of the high temperature annealed AuNPs has been optimized from three parameters aspect (thickness of evaporated Au film, annealing time and annealing temperatures), which can be effect on the size, shape and surface coverage, then influenced on the biosensing detection based on plasmonics. Through the SERS tests of annealed AuNPs on the glass coverslips after modified by the Raman model molecule BPE to certificating the optimized parameters, the LSPR and SERS measurements of the different concentrations of *Brett-DNA* on the

nanostructured coverslips were investigated. The results shown a low limit of detection of SERS measurements of *Brett-DNA*, hence, a sensitively genosensor based on nanostructured ultrafine glass supports is confirmed.

Further, two protocol has been conducted to preparing AuNIs on the QCM crystal quartz to develop a specific biosensor with acoustic detection. In the chapter 4, the Q-TEM grid evaporated 30 nm and 50 nm thickness of gold, respectively, were prepared, and biofunctionalized with gliadin protein biomolecules for the investigation of the acoustic measurements. The results indicate that the AuNIs modified QCM crystal quartz can be a sensitively platform for the acoustic biosensing detection.

At last, on the basis of these three different gold nanostructures production on the solid substrates and the three biosensing detection, in the chapter 5, the influence of buffers on stability of the annealed AuNPs has been investigated. The SSPE and PBS buffers were prepared for the modification on the annealed AuNPs on the solid substrates, followed by the changes of the modified AuNPs in different work conditions were monitored with SEM, AFM and LSPR measurements. The results shown that the AuNPs are less affected by SSPE and PBS buffers under wet work condition. And It's helpful to understand the changes of the nanostructures which modified by biomolecules in the biosensing process.

Even though manufacturing the gold nanostructures on the solid substrates, whatever the ITO strips, glass coverslips and QCM crystal quartz have been proved a controlled and easier fabrication, in the same time the SMM, LSPR, SERS and acoustic technologies have been confirmed to be the interesting, potential and

prospect biosensing detection methods, on the basis of the existing nanosensing research results, there are still challenges and many directions for further research. In noble metal-based biosensors, future challenges could extend the range of different biomolecules that can be sensed or detected by increasing sensitivity and providing faster and more versatile detection methods. A further challenge for progress in this area is to extend the application of these sensors to real samples in the clinic, providing more opportunities for these nanobiosensors to move from the laboratory to actual clinical applications. Additionally, the development of renewable, convenient, and low-cost biosensors is challenging. One of the most important challenges is related to the structure, stability, and sensitivity of biomolecules. Developing templates for studying novel biomolecules or for integrating multiple functional biological elements into a single platform through inter-biomolecular linkages is also an important part of the research. Furthermore, the development of novel nanomaterials or complexes between different materials to improve or enhance the detection environment and level of biosensing, and therefore sensor material substrates, is also necessary.

Chapter 6 French summary

6.1 Introduction

Actuellement, les progrès technologiques réalisés dans le domaine des nanotechnologies ont contribué de manière significative à l'expansion du marché des biocapteurs et il existe un grand intérêt pour le développement de biocapteurs sensibles et sélectifs. Ces nouvelles recherches peuvent avoir un fort impact sur la vie quotidienne, en favorisant le diagnostic médical ou la sécurité alimentaire. Un biocapteur est défini comme un dispositif qui utilise des réactions biochimiques spécifiques pour détecter des composés chimiques ou des agents pathogènes. Les biocapteurs peuvent être classés i) suivant la nature de la transduction utilisée: optique (résonance plasmonique de surface (LSPR), réfractométrie, fluorimétrie, interférométrie), électrochimique (ampérométrie, potentiométrie, conductimétrie, impédancemétrie) et physique (calorimétrique, électronique, piézoélectrique, magnétique); ii) sur la base des différentes matières bioactives des biocapteurs : immunocapteurs, génocapteurs, capteurs enzymatiques, capteurs microbiens, capteurs tissulaires et cellulaires, etc. ; iii) en fonction des différentes méthodes d'interaction entre l'élément d'identification (la sonde) et l'analyte (la cible) : biocapteur catalytique et biocapteur d'affinité. Dans le cadre de cette thèse, les surfaces actives ont toutes été développées en biofonctionnalisant des nanostructures conductrices obtenues par recuit d’un film évaporé sur substrat de verre ou sur monocristal de quartz, procédé bas coût et reproductible. Deux méthodes de détection ont été utilisées : variation de fréquence liée à une modification de masse (acoustique), modification des propriétés de réflexion ou

de transmission dans le domaine de l'optique et des micro-ondes appliquées soit à des immunocapteurs, soit à des génocapteurs. Enfin, la biodétection s'est faite sans recours à des marqueurs, méthode plus simple, plus rapide et à coût globalement plus faible.

La première étude a porté sur la détection d'une protéine en réalisant un immunocapteur. L'interaction entre la cible et la sonde est obtenue par le suivi de la variation des propriétés de réflexion dans la gamme des micro-ondes en utilisant un microscope AFM modifié.

La seconde a concerné le développement d'un génocapteur pour détecter des levures du vin en utilisant une mesure optique basée sur la génération des plasmons de surface localisés ou sur la Spectroscopie Raman Exaltée de Surface.

La troisième s'est intéressée à la biodétection des mêmes levures que celles détectées dans la seconde étude à l'aide d'un génocapteur et de la gliadine en développant un immunocapteur et en suivant dans les deux cas la réaction d'affinité par la mesure du changement de fréquence de résonance d'un cristal de quartz (détection acoustique).

6.2 Détection par spectroscopie micro-ondes de la protéine Hsp70 humaine

Des nanoparticules (AuNP) ont été synthétisées, à partir du recuit thermique d'un film d'or évaporé sur des substrats conducteurs en oxyde d'indium-étain (ITO) et en verre. Ce recuit a été réalisé dans un four à 550°C, pendant 8 heures. Ces surfaces actives sont utilisées pour détecter la protéine humaine (Hsp70), biomarqueur du stress

en utilisant comme méthode de détection la spectroscopie diélectrique dans le domaine des micro-ondes.

La première partie de l'étude s'est intéressée à l'influence du substrat sur la morphologie des nanoparticules. La figure 6.1 représente la morphologie et la distribution en taille des AuNP obtenues après recuit d'un film d'or d'épaisseur 4 nm. On observe sur les figures A et B un dépôt homogène d'or et d'apparence similaire. Les figures C et D confirment la formation de nanoparticules dont la distribution en taille est donnée figures E et F. On constate que la taille des nanoparticules est plus élevée sur substrat conducteur d'ITO.

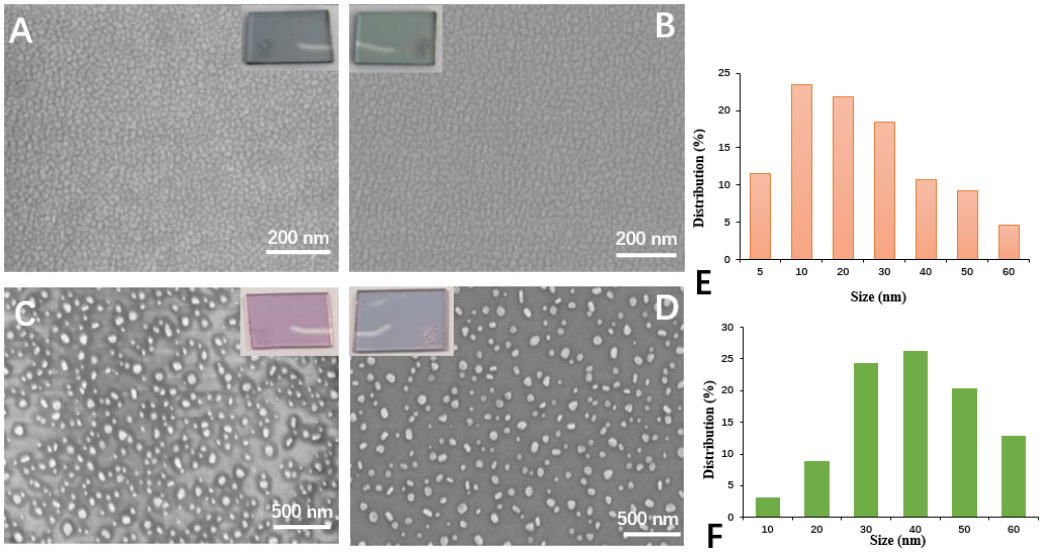

Figure 6. 1 Images MEB de films d'or (4nm) tels qu'évaporés (A) sur substrat de verre ; (B) sur substrat ITO et après recuit à 550 °C, pendant 8h (C) sur substrat de verre (D) sur substrat ITO ; distribution de taille des AuNP recuits sur substrat de verre (E) et substrat ITO (F). Insérées dans les images MEB, des photographies de substrats.

La suite de l'étude s'est focalisée sur les substrats en verre (notés SiO_2) et a consisté à étudier étape par étape (cf. **Figure 6.2)** à l'aide de la spectroscopie micro-

ondes la modification des propriétés réflexives de la surface du substrat : 1) SiO_2 seul ; 2) SiO_2 plus AuNPs ; 3) SiO_2 plus AuNPs plus thiol ; 4) SiO_2 plus AuNPs plus thiol et trois concentrations différentes de protéines (12, 25 et 50 ng/µL/cm^2).

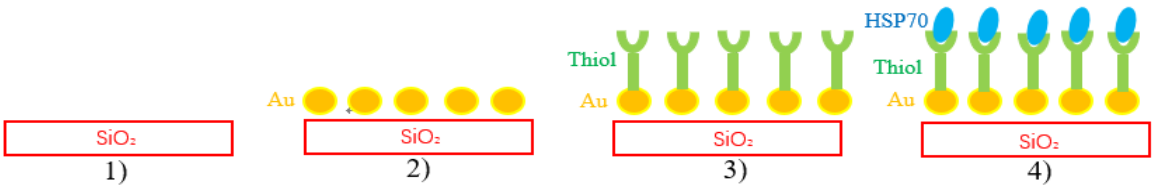

Figure 6. 2 Différentes surfaces analysées par spectroscopie micro-onde.

L'influence de la fréquence sur la mesure est étudiée en réalisant un balayage entre 1 et 10 GHz avec 64001 points d'acquisition. Les signaux d'amplitude en fonction de la fréquence (**Figure 6.3)** pour chaque étape de modification de la surface (**Figure 6.2)** ont été comparés dans le cas de substrats recouverts au départ avec trois épaisseurs de film d'or différentes (2 nm, 4 nm et 8 nm, respectivement) et pour différentes concentrations de protéines HSP70 (12, 25 et 50 ng/µL/cm^2).

On constate **Figure 6.3A, Figure 6.3B et Figure 6.3C**, correspondant respectivement à des films déposés de 2nm, 4nm et 8nm, une évolution monotone de l'atténuation au fur et à mesure de la progression du procédé décrit figure 6.2 pour la fréquence de 4.33 GHz.

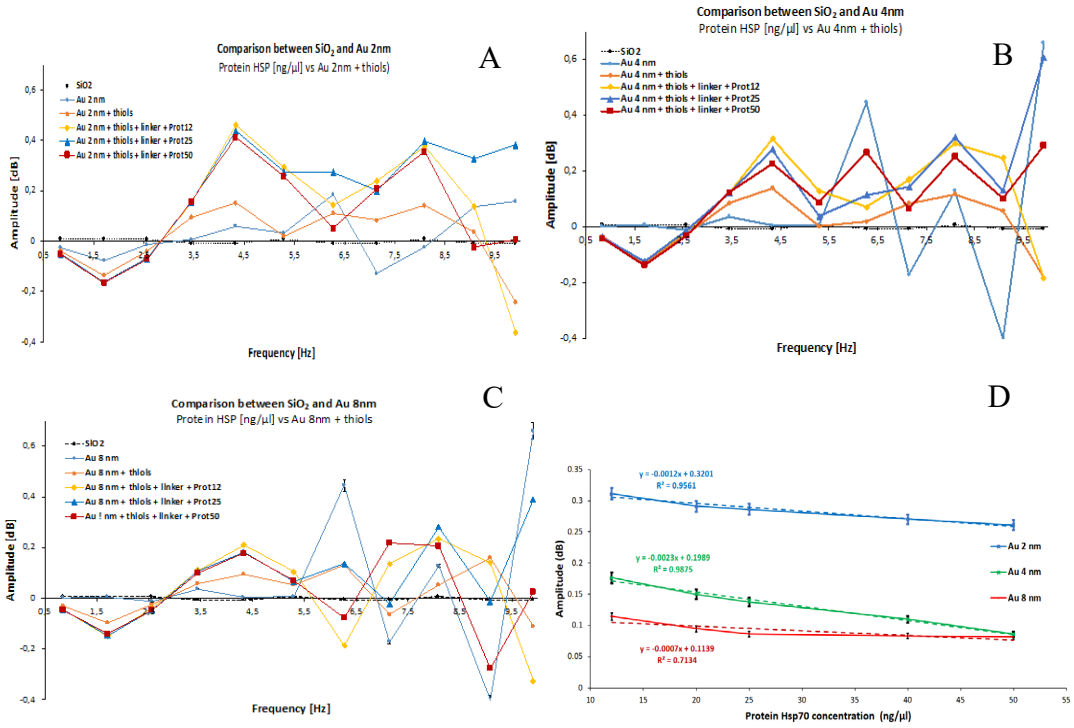

Figure 6. 3 Caractérisation spectrale de matériaux ayant une épaisseur de film d'or de A) 2 nm, B) 4 nm et C) 8 nm pour différentes concentrations de protéines Hsp70 (12, 25 et 50 ng/µL/cm^2) ; D) Courbes d'étalonnage du Hsp70 déposé sur des nanostructures d'or (2nm, 4nm et 8 nm, respectivement) à 4,33 GHz.

Cinq concentrations de HSP70 ont été testées à cette fréquence (**Figure 6.3D)**. Cette figure montre que l'amplitude du signal diminue à mesure que la taille des nanoparticules augmente, sauf pour la concentration la plus élevée de50 ng/µL/cm^2 pour des films d'or déposés de 4 nm et de 8 nm. Une évolution linéaire de l'amplitude en fonction des cinq concentrations de protéines a été observée avec des substrats sur lesquels 2 nm (R^2=0,96) et 4 nm (R^2=0,99) d'or ont été déposés. La valeur de pente est égale à -23,10^{-4} pour 4 nm d'or déposé contre -13,14^{-4} pour 2 nm. Ceci indique que la sensibilité du dispositif est meilleure pour 4 nm.

Pour un substrat sur lequel 8nm d'or ont été évaporés, on constate une saturation

de la réponse pour des concentrations de protéines supérieures à 25 ng/µL/cm^2.

6.3 Détection SERS de la levure Brettanomyces bruxellensis utilisant des surfaces conductrices nanostructurées sur substrats de verre

6.3.1 Première étape: préparation et optimisation des plates-formes SERS basées sur des nanostructures d'or recuites sur un substrat de verre

Étant donné que les paramètres du processus de fabrication jouent un rôle important sur la morphologie des nanoparticules et par conséquent sur les propriétés des SERS, nous avons étudié l'influence de trois paramètres (l'épaisseur du film d'or évaporé, la température de recuit et le temps de recuit) sur les nanostructures réalisées sur les lamelles de verre. La **Figure 6.4** montre les images MEB d'échantillons de lamelles de verre recouvertes de couches minces d'or (2 nm, 4 nm, 6 nm et 8 nm) ayant subi 3 heures de recuit, à trois températures différentes (350 °C, 450 °C et 550 °C).

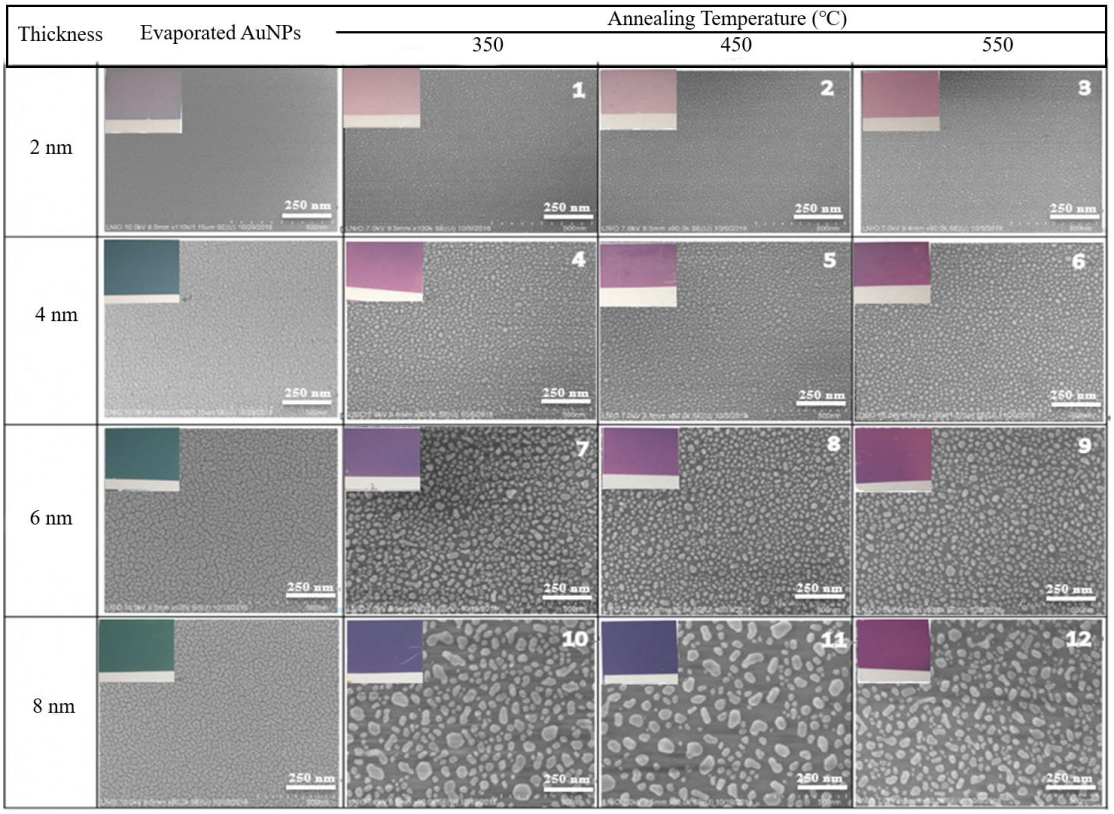

Figure 6. 4 Images MEB de lamelles de verre carrées recouvertes de couches minces d'or (2 nm, 4 nm, 6 nm et 8 nm) après 3 heures de recuit, à trois températures différentes (350 °C, 450 °C et 550 °C).

On constate que pour les lamelles recouvertes d'or de 4 nm recuit à 550 °C pendant 3 heures, les tailles de nanoparticules vont de 10 nm (37,9 %) à 15 nm (38,8 %). Pour ces mêmes substrats, on observe la plus grande couverture par les nanoparticules de la surface (60,41 %) et les distances inter-particulaires les plus faibles par rapport aux autres épaisseurs d'or testées (2 nm, 6 nm et 8 nm, respectivement). La diminution du temps de recuit du film pour une épaisseur de 4 nm conduit à un taux de couverture plus faible (56,51% pour 1h contre 60,41% pour 3h). Cette étude a permis de choisir les paramètres les mieux adaptés pour la préparation des surfaces actives (évaporation d'un film d'or de 4nm, recuit 3 h à 550°C). Il a été également vérifié que ce substrat ne

présentait pas de pics SERS parasites susceptibles de compliquer l'interprétation des spectres en présence de biomolécules.

L'efficacité de détection des surfaces actives est étudiée en utilisant une molécule modèle (BPE) qui présente l'avantage de donner des spectres SERS facilement identifiables et exploitables. Cinq solutions de concentrations différentes (10^{-3}, 10^{-5}, 10^{-7}, 10^{-9} et 10^{-12} M, respectivement) ont été préparées à partir d'une solution mère concentrée à 97 % dans l'eau pour être ensuite testées (**Figure 6.5**).

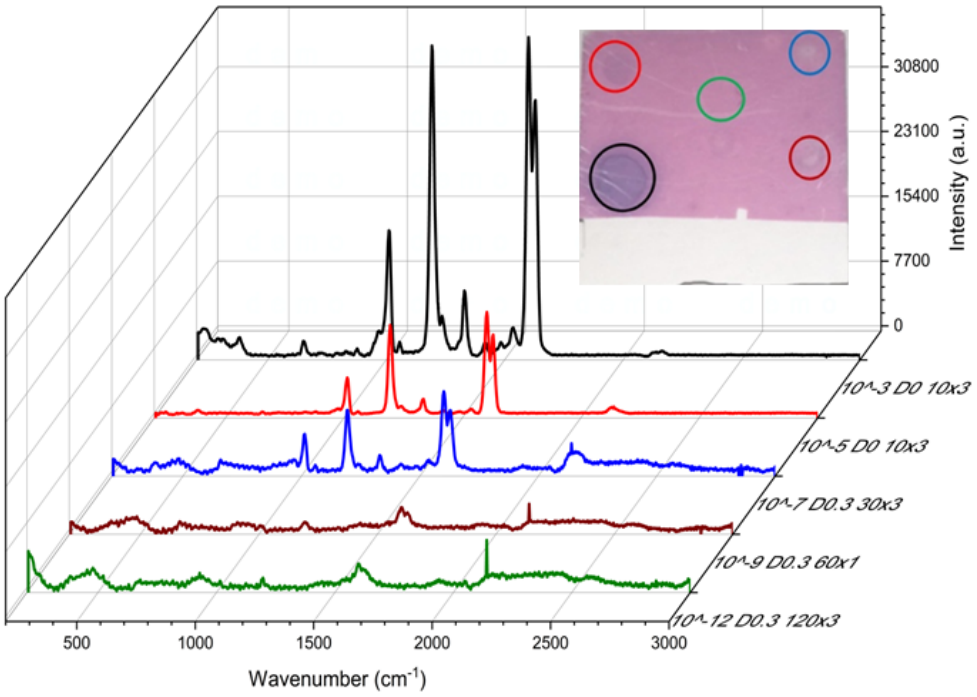

Figure 6. 5 Spectres SERS de molécules de BPE de différentes concentrations (10^{-3}, 10^{-5}, 10^{-7}, 10^{-9} et 10^{-12} M) à l'aide de lamelles de verre sur laquelle 4nm d'or ont été évaporés puis recuits à 550 °C pendant 3 h sur une plaque chauffante. Photographie insérée dans le graphe montant la surface de la lamelle après le dépôt de cinq gouttes de concentrations différentes de BPE.

La **Figure 6.6** présente les spectres SERS obtenus sur les surfaces actives

développées dans le cadre de ces travaux. Comme cela a été rapporté, les pics principaux à 1601 et 1630 cm^{-1} correspondent au mode d'étirement C-N dans la vibration du cycle pyridyle et du groupe vinyle du BPE respectivement, tandis que les pics à 1193 et 1235 cm^{-1} se réfèrent au mode de respiration du cycle pyridine et au mouvement vibratoire de l'atome d'azote dans le pyridyle.

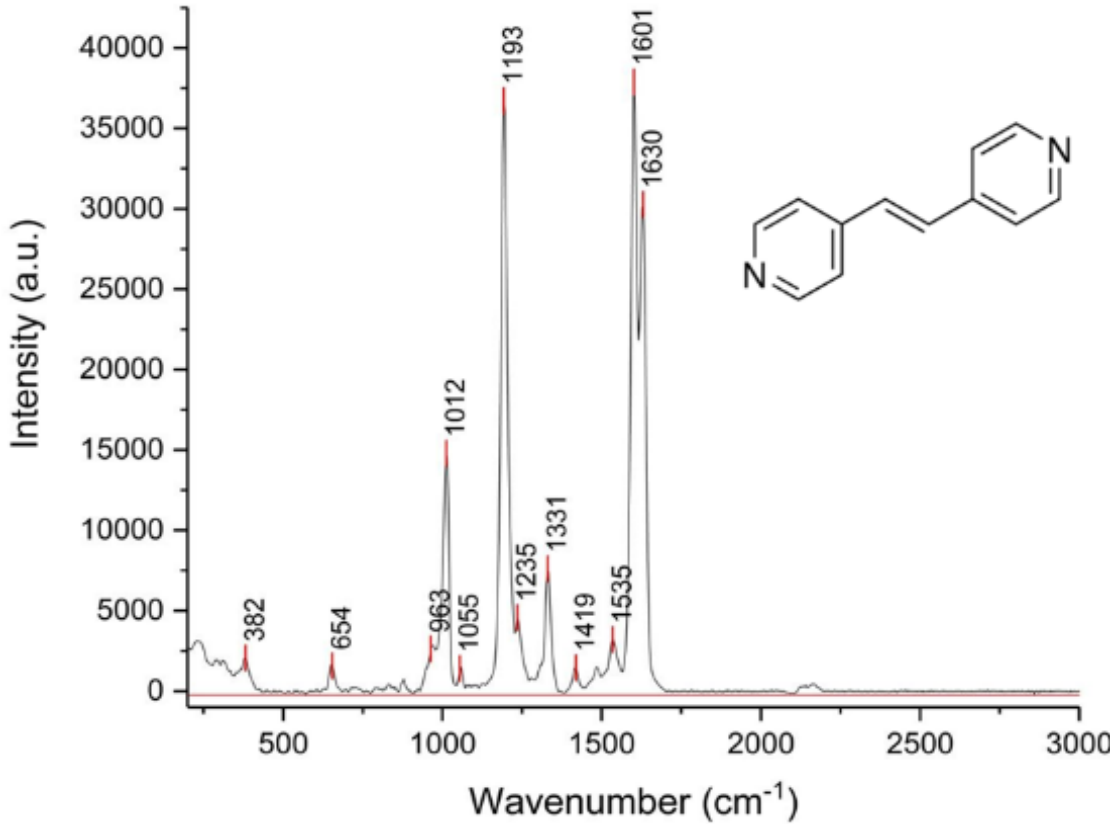

Figure 6. 6 Spectre SERS d'une molécule de BPE (1 mM) sur une lamelle d'or nanostructurée (4 nm Au, 550 °C pendant 3 h sur une plaque chauffante) pour 3 acquisitions de 10 secondes et en utilisant un filtre D0.

6.3.2 Deuxième étape : Mesures SERS sur la levure Brettanomyces bruxellensis

Les surfaces actives précédemment validées par l'étude avec la molécule BPE vont être utilisées pour la détection de la levure Brettanomyces bruxellensis.

Afin de créer un environnement favorable à la fixation de la sonde sur les

nanoparticules et à son hybridation ultérieure avec le brin complémentaire d'ADN de Brett qui constitue la cible, différents tampons aqueux ont été testés (**Figure 6.7**) : solution saline tampon de phosphate (PBS), SSPE (chlorure de sodium 3 M, phosphate de sodium dibasique 0,23 M, acide éthylènediaminetétraacétique 25 mM, pH 7,4), tampon TE et tampon de polyéthylèneglycol (PEG). Le protocole consiste en un dépôt d'une goutte de tampon d'un volume de 2 µL, sur la surface active. Après l'analyse SERS, le SSPE a été choisi pour réaliser la biofonctionnalisation.

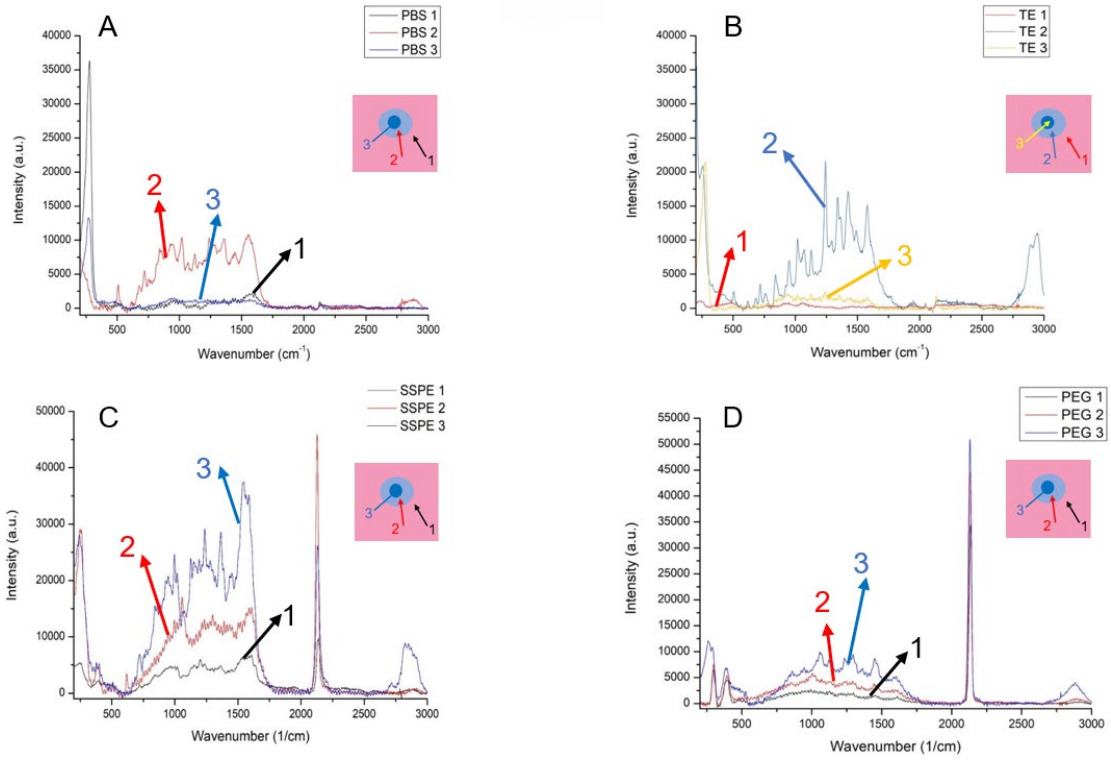

Figure 6. 7 Spectres SERS de 2 µL de gouttes de tampon PBS (A), de tampon TE (B), de 1 x SSPE (C), de tampon PEG (D) sur la surface active. Le temps d'acquisition était de 10 sec x 3 fois avec le filtre D0.3.

En outre, le spectre SERS de la sonde Brett-Thiol (100 pmol/µL) dans l'eau et le tampon aqueux 1xSSPE ont également été comparés dans ce travail. Dans le cas de

l'eau comme tampon, l'augmentation la plus significative de l'intensité SERS (6500 u.a.) a été obtenue à 1604,87 cm^{-1} alors que pour le 1xSSPE, un pic très intense (25000 u.a.) a été obtenu à presque le même nombre d'onde (1600,07 cm^{-1}).

Pour évaluer la spécificité de la sonde Brett-Thiol, différentes souches de levure que l'on peut trouver dans les caves ou les vignobles ont été testées. Les levures choisies appartiennent à l'ordre des Saccharomycétales qui comprend 4 genres (*Pichiacées, Débaryomycètes, Saccharomycodacées* et *Saccharomycètes*). Chaque genre contient des microorganismes spécifiques qui ont été partiellement ou totalement étudiés avec la technique SERS.

Dans le cas de *Brettanomyces bruxellensis* (*genre Pichiaceae*), 3 espèces ont été étudiées par spectroscopie : *Candida ethanolica, Dekkera bruxelensis DKA* et *Dekkera bruxelensis DSMZ*. Expérimentalement, les spectres SERS de *Brettanomyces bruxellensis DKA* et de *Brettanomyces bruxellensis DSMZ* 70726 présentent de fortes modifications à 1250 et 1450 cm^{-1}. En outre, les spectres SERS du *genre Saccharomycodaceae* et des *Debaryomycetaceae* (*Millerozyma farinosa*) et *Saccharomycodaceae* (*Hansenula uvarum*) sont également enregistrés et mettent en évidence les pics les plus pertinents à 1250-1500 cm^{-1} (**Figure 6.8**). Par conséquent, les levures de la classe des Saccharomycètes présentent des modifications majeures des spectres SERS soit à 1205-1500 cm^{-1} ou/ et 1550-1800 cm^{-1}.

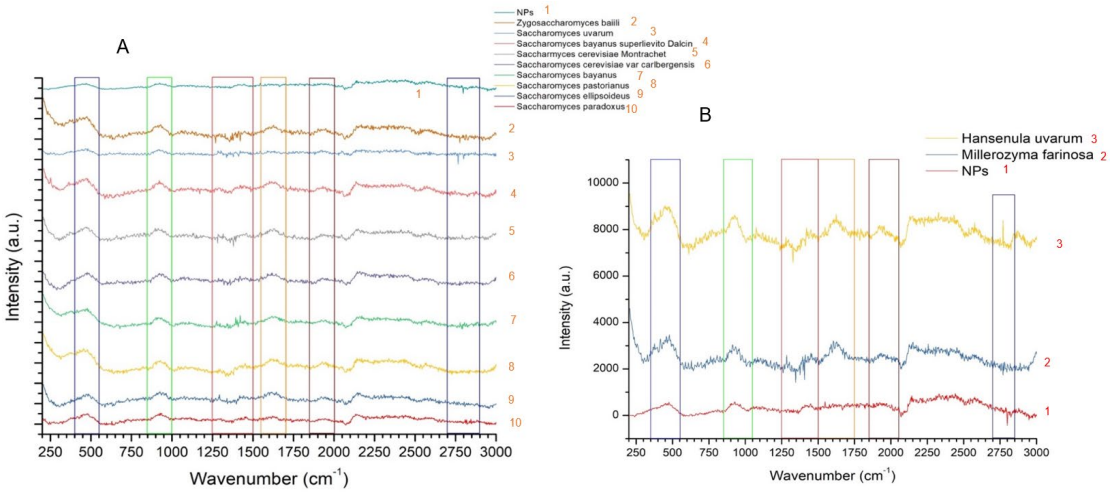

Figure 6. 8 Spectres SERS de différents microorganismes de *Saccharomycetales* (A), et *Debaryomycetaceae* (*Millerozyma farinosa*) et *Saccharomycodaceae* (*Hansenula uvarum*) (B), en utilisant un temps d'acquisition de 10 sec x 3 fois avec le filtre D0.

Sur la base de l'étude des spectres SERS ci-dessus, l'ADN de Brett (tests spécifiques) et les souches d'ADN de quatorze levures présentes dans le vin (tests non spécifiques) ont été choisis. Cinq concentrations d'ADN de Brett complémentaire et de séquence non complémentaire : 1 pg/µL, 10 pg/µL, 100 pg/µL, 1 ng/µL et 10 ng/µL, et les spectres SERS des Brett-génosenseurs spécifiques et non spécifiques ont été mesurés **(Figure 6.9)**. À partir des spectres SERS obtenus, les valeurs d'intensité de pics plus représentatifs à 1294 cm^{-1} dans le cas de tests spécifiques ont été utilisées pour tracer l'étalonnage, et il a été constaté que la limite de détection est par conséquent estimée à 0,1 ng/µL et que la gamme dynamique du génocapteur s'étend de la valeur de la limite de détection à la concentration la plus élevée (10 ng/µL) testée dans cette expérience.

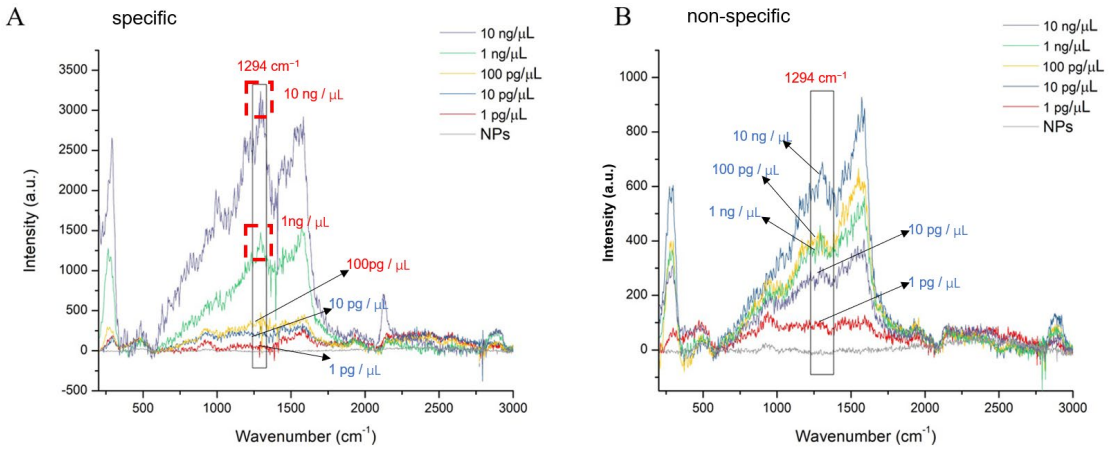

Figure 6. 9 Spectres SERS de (A) capteurs de Brett spécifiques et (B) non spécifiques. Le temps d'acquisition a été fixé à 10 s x 3 fois en utilisant un filtre D 0,3.

Enfin, à l'exception du spectre SERS du génocapteur ADN de Brett, les investigations complémentaires des biocapteurs sélectifs de levure proposés ont également été détectées par résonance plasmonique de surface (LSPR) localisée (**Figure 6.10)**. Les données spectroscopiques ont été recueillies pour évaluer la (bio)fonctionnalisation spécifique et non spécifique de l'ADN de Brett. Il a été constaté que dans le cas de l'ADN de Brett spécifique (**Figure 6.10A**) et de l'ADN réel des biocapteurs d'ADN de Brettanomyces bruxellensis (**Figure 6.10C**), l'évolution de la LSPR est logique avec l'augmentation des concentrations d'ADN cible, tandis que des augmentations aléatoires des pics LSPR sont enregistrées pour les biocapteurs d'ADN de levure non spécifique (contrôle) (**Figure 6.10B**).

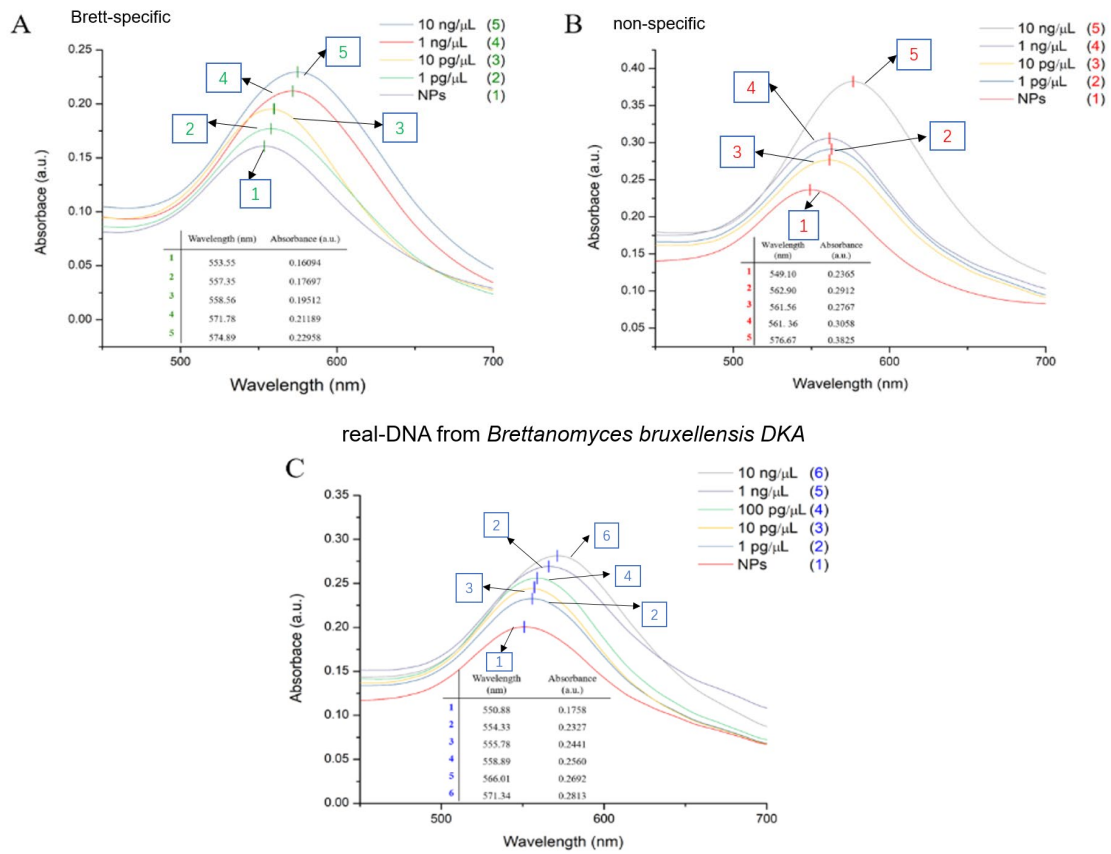

Figure 6. 10 Spectres LSPR des génosenseurs basés sur l'ADN de Brett spécifique (A), non spécifique (B) et réel de *Brettanomyces bruxellensis DKA* (C). Les encadrés montrent les valeurs de l'absorbance maximale et la position du pic de longueur d'onde des nanoparticules d'or nues et modifiées avec différentes concentrations d'ADN sur les lamelles.

6.4 Détection acoustique de la gliadine à l'aide d'une microbalance à cristal de quartz

Dans cette étude, deux configurations ont été étudiées : une (Q TEM grid) pour laquelle 30 nm d'or ont été évaporés à travers des grilles TEM à trois secteurs et une (QCM color) pour laquelle des nano-îlots d'or ont été formés par recuit de couches minces d'or évaporé à différentes épaisseurs (2 nm, 4 nm et 6 nm, respectivement)

(**Figure 6.11)**. L'imagerie MEB a été utilisée pour caractériser les surfaces modifiées par le dépôt (Q TEM grid) et les recuits des couches minces (QCM color). La taille des nano-ilots a été analysée ainsi que le taux de couverture de la surface.

Figure 6. 11 Cristal de type « Q TEM Grid »(A) ; cristal de type « QCM color » à quatre secteurs, trois pour lesquels de l'or a été évaporé à différentes épaisseurs (2 nm, 4 nm et 6 nm) et un pour lequel l'électrode n'a pas été modifiée (0 nm)(B).

Des anticorps anti-gliadine ont été déposés sur les deux types de surfaces actives présentés précédemment et sur un cristal commercial non modifié (S-QCM), avec la biofonctionnalisation la plus adaptée.

Les **Figures 6.12A**, **6.12B** et **6.12C** illustrent les sensorgrammes obtenus sur des cristaux de type «S-QCM » et de type « Q TEM grid » réalisés avec deux épaisseurs d'or (30 nm et 50 nm)

Ces surfaces actives sont équipées de sonde anti-gliadine et mise en contact avec des gouttes de gliadine (10 µL), pour des concentrations allant de 10^{-4} mg/L (0,0001 ppm) à 1 mg/L (1 ppm).

A

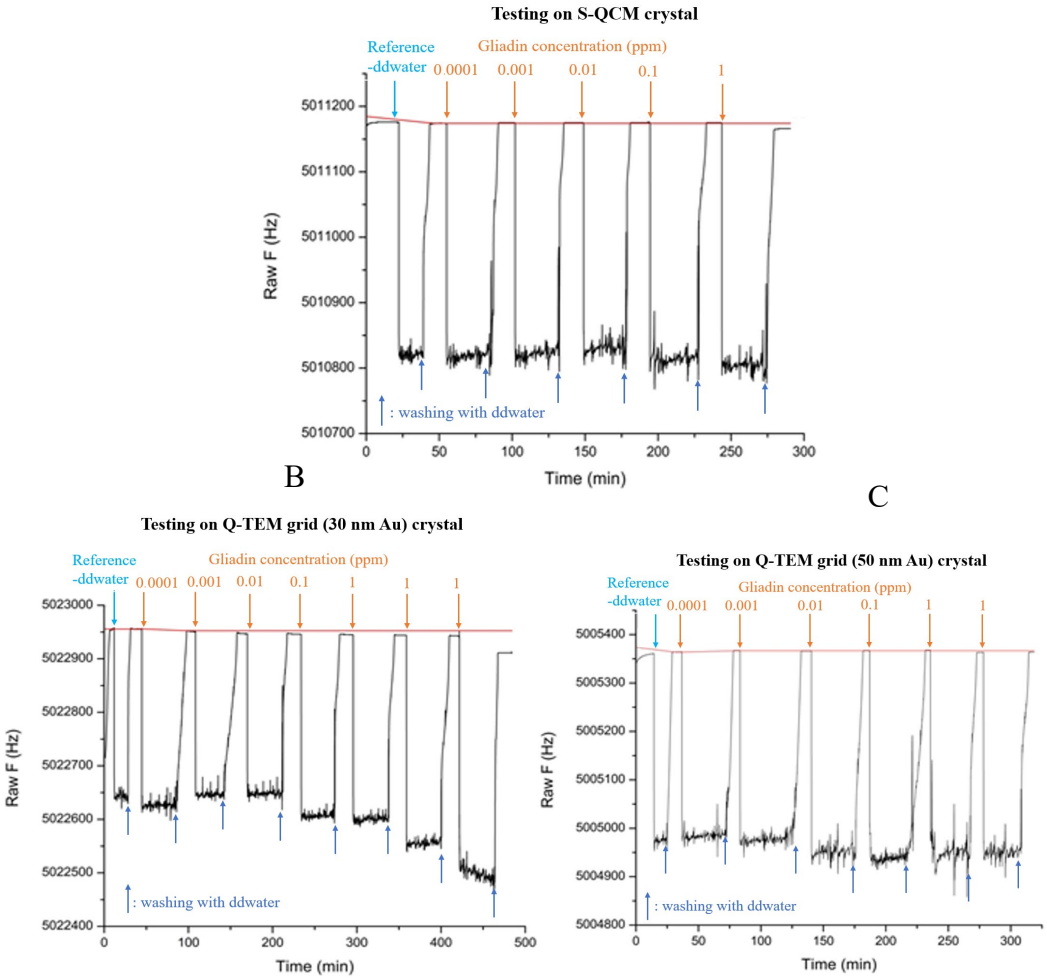

Figure 6. 12 Capteur acoustique utilisant A) un cristal de type « SQCM » B) et C) des cristaux de type « Q TEM grid » avec respectivement 30 nm et 50 nm d'or évaporé. Ces trois cristaux ont été biofonctionnalisés avec un anticorps anti-gliadine et exposés à différentes concentrations de gliadine.

La détection de la gliadine à l'aide de cristal de type Q TEM grid pour une épaisseur d'or déposé de 30 nm est beaucoup plus performante que celle effectuée avec un cristal commercial standard en termes de limite de détection (1000 fois plus basse) et de sensibilité.

De bonnes performances ont été également observées avec les cristaux de type « QCM color » qui constituent un procédé simple et peu coûteux pour réaliser des nano-

ilots d'or de façon contrôlée et reproductible.

6.5 Conclusions et perspectives

Cette thèse a été consacrée au développement de surfaces actives à partir de procédés simples et peu coûteux pour réaliser des nanoparticules d'or sur substrat ou pour structurer géographiquement une électrode. Le premier procédé est basé sur le recuit contrôlé d'un film évaporé de quelques nanomètres d'épaisseur, le second sur l'évaporation d'or à travers un masque adapté (par exemple une grille de TEM).

Ces surfaces actives ont été testées dans différentes configurations de biocapteurs après avoir été optimisées pour conduire aux meilleures performances possibles en termes de limite de détection et de sensibilité.

Leur structure été étudiée par imagerie MEB et AFM depuis le dépôt du film jusqu'à son traitement thermique. Ce travail a permis de montrer l'influence du substrat sur la taille des nanoparticules et leur distribution mais qu'il était aussi possible de contrôler taille et distribution en jouant sur l'épaisseur du dépôt, la température de recuit et sa durée.

La stabilité des nanoparticules a été contrôlée grâce à un choix adapté du procédé de biofonctionnalisation, les solutions tampons nécessaires à cette action pouvant se montrer particulièrement agressives.

Le bénéfice du recours à la structuration de l'électrode a été mise en évidence sur deux types de capteurs (génocapteur et immunocapteur) et pour trois types de détection (acoustique, par spectroscopie diélectrique micro-ondes, optique (LSPR ou SERS)). Il

a été montré qu'elle devait être adaptée à chaque dispositif.

A l'issue de cette these, trois types de biocapteurs basés sur des nanostructures ont donc été développés montrant des performances prometteuses:

- Détection de la protéine Hsp70 par mesures diélectriques dans la gamme des micro-ondes.
- Génosenseur à ADN de *Brett* basé sur des mesures LSPR et SERS. Afin de développer une plate-forme de biodétection plus sensible et plus stable avec des AuNP sur les substrats solides, le protocole de fabrication des AuNP recuits à haute température a été optimisé. Les résultats ont montré une faible limite de détection.
- Immunosenseur pour la détection de la glidaine utilisant la détection acoustique. Différents types de surfaces ont été étudiés, montrant tout l'intérêt de structurer l'électrode avant sa biofonctionnalisation.

Il reste des défis à relever et de nombreuses pistes de recherche. En ce qui concerne les biocapteurs à base de métaux nobles, les défis futurs pourraient concerner l'élargissement de la gamme des différentes biomolécules pouvant être détectées en augmentant la sensibilité et en fournissant des méthodes de détection plus rapides et plus polyvalentes. Un autre défi à relever pour progresser dans ce domaine est d'étendre l'application de ces capteurs à des échantillons réels, en particulier dans le domaine du diagnostic. En outre, le développement de biocapteurs renouvelables, pratiques et peu coûteux est un défi. L'un des défis les plus importants est lié à la structure, la stabilité et la sensibilité des biomolécules. Le développement de modèles pour l'étude de

nouvelles biomolécules ou pour l'intégration de multiples éléments biologiques fonctionnels dans une seule plateforme par le biais de liens inter-biomoléculaires est également une partie importante de la recherche. En outre, le développement de nouveaux nanomatériaux ou de complexes entre différents matériaux pour améliorer ou renforcer l'environnement de détection et le niveau de biodétection, et donc les substrats des matériaux de capteurs, est également nécessaire.

Scientific production

Articles:

1. Ionescu R.E., Selon R., Pocholle N., **Zhou L.**, Rumyantseva A., Bourillot E., Lesniewska E. Microwave Spectroscopic Detection of Human Hsp70 Protein on Annealed Gold Nanostructures on ITO Glass strips. *Biosensors* **2018**, 8, 118.
2. **Zhou L.**, Poggesi S., Casari Bariani G., Mittapalli R., Adam P.M., Manzano M., & Ionescu R.E. Robust SERS Platforms Based on Annealed Gold Nanostructures Formed on Ultrafine Glass Substrates for Various (Bio)Applications. *Biosensors* **2019**, 9 (2), 53.
3. Ionescu R.E., Poggesi S., **Zhou L.**, Casari Bariani G., Mittapalli R., Adam P.M., Manzano M. Surface Enhanced Raman Spectroscopy detection of Brettanomyces bruxellensis yeast on nanostructured ultrafine glass supports. *Optik* **2020**, 203, 193956.
4. Casari Bariani, G., **Zhou, L.**, Poggesi, S., Mittapalli, R., Manzano, M., & Ionescu, R. E. Acoustic Multi-Detection of Gliadin Using QCM Crystals Patterned with Controlled Sectors of TEM Grid and Annealed Nanoislands on Gold Electrode. *Nanomaterials* **2020**, 10(4), 790.
5. **Zhou L.**, Ionescu R.E. Influence of Saline Buffers over the Stability of High-Annealed Gold Nanoparticles Formed on Coverslips for Biological and Chemosensing Applications. *Bioengineering* **2020**, 7(3), 68.

Workshops:

1. **Zhou L**., Ionescu R.E. Design of ultrasensitive nanobiosensors using localized surface plasmon resonance and electrochemistry. 2017 L2n Ph.D. Students Workshop, Troyes, France, 12 December **2017**. (Oral presentation)
2. **Zhou L**., Poggesi S., Casari Bariani G., Mittapalli R., Manzano M., & Ionescu R.E. Active Nanostructures for Rapid Bio-diagnostics. 2018 L2n Ph.D. Students Workshop, Troyes, France, 13 December **2018**. (Poster presentation)
3. **Zhou L**., Poggesi S., Casari Bariani G., Mittapalli R., Adam P.M., Manzano M., & Ionescu R.E. Robust SERS platforms based on annealed gold nanostructures formed on ultrafine glass substrates for various (bio)applications. 2019 UTT WHAT'S UP DOC event, Troyes, France, 11 April **2019**. (Poster presentation)

Conferences:

1. 2020 Conference on Lasers and Electro-Optics (CLEO), presented in an all-virtual, web conference format, from 11-15 May **2020**. (Participation)
2. 2020 Conference on Microsystems & Nanoengineering (MINE) Young Scientists Forum, presented in an all-virtual, web conference format, from 7-10 July **2020**. (Participation)
3. 2020 Conference on SPIE Optics and Photonics, presented in an all-virtual, web conference format, from 24 - 28 August **2020**. (Participation)

References

1. Sepúlveda, B., Angelomé, P. C., Lechuga, L. M. & Liz-Marzán, L. M. LSPR-based nanobiosensors. *Nano Today* **4**, 244–251 (2009).
2. Zhang, Y., Wang, G., Yang, L., Wang, F. & Liu, A. Recent advances in gold nanostructures based biosensing and bioimaging. *Coord. Chem. Rev.* **370**, 1–21 (2018).
3. Grabar, K. C., Freeman, R. Griffith., Hommer, M. B. & Natan, M. J. Preparation and Characterization of Au Colloid Monolayers. *Anal. Chem.* **67**, 735–743 (1995).
4. Jin, Y. *et al.* Controlled Nucleation and Growth of Surface-Confined Gold Nanoparticles on a (3-aminopropyl)trimethoxysilane-Modified Glass Slide: A Strategy for SPR Substrates. *Anal. Chem.* **73**, 2843–2849 (2001).
5. Benjamin, P., Weaver, C. & Mott, N. F. The adhesion of evaporated metal films on glass. *Proc. R. Soc. Lond. Ser. Math. Phys. Sci.* **261**, 516–531 (1962).
6. Jia, K., Bijeon, J.-L., Adam, P.-M. & Ionescu, R. E. Large Scale Fabrication of Gold Nano-Structured Substrates Via High Temperature Annealing and Their Direct Use for the LSPR Detection of Atrazine. *Plasmonics* **8**, 143–151 (2013).
7. IUPAC. Biosensor definition. *Gloss. Chem. Terms Used Biotechnol.* **143**, 148 (2014).
8. Najeeb, M. A., Ahmad, Z., Shakoor, R. A., Mohamed, A. M. A. & Kahraman, R. A novel classification of prostate specific antigen (PSA) biosensors based on transducing elements. *Talanta* **168**, 52–61 (2017).
9. Mungroo, N. A. & Neethirajan, S. Biosensors for the Detection of Antibiotics in Poultry Industry—A Review. *Biosensors* **4**, 472–493 (2014).

10. Lopez, G. A., Estevez, M. C., Soler, M. & Lechuga, L. M. Recent advances in nanoplasmonic biosensors: Applications and lab-on-a-chip integration. *Nanophotonics* **6**, 123–136 (2017).

11. Ali, J., Najeeb, J., Asim Ali, M., Farhan Aslam, M. & Raza, A. Biosensors: Their Fundamentals, Designs, Types and Most Recent Impactful Applications: A Review. *J. Biosens. Bioelectron.* **08**, (2017).

12. Ashley, J. *et al.* Molecularly imprinted polymers for sample preparation and biosensing in food analysis: Progress and perspectives. *Biosens. Bioelectron.* **91**, 606–615 (2017).

13. Nigam, V. K. & Shukla, P. Enzyme Based Biosensors for Detection of Environmental Pollutants--A Review. *J. Microbiol. Biotechnol.* **25**, 1773–1781 (2015).

14. Li, H. *et al.* Differentiation of live and heat-killed E. coli by microwave impedance spectroscopy. *Sens. Actuators B Chem.* **255**, 1614–1622 (2018).

15. Masson, J.-F. Surface Plasmon Resonance Clinical Biosensors for Medical Diagnostics. *ACS Sens.* **2**, 16–30 (2017).

16. Malekzad, H. *et al.* Noble metal nanostructures in optical biosensors: Basics, and their introduction to anti-doping detection. *TrAC Trends Anal. Chem.* **100**, 116–135 (2018).

17. Damborský, P., Švitel, J. & Katrlík, J. Optical biosensors. *Essays Biochem.* **60**, 91–100 (2016).

18. Guo, S. & Dong, S. Biomolecule-nanoparticle hybrids for electrochemical

biosensors. *TrAC Trends Anal. Chem.* **28**, 96–109 (2009).

19. Lei, J. & Ju, H. Signal amplification using functional nanomaterials for biosensing. *Chem. Soc. Rev.* **41**, 2122–2134 (2012).

20. Zhou, S., Yuan, L., Hua, X., Xu, L. & Liu, S. Signal amplification strategies for DNA and protein detection based on polymeric nanocomposites and polymerization: A review. *Anal. Chim. Acta* **877**, 19–32 (2015).

21. de la Escosura-Muñiz, A., Ambrosi, A. & Merkoçi, A. Electrochemical analysis with nanoparticle-based biosystems. *TrAC Trends Anal. Chem.* **27**, 568–584 (2008).

22. Farka, Z., Juřík, T., Kovář, D., Trnková, L. & Skládal, P. Nanoparticle-Based Immunochemical Biosensors and Assays: Recent Advances and Challenges. *Chem. Rev.* **117**, 9973–10042 (2017).

23. Aldewachi, H. *et al.* Gold nanoparticle-based colorimetric biosensors. *Nanoscale* **10**, 18–33 (2018).

24. Liu, L., Wu, C. & Zhang, S. Ultrasensitive Detection of DNA and Ramos Cell Using In Situ Selective Crystallization Based Quartz Crystal Microbalance. *Anal. Chem.* **89**, 4309–4313 (2017).

25. Lee, J. H., Cho, H. Y., Choi, H. K., Lee, J. Y. & Choi, J. W. Application of gold nanoparticle to plasmonic biosensors. *Int. J. Mol. Sci.* **19**, (2018).

26. Sau, T. K. & Rogach, A. L. Nonspherical Noble Metal Nanoparticles: Colloid-Chemical Synthesis and Morphology Control. *Adv. Mater.* **22**, 1781–1804 (2010).

27. Jain, P. K. & El-Sayed, M. A. Plasmonic coupling in noble metal nanostructures. *Chem. Phys. Lett.* **487**, 153–164 (2010).

28. Daniel, M.-C. & Astruc, D. Gold Nanoparticles: Assembly, Supramolecular Chemistry, Quantum-Size-Related Properties, and Applications toward Biology, Catalysis, and Nanotechnology. *Chem. Rev.* **104**, 293–346 (2004).

29. Vajtai, R. *Springer Handbook of Nanomaterials*. (Springer Science & Business Media, 2013).

30. F.R.S, M. F. E. D. C. L. LIX. Experimental relations of gold (and other metals) to light. The bakerian lecture. *Lond. Edinb. Dublin Philos. Mag. J. Sci.* **14**, 512–539 (1857).

31. Brown, D. H. & Smith, W. E. The chemistry of the gold drugs used in the treatment of rheumatoid arthritis. *Chem. Soc. Rev.* **9**, 217 (1980).

32. Schmid, G. Large clusters and colloids. Metals in the embryonic state. *Chem. Rev.* **92**, 1709–1727 (1992).

33. Mie, G. Beiträge zur Optik trüber Medien, speziell kolloidaler Metallösungen. *Ann. Phys.* **330**, 377–445 (1908).

34. Pines, D. & Bohm, D. A Collective Description of Electron Interactions: II. Collective vs Individual Particle Aspects of the Interactions. *Phys. Rev.* **85**, 338–353 (1952).

35. Ritchie, R. H. Plasma Losses by Fast Electrons in Thin Films. *Phys. Rev.* **106**, 874–881 (1957).

36. Yi, M. *et al.* Fluorescence Enhancement Caused by Plasmonics Coupling Between Silver Nano-Cubes and Silver Film. *Plasmonics* **6**, 213–217 (2011).

37. Li, S. *et al.* The fabrication of scatheless triangle nanoparticles for biosensor.

Microelectron. Eng. **111**, 87–90 (2013).

38. Chen, C.-D., Cheng, S.-F., Chau, L.-K. & Wang, C. R. C. Sensing capability of the localized surface plasmon resonance of gold nanorods. *Biosens. Bioelectron.* **22**, 926–932 (2007).

39. Baby, T. T., Aravind, S. S. J., Arockiadoss, T., Rakhi, R. B. & Ramaprabhu, S. Metal decorated graphene nanosheets as immobilization matrix for amperometric glucose biosensor. *Sens. Actuators B Chem.* **145**, 71–77 (2010).

40. Chang, C.-Y. *et al.* Flexible Localized Surface Plasmon Resonance Sensor with Metal–Insulator–Metal Nanodisks on PDMS Substrate. *Sci. Rep.* **8**, 11812 (2018).

41. Khan, I., Saeed, K. & Khan, I. Nanoparticles: Properties, applications and toxicities. *Arab. J. Chem.* **12**, 908–931 (2019).

42. Alex, S. & Tiwari, A. Functionalized Gold Nanoparticles: Synthesis, Properties and Applications—A Review. *J. Nanosci. Nanotechnol.* **15**, 1869–1894 (2015).

43. Zeng, S. *et al.* A review on functionalized gold nanoparticles for biosensing applications. *Plasmonics* **6**, 491–506 (2011).

44. Mizukoshi, Y. *et al.* Sonochemical Preparation of Bimetallic Nanoparticles of Gold/Palladium in Aqueous Solution. *J. Phys. Chem. B* **101**, 7033–7037 (1997).

45. Maye, M. M., Zheng, W., Leibowitz, F. L., Ly, N. K. & Zhong, C.-J. Heating-Induced Evolution of Thiolate-Encapsulated Gold Nanoparticles: A Strategy for Size and Shape Manipulations. *Langmuir* **16**, 490–497 (2000).

46. Martin, M. N., Basham, J. I., Chando, P. & Eah, S.-K. Charged Gold Nanoparticles in Non-Polar Solvents: 10-min Synthesis and 2D Self-Assembly. *Langmuir* **26**,

7410–7417 (2010).

47. Sun, Y. & Xia, Y. Shape-Controlled Synthesis of Gold and Silver Nanoparticles. *Science* **298**, 2176–2179 (2002).

48. Henglein, A. & Meisel, D. Radiolytic Control of the Size of Colloidal Gold Nanoparticles. *Langmuir* **14**, 7392–7396 (1998).

49. Zhou, Y., Wang, C. Y., Zhu, Y. R. & Chen, Z. Y. A Novel Ultraviolet Irradiation Technique for Shape-Controlled Synthesis of Gold Nanoparticles at Room Temperature. *Chem. Mater.* **11**, 2310–2312 (1999).

50. Sau, T. K. & Murphy, C. J. Room Temperature, High-Yield Synthesis of Multiple Shapes of Gold Nanoparticles in Aqueous Solution. *J. Am. Chem. Soc.* **126**, 8648–8649 (2004).

51. Hu, J. *et al.* Synthesis and Properties of Tadpole-Shaped Gold Nanoparticles. *J. Am. Chem. Soc.* **126**, 9470–9471 (2004).

52. Kuo, C.-H., Chiang, T.-F., Chen, L.-J. & Huang, M. H. Synthesis of Highly Faceted Pentagonal- and Hexagonal-Shaped Gold Nanoparticles with Controlled Sizes by Sodium Dodecyl Sulfate. *Langmuir* **20**, 7820–7824 (2004).

53. Rodríguez-Fernández, J., Pastoriza-Santos, I., Pérez-Juste, J., García de Abajo, F. J. & Liz-Marzán, L. M. The Effect of Silica Coating on the Optical Response of Sub-micrometer Gold Spheres. *J. Phys. Chem. C* **111**, 13361–13366 (2007).

54. Xia, Y. *et al.* Gold Nanocages: From Synthesis to Theranostic Applications. *Acc. Chem. Res.* **44**, 914–924 (2011).

55. Sau, T. K. & Murphy, C. J. Seeded High Yield Synthesis of Short Au Nanorods in

Aqueous Solution. *Langmuir* **20**, 6414–6420 (2004).

56. Lee, Y. H., Yan, Y., Polavarapu, L. & Xu, Q.-H. Nonlinear optical switching behavior of Au nanocubes and nano-octahedra investigated by femtosecond Z-scan measurements. *Appl. Phys. Lett.* **95**, 023105 (2009).

57. Jin, R., Egusa, S. & Scherer, N. F. Thermally-Induced Formation of Atomic Au Clusters and Conversion into Nanocubes. *J. Am. Chem. Soc.* **126**, 9900–9901 (2004).

58. Wang, H. *et al.* Controlled Texturing Modifies the Surface Topography and Plasmonic Properties of Au Nanoshells. *J. Phys. Chem. B* **109**, 11083–11087 (2005).

59. Lohmüller, T. *et al.* Nanopatterning by block copolymer micelle nanolithography and bioinspired applications. *Biointerphases* **6**, MR1–MR12 (2011).

60. Cao, Y. C., Jin, R. & Mirkin, C. A. Nanoparticles with Raman Spectroscopic Fingerprints for DNA and RNA Detection. *Science* **297**, 1536–1540 (2002).

61. Turkevich, J., Stevenson, P. C. & Hillier, J. A study of the nucleation and growth processes in the synthesis of colloidal gold. *Discuss. Faraday Soc.* **11**, 55–75 (1951).

62. Frens, G. Particle size and sol stability in metal colloids. *Kolloid-Z. Z. Für Polym.* **250**, 736–741 (1972).

63. Frens, G. Controlled Nucleation for the Regulation of the Particle Size in Monodisperse Gold Suspensions. *Nat. Phys. Sci.* **241**, 20–22 (1973).

64. Stobiecka, M., Deeb, J. & Hepel, M. Ligand exchange effects in gold nanoparticle assembly induced by oxidative stress biomarkers: Homocysteine and cysteine. *Biophys. Chem.* **146**, 98–107 (2010).

65. Stobiecka, M., Coopersmith, K. & Hepel, M. Resonance elastic light scattering

(RELS) spectroscopy of fast non-Langmuirian ligand-exchange in glutathione-induced gold nanoparticle assembly. *J. Colloid Interface Sci.* **350**, 168–177 (2010).

66. Stobiecka, M. & Hepel, M. Rapid functionalization of metal nanoparticles by moderator-tunable ligand-exchange process for biosensor designs. *Sens. Actuators B Chem.* **149**, 373–380 (2010).

67. Song, L., Jiang, Q., Wang, Z.-G. & Ding, B. Self-Assembled DNA Nanostructures for Biomedical Applications. *ChemNanoMat* **3**, 713–724 (2017).

68. Mirkin, C. A., Letsinger, R. L., Mucic, R. C. & Storhoff, J. J. A DNA-based method for rationally assembling nanoparticles into macroscopic materials. *Nature* **382**, 607–609 (1996).

69. Alivisatos, A. P. *et al.* Organization of 'nanocrystal molecules' using DNA. *Nature* **382**, 609–611 (1996).

70. Bidault, S., García de Abajo, F. J. & Polman, A. Plasmon-Based Nanolenses Assembled on a Well-Defined DNA Template. *J. Am. Chem. Soc.* **130**, 2750–2751 (2008).

71. Mastroianni, A. J., Claridge, S. A. & Alivisatos, A. P. Pyramidal and Chiral Groupings of Gold Nanocrystals Assembled Using DNA Scaffolds. *J. Am. Chem. Soc.* **131**, 8455–8459 (2009).

72. Lo, P. K., Altvater, F. & Sleiman, H. F. Templated Synthesis of DNA Nanotubes with Controlled, Predetermined Lengths. *J. Am. Chem. Soc.* **132**, 10212–10214 (2010).

73. Storhoff, J. J. *et al.* What Controls the Optical Properties of DNA-Linked Gold

Nanoparticle Assemblies? *J. Am. Chem. Soc.* **122**, 4640–4650 (2000).

74. Kanaras, A. G., Wang, Z., Brust, M., Cosstick, R. & Bates, A. D. Enzymatic Disassembly of DNA–Gold Nanostructures. *Small* **3**, 590–594 (2007).

75. Huo, F., Lytton-Jean, A. K. R. & Mirkin, C. A. Asymmetric Functionalization of Nanoparticles Based on Thermally Addressable DNA Interconnects. *Adv. Mater.* **18**, 2304–2306 (2006).

76. Kim, J.-Y. & Lee, J.-S. Synthesis and Thermally Reversible Assembly of DNA−Gold Nanoparticle Cluster Conjugates. *Nano Lett.* **9**, 4564–4569 (2009).

77. Xiong, H., van der Lelie, D. & Gang, O. Phase Behavior of Nanoparticles Assembled by DNA Linkers. *Phys. Rev. Lett.* **102**, 015504 (2009).

78. McMillan, R. A. *et al.* Ordered nanoparticle arrays formed on engineered chaperonin protein templates. *Nat. Mater.* **1**, 247–252 (2002).

79. Hu, M., Qian, L., Briñas, R. P., Lymar, E. S. & Hainfeld, J. F. Assembly of Nanoparticle–Protein Binding Complexes: From Monomers to Ordered Arrays. *Angew. Chem. Int. Ed.* **46**, 5111–5114 (2007).

80. Lamm, M. S. *et al.* Laterally Spaced Linear Nanoparticle Arrays Templated by Laminated β-Sheet Fibrils. *Adv. Mater.* **20**, 447–451 (2008).

81. Sun, J. *et al.* Core-controlled polymorphism in virus-like particles. *Proc. Natl. Acad. Sci.* **104**, 1354–1359 (2007).

82. Vieu, C. *et al.* Electron beam lithography: resolution limits and applications. *Appl. Surf. Sci.* **164**, 111–117 (2000).

83. Lee, H.-S. *et al.* Electron Beam Projection Nanopatterning Using Crystal Lattice

Images Obtained from High Resolution Transmission Electron Microscopy. *Adv. Mater.* **19**, 4189–4193 (2007).

84. Chen, Y. Nanofabrication by electron beam lithography and its applications: A review. *Microelectron. Eng.* **135**, 57–72 (2015).

85. Kwag, H. R., Cho, J.-H., Park, S.-Y., Park, J. & Gracias, D. H. Self-folding nanostructures with imprint patterned surfaces (SNIPS). *Faraday Discuss.* **191**, 61–71 (2016).

86. Zin, M. T. *et al.* Surface-plasmon-enhanced fluorescence from periodic quantum dot arrays through distance control using biomolecular linkers. *Nanotechnology* **20**, 015305 (2008).

87. Huang, X. & El-Sayed, M. A. Gold nanoparticles: Optical properties and implementations in cancer diagnosis and photothermal therapy. *J. Adv. Res.* **1**, 13–28 (2010).

88. Alvarez, M. M. *et al.* Optical Absorption Spectra of Nanocrystal Gold Molecules. *J. Phys. Chem. B* **101**, 3706–3712 (1997).

89. Cao, J., Sun, T. & Grattan, K. T. V. Gold nanorod-based localized surface plasmon resonance biosensors: A review. *Sens. Actuators B Chem.* **195**, 332–351 (2014).

90. Melinger, J. S. *et al.* Ultrafast Dynamics of Gold-Based Nanocomposite Materials †. *J. Phys. Chem. A* **107**, 3424–3431 (2003).

91. Templeton, A. C., Wuelfing, W. P. & Murray, R. W. Monolayer-Protected Cluster Molecules. *Acc. Chem. Res.* **33**, 27–36 (2000).

92. Boal, A. K. & Rotello, V. M. Intra- and Intermonolayer Hydrogen Bonding in

Amide-Functionalized Alkanethiol Self-Assembled Monolayers on Gold Nanoparticles. *Langmuir* **16**, 9527–9532 (2000).

93. Sokolov, K. *et al.* Real-Time Vital Optical Imaging of Precancer Using Anti-Epidermal Growth Factor Receptor Antibodies Conjugated to Gold Nanoparticles. *Cancer Res.* **63**, 1999–2004 (2003).

94. El-Sayed, I. H., Huang, X. & El-Sayed, M. A. Surface Plasmon Resonance Scattering and Absorption of anti-EGFR Antibody Conjugated Gold Nanoparticles in Cancer Diagnostics: Applications in Oral Cancer. *Nano Lett.* **5**, 829–834 (2005).

95. Jain, P. K., Lee, K. S., El-Sayed, I. H. & El-Sayed, M. A. Calculated Absorption and Scattering Properties of Gold Nanoparticles of Different Size, Shape, and Composition: Applications in Biological Imaging and Biomedicine. *J. Phys. Chem. B* **110**, 7238–7248 (2006).

96. Jing, C. *et al.* Chrominance to Dimension: A Real-Time Method for Measuring the Size of Single Gold Nanoparticles. *Anal. Chem.* **84**, 4284–4291 (2012).

97. Link, S. & El-Sayed, M. A. Optical Properties and Ultrafast Dynamics of Metallic Nanocrystals. *Annu. Rev. Phys. Chem.* **54**, 331–366 (2003).

98. El-Sayed, I. H., Huang, X. & El-Sayed, M. A. Selective laser photo-thermal therapy of epithelial carcinoma using anti-EGFR antibody conjugated gold nanoparticles. *Cancer Lett.* **239**, 129–135 (2006).

99. Huang, X., El-Sayed, I. H., Qian, W. & El-Sayed, M. A. Cancer Cell Imaging and Photothermal Therapy in the Near-Infrared Region by Using Gold Nanorods. *J. Am. Chem. Soc.* **128**, 2115–2120 (2006).

100. Hung, S. H., Lee, J. Y., Hu, C. C. & Chiu, T. C. Gold-nanoparticle-based fluorescent “turn-on” sensor for selective and sensitive detection of dimethoate. *Food Chem.* **260**, 61–65 (2018).

101. Roda, A. *et al.* Progress in chemical luminescence-based biosensors: A critical review. *Biosens. Bioelectron.* **76**, 164–179 (2016).

102. Stern, E. *et al.* Label-free biomarker detection from whole blood. *Nat. Nanotechnol.* **5**, 138–142 (2010).

103. Wilson, G. S. & Hu, Y. Enzyme-Based Biosensors for in Vivo Measurements. *Chem. Rev.* **100**, 2693–2704 (2000).

104. Wang, J. Electrochemical Glucose Biosensors. *Chem. Rev.* **108**, 814–825 (2008).

105. Moschopoulou, G., Valero, T. & Kintzios, S. Superoxide determination using membrane-engineered cells: An example of a novel concept for the construction of cell sensors with customized target recognition properties. *Sens. Actuators B Chem.* **175**, 78–84 (2012).

106. Darain, F., Park, D.-S., Park, J.-S. & Shim, Y.-B. Development of an immunosensor for the detection of vitellogenin using impedance spectroscopy. *Biosens. Bioelectron.* **19**, 1245–1252 (2004).

107. Akbari Nakhjavani, S. *et al.* Gold and silver bio/nano-hybrids-based electrochemical immunosensor for ultrasensitive detection of carcinoembryonic antigen. *Biosens. Bioelectron.* **141**, 111439 (2019).

108. Noi, K., Iijima, M., Kuroda, S. & Ogi, H. Ultrahigh-sensitive wireless QCM

with bio-nanocapsules. *Sens. Actuators B Chem.* **293**, 59–62 (2019).

109. Hou, K. *et al.* Rapid Detection of Bifidobacterium bifidum in Feces Sample by Highly Sensitive Quartz Crystal Microbalance Immunosensor. *Front. Chem.* **8**, (2020).

110. Cervera-Chiner, L., March, C., Arnau, A., Jiménez, Y. & Montoya, Á. Detection of DDT and carbaryl pesticides in honey by means of immunosensors based on high fundamental frequency quartz crystal microbalance (HFF-QCM). *J. Sci. Food Agric.* **100**, 2468–2472 (2020).

111. Pohanka, M. QCM immunosensor for the determination of Staphylococcus aureus antigen. *Chem. Pap.* **74**, 451–458 (2020).

112. Fernández-Benavides, D. A. *et al.* A novel bismuth-based lead-free piezoelectric transducer immunosensor for carbaryl quantification. *Sens. Actuators B Chem.* **285**, 423–430 (2019).

113. Hwang, B. H., Shin, H. H. & Cha, H. J. Optimization of DNA microarray biosensors enables rapid and sensitive detection. *Biotechnol. Bioprocess Eng.* **22**, 469–473 (2017).

114. Brinciotti, E. *et al.* Probing resistivity and doping concentration of semiconductors at the nanoscale using scanning microwave microscopy. *Nanoscale* **7**, 14715–14722 (2015).

115. Tuca, S.-S. *et al.* Calibrated complex impedance of CHO cells andE.colibacteria at GHz frequencies using scanning microwave microscopy. *Nanotechnology* **27**, 135702 (2016).

116. Gramse, G. *et al.* Calibrated complex impedance and permittivity measurements with scanning microwave microscopy. *Nanotechnology* **25**, 145703 (2014).

117. Biagi, M. C. *et al.* Nanoscale Electric Permittivity of Single Bacterial Cells at Gigahertz Frequencies by Scanning Microwave Microscopy. *ACS Nano* **10**, 280–288 (2016).

118. Lai, K., Kundhikanjana, W., Kelly, M. A. & Shen, Z.-X. Nanoscale microwave microscopy using shielded cantilever probes. *Appl. Nanosci.* **1**, 13–18 (2011).

119. Imtiaz, A., Wallis, T. M. & Kabos, P. Near-Field Scanning Microwave Microscopy: An Emerging Research Tool for Nanoscale Metrology. *IEEE Microw. Mag.* **15**, 52–64 (2014).

120. Plassard, C. *et al.* Detection of defects buried in metallic samples by scanning microwave microscopy. *Phys. Rev. B* **83**, 121409 (2011).

121. Gramse, G. *et al.* Quantitative sub-surface and non-contact imaging using scanning microwave microscopy. *Nanotechnology* **26**, 135701 (2015).

122. Imtiaz, A. *et al.* Frequency-selective contrast on variably doped p-type silicon with a scanning microwave microscope. *J. Appl. Phys.* **111**, 093727 (2012).

123. Buchter, A. *et al.* Scanning microwave microscopy applied to semiconducting GaAs structures. *Rev. Sci. Instrum.* **89**, 023704 (2018).

124. Tai, T., Ghamsari, B. G. & Anlage, S. M. Nanoscale Electrodynamic Response of Nb Superconductors. *IEEE Trans. Appl. Supercond.* **23**, 7100104–7100104 (2013).

125. Xu, H., Anlage, S. M., Hu, L. & Gruner, G. Microwave shielding of transparent and conducting single-walled carbon nanotube films. *Appl. Phys. Lett.* **90**, 183119

(2007).

126. Kalugin, N. G. *et al.* Few-layer graphene characterization by near-field scanning microwave microscopy. *Propos. Publ. Appl. Phys. Lett.* (2010).

127. Farina, M. *et al.* Tomographic effects of near-field microwave microscopy in the investigation of muscle cells interacting with multi-walled carbon nanotubes. *Appl. Phys. Lett.* **101**, 203101 (2012).

128. Oh, Y. J. *et al.* High-frequency electromagnetic dynamics properties of THP1 cells using scanning microwave microscopy. *Ultramicroscopy* **111**, 1625–1629 (2011).

129. Lai, K. *et al.* Tapping mode microwave impedance microscopy. *Rev. Sci. Instrum.* **80**, 043707 (2009).

130. Jin, X. *et al.* Broadband Scanning Microwave Microscopy of a Biological Cell with Unprecedented Image Quality and Signal-to-Noise Ratio. in *2019 IEEE MTT-S International Microwave Symposium (IMS)* 216–219 (2019). doi:10.1109/MWSYM.2019.8700966.

131. Park, J., Hyun, S., Kim, A., Kim, T. & Char, K. Observation of biological samples using a scanning microwave microscope. *Ultramicroscopy* **102**, 101–106 (2005).

132. Farina, M., Donato, A. D., Mencarelli, D., Venanzoni, G. & Morini, A. High Resolution Scanning Microwave Microscopy for Applications in Liquid Environment. *IEEE Microw. Wirel. Compon. Lett.* **22**, 595–597 (2012).

133. Jin, X. *et al.* Quantitative Scanning Microwave Microscopy of the Evolution

of a Live Biological Cell in a Physiological Buffer. *IEEE Trans. Microw. Theory Tech.* **67**, 5438–5445 (2019).

134. Kim, S. *et al.* Distance control for a near-field scanning microwave microscope in liquid using a quartz tuning fork. *Appl. Phys. Lett.* **86**, 153506 (2005).

135. Farina, M. *et al.* Investigation of Fullerene Exposure of Breast Cancer Cells by Time-Gated Scanning Microwave Microscopy. *IEEE Trans. Microw. Theory Tech.* **64**, 4823–4831 (2016).

136. Fabi, G. *et al.* Electrical properties of Jurkat cells: an inverted scanning microwave microscope study. in *2020 IEEE/MTT-S International Microwave Symposium (IMS)* 237–240 (2020). doi:10.1109/IMS30576.2020.9223785.

137. Shabaninezhad, M. & Ramakrishna, G. Theoretical investigation of size, shape, and aspect ratio effect on the LSPR sensitivity of hollow-gold nanoshells. *J. Chem. Phys.* **150**, 144116 (2019).

138. Focsan, M. *et al.* Flexible and Tunable 3D Gold Nanocups Platform as Plasmonic Biosensor for Specific Dual LSPR-SERS Immuno-Detection. *Sci. Rep.* **7**, 14240 (2017).

139. Sai, V. V. R., Kundu, T. & Mukherji, S. Novel U-bent fiber optic probe for localized surface plasmon resonance based biosensor. *Biosens. Bioelectron.* **24**, 2804–2809 (2009).

140. Konwar Boruah, S., Kumar Boruah, P., Sarma, P., Medhi, C. & Kumar Medhi, O. Green Synthesis Of Gold Nanoparticles Using Camellia Sinensis And Kinetics Of The Reaction. *Adv. Mater. Lett.* **3**, 481–486 (2012).

141. Scholl, J. A., Koh, A. L. & Dionne, J. A. Quantum plasmon resonances of individual metallic nanoparticles. *Nature* **483**, 421–427 (2012).

142. Samsuri, N. D., Mukhtar, W. M., Abdul Rashid, A. R., Ahmad Dasuki, K. & Awangku Yussuf, A. A. R. Hj. Synthesis methods of gold nanoparticles for Localized Surface Plasmon Resonance (LSPR) sensor applications. *EPJ Web Conf.* **162**, 01002 (2017).

143. Estevão, J. As Especificidades dos Futuros de Eletricidade - Aplicação ao Mercado Ibérico. *Universidade Téc. Lisb.* 131–167 (2011) doi:10.1007/978-3-319-24606-2.

144. Vestergaard, M. C., Kerman, K., Hsing, I. M. & Tamiya, E. Nanobiosensors and nanobioanalyses. *Nanobiosensors Nanobioanalyses* 1–379 (2015) doi:10.1007/978-4-431-55190-4.

145. Fleischmann, M., Hendra, P. J. & McQuillan, A. J. Raman spectra of pyridine adsorbed at a silver electrode. *Chem. Phys. Lett.* **26**, 163–166 (1974).

146. Kumar, S., Kumar, P., Das, A. & Pathak, C. S. Surface-Enhanced Raman Scattering: Introduction and Applications. *Recent Adv. Nanophotonics - Fundam. Appl.* (2020) doi:10.5772/intechopen.92614.

147. Mitchell, J. Small Molecule Immunosensing Using Surface Plasmon Resonance. *Sensors* **10**, 7323–7346 (2010).

148. Liedberg, B., Nylander, C. & Lunström, I. Surface plasmon resonance for gas detection and biosensing. *Sens. Actuators* **4**, 299–304 (1983).

149. Sagle, L. B., Ruvuna, L. K., Ruemmele, J. A. & Van Duyne, R. P. Advances in

localized surface plasmon resonance spectroscopy biosensing. *Nanomed.* **6**, 1447–1462 (2011).

150. Zheng, Y. B., Kiraly, B., Weiss, P. S. & Huang, T. J. Molecular plasmonics for biology and nanomedicine. *Nanomed.* **7**, 751–770 (2012).

151. Stewart, M. E. *et al.* Nanostructured Plasmonic Sensors. *Chem. Rev.* **108**, 494–521 (2008).

152. Zhao, J., Zhang, X., Yonzon, C. R., Haes, A. J. & Van Duyne, R. P. Localized surface plasmon resonance biosensors. *Nanomed.* **1**, 219–228 (2006).

153. Mayer, K. M. & Hafner, J. H. Localized Surface Plasmon Resonance Sensors. *Chem. Rev.* **111**, 3828–3857 (2011).

154. Szunerits, S. & Boukherroub, R. Sensing using localised surface plasmon resonance sensors. *Chem. Commun.* **48**, 8999–9010 (2012).

155. Lee, J.-H., Kim, B.-C., Oh, B.-K. & Choi, J.-W. Highly sensitive localized surface plasmon resonance immunosensor for label-free detection of HIV-1. *Nanomedicine Nanotechnol. Biol. Med.* **9**, 1018–1026 (2013).

156. Hall, W. P., Ngatia, S. N. & Van Duyne, R. P. LSPR Biosensor Signal Enhancement Using Nanoparticle−Antibody Conjugates. *J. Phys. Chem. C* **115**, 1410–1414 (2011).

157. Tu, Q., Eisen, J. & Chang, C. Surface-enhanced Raman spectroscopy study of indolic molecules adsorbed on gold colloids. *J. Biomed. Opt.* **15**, 020512 (2010).

158. Feng, S. *et al.* A noninvasive cancer detection strategy based on gold nanoparticle surface-enhanced raman spectroscopy of urinary modified nucleosides

isolated by affinity chromatography. *Biosens. Bioelectron.* **91**, 616–622 (2017).

159. Mohammadniaei, M., Yoon, J., Lee, T. & Choi, J.-W. Spectroelectrochemical detection of microRNA-155 based on functional RNA immobilization onto ITO/GNP nanopattern. *J. Biotechnol.* **274**, 40–46 (2018).

160. Kneipp, K. *et al.* Single molecule detection using surface-enhanced Raman scattering (SERS). *Phys. Rev. Lett.* **78**, 1667 (1997).

161. Kneipp, J., Kneipp, H. & Kneipp, K. SERS—a single-molecule and nanoscale tool for bioanalytics. *Chem. Soc. Rev.* **37**, 1052–1060 (2008).

162. McNay, G., Eustace, D., Smith, W. E., Faulds, K. & Graham, D. Surface-Enhanced Raman Scattering (SERS) and Surface-Enhanced Resonance Raman Scattering (SERRS): A Review of Applications. *Appl. Spectrosc.* **65**, 825–837 (2011).

163. D. Porter, M., J. Lipert, R., M. Siperko, L., Wang, G. & Narayanan, R. SERS as a bioassay platform: fundamentals, design, and applications. *Chem. Soc. Rev.* **37**, 1001–1011 (2008).

164. Campion, A. & Kambhampati, P. Surface-enhanced Raman scattering. *Chem. Soc. Rev.* **27**, 241–250 (1998).

165. Gao, W. *et al.* Intuitive Label-Free SERS Detection of Bacteria Using Aptamer-Based in Situ Silver Nanoparticles Synthesis. *Anal. Chem.* **89**, 9836–9842 (2017).

166. Sun, K., Huang, Q., Meng, G. & Lu, Y. Highly Sensitive and Selective Surface-Enhanced Raman Spectroscopy Label-free Detection of 3,3′,4,4′-Tetrachlorobiphenyl Using DNA Aptamer-Modified Ag-Nanorod Arrays. *ACS Appl.*

Mater. Interfaces **8**, 5723–5728 (2016).

167. Prinz, J., Heck, C., Ellerik, L., Merk, V. & Bald, I. DNA origami based Au–Ag-core–shell nanoparticle dimers with single-molecule SERS sensitivity. *Nanoscale* **8**, 5612–5620 (2016).

168. Liu, B. *et al.* Ultrasensitive Detection of Protein with Wide Linear Dynamic Range Based on Core–Shell SERS Nanotags and Photonic Crystal Beads. *ACS Sens.* **2**, 1035–1043 (2017).

169. Zhang, H., Harpster, M. H., Park, H. J., Johnson, P. A. & Wilson, W. C. Surface-Enhanced Raman Scattering Detection of DNA Derived from the West Nile Virus Genome Using Magnetic Capture of Raman-Active Gold Nanoparticles. *Anal. Chem.* **83**, 254–260 (2011).

170. Sun, F. *et al.* Stealth Surface Modification of Surface-Enhanced Raman Scattering Substrates for Sensitive and Accurate Detection in Protein Solutions. *ACS Nano* **9**, 2668–2676 (2015).

171. Bi, L. *et al.* Fabrication of large-scale gold nanoplate films as highly active SERS substrates for label-free DNA detection. *Biosens. Bioelectron.* **43**, 193–199 (2013).

172. Sivashanmugan, K., Liao, J.-D., Liu, B. H. & Yao, C.-K. Focused-ion-beam-fabricated Au nanorods coupled with Ag nanoparticles used as surface-enhanced Raman scattering-active substrate for analyzing trace melamine constituents in solution. *Anal. Chim. Acta* **800**, 56–64 (2013).

173. Gu, H.-X., Hu, K., Li, D.-W. & Long, Y.-T. SERS detection of polycyclic

aromatic hydrocarbons using a bare gold nanoparticles coupled film system. *Analyst* **141**, 4359–4365 (2016).

174. Li, Y., Dykes, J., Gilliam, T. & Chopra, N. A new heterostructured SERS substrate: free-standing silicon nanowires decorated with graphene-encapsulated gold nanoparticles. *Nanoscale* **9**, 5263–5272 (2017).

175. Potara, M., Gabudean, A.-M. & Astilean, S. Solution-phase, dual LSPR-SERS plasmonic sensors of high sensitivity and stability based on chitosan -coated anisotropic silver nanoparticles. *J. Mater. Chem.* **21**, 3625–3633 (2011).

176. Ferreira, G. N. M., da-Silva, A.-C. & Tomé, B. Acoustic wave biosensors: physical models and biological applications of quartz crystal microbalance. *Trends Biotechnol.* **27**, 689–697 (2009).

177. Liu, Y., Jaiswal, A., Poggi, M. A. & Wilson, W. D. Surface Plasmon Resonance and Quartz Crystal Microbalance Methods for Detection of Molecular Interactions. in *Chemosensors* 329–344 (John Wiley & Sons, Ltd, 2011). doi:10.1002/9781118019580.ch16.

178. SAUERBREY, G. Use of quartz vibrator for weighting thin films on a microbalance. *Z. Phys.* **155**, 206–212 (1959).

179. Encarnação, J. M. *et al.* Piezoelectric biosensors for biorecognition analysis: Application to the kinetic study of HIV-1 Vif protein binding to recombinant antibodies. *J. Biotechnol.* **132**, 142–148 (2007).

180. Keiji Kanazawa, K. & Gordon, J. G. The oscillation frequency of a quartz resonator in contact with liquid. *Anal. Chim. Acta* **175**, 99–105 (1985).

181. Martin, S. J., Granstaff, V. Edwards. & Frye, G. C. Characterization of a quartz crystal microbalance with simultaneous mass and liquid loading. *Anal. Chem.* **63**, 2272–2281 (1991).

182. Voinova, M. V., Rodahl, M., Jonson, M. & Kasemo, B. Viscoelastic Acoustic Response of Layered Polymer Films at Fluid-Solid Interfaces: Continuum Mechanics Approach. *Phys. Scr.* **59**, 391 (1999).

183. Rodahl, M. & Kasemo, B. A simple setup to simultaneously measure the resonant frequency and the absolute dissipation factor of a quartz crystal microbalance. *Rev. Sci. Instrum.* **67**, 3238–3241 (1996).

184. Chen, J. Y., Penn, L. S. & Xi, J. Quartz crystal microbalance: Sensing cell-substrate adhesion and beyond. *Biosens. Bioelectron.* **99**, 593–602 (2018).

185. Saitakis, M. & Gizeli, E. Acoustic sensors as a biophysical tool for probing cell attachment and cell/surface interactions. *Cell. Mol. Life Sci.* **69**, 357–371 (2012).

186. Skládal, P. Piezoelectric biosensors. *TrAC Trends Anal. Chem.* **79**, 127–133 (2016).

187. Efremov, V., Lakshmanan, R. S., Byrne, B. & Killard, A. J. Simple and convenient measurement of RBC deformability using QCM integrated with a novel model of cell viscoelasticity. *Sens. Actuators B Chem.* **266**, 472–476 (2018).

188. Funari, R. *et al.* Detection of parathion and patulin by quartz-crystal microbalance functionalized by the photonics immobilization technique. *Biosens. Bioelectron.* **67**, 224–229 (2015).

189. Chu, P.-T., Lin, C.-S., Chen, W.-J., Chen, C.-F. & Wen, H.-W. Detection of

Gliadin in Foods Using a Quartz Crystal Microbalance Biosensor That Incorporates Gold Nanoparticles. *J. Agric. Food Chem.* **60**, 6483–6492 (2012).

190. Vaughan, R. D., O'Sullivan, C. K. & Guilbault, G. G. Development of a quartz crystal microbalance (QCM) immunosensor for the detection of Listeria monocytogenes. *Enzyme Microb. Technol.* **29**, 635–638 (2001).

191. Su, X.-L. & Li, Y. A QCM immunosensor for Salmonella detection with simultaneous measurements of resonant frequency and motional resistance. *Biosens. Bioelectron.* **21**, 840–848 (2005).

192. Pirinçci, Ş. Ş. *et al.* Label-Free QCM Immunosensor for the Detection of Ochratoxin A. *Sensors* **18**, 1161 (2018).

193. Fulgione, A. *et al.* QCM-based immunosensor for rapid detection of Salmonella Typhimurium in food. *Sci. Rep.* **8**, 16137 (2018).

194. Della Ventura, B., Sakač, N., Funari, R. & Velotta, R. Flexible immunosensor for the detection of salivary α-amylase in body fluids. *Talanta* **174**, 52–58 (2017).

195. Ventura, B. D. *et al.* Effective antibodies immobilization and functionalized nanoparticles in a quartz-crystal microbalance-based immunosensor for the detection of parathion. *PLOS ONE* **12**, e0171754 (2017).

196. Maglio, O. *et al.* A Quartz Crystal Microbalance Immunosensor for Stem Cell Selection and Extraction. *Sensors* **17**, 2747 (2017).

197. Liu, F., Li, F., Nordin, A. N. & Voiculescu, I. A Novel Cell-Based Hybrid Acoustic Wave Biosensor with Impedimetric Sensing Capabilities. *Sensors* **13**, 3039–3055 (2013).

198. Casari Bariani, G. *et al.* Acoustic Multi-Detection of Gliadin Using QCM Crystals Patterned with Controlled Sectors of TEM Grid and Annealed Nanoislands on Gold Electrode. *Nanomaterials* **10**, 790 (2020).

199. Kampinga, H. H. & Bergink, S. Heat shock proteins as potential targets for protective strategies in neurodegeneration. *Lancet Neurol.* **15**, 748–759 (2016).

200. Macario, A. J. L. & Macario, E. C. de. The Pathology of Cellular Anti-stress Mechanisms: A New Frontier. *Stress* **7**, 243–249 (2004).

201. Gallucci, S. & Matzinger, P. Danger signals: SOS to the immune system. *Curr. Opin. Immunol.* **13**, 114–119 (2001).

202. Seigneuric, R. *et al.* Heat Shock Proteins as Danger Signals for Cancer Detection. *Front. Oncol.* **1**, (2011).

203. Ionescu, R. E. *et al.* Microwave Spectroscopic Detection of Human Hsp70 Protein on Annealed Gold Nanostructures on ITO Glass Strips. *Biosensors* **8**, 118 (2018).

204. Laisne, A., Ewald, M., Ando, T., Lesniewska, E. & Pompon, D. Self-Assembly Properties and Dynamics of Synthetic Proteo–Nucleic Building Blocks in Solution and on Surfaces. *Bioconjug. Chem.* **22**, 1824–1834 (2011).

205. Giocondi, M.-C. *et al.* Surface topography of membrane domains. *Biochim. Biophys. Acta BBA - Biomembr.* **1798**, 703–718 (2010).

206. Aybeke, E. N. *et al.* HS-AFM and SERS Analysis of Murine Norovirus Infection: Involvement of the Lipid Rafts. *Small* **13**, 1600918 (2017).

207. Njemini, R., Demanet, C. & Mets, T. Comparison of two ELISAs for the

determination of Hsp70 in serum. *J. Immunol. Methods* **306**, 176–182 (2005).

208. Saha, K., Agasti, S. S., Kim, C., Li, X. & Rotello, V. M. Gold Nanoparticles in Chemical and Biological Sensing. *Chem. Rev.* **112**, 2739–2779 (2012).

209. Hu, J., Wang, Z. & Li, J. Gold Nanoparticles With Special Shapes: Controlled Synthesis, Surface-enhanced Raman Scattering, and The Application in Biodetection. *Sensors* **7**, 3299–3311 (2007).

210. Kim, W. *et al.* A label-free cellulose SERS biosensor chip with improvement of nanoparticle-enhanced LSPR effects for early diagnosis of subarachnoid hemorrhage-induced complications. *Biosens. Bioelectron.* **111**, 59–65 (2018).

211. Jiang, Y., Sun, D.-W., Pu, H. & Wei, Q. Ultrasensitive analysis of kanamycin residue in milk by SERS-based aptasensor. *Talanta* **197**, 151–158 (2019).

212. Sur, U. K. & Chowdhury, J. Surface-enhanced Raman scattering: overview of a versatile technique used in electrochemistry and nanoscience. *Curr. Sci.* **105**, 923–939 (2013).

213. Schlücker, S. Surface-Enhanced Raman Spectroscopy: Concepts and Chemical Applications. *Angew. Chem. Int. Ed.* **53**, 4756–4795 (2014).

214. Fikiet, M. A. *et al.* Surface enhanced Raman spectroscopy: A review of recent applications in forensic science. *Spectrochim. Acta. A. Mol. Biomol. Spectrosc.* **197**, 255–260 (2018).

215. Szlag, V. M. *et al.* Molecular Affinity Agents for Intrinsic Surface-Enhanced Raman Scattering (SERS) Sensors. *ACS Appl. Mater. Interfaces* **10**, 31825–31844 (2018).

216. Ilkhani, H., Hughes, T., Li, J., Zhong, C. J. & Hepel, M. Nanostructured SERS-electrochemical biosensors for testing of anticancer drug interactions with DNA. *Biosens. Bioelectron.* **80**, 257–264 (2016).

217. Magdas, D. A., Cinta Pinzaru, S., Guyon, F., Feher, I. & Cozar, B. I. Application of SERS technique in white wines discrimination. *Food Control* **92**, 30–36 (2018).

218. Yoo, S. M. & Lee, S. Y. Optical Biosensors for the Detection of Pathogenic Microorganisms. *Trends Biotechnol.* **34**, 7–25 (2016).

219. Barhoumi, A., Zhang, D., Tam, F. & Halas, N. J. Surface-Enhanced Raman Spectroscopy of DNA. *J. Am. Chem. Soc.* **130**, 5523–5529 (2008).

220. Chan, T.-Y. *et al.* SERS Detection of Biomolecules by Highly Sensitive and Reproducible Raman-Enhancing Nanoparticle Array. *Nanoscale Res. Lett.* **12**, 344 (2017).

221. Jaworska, A., Pyrak, E. & Kudelski, A. Comparison of the efficiency of generation of Raman radiation by various Raman reporters connected via DNA linkers to different plasmonic nano-structures. *Vib. Spectrosc.* **101**, 34–39 (2019).

222. Joseph, M. M. *et al.* Exploring the margins of SERS in practical domain: An emerging diagnostic modality for modern biomedical applications. *Biomaterials* **181**, 140–181 (2018).

223. Tran, V., Walkenfort, B., König, M., Salehi, M. & Schlücker, S. Rapid, Quantitative, and Ultrasensitive Point-of-Care Testing: A Portable SERS Reader for Lateral Flow Assays in Clinical Chemistry. *Angew. Chem. Int. Ed.* **58**, 442–446

(2019).

224. Ngo, H. T., Wang, H.-N., Fales, A. M. & Vo-Dinh, T. Plasmonic SERS biosensing nanochips for DNA detection. *Anal. Bioanal. Chem.* **408**, 1773–1781 (2016).

225. Agnolucci, M., Tirelli, A., Cocolin, L. & Toffanin, A. Brettanomyces bruxellensis yeasts: impact on wine and winemaking. *World J. Microbiol. Biotechnol.* **33**, 180 (2017).

226. Oelofse, A., Pretorius, I. S. & Du Toit, M. Significance of Brettanomyces and Dekkera during winemaking : a synoptic review. (2008).

227. Pollnitz, A. P., Pardon, K. H. & Sefton, M. A. Quantitative analysis of 4-ethylphenol and 4-ethylguaiacol in red wine. *J. Chromatogr. A* **874**, 101–109 (2000).

228. Berbegal, C. *et al.* Starter cultures as biocontrol strategy to prevent Brettanomyces bruxellensis proliferation in wine. *Appl. Microbiol. Biotechnol.* **102**, 569–576 (2018).

229. Lentz, M. & Harris, C. Analysis of Growth Inhibition and Metabolism of Hydroxycinnamic Acids by Brewing and Spoilage Strains of Brettanomyces Yeast. *Foods* **4**, 581–593 (2015).

230. Suárez, R., Suárez-Lepe, J. A., Morata, A. & Calderón, F. The production of ethylphenols in wine by yeasts of the genera Brettanomyces and Dekkera: A review. *Food Chem.* **102**, 10–21 (2007).

231. Steensels, J. *et al.* Brettanomyces yeasts — From spoilage organisms to valuable contributors to industrial fermentations. *Int. J. Food Microbiol.* **206**, 24–38

(2015).

232. Robinson, A. L. *et al.* Origins of Grape and Wine Aroma. Part 1. Chemical Components and Viticultural Impacts. *Am. J. Enol. Vitic.* **65**, 1–24 (2014).

233. Manzano, M., Cocolin, L., Longo, B. & Comi, G. PCR–DGGE differentiation of strains of Saccharomyces sensu stricto. *Antonie Van Leeuwenhoek* **85**, 23–27 (2004).

234. Tofalo, R., Schirone, M., Corsetti, A. & Suzzi, G. Detection of Brettanomyces spp. in Red Wines Using Real-Time PCR. *J. Food Sci.* **77**, M545–M549 (2012).

235. Serpaggi, V., Remize, F., Grand, A. S.-L. & Alexandre, H. Specific identification and quantification of the spoilage microorganism Brettanomyces in wine by flow cytometry: A useful tool for winemakers. *Cytometry A* **77A**, 497–499 (2010).

236. Stender, H. *et al.* Identification of Dekkera bruxellensis(Brettanomyces) from Wine by Fluorescence In Situ Hybridization Using Peptide Nucleic Acid Probes. *Appl. Environ. Microbiol.* **67**, 938–941 (2001).

237. Cecchini, F., Manzano, M., Mandabi, Y., Perelman, E. & Marks, R. S. Chemiluminescent DNA optical fibre sensor for Brettanomyces bruxellensis detection. *J. Biotechnol.* **157**, 25–30 (2012).

238. Borisova, B. *et al.* Disposable electrochemical immunosensor for Brettanomyces bruxellensis based on nanogold-reduced graphene oxide hybrid nanomaterial. *Anal. Bioanal. Chem.* **409**, 5667–5674 (2017).

239. Villalonga, M. L. *et al.* Disposable electrochemical biosensors for

Brettanomyces bruxellensis and total yeast content in wine based on core-shell magnetic nanoparticles. *Sens. Actuators B Chem.* **279**, 15–21 (2019).

240. Lemma, T., Wang, J., Arstila, K., Hytönen, V. P. & Toppari, J. J. Identifying yeasts using surface enhanced Raman spectroscopy. *Spectrochim. Acta. A. Mol. Biomol. Spectrosc.* **218**, 299–307 (2019).

241. Uusitalo, S. *et al.* Surface-enhanced Raman spectroscopy for identification and discrimination of beverage spoilage yeasts using patterned substrates and gold nanoparticles. *J. Food Eng.* **212**, 47–54 (2017).

242. Manzano, M., Vizzini, P., Jia, K., Adam, P.-M. & Ionescu, R. E. Development of localized surface plasmon resonance biosensors for the detection of Brettanomyces bruxellensis in wine. *Sens. Actuators B Chem.* **223**, 295–300 (2016).

243. Su, X., Xu, Y., Zhao, H., Li, S. & Chen, L. Design and preparation of centrifugal microfluidic chip integrated with SERS detection for rapid diagnostics. *Talanta* **194**, 903–909 (2019).

244. Zhang, D. *et al.* Hydrophobic Slippery Surface-Based Surface-Enhanced Raman Spectroscopy Platform for Ultrasensitive Detection in Food Safety Applications. *Anal. Chem.* **91**, 4687–4695 (2019).

245. Zeng, Y., Koo, K. M., Trau, M., Shen, A.-G. & Hu, J.-M. Watching SERS glow for multiplex biomolecular analysis in the clinic: A review. *Appl. Mater. Today* **15**, 431–444 (2019).

246. Zhou, L. *et al.* Robust SERS Platforms Based on Annealed Gold Nanostructures Formed on Ultrafine Glass Substrates for Various (Bio)Applications.

Biosensors **9**, 53 (2019).

247. Ionescu, R. E. *et al.* Surface Enhanced Raman Spectroscopy detection of Brettanomyces bruxellensis yeast on nanostructured ultrafine glass supports. *Optik* 163956 (2019) doi:10.1016/j.ijleo.2019.163956.

248. Vaskevich, A. & Rubinstein, I. Localized Surface Plasmon Resonance (LSPR) Transducers Based on Random Evaporated Gold Island Films: Properties and Sensing Applications. in *Nanoplasmonic Sensors* (ed. Dmitriev, A.) 333–368 (Springer, 2012). doi:10.1007/978-1-4614-3933-2_14.

249. Bonyár, A. *et al.* Investigation of the performance of thermally generated gold nanoislands for LSPR and SERS applications. *Sens. Actuators B Chem.* **255**, 433–439 (2018).

250. Wu, K. *et al.* Gold Nanoparticles Sliding on Recyclable Nanohoodoos—Engineered for Surface-Enhanced Raman Spectroscopy. *Adv. Funct. Mater.* **28**, 1704818 (2018).

251. Rosell, C. M., Barro, F., Sousa, C. & Mena, M. C. Cereals for developing gluten-free products and analytical tools for gluten detection. *J. Cereal Sci.* **59**, 354–364 (2014).

252. Hadjivassiliou, M. *et al.* Gluten sensitivity: from gut to brain. *Lancet Neurol.* **9**, 318–330 (2010).

253. *Concerning the Composition and Labelling of Foodstuffs Suitable for People Intolerant to Gluten*. *OJ L* vol. 016 (2009).

254. Skerritt, J. H. & Hill, A. S. Monoclonal antibody sandwich enzyme

immunoassays for determination of gluten in foods. *J. Agric. Food Chem.* **38**, 1771–1778 (1990).

255. Morón, B. *et al.* Sensitive detection of cereal fractions that are toxic to celiac disease patients by using monoclonal antibodies to a main immunogenic wheat peptide. *Am. J. Clin. Nutr.* **87**, 405–414 (2008).

256. Sealey-Voyksner, J. A., Khosla, C., Voyksner, R. D. & Jorgenson, J. W. Novel aspects of quantitation of immunogenic wheat gluten peptides by liquid chromatography–mass spectrometry/mass spectrometry. *J. Chromatogr. A* **1217**, 4167–4183 (2010).

257. Salmanowicz, B. P. & Nowak, J. Diversity of Monomeric Prolamins in Triticale Cultivars Determined by Capillary Zone Electrophoresis. *J. Agric. Food Chem.* **57**, 2119–2125 (2009).

258. Mamone, G., Picariello, G., Addeo, F. & Ferranti, P. Proteomic analysis in allergy and intolerance to wheat products. *Expert Rev. Proteomics* **8**, 95–115 (2011).

259. Mujico, J. R., Lombardía, M., Mena, M. C., Méndez, E. & Albar, J. P. A highly sensitive real-time PCR system for quantification of wheat contamination in gluten-free food for celiac patients. *Food Chem.* **128**, 795–801 (2011).

260. Svigelj, R. *et al.* Selection of Anti-gluten DNA Aptamers in a Deep Eutectic Solvent. *Angew. Chem.* **130**, 13032–13036 (2018).

261. Masdor, N. A., Altintas, Z. & Tothill, I. E. Sensitive detection of Campylobacter jejuni using nanoparticles enhanced QCM sensor. *Biosens. Bioelectron.* **78**, 328–336 (2016).

262. Funari, R. *et al.* Label-Free Detection of Gliadin in Food by Quartz Crystal Microbalance-Based Immunosensor. *J. Agric. Food Chem.* **65**, 1281–1289 (2017).

263. Niu, L. M., Liu, Y., Lian, K. Q., Ma, L. & Kang, W. J. Characterization of a sensitive biosensor based on an unmodified DNA and gold nanoparticle composite and its application in diquat determination. *Arab. J. Chem.* **11**, 655–661 (2018).

264. Malekzad, H., Zangabad, P. S., Mirshekari, H., Karimi, M. & Hamblin, M. R. Noble metal nanoparticles in biosensors: recent studies and applications. *Nanotechnol. Rev.* **6**, 301–329 (2017).

265. M. Cobley, C., Chen, J., Chul Cho, E., V. Wang, L. & Xia, Y. Gold nanostructures : a class of multifunctional materials for biomedical applications. *Chem. Soc. Rev.* **40**, 44–56 (2011).

266. You, Z. *et al.* Laser-induced noble metal nanoparticle-graphene composites enabled flexible biosensor for pathogen detection. *Biosens. Bioelectron.* **150**, 111896 (2020).

267. Presnova, G. *et al.* Biosensor based on a silicon nanowire field-effect transistor functionalized by gold nanoparticles for the highly sensitive determination of prostate specific antigen. *Biosens. Bioelectron.* **88**, 283–289 (2017).

268. Qin, L. *et al.* “Gold rush” in modern science: Fabrication strategies and typical advanced applications of gold nanoparticles in sensing. *Coord. Chem. Rev.* **359**, 1–31 (2018).

269. Qu, F., Huang, W. & You, J. A fluorescent sensor for detecting dopamine and tyrosinase activity by dual-emission carbon dots and gold nanoparticles. *Colloids*

Surf. B Biointerfaces **162**, 212–219 (2018).

270. Wu, Y., Ali, M. R. K., Chen, K., Fang, N. & El-Sayed, M. A. Gold nanoparticles in biological optical imaging. *Nano Today* **24**, 120–140 (2019).

271. Guliy, O. I., Kanevskiy, M. V., Fomin, A. S., Staroverov, S. A. & Bunin, V. D. Progress in the use of an electro-optical sensor for virus detection. *Opt. Commun.* **465**, 125605 (2020).

272. Singh, R. *et al.* Colorimetric sensing approaches of surface-modified gold and silver nanoparticles for detection of residual pesticides: a review. *Int. J. Environ. Anal. Chem.* **0**, 1–17 (2020).

273. Chiorcea-Paquim, A.-M., Eritja, R. & Oliveira-Brett, A. M. Electrochemical and AFM Characterization of G-Quadruplex Electrochemical Biosensors and Applications. *J. Nucleic Acids* **2018**, 1–20 (2018).

274. Li, Q. *et al.* AFM-based force spectroscopy for bioimaging and biosensing. *RSC Adv.* **6**, 12893–12912 (2016).

275. Miranda-Castro, R. *et al.* Thioaromatic DNA monolayers for target-amplification-free electrochemical sensing of environmental pathogenic bacteria. *Biosens. Bioelectron.* **92**, 162–170 (2017).

276. Batule, B. S., Seok, Y. & Kim, M.-G. Paper-based nucleic acid testing system for simple and early diagnosis of mosquito-borne RNA viruses from human serum. *Biosens. Bioelectron.* **151**, 111998 (2020).

277. Liu, L., Wei, Y., Jiao, S., Zhu, S. & Liu, X. A novel label-free strategy for the ultrasensitive miRNA-182 detection based on MoS2/Ti3C2 nanohybrids. *Biosens.*

Bioelectron. **137**, 45–51 (2019).

278. Lotfi Zadeh Zhad, H. R., Rodríguez Torres, Y. M. & Lai, R. Y. A reagentless and reusable electrochemical aptamer-based sensor for rapid detection of Cd(II). *J. Electroanal. Chem.* **803**, 89–94 (2017).

279. Tan, Y. *et al.* An immobilization free DNAzyme based electrochemical biosensor for lead determination. *Analyst* **141**, 1121–1126 (2016).

280. Akhtar, N. *et al.* Fabrication of photo-electrochemical biosensors for ultrasensitive screening of mono-bioactive molecules: the effect of geometrical structures and crystal surfaces. *J. Mater. Chem. B* **5**, 7985–7996 (2017).

281. Alharbi, R., Irannejad, M. & Yavuz, M. A Short Review on the Role of the Metal-Graphene Hybrid Nanostructure in Promoting the Localized Surface Plasmon Resonance Sensor Performance. *Sensors* **19**, 862 (2019).

282. Jatschka, J., Dathe, A., Csáki, A., Fritzsche, W. & Stranik, O. Propagating and localized surface plasmon resonance sensing — A critical comparison based on measurements and theory. *Sens. Bio-Sens. Res.* **7**, 62–70 (2016).

283. Zhou, L. & Ionescu, R. E. Influence of Saline Buffers over the Stability of High-Annealed Gold Nanoparticles Formed on Coverslips for Biological and Chemosensing Applications. *Bioengineering* **7**, 68 (2020).

Lan ZHOU

Doctorat : Matériaux, Mécanique, Optique, Nanotechnologie

Année 2021

(Bio)fonctionnalisation de nanostructures recuites pour des applications de diagnostic

Les biocapteurs hautement sensibles issus de la nanotechnologie ont trouvé des applications dans divers domaines ces dernières années, grâce à la détection directe, en temps réel et sans marquage de nombreuses substances biologiques et chimiques. Dans le cadre de cette thèse, trois plates-formes de biodétection ont été développées en synthétisant des nanostructures d'or sur trois différents substrats, respectivement une lame de verre recouverte d'oxyde d'indium-étain (ITO), des lamelles de verre et un quartz utilisé dans les microbalances à quartz (QCM). Avec la première plateforme, des biomolécules ont été détectées de façon spécifique en utilisant une analyse spectroscopique dans le domaine des micro-ondes (SMM). La seconde a permis de réaliser un génocapteur utilisant comme méthode de détection optique soit la spectroscopie Raman exaltée de surface (SERS), soit la résonance plasmonique de surface (LSPR). La troisième a mis en œuvre la détection acoustique de l'interaction entre une biomolécule et des nanoparticules bio-fonctionnalisées et réparties de façon contrôlée sur la surface.

Mots clés : biocapteurs – nanostructures – spectroscopie de microondes – résonance plasmonique de surface – microbalances.

(Bio)functionalization of Annealed Nanostructures for Diagnostic Applications

Highly sensitive biosensors derived from nanotechnology have found applications in various fields in recent years, thanks to the direct, real-time and unmarked detection of many biological and chemical substances. In the framework of this thesis, three biodetection platforms were developed on glass substrates. Specifically, glass slide coated with thin layers of indium-tin oxide (ITO), glass coverslip and a quartz crystal microbalances (QCM) were nanostructured. With the first platform, biomolecules were detected by using scanning microwave microscopy (SMM) while the second platform made it possible the fabrication of optical genosensors based on either surface enhanced Raman spectroscopy (SERS) or localized surface plasmon resonance spectroscopy (LSPR). Finally, the third has implemented the acoustic detection of biomolecules on commercial quartz crystal modified with nanostructures in a controlled manner.

Keywords: biosensors – nanostructures – microwave spectroscopy – surface plasmon resonance – microbalances.

Thèse réalisée en partenariat entre :

Ecole Doctorale "Sciences pour l'Ingénieur"